University of Strathclyde

Department of Biomedical Engineering

Artifact Removal in Digital Retinal Images

By

Matteo Menolotto

A thesis presented for the degree
of Doctor of Philosophy

September 2020

This thesis is the result of the author's original research. It has been composed by the author and has not been previously submitted for examination which has led to the award of a degree.

Signed: 

Date: 13/07/2020

“Perché si vede più certa la cosa l’occhio ne’ sogni

che colla immaginazione stando desto”

“The eye sees a thing more clearly in dreams
than the imagination awake”

Leonardo da Vinci

PREVIOUSLY PUBLISHED WORK

PUBLICATIONS

Coghill I, Jordan KC, **Menolotto M**, Black RA, Livingstone IA, Giardini ME. Synthetic stereo images of the optic disc from the CORD dataset. In41st Annual International Conference of the IEEE Engineering in Medicine and Biology Society (EMBC) 2019 Jul 23.

Jordan KC, **Menolotto M**, Bolster NM, Livingstone IA, Giardini ME. A review of feature-based retinal image analysis. Expert Review of Ophthalmology. 2017 May 4;12(3):207-20.

ALSO, UNRELATED TO THIS THESIS

Menolotto M, Rossi S, Dario P, Della Torre L. Towards the development of a wearable electrical impedance tomography system: a study about the suitability of a low power bioimpedance front-end. In2015 37th Annual International Conference of the IEEE Engineering in Medicine and Biology Society (EMBC) 2015 Aug 25 (pp. 3133-3136). IEEE.

CONFERENCE PRESENTATION

Menolotto M, Jordan K, Coghill I, Livingstone I, Gilmour K, Giardini M. Comprehensive Ophthalmic Research Database (CORD): A New Framework for Open Access Ophthalmic Data. In2019 Scottish Ophthalmological Club (SOC) spring meeting. 2019 Feb 22, Stirling.

DATASET

(CORD 2019, 30 March 2019). *CORD Comprehensive Ophthalmic Research Database* [Online]. Available: https://cord.bioe.strath.ac.uk/.

ACKNOWLEDGMENT

First and foremost, I would like to thank my supervisors, in particular Dr Mario Giardini, whose support, sound advice, motivation and infinite source of inspiration have been the lifeblood of my PhD journey and the kick that pushed me towards the finish line. Few are the persons that really had an impact on my way to think and approach to new problems. You are at the top of the list. I will be forever in your debt.

Thanks to Dr Iain Livingstone for his enthusiastic support and friendship during these years. Thank you also for the priceless help for the brainstorming, the clinical work and the data collection. In this regard a big thank you also to Dr Kenneth Gilmour.

Thanks to all the volunteers, who have kindly donated their time “and eyes” to my study, and thanks to the whole department of biomedical engineering of the University of Strathclyde and its staff. I felt like I was part of a big family since the very first day, which has been very important to me.

Thanks to my brilliant team mate Kirsty, undeniably the most important person I’ve met during my PhD, sharing joys and pains. Thank you for your friendship. Thank you for correcting my English, for your smile and for answering to all my strange questions, or at least for trying. I will really miss that.

Thanks to my PhD mates Sokratis, Cheral, Andre, Laura, Richard and Audrey. Your joyful and energetic friendship was very important to me. Thanks to the “new” team members Maria, Ian, Guillermo and Benedetta. Group meetings and lab time with you was never boring or lonely. I wish you all the best!

Thanks to all my friends around the world, who during these years never failed to show me their encouragement and love.

Finally, a massive thanks to my family. This wouldn’t be possible without their love and endless support. Thanks to my father and mother for believing in me and my dreams. Thanks to my brother and sister, there are days I wonder how empty life would be without you. We did it together!

ABSTRACT

Globally 2.2 million people are visually impaired and, of these, approximately 1 million present forms of visual impairment that could be addressed or prevented. Retinal imaging is a key step in the diagnosis and follow-up of major causes of visual impairment. As much as 20% of retinal images collected in the population are affected by artifacts, that render them ungradable both by expert graders and by the more recent automatic grading systems.

This work aims to develop an artifact removal strategy able to improve the effectiveness of retinal image grading, in particular for retinal feature segmentation. First, a large group of statistical parameters designed to measure image quality have been selected from the literature. A new ophthalmic database was then collected (CORD – the Comprehensive Ophthalmic Research Database), which includes retinal images with and without artifacts. A mathematical model describing artifacts on the basis of the interaction of the light with the eye during eye photography was then developed. CORD and the mathematical model were then used to train a binary classifier to distinguish pixels affected by distortions within the image without the need for interpretive knowledge of the image itself and, on the basis of this, to establish a validation criterion for quality improvement in retinal images. Finally, an algorithm was developed to isolate in retinal images the regions affected by artifacts, and to subtract from the images the additive contributions to the distortion.

The artifact clean-up has been shown to increase the textural information of the retinal images, by improving vessel segmentation by more than 10%. By avoiding the use of interpretative elements of the image, this improvement in the quality of retinal images is agnostic to specific disease processes, and thus potentially applicable to population screening. Further work is necessary to improve the cosmetic quality of the images, to optimise the artifact removal strategy, and to relate the feature extraction improvement to clinical performance.

CONTENTS

LIST OF FIGURES

LIST OF TABLES

LIST OF ABBREVIATIONS AND ACRONYMS

Acc	Accuracy
AUC	Area under the curve
BLF	Bilateral filter
BM	Blur metrics
BVC	Blood vessel contrast
BVD	Blood vessel density
CCD	Charge coupled device
CIE	Commission Internationale de l'Eclairage
CMY	Cyan, magenta, yellow
CNN	Convolutional neural network
CORD	Comprehensive ophthalmic research database
CSF	Contrast sensitivity function
CSQ	Clinical standard quality
DD	Disk diameter
DR	Diabetic retinopathy
ELM	Extreme learning machine
FN	False negative
FOV	Field of view
FP	False positive
HSI	Hue, saturation, intensity
IOP	Intraocular pressure
IQR	Interquartile range
ITU	International telecommunication union
LCR	Local contrast ratio
LSCD	Limbal stem cell deficiency
NCA	Neighbourhood component analysis
NCD	Number of correct detections
OC	Optic cup
OCT	Optical coherent tomography
OD	Optic disk
ONH	Optic nerve head
PSF	Point spread function
RGB	Red, green, blue
ROI	Region of interest
SBF	Sliding band filter
Se	Sensitivity
SLO	Scanning laser ophthalmoscope
SNR	Signal-to-noise ratio
Sp	Specificity
SVM	Support vector machine
TN	True negative
TP	True positive
WHO	World health organization

CHAPTER 1. INTRODUCTION

1.1 BACKGROUND

The recent employment of mobile technology (mHealth) (Bastawrous *et al.*, 2016, Giardini *et al.*, 2014), as a portable, easy to use and inexpensive solution for retinal imaging, has shown promising results in boosting the image collection for retinal screening programmes in hard-to-reach areas (S. Philip *et al.*, 2007a). These technology are becoming attractive, particularly in areas where the number of ophthalmologists and clinical facilities are inadequate for the assessment workload (Soto-Pedre *et al.*, 2015). Many of these settings include middle- and low-income countries, but also the isolated communities (e.g. Northern European periphery and islands). However, the implementation of such solutions must be accompanied by effective strategies to face the increased assessment burden enabled by mHealth. The use of automatic or semiautomatic software for the identification of pathological signs in digital retinal images can be a valid aid. The health systems of many industrial countries are currently exploring with keen interest such software, with the prospective of addressing the increasing burden of diabetic and cardiovascular cases (Organization, 2011).

The problem with automatic software concerns the robustness of the assessment process, which highly depends on the quality of the digital image itself. The rate of inadequate quality images (unusable for diagnostic evaluations) in regular retinal screening programmes can reach over one fifth of the total (Yu *et al.*, 2012b, Teng,Lefley and Claremont, 2002, Liesenfeld *et al.*, 2000, Scanlon *et al.*, 2003). This has a direct impact on the workflow of the diagnostic chain (e.g. implementation of subjective/objective quality evaluation tests, recall of patients, false positive, etc.), hence on the effectiveness of the screening. In several mHealth applications, where the limits of the device's optics and the uncontrolled environment illumination cause noise and artifacts, the consequent production of "*non-clinical standard quality images*" can be

even more significant. To mitigate the effect of such distortions on digital retinal images, and improve the effectiveness of mHealth solutions for retinal screening, appropriate *ad hoc* image clean-up strategies need to be developed.

In this work, two different problems are considered in particular: the identification of suitable image quality evaluation systems and the development of filtering algorithms. While for the first topic there is a plethora of different solutions in the retinal imaging field, usually targeted for classification purpose (not-acceptable/acceptable) (M. Niemeijer,Abramoff and van Ginneken, 2006, Pires Dias,Oliveira and da Silva Cruz, 2014, Yu *et al.*, 2012b, Bartling,Wanger and Martin, 2009), for the second the research production is limited. There are many reasons that have led the research community to prefer the development of image quality evaluators rather than try to restore the retinal image content:

- difficulties in determining the statistical characteristic of the features of a digital retinal image that convey the clinical information,
- the lack of publicly available data on retinal image artifacts for noise modelling
- the difficulties in assessing the performance of artifact filtering strategies from a clinical perspective.

However, to take full advantage of the capabilities enabled by mHealth, the development of clean-up algorithms and the better understanding of the impact of image artifacts on the clinical content of retinal images are very much needed.

1.2 AIM OF THE STUDY

This thesis reports the work around the creation of a clean-up strategy for retinal images, designed to mitigate the distortions on some of the most important anatomical features used for clinical assessment (specifically, the blood vessel tree and the optic nerve head) caused by the common artifacts, and able to enhance those statistical components of the digital image that are known to be proxy of the clinical information. To achieve this, an extensive

literature review regarding the state of the art in retinal imaging segmentation and image quality evaluation has been carried out. From this, a wide range of objective statistical parameters have been selected as suitable indicators of the quality/quantity of the clinical information in fundoscopy. Secondly, a simplified mathematical model of the eye, describing how the interaction between the light and the anatomical structure of the eye can originate scattering phenomena and artifacts, was developed. In parallel, a comprehensive ophthalmic database (CORD) was created, with the unique feature of including retinal images affected by artifacts along with the clinical standard quality counterparts (CORD project (*CORD Comprehensive Ophthalmic Research Database*, CORD 2019)). This database was then used to determine a set of statistical evaluators capable of distinguishing between clinical standard quality images and images affected by artifact via clustering. The same paradigm was then used to validate the mathematical model and to assess the performance of the clean-up strategy used on the retinal images affected by artifact collected in CORD.

Specifically, the aims of this study have been:

1. Identification of objective statistical features as proxy of clinical information suitable for image quality classification.
2. The creation of a mathematical model that simulates the generation of artifacts in retinal imaging.
3. Creation of a comprehensive ophthalmic database to inform the parameters required by the model, that includes images affected by a wide variety of common artifact in fundoscopy.
4. Development of a clean-up strategy able to enhance the proxy of clinical information carried by the blood vessels and the optic disc.

1.3 THESIS STRUCTURE

CHAPTER 2 introduces the principles of retinal imaging, its clinical usage and its impact on the clinical workflow, particularly for population screening. Here, the description of the anatomy and the optical properties of the eye is provided, along with an overview of the principal retinal imaging techniques

commonly used in ophthalmology. Subsequently, the main features of a retinal image are described, with particular focus on their diagnostic relevance in the detection and prevention of retinopathies, neuropathies and cardiovascular diseases.

The core topic of clinical quality in digital retinal imaging is then analysed in **CHAPTER 3**. Texture, in the context of this work, is defined as the distribution of pixel colour and luminance which conveys information on the structural arrangement of the different retinal structures (e.g. blood vessels, dark lesions, etc.) and on how they differ between a healthy and a pathological retina. In particular, the importance of the textural information in the diagnostic assessment process is discussed, highlighting how texture is differently interpreted by clinicians and computer vision algorithms. A wide range of the statistical descriptors for quality in retinal imaging is then presented, analysing the advantages and the limits of using evaluators commonly used in digital imaging to define criteria to infer the quality of the clinical content of a retinal image.

The creation of such a dataset is described in **CHAPTER 4**. This comprehensive dataset has been collected from volunteers, including many novelties in ophthalmic datasets: quality-related subject information (age, sex, pigmentation), ophthalmic measurements, images from multiple imaging techniques and modalities and, crucial for this work, a subset of images affected by artifacts. Such a subset, together with the good quality images counterparts, is used to identify the statistical descriptors where the variability is higher in the presence of quality distortions. The descriptors are then used to build a quality classifier able to classify retinal images as clinical quality images and artifact images via clustering, as described at the end of the chapter.

In **CHAPTER 5**, the development of a new phenomenological model that describes the formation of artifacts on retinal images is presented. This simplified mathematical model is used to simulate the interaction between the main optical anatomical components of the eye and the light, during

fundoscopy, in non-ideal conditions or in presence of pathological opacification of the clear structures of the eye. The model is then implemented as a computational simulator (Matlab) of artifacts and validated against a set of fundus images affected by artifacts from CORD. In the context of this work, the artifact simulator is used for data augmentation (to reach sufficient number of images affected by artifacts to train the machine learning algorithm for artifact pixel classification) and to establish the correct algorithmic approach to reduce the artifact distortion on the image.

The algorithmic steps of the artifact clean-up strategy developed in this work, the description of each processing stage and the final results are presented in **CHAPTER 6**. The chapter begins by defining the physical and mathematical assumptions around the algorithmic approach of the clean-up strategy. It proceeds with the punctual description of each processing block, providing the numerical values used for the computer simulation on the CORD images affected by artifacts. It concludes presenting the results of the clean-up process.

Discussion and conclusions over the implementation of the clean-up strategy and its possible use in clinical practice is highlighted in the last chapter, **CHAPTER 7**. The review of the aims of this study is discussed with emphasis on the benefits for the clinical workload, especially in screening programmes. The closing section proposes recommendations for future works and implementations.

1.4 PRINCIPAL RESULTS AND NOVELTY

The work has entailed the acquisition of a retinal image database (CORD). CORD is the first database to date to contain a wide range of multimodal data from the same eye, correlated with information regarding the devices settings that generated those data, and a systematic subset of images affected by standard artifacts. The use of such a subset was crucial for the creation of a feature-agnostic image quality classifier for retinal images, also original to this thesis. Moreover, uniquely to this thesis, the selection of statistical features

used in the classifier is the result of a distance metric learning process that aims to identify the features that are mostly affected by image artifacts.

Another significant contribution has been the creation of an artifact simulator, here used for data augmentation and to justify the mathematical approach in the image clean-up process. This simple, modular and parametric approach can (in principle) also be used to indirectly infer diagnostic information starting from the image affected by distortion caused by pathological conditions (e.g. cataract). It can be reasonably envisaged that this can be used as a diagnostic tool, with benefits for a medical imaging diagnostic and screening programme.

Finally, a clean-up process for retinal image artifacts that is able to retrieve part of the textural content of an image, uniquely agnostic to the specific textural elements to be retrieved, has been developed.

CHAPTER 2. LITERATURE REVIEW

2.1 RETINAL IMAGING

Since its inception in 1970s, digital imaging has started a real revolution in the medical world, transforming diagnostic and enabling the creation of new medical techniques. What was previously a film photograph now is a matrix of digital pixels, of which intensity level can be enhanced, quantified, and correlated to each other by advanced image processing tools, disclosing more information content then what was previously accessible. Ophthalmology, as we know it today, is the perfect example of this new digital age (Chatziralli *et al.*, 2012, Millbank, 2013). Retinal imaging (or fundoscopy), in particular, has fully exploited this transformation becoming the elective diagnostic technique for large number of age-related diseases and diabetes complications, which are amongst the leading causes of visual impairment and blindness in the world (Pascolini and Mariotti, 2012b). The retina is the only part of the human body where blood vessels and neurons can directly be observed with non-invasive techniques. It is therefore considered as the window to the general health of a person, through which we haven't yet finished exploring the whole landscape (Abramoff,Garvin and Sonka, 2010).

The complexity and the richness of the retina's features, and therefore of the digital retinal image, is particularly appealing both for doctors and image processing developers. More and more elements of the eye are being discovered to have a direct connection with cardiovascular conditions and brain diseases thanks to the observation of the morphological changes enabled by fundoscopy (London,Benhar and Schwartz, 2013, Gerald Liew and Wang, 2011). In this chapter, a brief overview of the anatomical structures and function of the eye is provided, followed by the description of the state of the

art of retinal imaging techniques and imaging acquisition strategies employed by modern ophthalmology for population screening.

2.1.1 THE EYE: ANATOMY AND FUNCTION

The principal anatomical structures of the human eye are shown in **Figure 2.1**. The human eye can be divided into two halves, the *anterior* and *posterior segments*. The anterior segment is composed by transparent structures that interface between the external world and the retina, the actual light-sensitive structure of the eye, and, thanks to their curvature and refractive index, provide the refractive power of the eye. It is functionally composed of the cornea, the lens, and the iris. The posterior segment of the eye is referred to as the *fundus*, where the retina lies, and it is connected to the visual cortex of the brain via the optic nerve (Atchison and Smith, 2000, Rosenfield and Logan, 2009).

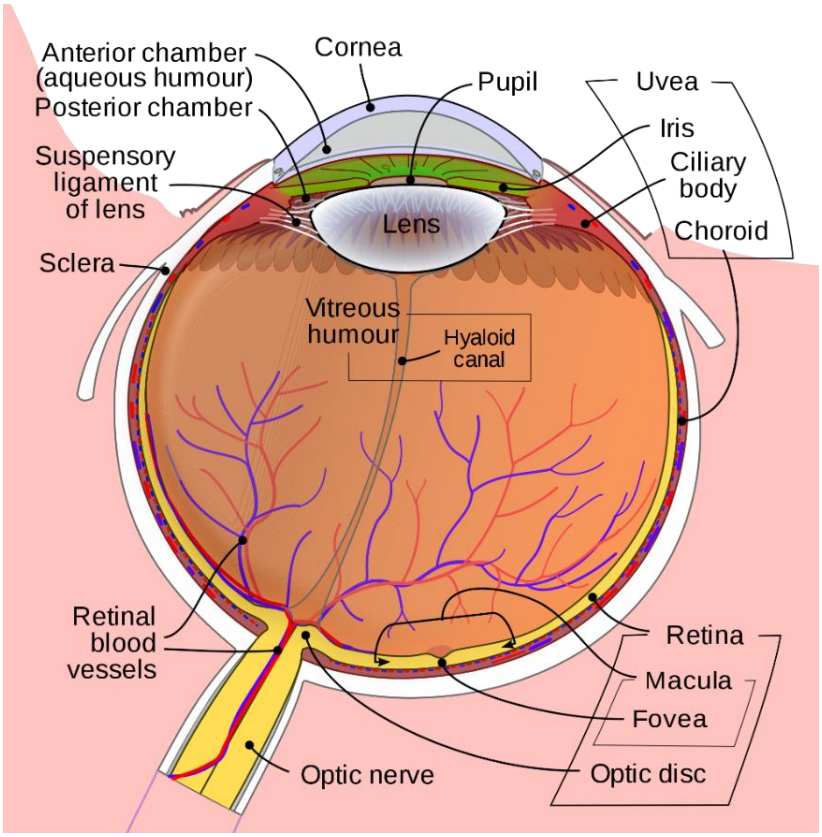

Figure 2.1 The horizontal cross section of the right eye as seen from above, nasal side on the left (Rhcastilhos. And Jmarchn).

Sclera and cornea

The spherical outer layer of the eye ball consists of the sclera, a white, opaque fibrous tissue that serves as a protection against injuries, and for mechanical support. In the anterior segment of the eye, the sclera becomes a transparent structure called cornea. The majority of the refractive power of the eye (two third) is provided by the combination of this multi-layer structure and the anterior chamber (Atchison and Smith, 2000). From the cross-sectional view (**Figure 2.2**), six different layers can be identified: tear film, the epithelium, Bowman's membrane, the stroma, Descemet's membrane and the endothelium.

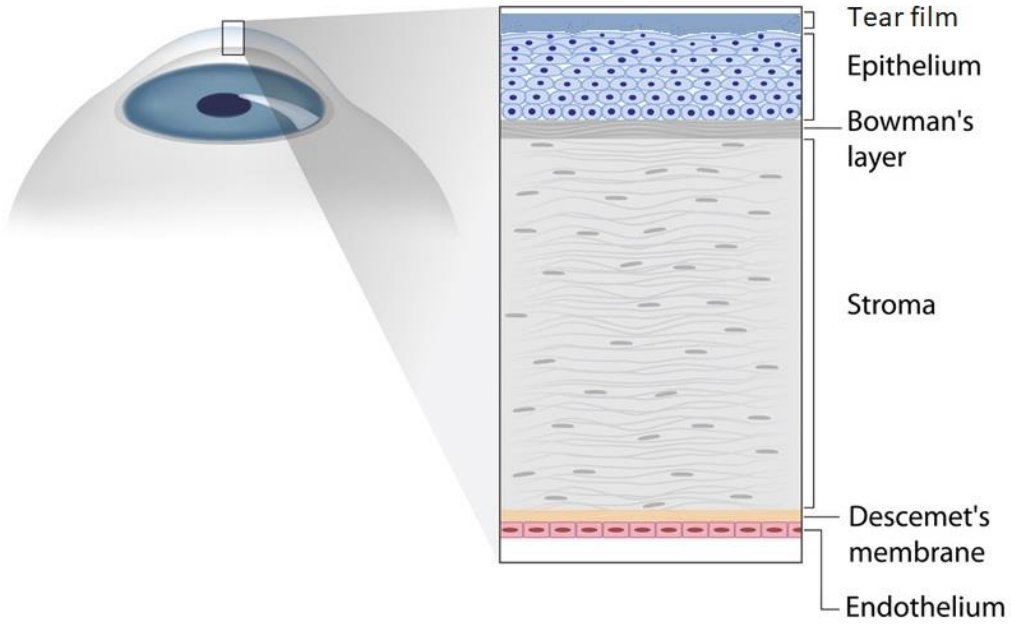

Figure 2.2 Structure of the cornea (adapted from(*Eye7 Eye Hospitals*)(*Eye7 Eye Hospitals*)(*Eye7 Eye Hospitals*)(*Eye7 Eye Hospitals*) (*Eye7 Eye Hospitals*)).

The *tear film* is a 4-7 µm thick mucous layer composed 98% by water. It plays a key role in clear vision as it moistens the cornea and smooth out any roughness caused by the surface epithelial cells. The corneal *epithelium* is a 50 µm thick chemical barrier of the outer cornea which protects the eye against water, large molecules, and toxic substances. This is followed by *Bowman's membrane* which is a thin layer (8–14 µm) of randomly arranged collagen fibrils above the 500 µm thick *stroma*. The stroma is composed of approximately 250

stacked collagen *lamellae*. Each lamella has a thickness of about 2 μm where the collagen fibrils run parallel to each other. Each lamella run across the cornea at an angle to each other forming an ordered structure that guarantees the transparency while enhancing mechanical strength. Underneath the stroma lies the *Descemet's membrane* (approximately 10 μm thick) which forms the basement layer of *endothelial cells*. The innermost corneal layer is the 5 μm thick *endothelium*. It is composed of hexagonal cells arranged in a honeycomb lattice and allows leakage of nutrients to the upper layers of the cornea. At the same time, the endothelium regulates the fluid balance by actively pumping water out of the cornea to keep it clear and transparent.

Thanks to several population studies, the geometrical and the optical properties of the eye have been statistically evaluated (Sorsby, 1956, Stenstrom and Woolf, 1948, Hogan, 1971, Patel,Marshall and Fitzke, 1993). As for the cornea, experimental distributions of the vertex radii (*R*) and the surface power (*F*) are provided in **Table 2.1**. From these data, some practical equations have been drawn to describe the correlation between the geometric and optic characteristic of the cornea. For instance the existing linear correlation between the anterior and posterior radii of curvature, $R_a = 0.81R_p$ (Patel,Marshall and Fitzke, 1993), from which the surface power can be calculated using the equation

$$F = (n' - n)/R, \tag{1}$$

where n' and n are the refractive indexes of the anterior and posterior surfaces respectively. The total power of the cornea can be calculated from the "thick lens" equation:

$$F = F_a + F_p - F_a F_p d/\mu \tag{2}$$

where d is the vertex corneal thickness and μ is the refractive index of the cornea.

Table 2.1 Thickness of the corneal layers according to Hogan et al. (Hogan, 1971), and radii of curvature R, corresponding power F and asphericity of the anterior surface of the cornea, assuming corneal refractive index 1.376, aqueous index 1.336 and corneal thickness 0.5mm (Patel,Marshall and Fitzke, 1993).

	Anterior	Posterior	Q

Corneal layers	Thickness (μm)	Total thickness	*R*(mm)	*F*(D)	*R*(mm)	*F*(D)		Total F(D)
Tear film	4-7							
Epithelium	50							
Bowman's membrane	8-14							
Stroma	500	~580	7.68±0.40	49.0	5.81±0.41	-6.9	-0.01±0.25	42.2
Descemet's membrane	10-12							
Endothelium	5							

The characteristic asphericity (Q) is caused by the increase in the radius of curvature of the cornea as we move away from the surface apex. The sign and value of Q determines the conicity of the cornea, knowing that a conicoid can be express in the form

$$h^2 + (1 + Q)Z^2 - 2ZR = 0 \ , \tag{3}$$

where Z is the optical axis and $h^2 = X^2 + Y^2$. Sometime asphericity is expressed in terms of a quantity p, which is related to Q by:

$$p = (1 + Q). \tag{4}$$

Between the cornea and the lens there is the anterior chamber, which contains a fluid called aqueous humour. In the middle layer of the eye we find the uveal tract, which is composed of the iris, the ciliary body and the choroid. The iris plays an important optical function by regulating the size of the pupil aperture. The ciliary body regulates accommodation of the lens, and both the ciliary body and the choroid support important vegetative processes (Atchison and Smith, 2000).

Lens

Behind the iris, we find the other important optical structure of the eye, the lens. Like the cornea, it is a transparent structures containing no blood vessels. The nutrients are provided by the aqueous humour. The lens bulk is a mass of

cellular tissue of non-uniform gradient index, contained within an elastic capsule (**Figure 2.3**).

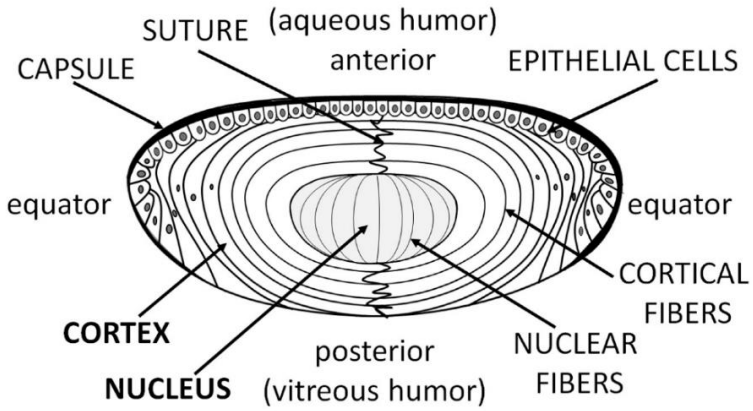

Figure 2.3 Diagram of the eye lens, showing the location of the lens cortex, nucleus, epithelial cells, and layers composed of hundreds of fibre cells (Widomska and Subczynski, 2019).

The anterior layer of epithelial cells maintains the lens by replacing the old layers throughout the entire life. The new cells are originated at the equator and migrate by elongation towards the centre, at the sutures. In this migration the cells lose their nuclei and intracellular organelles, keeping the structure clear. Because of its continual growth, lenticular parameters are age-dependent. A set of ligaments connect the capsule to the ciliary body, the muscles that determine the shape of the lens, by their contraction or relaxation, during the accommodation process. In fact, by changing the shape of the lens, its equivalent power changes, allowing the eye to focus on object at different distances. Geometrical and optical parameters of the lens are summarised in **Table 2.2**.

Table 2.2 Population distribution of in vivo lens vertex radii of curvature, thickness and surface asphericity for relaxed eye (Brown, 1974, Liou and Brennan, 1997).

	Radii of curvature		Thickness (mm)	Asphericity	
	Anterior (mm)	Posterior (mm)		Anterior	Posterior
Lens	12.4±2.6	-8.1±1.6	3.6	-0.94	+0.96

Retina

The retina is an upstream part of the brain which detects light and converts the stimulus to neuronal signal, which are then transmitted by the optic nerve to the visual centres of the brain, where the vision is processed (Atchison and Smith, 2000). It consists of numerous cellular and pigmented layers and a nerve fibre layer (**Figure 2.4**). These layers have different role and optical significance, with the amount of incoming light that is specular reflected, scattered or absorbed by each layer being of particular importance. More insights regarding optical properties of the eye's tissues are discussed in **Chapter 4**. The thickness of the retina varies from ~100 μm at the foveal centre to ~600 μm near the optic disc (Atchison and Smith, 2000, Kaschke,Donnerhacke and Rill, 2013).

The light-sensitive layer is placed at the back of the retina, and is formed by two type of cells: *rods* and *cones*. The different function and sensitivity of these receptors reflect their distribution across the retina (**Figure 2.4**). Rods, generally longer and narrower than cones, are not involved in colour vision but are high-sensitive to low-level light. This is mostly achieved by the extensive nerve fibres network, that connects each rod with other hundreds of other rods, which makes them very sensitive to light but poor in spatial resolution. For this reason, objects that appear bright coloured in day light when seen in moonlight appear colourless, phenomenon known as *scotopic* vision.

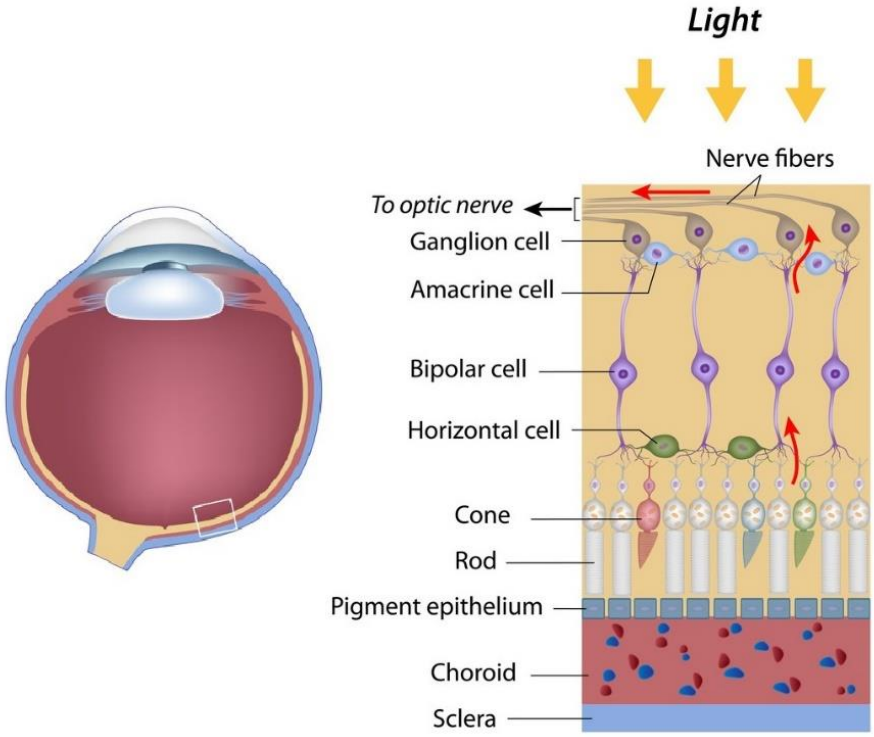

Figure 2.4 Layers of the retina (*The Discovery Eye Foundation*)(*The Discovery Eye Foundation*)(*The Discovery Eye Foundation*)(*The Discovery Eye Foundation*)(*The Discovery Eye Foundation*).

In contrast, cones are connected with fewer other cones so they work at a higher light level and are capable of higher spatial resolution. Cones recover from exposure to light more quickly than rods, and thanks to the existing of different typologies of cones, colour vision, or *photopic* vision, is possible. The area where cones are more concentrated is the macula, which is 1.5 mm wide, and completely free from rods in its central 1° field (Kaschke,Donnerhacke and Rill, 2013, Rosenfield and Logan, 2009). Here, at the centre of the macula, called fovea, the best resolution is attained. The first connection between the cones and the bipolar cells of the neuronal network occurs outside the fovea. Consequently, there are no tissue layers such as ganglion cell and nerve fibre layers (**Figure 2.4**) above the foveal cones, which could cause a low image quality due to scattering of light by these layers. For the same reason, the central part of the macula (500 µm in diameter) contains no retinal capillaries (foveal avascular zone) (Atchison and Smith, 2000). Since rods are not present

in the fovea, this area is basically night-blind. At one common exit point, the nerve fibres penetrate all the outer layer and connect to the brain. Here, at the optic nerve head, the retina does not comprise any photoreceptors. The optic nerve head is located about 10° nasally relative to the optical axis and 1.5° upwards relative to the fovea (**Figure 2.5**).

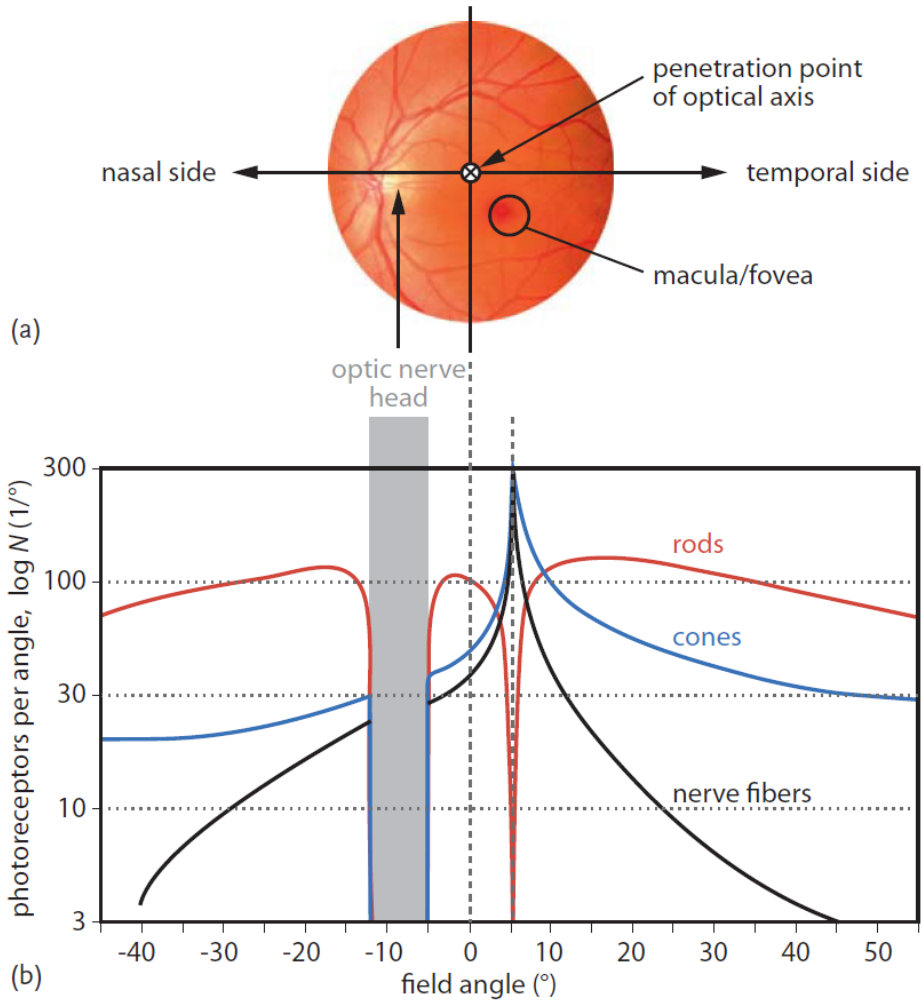

Figure 2.5 a) Functional areas of the retina. b) The density distribution of photoreceptors and nerve fibres across the retina relative to the optical axis (0^0) (Blechinger and Achtner, 2008).

Visual performance

Accommodation – The refractive power of the eye lens can be changed only within a limited range. The upper and lower limits of attainable refractive power determine the *range of accommodation* within which sharp vision is

possible. The endpoints of the range of accommodation are called *far* and *near point*, respectively s_{far} and s_{near}. The inverse distances are called the *far* point refraction $\mathrm{A_{far}} = 1/\mathrm{s_{far}}$ and near point refraction $\mathrm{A_{near}} = 1/\mathrm{s_{near}}$ (**Figure 2.6**). The difference between far and near point refraction is referred to as the amplitude of accommodation

$$\Delta\mathrm{A_{max}} = \mathrm{A_{far}} - \mathrm{A_{near}} \tag{5}$$

The amplitude of accommodation is not constant during life. With advancing age, the elasticity of the lens and thus the range of accommodation decreases. As a consequence, humans usually need spectacles for near vision at the age of approximately 50 (Kaschke,Donnerhacke and Rill, 2013). This reduction of $\Delta\mathrm{A_{max}}$ (**Figure 2.6**), called *presbyopia*, is *not* a refractive error or an eye disease, but a common consequence of aging.

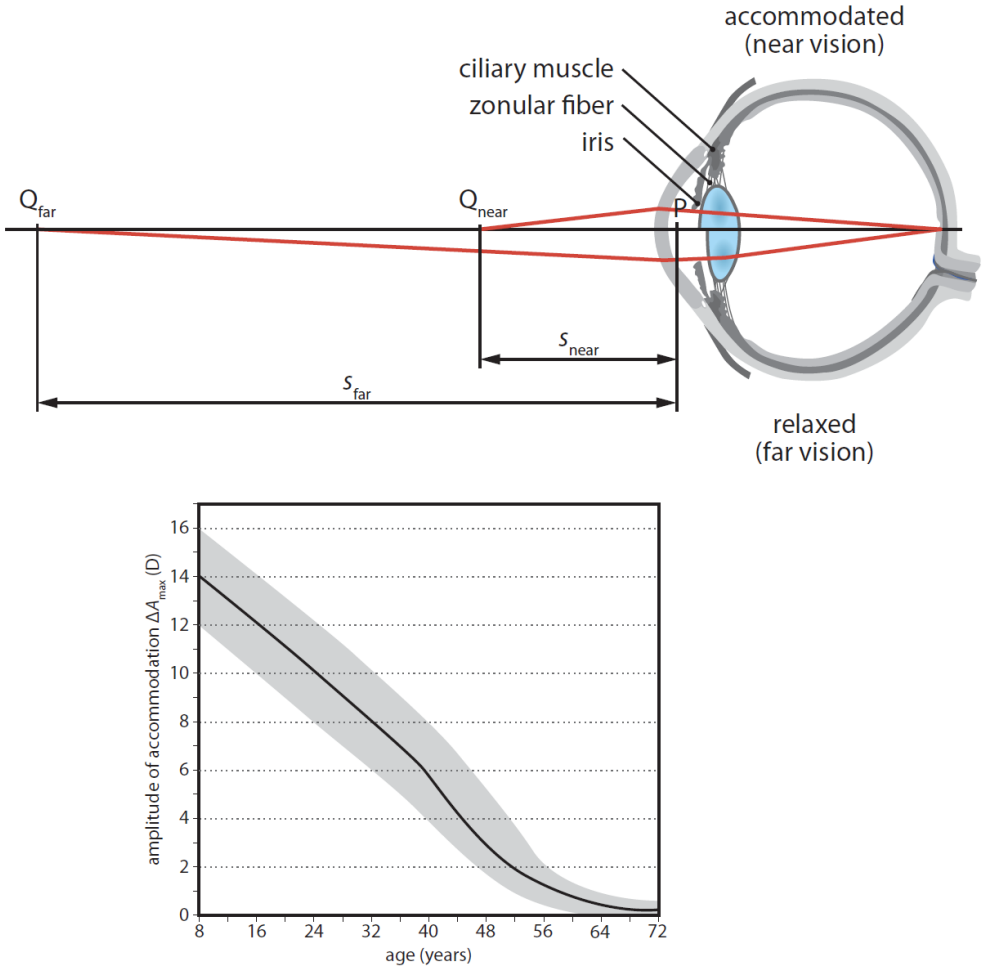

Figure 2.6 Top: physiology of accommodation. When the ciliary muscles are contracted and the zonular fibres are relaxed the lens acquires a more spherical lens (near vision). Bottom: age-dependence of the amplitude of accommodation (Kaschke,Donnerhacke and Rill, 2013).

Light adaption – The eye is able to maintain a high sensitivity to small changes in light intensity across a broad range of ambient luminance levels. Full operation of human vision is possible for a luminance between 10^{-6} and 10^{8} cd/m^2 (Geisler and Banks, 1995). To achieve this, the eye uses two basic mechanisms to adapt to the given ambient light conditions. The first relies on the photoreceptors which are engaged at different illumination level. Rods are used in the scotopic vision and can bear a magnitude of luminance up to 8 orders of magnitude. Cones operates at higher intensity, covering a range of 11 order of magnitude. This adaptation mechanism is regulated by biochemical and neural stimuli and takes few minutes to adjust to the optimal level. To protect the eye from more rapid changes of luminance intensity a faster

mechanism, the so-called *pupil-reflex,* takes place. The inner diameter of the iris diaphragm can shrink, reducing the diameter from 8 mm to 2 mm (**Figure 2.7**), therefore reducing the area of the aperture stop by a factor of 16.

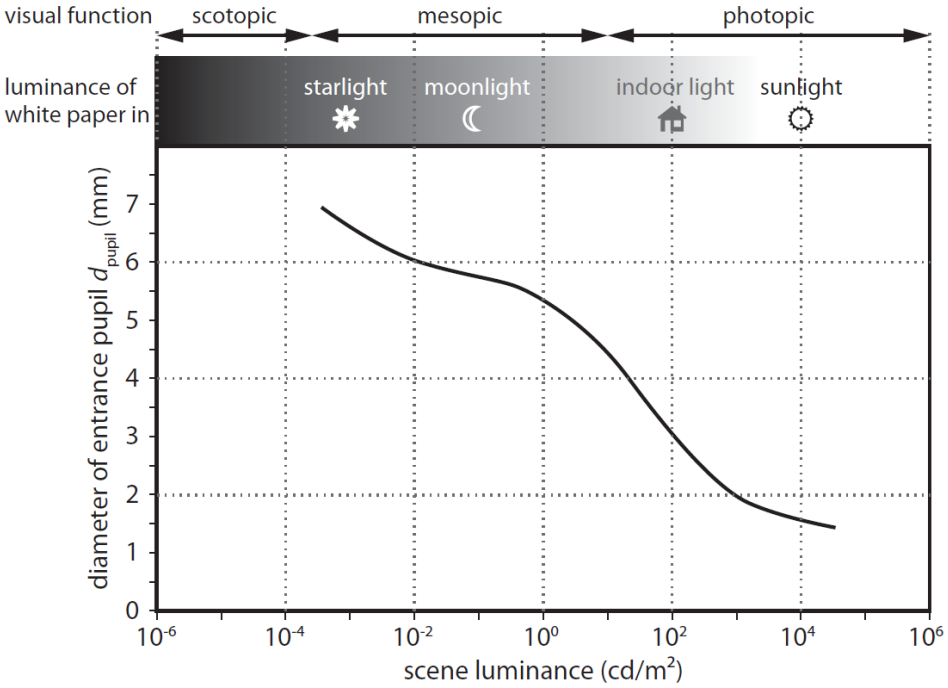

Figure 2.7 Range of illumination levels which can be handled by the eye (Kaschke,Donnerhacke and Rill, 2013).

Spectral properties – The spectrum of the light passing through the clear structures of the eye and reaching the retina is highly determined by the absorption and scattering phenomena of such layers. **Figure 2.8** shows the transmittance spectrum at different passages through the eye. It can be observed that wavelengths below 400 nm and above 1400 nm are totally absorbed by the eye's ocular media, whereas the transmittance remains higher than 0.6 in the spectral range between 420 and 920 nm.

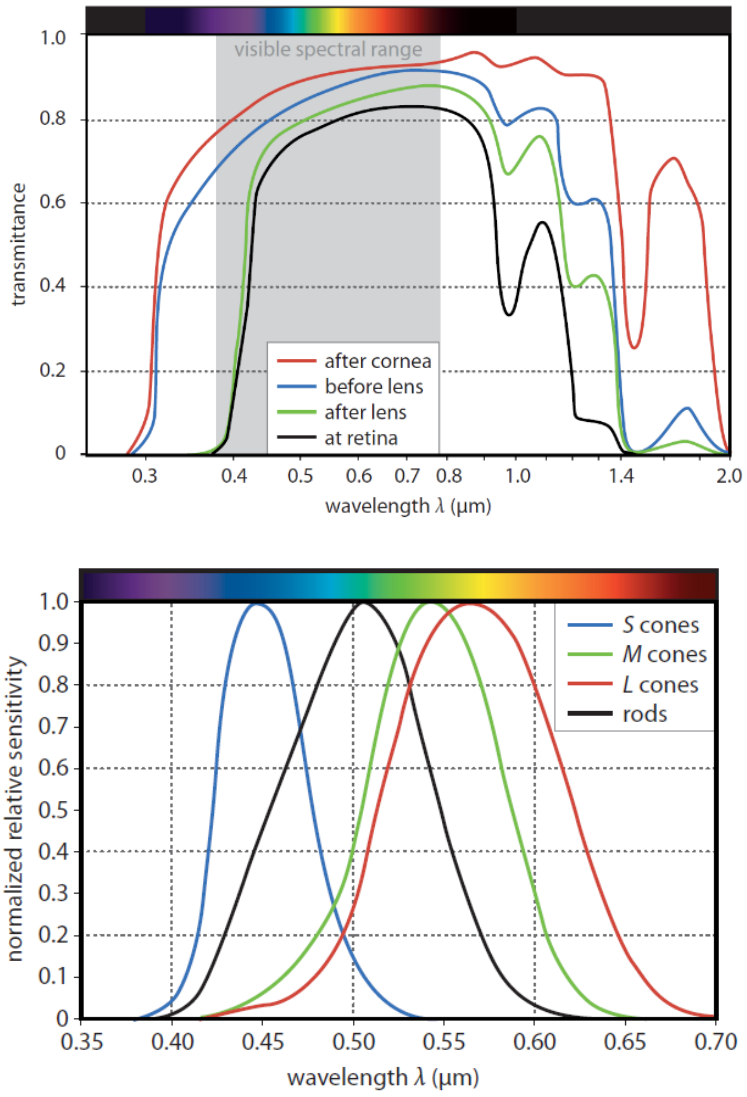

Figure 2.8 Top: Spectral transmittance inside the eye after the incident light has passed the cornea (red), the aqueous humour (blue), the lens (green), and the vitreous (black). Bottom: dependence of normalized relative sensitivity of S, M, L cones, and rods on the wavelength (Blechinger and Achtner, 2008).

Light with wavelengths between 380 and 780 nm can then be processed by the retina, which actually determines the *visible spectrum*. From the mean value of the sensitivity curves of all cones in **Figure 2.8**-top, we obtain a maximum sensitivity at a wavelength of 555nm under photopic conditions. The signals of *S*, *M*, and *L* cones are combined in the brain, resulting in a visual stimulus interpreted as a *colour*. Hence, the colour at which an object appears to us is *not* an inherent property of the object itself, but rather depends on our

visual impression. To give an example, the colour white appears white under illumination at different colour temperatures because, even though the spectrum of the reflected light is wildly different, the vision process combines the photoreceptor signal with prior knowledge to form the perceived colour.

2.1.2 RETINAL IMAGING TECHNOLOGY AND TECHNIQUES

Fundus observation has a relatively short history. The first device capable of observe directly the retina was developed by the eclectic inventor Charles Babbage in 1847 (Keeler, 2003). The paternity of what we now refer to as ophthalmoscope is however attributed to Hermann von Helmholtz (1851). This instrument allowed viewing the interior of a living eye through the pupil for the very first time. The first prototype included a partially transmitting mirror, used to project an external illumination onto the retina, and an additional lens, used to compensate the refractive error of the patient's or/and physician's eye. That simple intuition opened the way to modern fundoscopy.

Today's ophthalmoscopes are not much different from Helmholtz's configuration. To see the retina, the primary condition is that the illumination and the observational paths must be arranged such that the area illuminated and the area observed overlap. Consequently, a beam splitter, pinhole mirror, or half mirror must be added to the observation beam path to attain the required overlap (**Figure 2.9**).

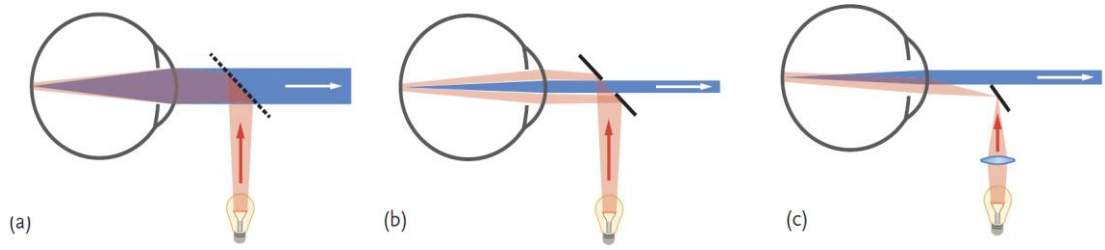

Figure 2.9 General arrangement of illumination and observation beam paths for fundus observation using (a) beam splitter, (b) pinhole mirror and (c) half mirror (or prism) (Kaschke,Donnerhacke and Rill, 2013).

Based on these conditions, two type of ophthalmoscope configurations can be distinguished (Kaschke,Donnerhacke and Rill, 2013, Rosenfield and Logan, 2009):

1. *Direct ophthalmoscopes* in which the patient's fundus is directly observed, and
2. *Indirect ophthalmoscopes* in which an intermediate image of the retina is created and observed.

In direct ophthalmoscopy the illumination and observation beam paths are usually slightly tilted relative to each other to minimize interference caused by corneal reflections. The light source is commonly provided by a xenon-halogen bulb or an LED, which is focused by a condenser and an objective lens onto the tilted mirror. In case the physician and the patient are both emmetropic (without refractive errors), no compensation lens is required (**Figure 2.10**).

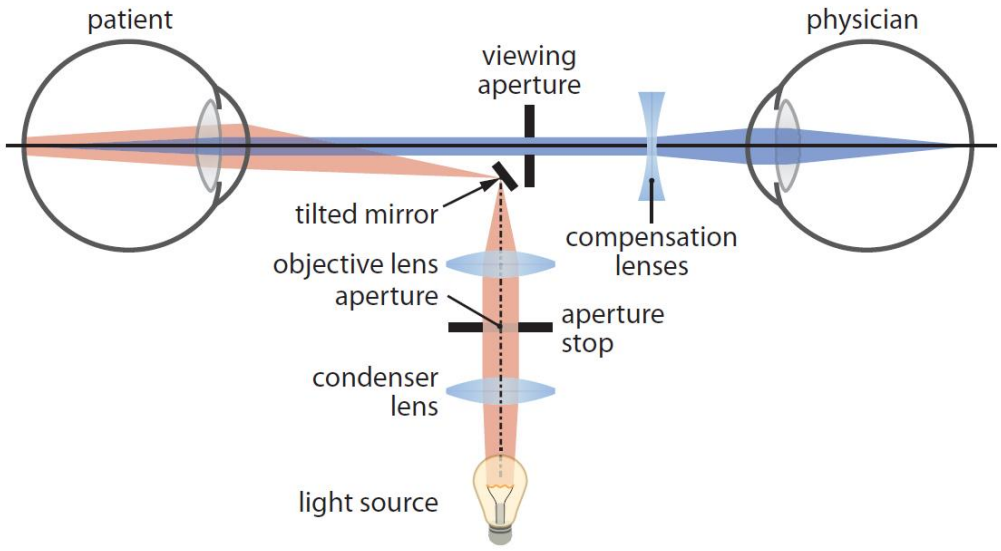

Figure 2.10 Principle of a direct ophthalmoscope. Illumination beam path in red, and the observation path in blue (Kaschke,Donnerhacke and Rill, 2014).

Otherwise, a positive or negative lens can be used to focus the patient's retina onto the physician's one. In this way the image of the retina is not magnified and perceived upright, as the visual cortex of the brain apply an inversion of the image. In this configuration, the portion of the retina that can

be observed, also known as field of view (FOV) or angle of coverage, is given by (Smith,GEORGE and Atchison, 1997):

$$\alpha_{fov} = \frac{d_{pat}+d_{phy}}{L} \quad (1)$$

$$d_{fov} \approx \frac{\alpha_{fov}}{D_{eye}} \quad (2)$$

with $[\alpha_{fov}] = \text{rad}$. d_{pat} is the diameter of the patient's pupil, d_{phy} is the diameter of the physician's pupil, or the diameter of the observation aperture of the ophthalmoscope if this is smaller, and L denotes the distance between the patient's and the physician's pupil. d_{fov} is the diameter of the FOV on the retina, as per **Figure 2.11**.

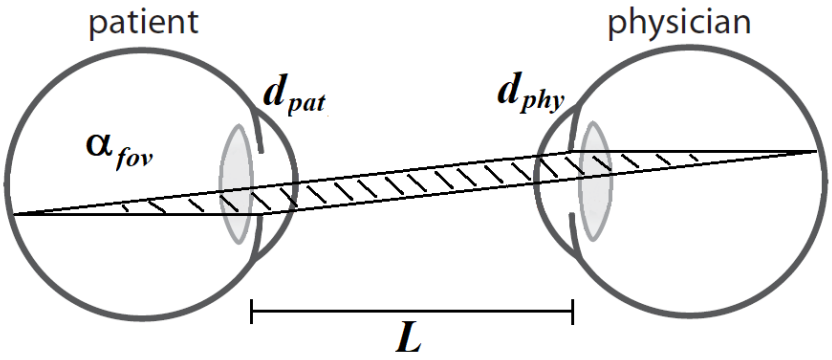

Figure 2.11 Principles of a direct ophthalmoscope. The observable portion of the patient's retina (α_{fov}) is directly proportional of the pupil aperture of the patient and the physician, and indirectly proportional to the distance between them.

Equation 1 describe how the FOV increases when the patient's or the physician's pupil is dilated or when the distance between the two decreases. Considering an emmetropic eye, if $D_{eye} \approx 60D$, $L = 35\text{mm}$, $d_{pat} = 5\text{mm}$ and $d_{phy} = 2\text{mm}$, it follows that $\alpha_{fov} = 0{,}2\text{rad} \approx 11.5°$, which corresponds to the visualisation of a portion of retina of $d_{fov} \approx 3.3\text{mm}$.

In contrast, in the indirect configuration a lens is added between the physician and the patient. It is positioned close to the patient eye, forming a magnified image of the patient's pupil in the physician's pupil plane (**Figure 2.13**). As a result, the ophthalmoscopy lens together with the optics of the patient's eye form an enlarged, inverted, and reversed intermediate image of

the patient's fundus. An evolution of this last configuration is the widely used binocular indirect ophthalmoscope, which provides a 3D impression of the patient's retina, suitable for evaluating glaucoma and retinal detachment (**Figure 2.12**) (Kaschke,Donnerhacke and Rill, 2013).

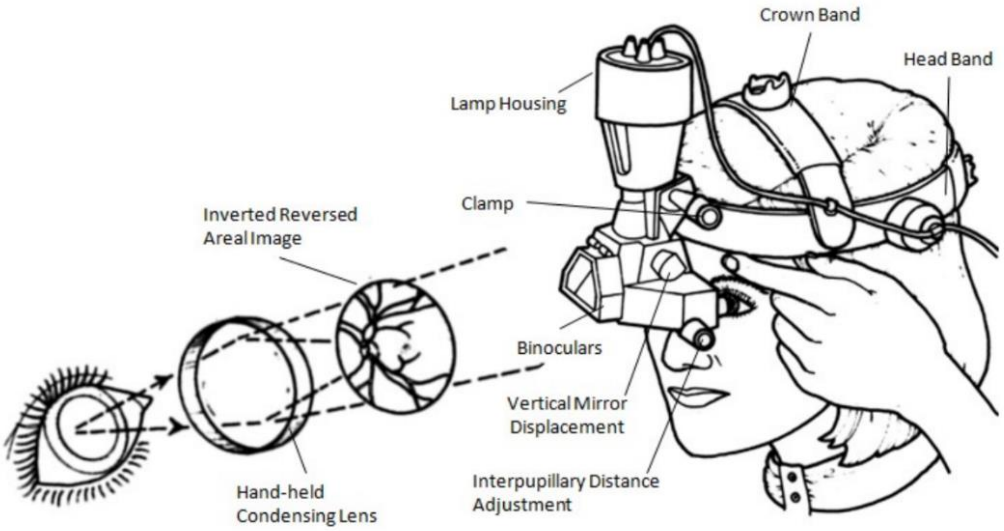

Figure 2.12 Conventional binocular indirect ophthalmoscope (Kong *et al.*, 2009).

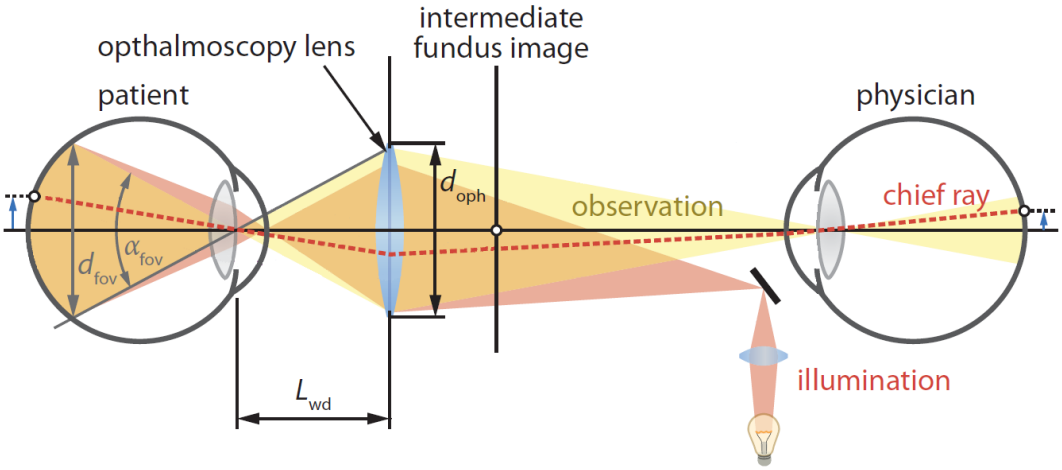

Figure 2.13 Ray diagram of an indirect ophthalmoscope which shows the illumination beam path (red) and the observation path (yellow). L_{wd} is the working distance of the ophthalmoscopy lens, α_{fov} denotes the angle of the retinal FOV, d_{fov} the corresponding diameter of the FOV, and d_{oph} the free diameter of the ophthalmoscopy lens (Kaschke,Donnerhacke and Rill, 2013).

This limited FOV provided by direct ophthalmoscopy is primarily due to the large distance L. In indirect ophthalmoscopy this problem is overcome by imaging both pupils into one common intermediate plane (**Figure 2.13**). In this configuration the FOV observable can be calculated as

$$\frac{\alpha_{fov}}{2} = \tan^{-1}\left(\frac{d_{oph}/2}{L_{wd}}\right) \Rightarrow \alpha_{fov} \approx \frac{d_{oph}}{L_{wd}} \quad (3)$$

where L_{wd} is the working distance of the ophthalmic device from the patient's pupil, d_{oph} is the focal distance of the optics of the ophthalmic instrument, D_{eye} is the total refractive power of the patient. As an example, using the previous data, and considering $d_{oph} = 40\text{mm}$, $L_{wd} = -5.6\text{cm}$ and $D_{eye} \approx 60D$, we obtain $\alpha_{fov} = 0{,}7\text{rad}$ and, using Eq.2, $d_{fov} \approx 11.6\text{mm}$. The significant increase of the FOV is not the only advantage enabled by this configuration. Any possible refractive error of the patient, or the physician, can be easily compensated by adjusting the displacement of the intermediate image plane. This is the reason why indirect fundoscopy instrumentation, such as fundus cameras and optical coherence tomography (OCT) machines, have been chosen as the elective imaging devices to perform assessment of the retina within the clinical workflow (Kaschke,Donnerhacke and Rill, 2014).

A wide variety of imaging devices capable of picturing the fundus has been created based on these configurations. In this work we will focus on the three most widely used in ophthalmic practice: fundus camera, slit lamp and OCT machine.

Fundus Camera - Fundus cameras are the elective instruments used for photographic documentation of the eye fundus (Bernardes,Serranho and Lobo, 2011). The acquired images can be saved in digital format allowing the ophthalmologist to detect any pathology related signs, such as for age-related macular degeneration, glaucoma or diabetic retinopathy (DR), also using computer-aided diagnostic tools (Abramoff,Garvin and Sonka, 2010, Chatziralli *et al.*, 2012). Fundus cameras simplify the clinical documentation and progression control of diseases as well, thanks to the patient referral software that guide the clinician through the image acquisition session. Like in ophthalmoscopy the fundus images are acquired using white light. However,

the fundus camera can be operated in different imaging modalities which substantially expand the diagnostic options (Kaschke,Donnerhacke and Rill, 2013):

- *Monochrome images* - with the use of specific colour filters it is possible to highlight specific fundus structures. For example, when blue light is used, the retinal nerve fibre layer becomes clearly visible.
- *Fluorescence angiography imaging* - allows visualization of blood vessels of the retina and choroid with high contrast via the injection of a fluorescent dye into the bloodstream. Thus, leakages and blockages can be easily detected, and the haemodynamics can be analysed.
- *Fundus autofluorescence imaging* - is used to visualise the topographic distribution of substances which are relevant for the metabolism of the eye. The functional status of the retina can thus be diagnosed at the cellular level. A typical application is the diagnosis of disease-related changes in the retinal pigment epithelium by means of the autofluorescence of the metabolic pigment lipofuscin.
- *Stereo imaging* - normally, fundus cameras produce monocular images. However, acquiring images from two different angles (usually aided by a guided procedure) generates stereo image pairs which can provide a stereoscopic view of the fundus. For example, the stereo imaging mode is used to evaluate the depth and morphology of the optic nerve head in glaucoma diagnosis.
- *Wide-field images* – here, multiple images of different region of the same retina are used to create a wide map of the retina. To obtain that, the patient is invited to focus onto different spatial distributed targets. Each time, an image is acquired and, via image processing software all these images of different portion of the retina are registered (stitched together) forming a big image of the fundus.

The main optical components of a fundus camera are the illumination system (red beam path in **Figure 2.14a**) and the observation system (blue beam path in **Figure 2.14a**) (Kaschke,Donnerhacke and Rill, 2013). The beam

paths of both systems are merged by a pinhole mirror and pass through an aspheric objective lens as well as the refractive parts of the patient's eye. Here, the objective lens L_{obj} plays the same role as the ophthalmoscopy lens of an indirect ophthalmoscope, forming a real intermediate image of the illuminated fundus in front of the pinhole mirror. Behind the pinhole mirror, a second intermediate image is formed by the main objective lens L_{mo}. With a movable focusing lens L_{foc}, the rays are then parallelized (focus at infinity). This flexible configuration enables multiple optical interfaces, which can be used to attach

- high-resolution cameras for image acquisition,
- observer cameras (e.g., infrared CCDs for adjustment purposes in non mydriatic fundus cameras), and
- projection systems (e.g., for fixation targets)

Behind the pinhole mirror, an aperture stop is located which is imaged by L_{obj} into the patient's pupil plane with a decreased image size. It defines the diameter of the exit pupil of the observation beam path and thus the optical resolution of the fundus image.

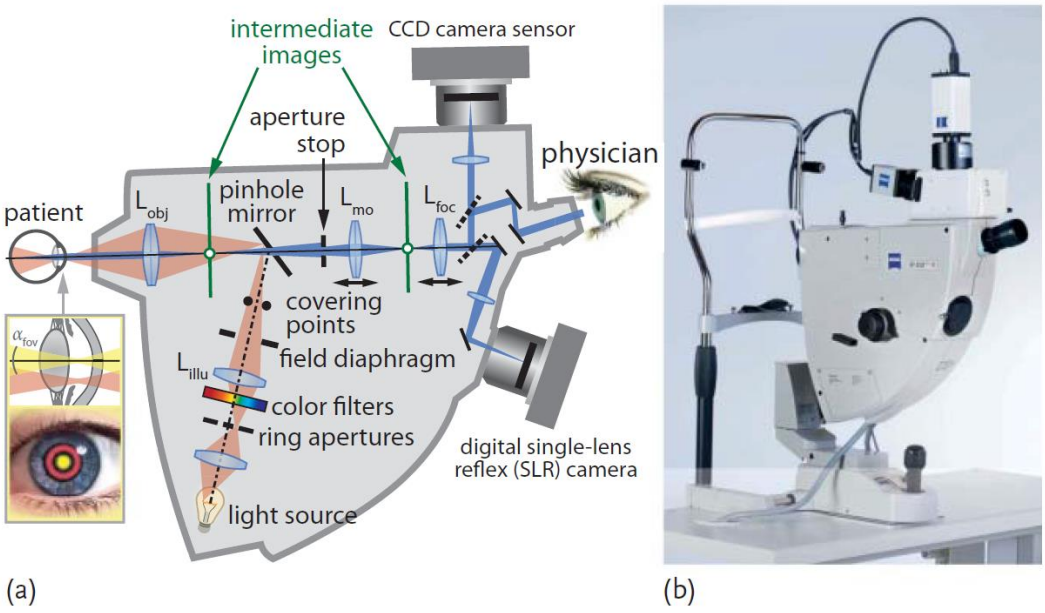

Figure 2.14 (a) Simplified schematic beam path of the ZEISS FF 450^{plus} fundus camera (Carl Zeiss AG, Germany). (b) photograph of the ZEISS FF 450^{plus} fundus camera.

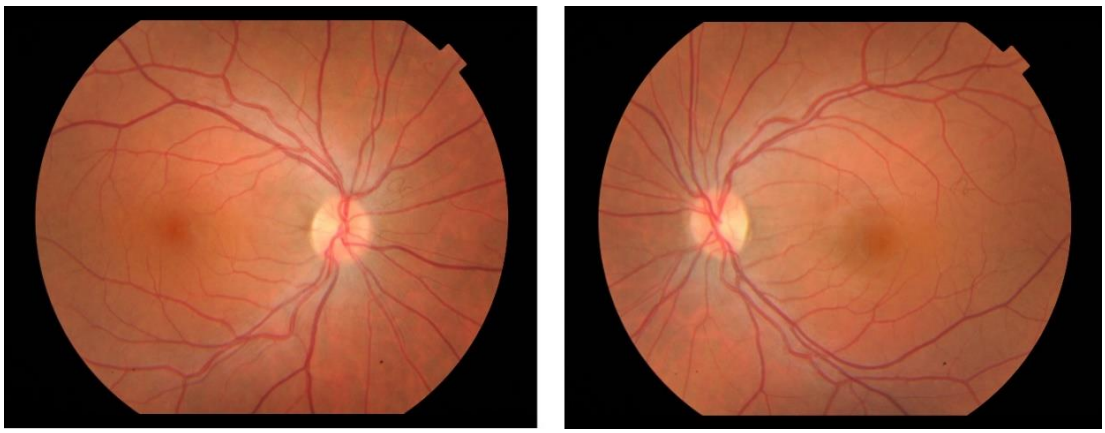

Figure 2.15 Example of retinal images acquired using a fundus camera (Topcon TRC-50DX Type IA fundus camera fitted with the body of a Nikon D300s (Nikon Corp. Japan)), from CORD database (*CORD Comprehensive Ophthalmic Research Database*, CORD 2019).

Modern fundus cameras are capable of producing images that resemble very closely the coloration of a fundus, as seen during direct examination, which is a fundamental factor in diagnostics. High-resolution ultra-widefield imaging is another standard feature in today's technology, with a resolution that goes below 10μm and a field of view of around 200° (>250° with montage post-processing of multiple images). The mechanical design and the digital/manual interfaces of fundus cameras available in the market are capable of offering a comfortable and minimal invasive experience for the patient. This is important for stability in long examination procedures and for making simpler and more reliable use of the device, which increases operator confidence in the results and adds plenty of different auto guided and partially automatic procedures.

Scanning Laser Ophthalmoscope (SLO) – provides wide field images of the fundus. The scanning device uses monochromatic laser light with different frequencies that sweeps across it in a raster fashion, collecting information from multiple layers of the fundus. Reflected light is collected by a light detector and a real-time, piece-by-piece image of the fundus is produced on a digital monitor. As the SLO only illuminates a small area of the fundus at any one time, only a small amount of the patient's pupil is used for illumination, allowing the rest of it to be available for light collection. Most SLO systems are confocal,

whereby a pinhole is placed in front of the detector, conjugate to the laser plane of focus (Webb,Hughes and Delori, 1987). The standard for SLO imaging has been set by Optos Panoramic200 (Optos, Inc., Marlborough, MA, USA). and its “Optomap” approach (Rosenfield and Logan, 2009) (**Figure 2.16**). This device uses a wide ellipsoidal mirror to image the retina through an undilated pupil. Collimated low-powered red and green laser beams are deflected in the horizontal and vertical meridians to scan the fundus in 0.25 seconds, producing a high resolution (up to 2000 × 2000 pixels) digital colour image of virtually the entire retina (200°). Peripheral retinal lesions, difficult to image with conventional retinal cameras, can be observed using this instrumentation.

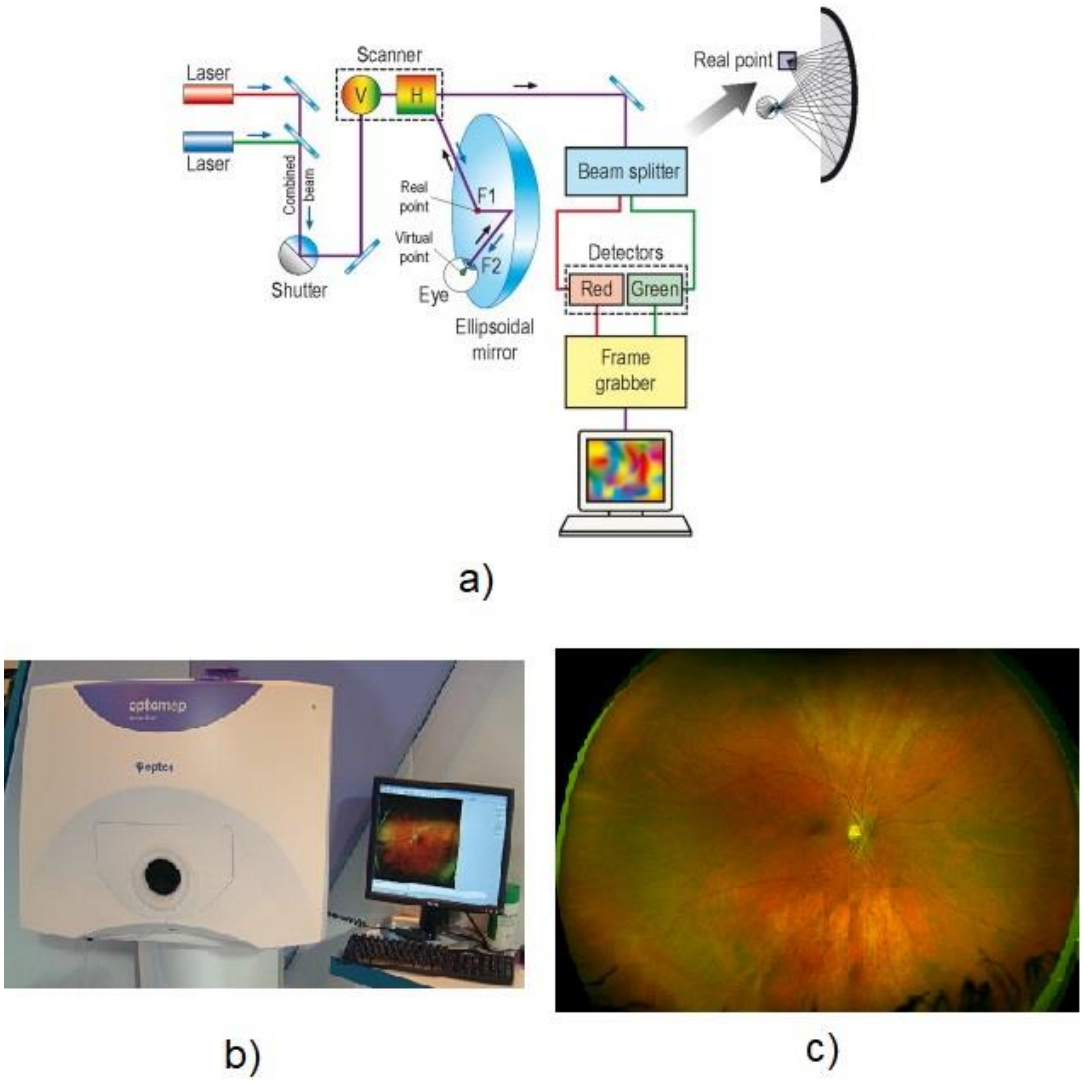

Figure 2.16 a) Scanning laser ophthalmoscope schematic. B) Optos Panoramic200 scanning laser ophthalmoscope. c) Example of ultra-widefield retinal image obtained via SLO (optomap image (*Ophthalmic Imaging*, 2008), Optos, Inc., Marlborough, MA, USA).

OCT – Optical Coherence Tomography machines are used to image retinal areas below the surface at high lateral and axial resolution (Drexler and Fujimoto, 2008). This imaging technique has somehow revolutionised ophthalmology, as this is now one of the most used imaging techniques in diagnostic use. The working principle is similar to an ultrasound B-mode imaging, where the incident light wave is backscattered and backreflected from various tissue layers, with intensity being measured over the time delay (**Figure 2.17**). Rather than through time-resolved detection, this is achieved through interferometric methods (Drexler and Fujimoto, 2008).

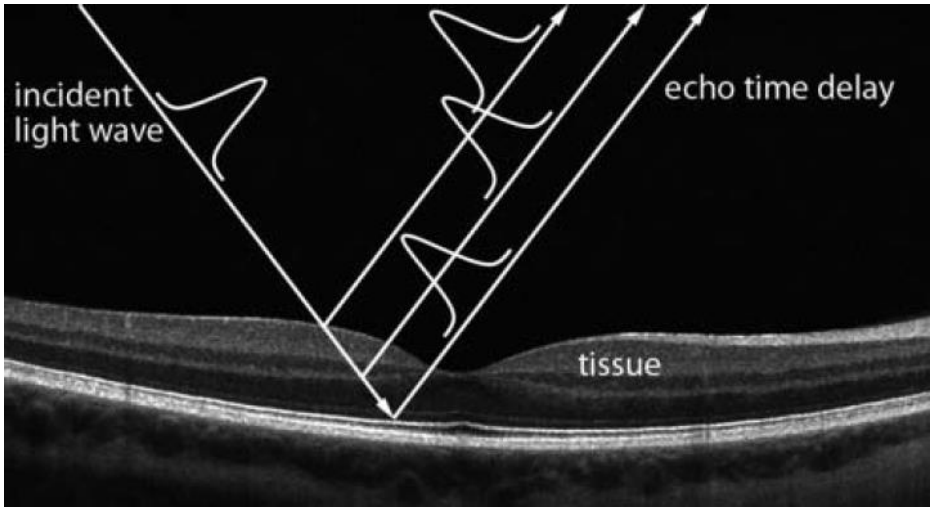

Figure 2.17 OCT 2D scan technique. The time delay of the reflected light is used to reconstruct the axial position of different tissue layers (Kaschke,Donnerhacke and Rill, 2014).

While the principles of the OCT go beyond the scope of this review, we note that this technique has bridged the gap between conventional ultrasound and confocal microscopy imaging, both in terms of resolution and depth of penetration, allowing volumetric and biometric quantitative assessment. The latest generation of OCT are extremely fast, with a high signal-to-noise ratio and no moving parts. To give some context, the most recent OCT machine produced by Zeiss, the CIRRUS 6000, has a depth scan of 2.9mm with an axial resolution of 5μm in tissue. These characteristics make OCT the elective diagnostic technique for macular thickness and advanced retina analysis, anterior segment examination and glaucoma detection (**Figure 2.18**).

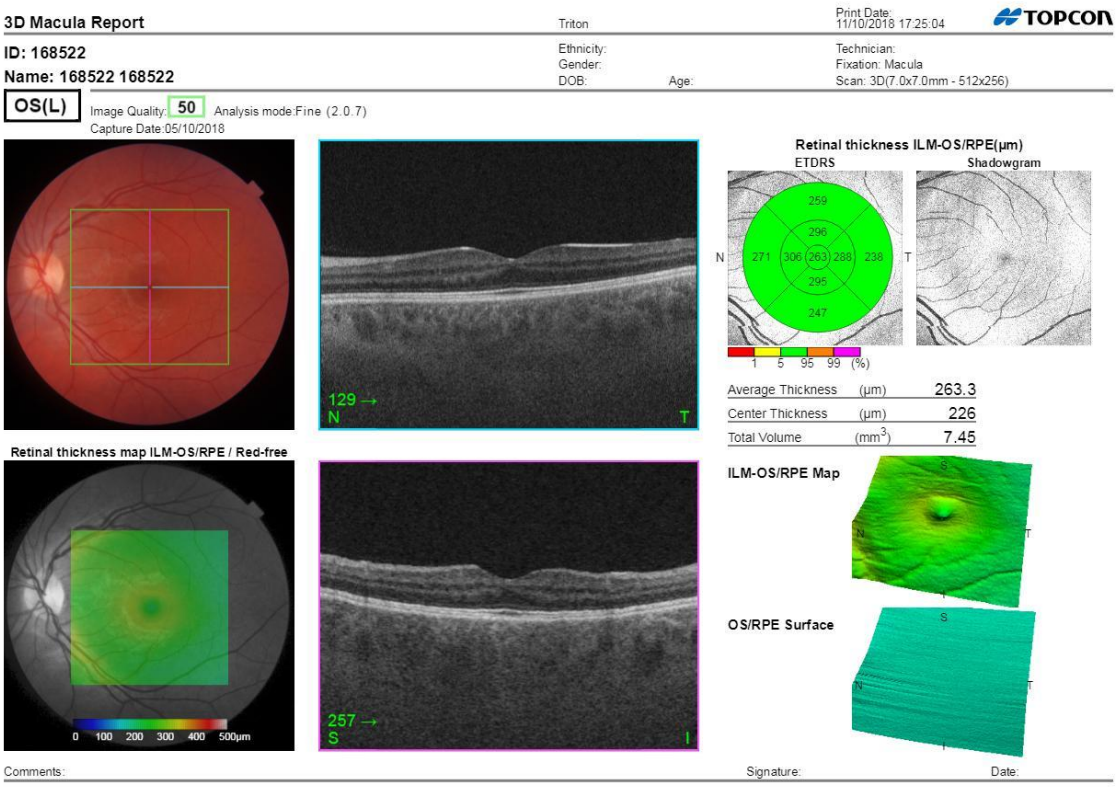

Figure 2.18 Overview of the data provided during an OCT examination (from CORD (*CORD Comprehensive Ophthalmic Research Database*, CORD 2019)). From the left, the first column represents the true colour (top) and the red free image (bottom) of the retina, macula centred. The green square represents the portion of the retina that has been scanned. The central column shows the 2D images of two different cross sections inside the scanning area. The column on the right displays some anatomical information and the 3D reconstruction of the surface of the retina that has been scanned.

Slit lamp - With a standard slit lamp, a direct observation of the posterior eye segment is not possible due to the refractive power of the eye's optical system (**Figure 2.19**). However, the fundus can be observed with an auxiliary lens placed in front of the eye which shifts the far point, and thus the intermediate image of the fundus, to the focal plane of the slit lamp microscope (Kaschke,Donnerhacke and Rill, 2013). For this purpose, positive or negative lenses with high optical power can be used (60D or 90D) (**Figure 2.20**). Positive lenses provide an inverted, real intermediate image. In principle, fundus observation with positive lenses corresponds to indirect ophthalmoscopy. The only difference is that the intermediate image is not viewed with the "naked eye", but with the slit lamp microscope. Compared to

negative lenses, the field of view of the fundus is generally larger with positive lenses, as positive lenses image the entrance pupil of the microscope with reduced size into the patient's pupil.

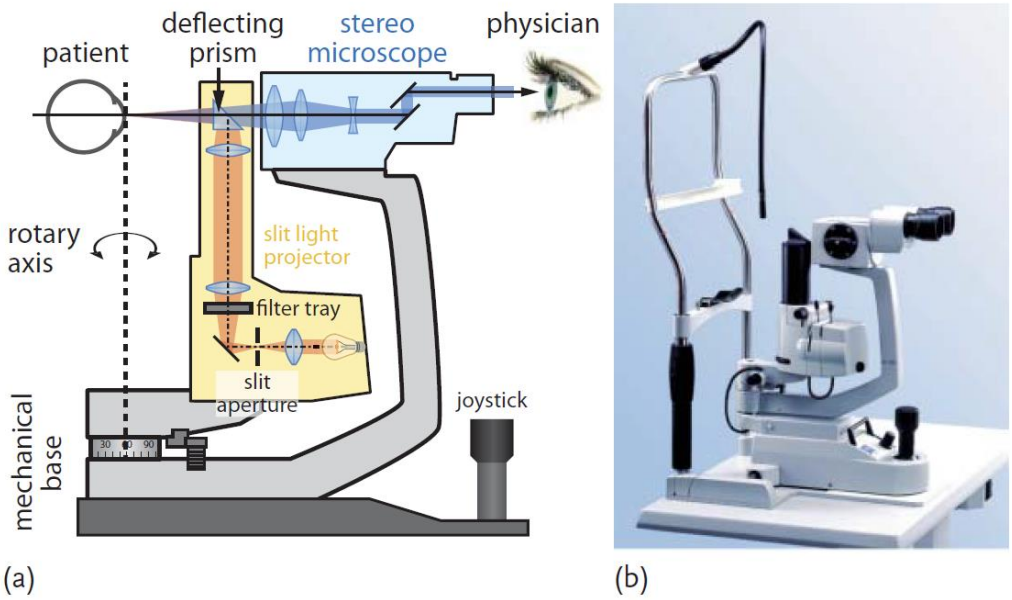

Figure 2.19 a) Basic configuration of a slit lamp. (b) Slit lamp (Kaschke,Donnerhacke and Rill, 2013).

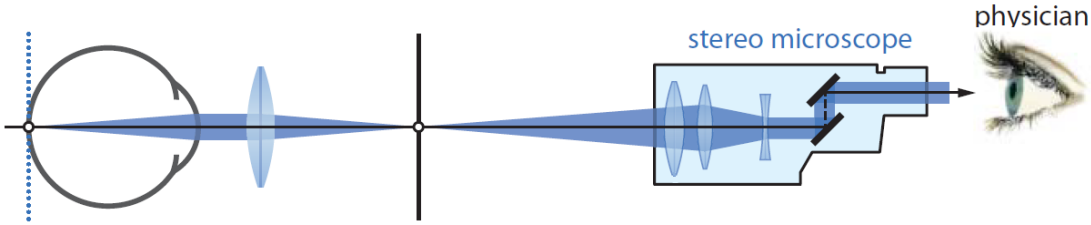

Figure 2.20 Principle of fundus observation via slit lamp. The slit lamp is transformed in an indirect ophthalmoscope by the means of an additional intermediate lens (Kaschke,Donnerhacke and Rill, 2013)

An important sub-group of auxiliary optics are mirror contact glasses. As they have built-in reflective surfaces, the accessible field of view reaches beyond the central fundus area (Rosenfield and Logan, 2009). This optical arrangement thus allows viewing of the peripheral parts of the eye right up to the iridocorneal angle, including the vitreous and the vitreoretinal interface. Commercially available Goldmann three-mirror contact lens usually consist of

a 64D central viewing lens and three lateral mirror surfaces which are arranged at 120° from each other, and tilted at an angle of 59°, 66°, and 73° each (**Figure 2.21**). The procedure requires a great deal of practice and can be uncomfortable for the patient.

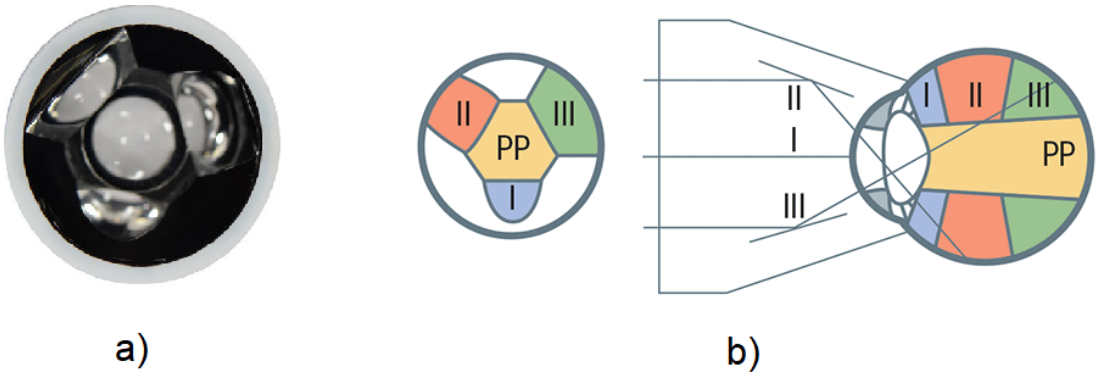

Figure 2.21 a) A Goldmann three-mirror lens. b) The central lens (PP) allows ones to access to the posterior pole, and the three peripheral mirrors 120° apart, at 73° (I), 67° (II) and 59° (III), allow the retinal periphery to be explored (Probert, 2016)

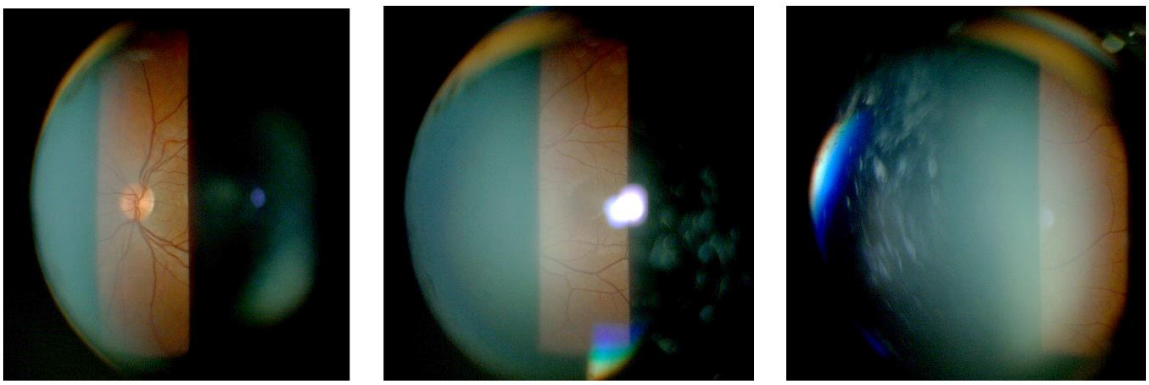

Figure 2.22 Example of slit lamp images of the fundus from CORD database (*CORD Comprehensive Ophthalmic Research Database*, CORD 2019).

Modern slit lamps offer state of the art optics, with anti-reflection coatings and magnification powers that can exceed 40x, to better visualise structural details of the front and the back of the eye. Standard slit lamps include also different illumination features and the colour filters (green filter to better

visualise blood vessels, blue filter to enhance contrast in fluorescence analysis and red filter for observation of the different retina layers).

2.1.3 IMPORTANCE OF FUNDUS IMAGING FOR RETINOPATHIES ASSESSMENT

Fundus imaging has been recognised as one of the most important diagnostic asset for ophthalmologists (Welch, 2014). Thanks to retinal imaging many common eye conditions can be detected, for example, DR (Donald S Fong *et al.*, 2004), age-related macular degeneration (Lim *et al.*, 2012) and glaucoma (Weinreb and Khaw, 2004). According to the World Health Organization these three conditions alone are responsible for 14% of the total avoidable blindness, more than 5 million people globally (Pascolini and Mariotti, 2012a). Moreover, retinal images can be used to identify systemic pathologies that impact on the morphology of the fundus, such as hypertension (Gerald Liew *et al.*, 2009, Sairenchi *et al.*, 2011), malaria (Beare *et al.*, 2006) and neurological conditions (Bidot *et al.*, 2013), as well as offer a source of biomarkers for chronic illness and long-term conditions (MacGillivray *et al.*, 2014). For these reasons, every general practitioner is expected to operate proficiently an ophthalmic imaging device within their basic training (Benbassat,Polak and Javitt, 2012).

The transition from analog to digital imaging, and the recent advancement in medical imaging technology, has enriched retinal imaging with new and more powerful capabilities. Being able to capture and immediately display any repeated images as well as store, transmit and instantly access them remotely, has radically shaped modern ophthalmology. Amongst the advantages, the implementation of computer-aided diagnostic is, in many ways, the most relevant one. Not only for the implementation of new techniques otherwise impossible, OCT and optical bioscopy to name a few, but also for the capability to address immanent and future diagnostic challenges (automatic assessment, large population screening, etc.) (Bruce *et al.*, 2013).

In this prospective, retinal images are the perfect candidates. Their rich level of detail and the high contrast of the anatomical and pathological features,

with respect to the background (**Figure 2.23**), make fundus images very appealing for computer vision scientists. Moreover, all this information is accessible via an imaging technique that is fast and non-invasive.

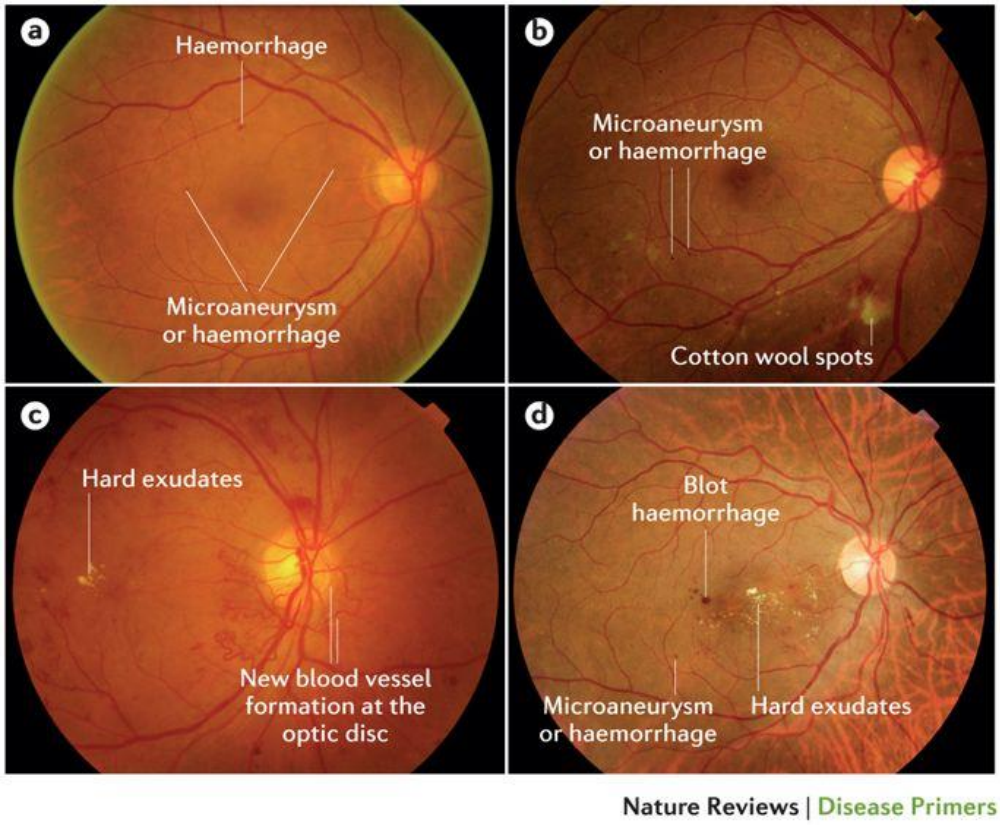

Figure 2.23 Clinical signs of diabetic retinopathy on fundoscopic examination (T. Y. Wong *et al.*, 2016).

2.2 SCREENING PROGRAMMES WORKFLOW

Systematic screening programmes have the potential to prevent visual impairments, and eventually blindness, if widespread and cost-effective principles are applied. To achieve this, an appropriate screening workflow must be designed. This allows the health service administrators to break down the screening process pipeline into its fundamental elements, maximizing efficiency and cost watching at every steps. In particular, the workflow has to take into consideration the following factors: the size of the population involved, the environmental and geographical limits, the health care service capabilities and the financial resources available. The economic aspects are

definitely essential in order to keep the healthcare provision running without structural problems. In the case of systemic diseases, such as DR, screenings have proven to be highly economically sustainable due to the long term benefits. Prevention within the diabetic community, in fact, largely reduces the social and economic impact of DR effects, leading to a sustainable system for the annual national health budget (Looker *et al.*, 2013, Bachmann and Nelson, 1998, Arun *et al.*, 2009).

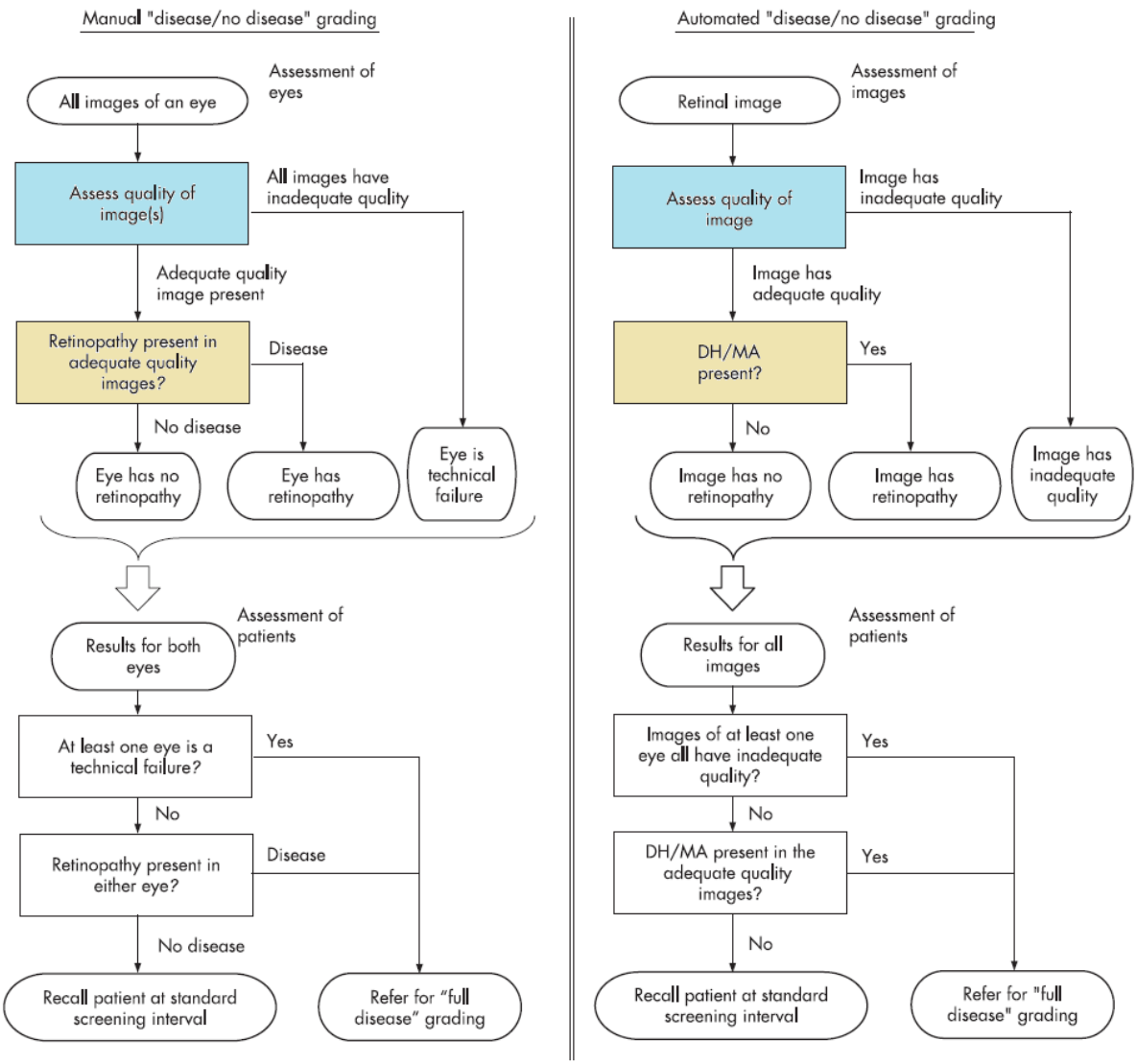

Figure 2.24 Flow charts of the ‘‘disease/no disease’’ manual and automated graded systems for assessment of eyes, images and patients. The automated system detected dot haemorrhages/microaneurysms for diabetic retinopathy screening (S. Philip *et al.*, 2007a).

It’s the case of United Kingdom, where every patient affected by diabetes mellitus over the age of 12 (almost 2 million people (Scanlon, 2008)) is offered an annual retinal examination as it has been shown to be a cost-effective way of reducing visual impairment (Cummings *et al.*, 2002). To handle such a huge number of patients, even for a high-income country, not only the image collection but also the clinical assessment process must follow an optimized scheme. Lately, great expectations have been placed on automatic and semi-automatic software. A good example of image grading workflow is offered by the Grampian Diabetes Retinal Screening Programme in North-East Scotland (**Figure 2.23**) (S. Philip *et al.*, 2007a). In particular, this programme was designed to validate the implementation of an automatic grading system in the assessment chain. The two nodal points in this flowchart of binary decisions are the image quality evaluation (cyan in **Figure 2.24**) and the pathological sign detection (pale yellow in **Figure 2.24**). Both of these steps imply the knowledge of good quality (or clinical standard quality or gradability) for a retinal image and the knowledge of the features associated with a pathological state (or, symmetrically, the knowledge of the features of a healthy retinal image, where everything outside this condition is considered as a potential pathological sign). However, while in the case of the physician this decision is made subjectively based on previous medical knowledge and experience, for software this decision has to be taken via objective measurements, hence the need to translate the human’s decision process into a digital process made of isolated quantifiable steps. This problem, as it will be described in more details further in this work, has different possible solutions, each of them are the very core of the current research activity in the field.

2.2.1 RETINAL IMAGING IN THE FIELD

Medical intervention directly in the field has a number of challenges, whether it’s a low-income setting or an island in the north of Europe. Field medical screening requires essentially three elements: a provisional or mobile setup to perform the medical tests under standard level of quality (e.g.

according to the UK National Institute for Clinical Excellence guidelines, DR screening tests should have sensitivity and specificity of at least 80% and 95% respectively, with a technical failure rate of less than 5% (Excellence, 2001)), trained personnel and an informatics system where personal data can be stored and used for referral, patient identification and follow-up.

In retinal imaging, instrumentation transportation and logistical issues are particularly relevant. Traditional tabletop retinal cameras are high-cost, bulky and designed for skilled operators. The transportation of such fragile piece of equipment over the screening site can represent a big challenge. While vans and trucks can be successfully employed in urban contexts as mobile units (Leese *et al.*, 2008), in rural settings this is not always applicable.

The geographical barriers and the limitations of the health care system, is what low- and middle-income countries, in particular, struggle to address. The vast majority of the “hard-to-reach” or “hidden” audience, in fact, live in low-income settings (Yip *et al.*, 2008, Grunfeld, 1997). The term hard-to-reach is not only used to identify those patients who are difficult to identify for geo-economic reasons (isolated remote or inaccessible areas due to lack of infrastructures) but also those groups that see western medicine with scepticism or mistrust (Bonevski *et al.*, 2014). The “*social cognitive theory*” explains how a person acquires and maintains specific behavioural patterns and how a person’s behaviour influences and is influenced by personal factors and the social environment (“*reciprocal determinism”*) (Bandura, 1977, Bandura, 2001). If the knowledge or importance of accessing screening programmes fails to be transmitted, no intervention strategies will be put in place by that community to overcome that barrier. The other major limit in these areas is the lack of specialists and medical facilities. In the work of Piyasena all this factors have been analysed in a systematic review (Piyasena *et al.*, 2019). Over a total of 77 different studies about problems related to systemic screening programmes were considered, 3 from low-income countries, 11 from middle-income countries, 7 from upper middle-income countries and 56 from high-income countries. Lack of knowledge (19/77), lack of awareness of the screening programme (15/77) and low educational attainment and poor

literacy (16/77) were amongst the principal problems identified at user level (**Figure 2.25**). The reduction of effectiveness of screening programmes has therefore to be accounted for a combination of structural and social factors.

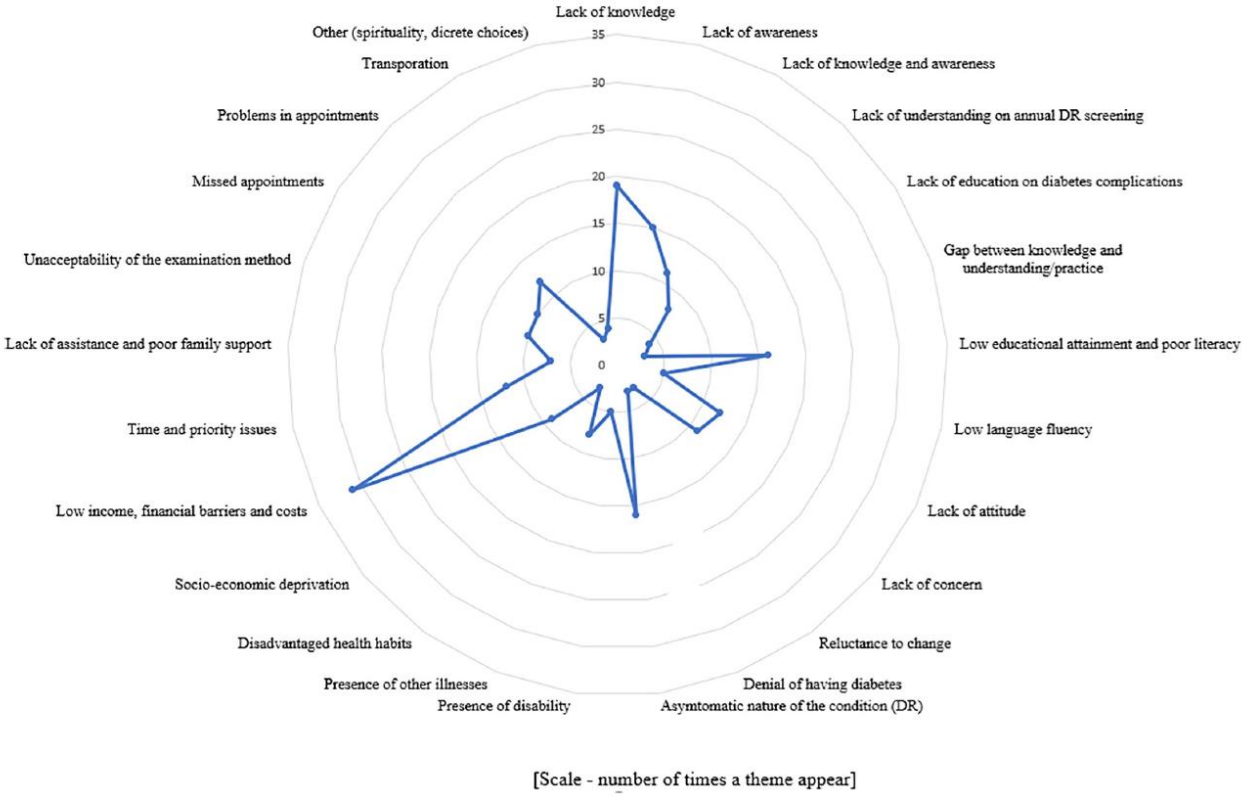

Figure 2.25 Harvest plot showing screening programme user barriers (Piyasena *et al.,* 2019).

2.2.2 MOBILE TECHNOLOGY FOR RETINAL SCREENING

In this paragraph we focus exclusively on mobile technology developed for fundus imaging applications.

According to the definition of the World Health Organisation, mobile e-health or mHealth is *"the use of mobile and wireless technologies to support the achievement of health objectives"* (Organization, 2011). This branch of telemedicine has grown fast in the last decade, thanks to the following advantages (Perera, 2012):

1. *Portability* – Smartphones and tablets are generally small in size and weight, making their transportation easier and less expensive. The

operational functionality is provided by on-board batteries, which can also be recharged via low voltage systems (portable solar panels or other energy harvesting solutions) simplify usage even place disconnected from the main power line.

2. Inexpensive – Compared to classic ophthalmic tabletop devices (≥£10000) smartphones and tablets cost a fraction (<£1000)
3. Easy to use – The intuitively usage of mobile technology is one of the reasons for their incredible success in the market. For the same reason smartphone applications and add-on are relatively simple to master, reducing training time for healthcare personnel and locally recruited operators, boosting ground operations such as population screening.
4. Low barrier of acceptance – a smartphone device looks “familiar”, and there is widespread mobile literacy.
5. Accessibility – the low-price and the ease of use have determined the spread of this technology almost everywhere a mobile cellular network is installed. This has built over time a good literacy of mobile devices which makes them well recognisable for most of the populations, increasing their acceptability especially for medical intervention, respect to the classic bulky, immersive and noisy instrumentation.
6. Embedded computing power – mobile device functionalities are enabled by a processor, memory and hard storage, making them effectively a small computer. This can be exploited to develop image processing and data management system directly on-board.
7. Built in software – a running system operator can be of support for software applications and machine-user interface supports.
8. Internet connectivity - According to International Telecommunication Union (ITU), the number of mobile-cellular telephone subscriptions is greater than the global population. Growth in mobile cellular subscriptions in the last five years was driven by countries in Asia-Pacific and Africa regions. Nearly the entire world population (90%) now

lives within reach of a mobile cellular network. Furthermore, 90% of the global population can access the Internet through a 3G or higher speed network (ITU). Thanks to this spread, images and data acquired in the field can be transmitted in clinical facilities everywhere in the world, optimising resource management and clinical assessment capabilities.

As a result, some smartphone adapters for retinal image acquisition have been validated for screening in the field (Bastawrous *et al.*, 2016) and are now available for purchase on the market (**Table 2.3**).

Table 2.3 Commercially available smartphone adapters for retinal imaging under £1000, at the time of this work (September 2019). Prices are referred to August 2020. Where possible the field of view has been quoted.

Manufacturer	Smartphone adaptors	Description	Cost
Peek Vision	Peek Retina	CE registered class 1 medical device. It is a universal smartphone clip that enables retinal imaging through a dilated pupil. Exploiting the smartphone's inbuilt camera, the clip converts the device in a digital direct ophthalmoscope (Vision).	£180
D-Eye	D-Eye Retina	Works only with iPhone. Smartphone camera clip with illumination and corneal glare suppression filter. Can produce photos and video, with a field of view up to 20°, for clinical assessment (D-Eye).	$544
Volk	Volk iNview	It enables to capture wide-angle (50°) digital colour images of the fundus using an Apple iPhone or iPod. Is composed by a condensing lens attached to a smartphone clip. The user is assisted by an app that facilitate calibration and enables auto capture (Volk).	$799
oDocs Eye Care	oDocs Fundus	It's an open-source 3D printable adapter that converts any smartphone into a fundus camera. It consists of a clip with a mounting bracket for a condensing lens, which allows retinal imaging up to 40° of field of view (Care).	Cost of condensing lens ~£100
	oDocs nun	Capable of both mydriatic and non-mydriatic retinal imaging. It is a portable retinal examination device that can be used with a broad range of smartphones running on the iOS and Android platforms. The device can be used	$1120

		independently as a handheld ophthalmoscope or in conjunction with a smartphone (Care).	
Welch Allyn	iExaminer	Adapter designed to attach the PanOptic Ophthalmoscope to the iPhone. Requires the PanOptic Opthtalmosocope (included in the total cost).	~$1200

Figure 2.26 Smartphone adaptors for fundoscopy applications. a) Peek Retina, b) D-Eye Retina, c) Volk iNview, d) oDocs Fundus, e) oDocs nun and f) iExaminer.

Despite these advantages, mobile technology has been actively introduced in fundoscopy practice only recently. This slow adoption, respect to other telemedicine branches, has primarily been identified with privacy and security concerns, dissatisfaction about content availability (completeness of information regarding a clinical exam) and with the lack of integration of mobile technology in the healthcare screening workflow (N. M. Bolster,Bastawrous and Giardini, 2015, Gagnon *et al.*, 2015, Lo *et al.*, 2012, Maguire *et al.*, 2008).

While these issues are being addressed, the number of applications in ophthalmology screening are increasing across all the different income settings (Armfield,Gray and Smith, 2012, Ayatollahi *et al.*, 2017, Poyser *et al.*, 2019). The majority of the smartphone based retinal imaging adapter are designed as a clip that can be inserted in front of the camera, and generally include: an illumination source (usually LED) to generate the illumination beam, some basic optics (mirror or prism) to overlap the projected illumination beam with the observation area of the retina and a filter or diffuser to reduce illumination intensity and glare (Nigel M. Bolster *et al.*, 2014). Despite the potential for impact these devices have already shown in tackling population screening that there are still some limitations that need to be addressed in order to fully exploit this technology. In particular, image quality in smartphone based fundoscopy still represents a barrier in automatic classification/assessment of retinal images.

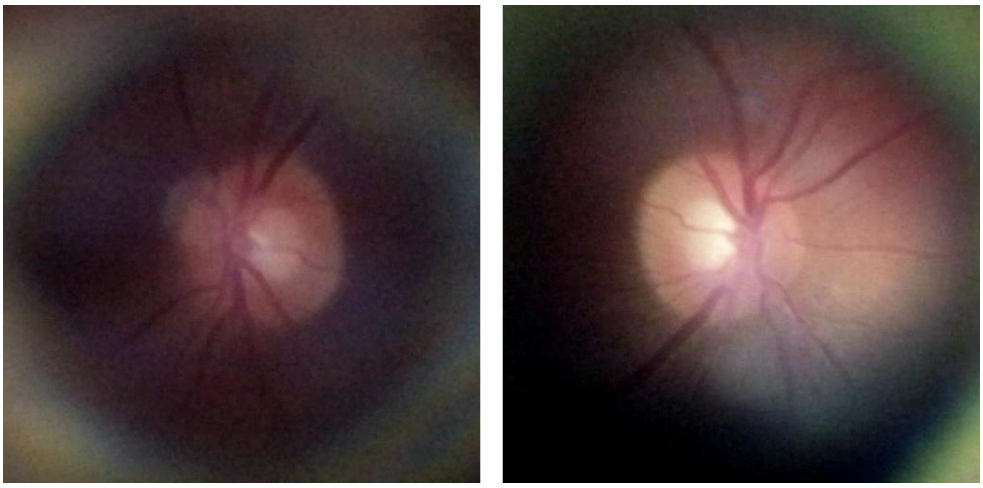

Figure 2.27 Representative mydriatic images of an healthy retina acquired with Peek Retina on a healthy subject (Bastawrous,Giardini and Jordan, 2014).

The substantial difference in quality and chromatic features compared to classic fundoscopy makes these images difficult to analyse for automatic software, necessitating expert manual grading. Some example of images acquired with smartphone adaptors are shown in **Figure 2.27** and **Figure 2.28** (to compare with **Figure 2.15**).

The factors that contribute to the general degradation of the quality of images acquired in the field with smartphone adapters are several. In first approximation, the chromatic degradation and the poor contrast of the images (especially in the peripheral ring) are the most prominent. These are caused by environmental factors and lack of stable link between the camera optics and the patient's eye. While the first is related with the image acquisition setting (provisional clinic or patient's home), where artifact caused by illumination/reflections are difficult to control, the second has more to do with design choice, where devices that use direct contact with the patient to stabilise the image acquisition have to deal with patient acceptability, hygiene and disinfection problems. In **Chapter 3** and **Chapter 4** the complete description of those phenomena are detailed.

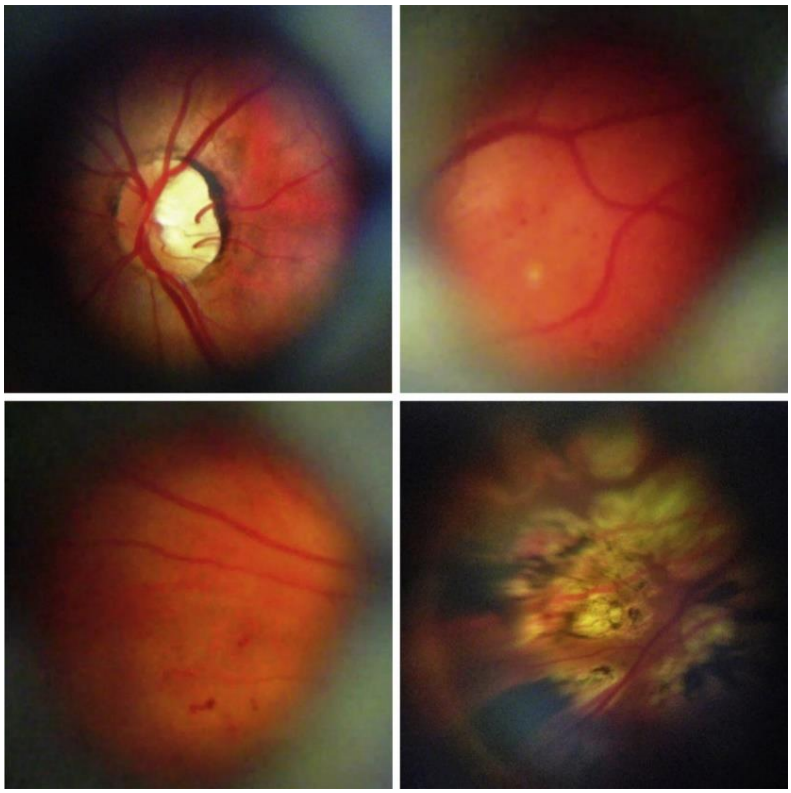

Figure 2.28 Representative retinal images of diabetic retinopathy taken with D-Eye. (Top left) Optic disc in a retina with no apparent diabetic retinopathy. (Top right) Mild non-proliferative diabetic retinopathy. (Bottom left) Moderate non-proliferative diabetic retinopathy. (Bottom right) Panretinal photocoagulation scars in a proliferative diabetic retinopathy. (Russo *et al.,* 2015)

The quality of the image sensor of mobile technology is not an issue as this has shown to constantly improve over time, with the new smartphone and tablet generations expected to be more and more suitable as clinical imaging tools. The image acquisition environment and modality (ambient illumination, reflections, device optics artifacts, device illumination artifacts, etc.), however, have a direct impact on the formation of noise and artifacts on mHealth retinal imaging.

CHAPTER 3. IMAGE QUALITY IN RETINAL IMAGING

3.1 RETINAL FEATURES: MORPHOLOGY AND CHROMATICITY

As described in the previous chapter, imaging the fundus of the eye is not very different from trying to peek inside a dark room through the door's keyhole (pupil). The light needs to be projected through the pupil, and the focus of the optics has to be adjusted to match the focal plane corresponding to the retina. For this reason, any element that interacts with the imaging acquisition process is potentially a source of unwanted alteration of the final image chromaticity and morphology. In the clinical setting these alterations are kept to a minimum, or, more properly, to a level that guarantees a high rate of images whose quality is sufficient to perform a clinical assessment. From now on, we will refer to this level of quality as "clinical quality". When collecting retinal images in the field, the sources of alteration are far less controllable, therefore the rate of clinical quality images can drop massively (Yu *et al.*, 2012b).

To understand the differences between the two scenarios, we shall look at **Figure 3.1**. Here, two true colour fundus images are compared: the left image comes from a fundus camera operating in a clinical facility, while the image on the right has been obtained with a smartphone operating in the field. A classic clinical quality retinal image appears as a rectangular picture displaying a circular portion of the retina on its centre (the FOV covered by classic fundoscopy can vary between 30° and 60°, ~5mm to ~10mm), framed by a black uniform background (**Figure 3.1**, top). The image obtained in a non-clinical setting by a mobile device, not primarily designed for fundoscopy, has the characteristic of a classic photo, with the chromaticity massively affected by the ambient light and the presence of some of the classic artifacts of photography (reflexes, fuzzy contours, poor contrast and so on, **Figure 3.1**

bottom). On both images though, the main anatomical features are displayed. In the image acquired with the smartphone, the morphology and chromatic information are still usable for clinical assessment. This is crucial because, for early detection of some pathologies, such as DR or glaucoma, this information might be sufficient for an effective diagnosis (Bastawrous *et al.*, 2016).

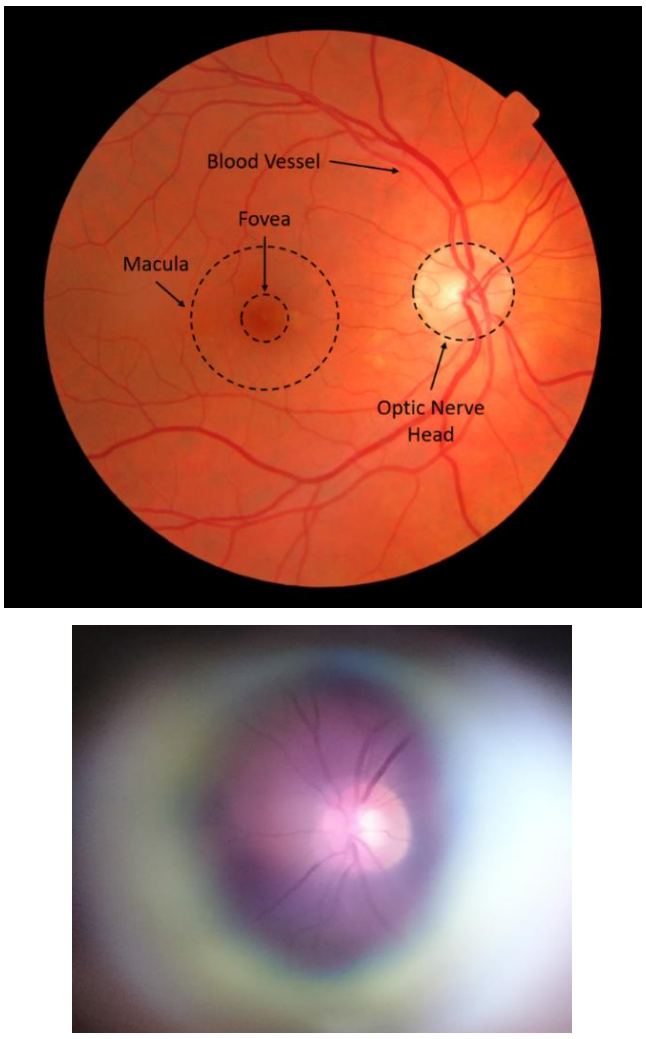

Figure 3.1 Example of classic true colour fundus image obtained via indirect ophthalmoscopy (top) and direct ophthalmoscopy (bottom). The retina on the top has been imaged using a fundus camera with a $FOV = 45°$ (MESSIDOR database (Etienne Decencière *et al.,* 2014)). The images on the bottom has been taken on a mydriatic eye using a smartphone in a non-clinical setting ($FOV \approx 14°$).

Understanding which are the important elements that allow a clinician to assess the health condition of a retina, is the topic of the following. The main anatomical features that can be found on a retinal image are (Qureshi *et al.*, 2012):

- Optic nerve head
- Blood vessels
- Macula (and Fovea)
- Abnormalities (dark lesions, bright lesions and new vessels)

Each of these features have a characteristic morphological and chromatic appearance, with small and well documented variations amongst subjects according to age, pigmentation, sex and so on. Therefore, any alteration of such appearance is a potential indicator of a pathological condition.

Great effort has been put in formalising this phenotypical appearance using measurable criteria, so that objective evaluation techniques can be developed. As it will be more extensively explained later, the same criteria can be used to set up an image segmentation algorithm, for instance, for abnormality classification. Below, the description of such criteria is presented.

Optic Nerve Head (ONH) – It appears as a bright circle, or slightly oval in shape, with yellow or white colouring, approximately 1.5mm in diameter (Goldbaum *et al.*, 1996). It can easily be identified due to its shape and high contrast with respect to the background (especially within the red and green channel or the RGB colour space) and because the blood vessel network converges at the ONH. Sometime called optic disc (OD), the ONH has a central round portion called the optic cup (OC). The portion of tissue between the disc margin and the cup is called neural rim or neuroretinal rim (**Figure 3.2**). The nasal region of the OC is in general the less accessible, because occluded by the blood vessels.

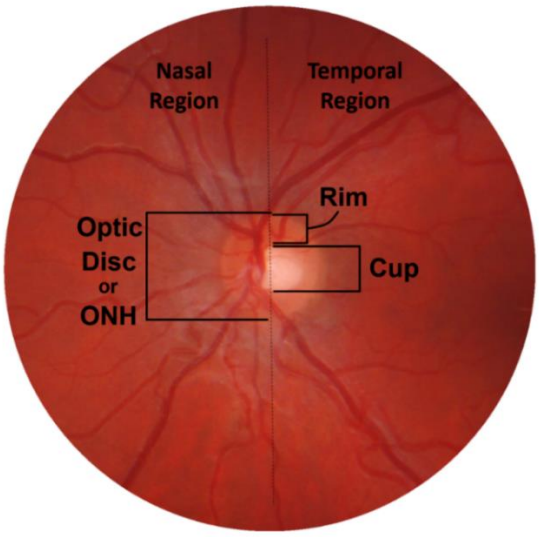

Figure 3.2 Retinal image centred on the Optic Nerve Head.

Measuring the dimensions of OD and OC is a key diagnostic procedure. For instance, glaucoma causes the degradation of the optic nerve fibres leading to an enlargement of the OC, and atrophy of the neuroretinal rim (Bourne, 2006). Parameters such as the vertical cup-to-disc ratio can provide a good indicator of such condition. In order to better determine the boundaries between the rim and the OC and between the entire ONH and the background, it is useful to get the 3D perspective of this retinal region (**Figure 3.3**).

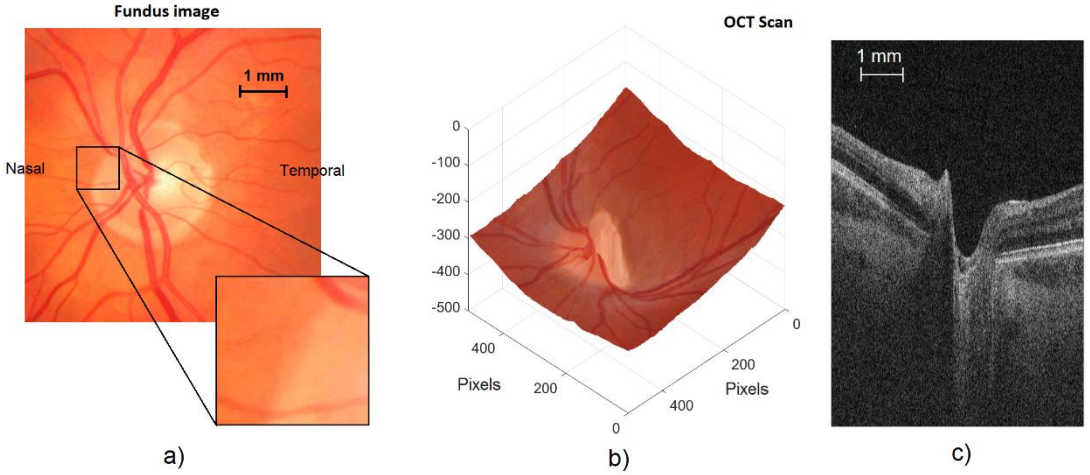

Figure 3.3 3D topography of the retina, centred on the ONH. a) represents the 2D portion of the retina that has been scanned (approximately 6 mm x 6 mm of retinal surface), with the edge between the ONH and the fundus magnified in the small square. b) represents the 3D reconstruction obtained by combining 256 OCT slices from CORD (image c) is an example of such slices). The slice c) represent a scan of approximately 6 mm x 11.6 mm of retina, and the depth of approximately 23 μm.

The ONH appears as a concavity from where the vasculature and the optic nerve emerge. The contour surrounding the dip raises with respect to the outer border of the OD. This characteristic morphology reflects the chromatic appearance of the rim and the OC in the retinal image.

Blood vessels – the four main arches, formed by the central retinal vein and artery, branch out from the optic nerve head to frame the temporal and the nasal side of the retina (**Figure 3.4**).

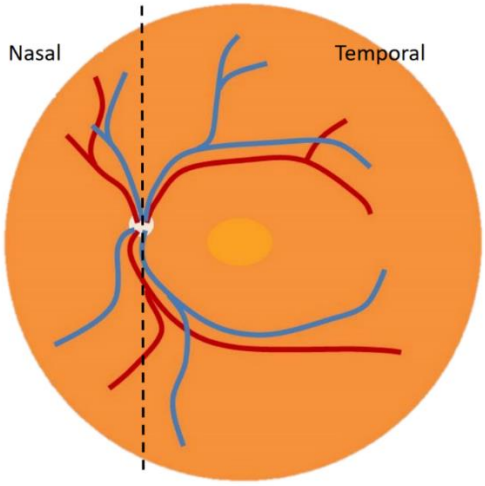

Figure 3.4 Blood vessel arches running out of the optic nerve head (left eye). The two nasal arches (left side) and the two temporal arches (central and right side), both composed by a pair of arteries (red) and veins (blue).

This prevents the blood vessels from creating an obstacle between the light coming through the transparent structures of the eye and the chromatic receptors of the retina. Blood vessels have the characteristic long tubular shape with a diameter that decreases as the distance from the optic nerve head increases. They also show a natural mild tortuosity which can become severe due to abnormal growing or vascular diseases (Han, 2012). Amongst the most important geometrical parameters that are measured to establish the presence of a pathological condition we can find: width (cross-section diameter), tortuosity (relative curvature), branching morphology (angle and coefficient), and fractal dimension of the vasculature (Jordan *et al.*, 2017).

Changes in these biomarkers are related to hypertension, obesity, cardiovascular disease, cerebrovascular diseases, and stroke (Heneghan *et al.*, 2002b, Leung *et al.*, 2004b, J. J. Wang *et al.*, 2006a, T. Y. Wong *et al.*, 2001, Patton *et al.*, 2005b).

As for the chromatic content, blood vessels have a red hue, with a lower saturation value with respect to the background. Another important chromatic feature is the central reflex of the large vessels, which is sometime exploited to identify the centreline of the vasculature in computer aided tools (Bhuiyan *et al.*, 2014, Muhammad Moazam Fraz *et al.*, 2012b). Altogether, the chromatic and morphologic information allows the detection of the blood vessels and artery/vein classification (**Figure 3.5**).

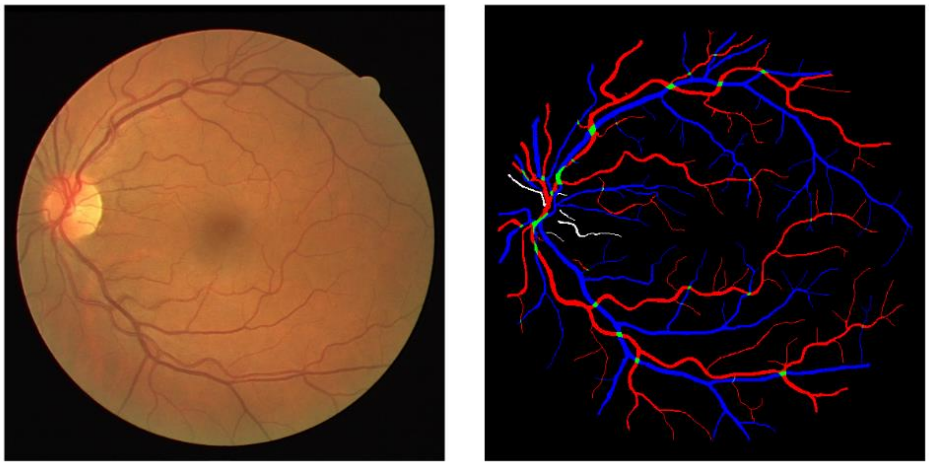

Figure 3.5 Blood vessel extraction and artery/vein classification example, from RITE (Hu,Abràmoff and Garvin, 2013). Arteries (red) and veins (blue) crosses each other in the green sections.

Macula and fovea – in the central area, surrounded by the vascular arcades, lies the macula. It appears as a circular region of approximately 5mm in diameter, with a gradual darkening appearance that reaches its maximum in the centre, the fovea. This appearance is due to the xanthophyll pigments which protect the photoreceptors, in particular the cones, where they have here their distribution density peak. Like for the ONH, the cross section obtained from the 3D topography shows how the macula profile is

characterised by a gradual bulge of the surface as we approach the fovea, and by a dip in the very centre of the fovea (**Figure 3.6**).

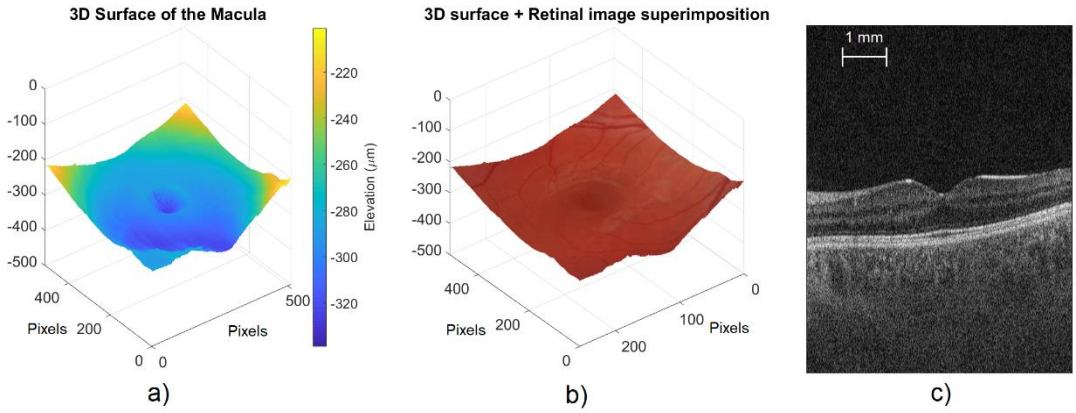

Figure 3.6 3D reconstruction of 7 mm x 7 mm portion of the retina, centred on the macula. a) 3D topography obtained by combining 256 OCT slices from CORD (image c) is an example of such slices). b) the same topography represented in a) with the superimposition of the corresponding retinal image, so to highlight the morphology of the macula. c) is an example of the OCT slice, which corresponds to approximately 7 mm x 13.56 mm of retina, and the depth of approximately 27 μm.

The localization of the macula is not always easy, since the different pigmentation can decrease the contrast of this area with respect to the background (especially in the blue channel where the contrast is maximum). This task usually relies on some anatomical assumptions regarding the relative position between the macula, the ONH and the vessel arches, far more easy to segment.

Abnormalities - In a clinically gradable retinal image these are the features that are associated with some pathological condition. There are three main observed abnormalities that indicate disease: bright lesions, dark lesions and new vessels (Patton *et al.*, 2006, Jordan *et al.*, 2017). Under bright lesions we have exudates (lipoproteins) and cotton wool spots (superficial retinal infarcts). Microaneurysms and hemorrhages (dot, blot and flame) are examples of dark lesions. New vessels are dark features that can be detected due to the fact they do not take paths of known non-pathological retinal vessels. In **Figure 3.7** a broad overview is shown.

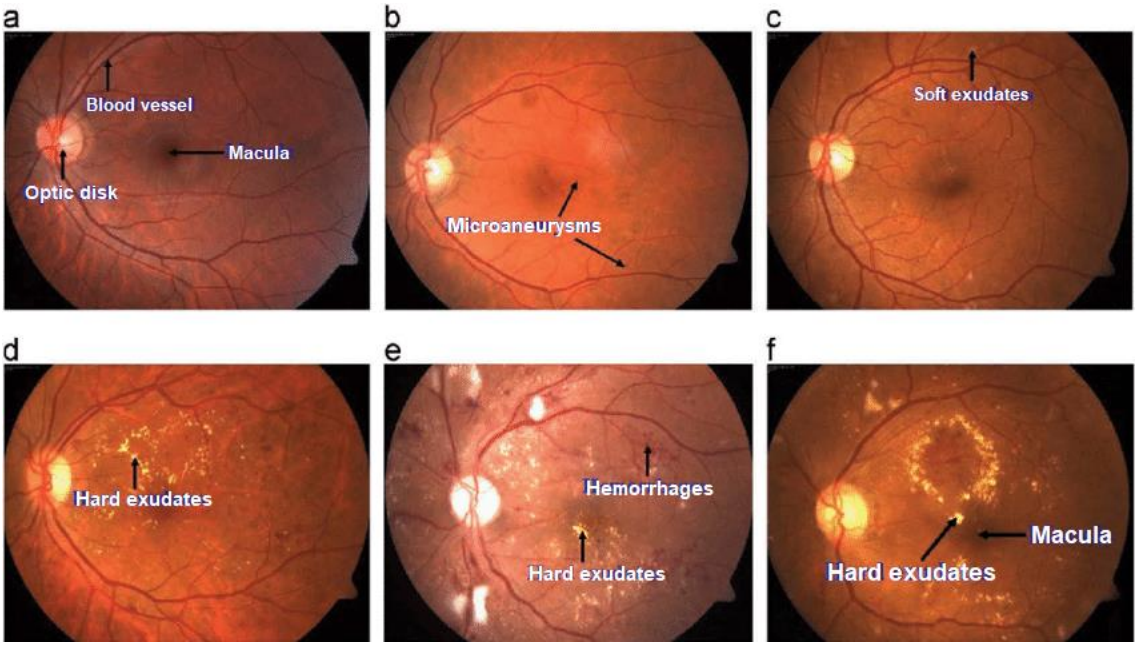

Figure 3.7 Broad overview of fundus images containing pathology: (a) Normal; (b) Mild NPDR; (c) Moderate NPDR; (d) Severe NPDR; (e) Prolific DR; (f) Macular oedema (M. M. Fraz et al., 2012a). Scale was kept the same for all the images for comparative reasons. Unfortunately, this scale makes microaneurysms and soft exudates not as visible as the other lesions. For a better visualisation of this kind of lesion refer to (M. M. Fraz et al., 2012a).

3.2 MANUAL VS AUTOMATIC ASSESSMENT

Clinicians usually examine directly the retinal images, by using their judgment and experience. The same visual strategies can be adopted by computer software if these are converted into numerical values (e.g. colours, sizes, thresholds). However, the mechanisms that make a clinical assessment so robust are difficult to be translated, because they are not fully understood. From the other side, computer image processing can exploit levels of information that are inaccessible for human operators (e.g. infrared light spectrum, spatial frequency domain).

3.2.1 HUMAN VISION: A COGNITIVE PROCESS

Over the years, biologists, neurologists and psychologists have coined many terms to define the mechanisms that underpin the ability of animals (and in particular humans) to explore the surroundings using vision and retrieve from it the information needed for their successful survival. Visual cognition,

high-level vision, mid-level vision and top-down processing are just some examples (Cavanagh, 2011). These are not synonyms nor complementary concepts. Rather, they refer to different approaches to the tangled problem of breaking down “vision” to its fundamental blocks. The truth is that we are only starting to scratch the surface on how visual perception works and how it is processed by our brain. For this reason, researchers in this field tends to avoid explicit models when presenting a new theory about visual cognition. Nonetheless, they all agree that this is one of the most challenging and exciting open question in front of us, and an answer is therefore needed. The flourishing of research works about this topic, especially in the last 20 years, is evidence of this (Tory and Moller, 2004, Xiao and Liu, 2013, Sakaguchi *et al.*, 2017, Pylyshyn, 1999).

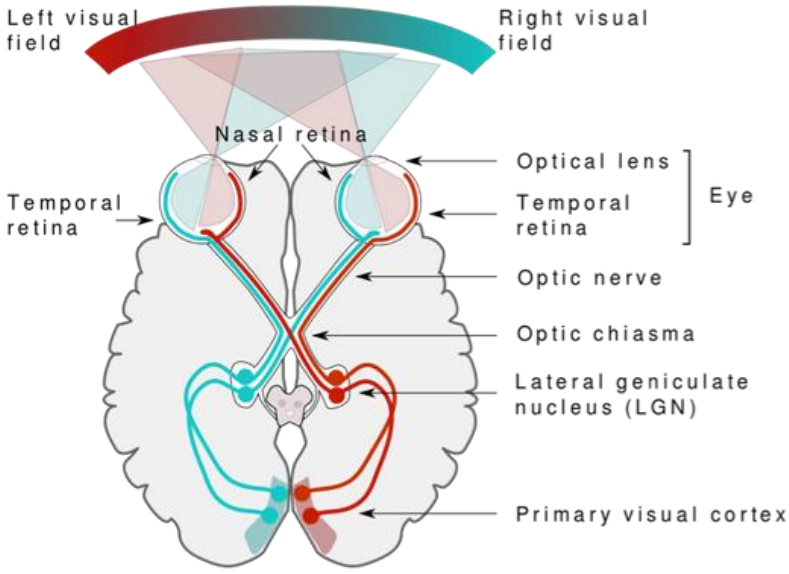

Figure 3.8 Visual system path, from retinas to the brain (Image created by Miquel Perello Nieto and distributed under CC BY-SA 4.0).

A common ground in this field it is considering vision as the combination of two processes: measurement and inference. In the measurement part, light-sensitive neurons transmit spatially localised signal intensities, for their parameter of interest (cones or rods), to the optic nerve and into the brain (**Figure 3.8**). The whole measurement chain is hard-wired, reflexive and

dependent by the surrounding context and attention, and the result is a raw and sketchy perception of the world (Cavanagh, 2011). To been able to identify surfaces, objects or even recognise faces the visual system must infer. To be clear, inference is not a guess, but a rule-based decision from partial data to the most appropriate solution. Deconstructing the mechanism of inference is difficult and advances in the field are very slow (Biederman, 1987). The majority of the researchers on vision have focused on the measurement components, which are accessible with in-vivo single cell recording and study of direct effects of specific stimuli on human behaviour. However, is clear that a large-scale information processing system oversees the whole visual computation. Thanks to the large improvement of computer vision and the more organic synergy between biologist and physiologist, the research effort on the inference mechanism is now experiencing a renewed push (Körding *et al.*, 2007, Norris and Kinoshita, 2008, Marewski *et al.*, 2010).

Regardless of the approach selected, the process of collecting information from the retina and use it to solve the inference problem is generally called *object knowledge*. This independent and sophisticated mechanism uses different areas of the brain, and their interconnections, to achieve the goal, and involves classes of process such as memory, experience and context information processing, which use 30% to 40% of the total cortical surface (Grossberg, 1997, Ungerleider, 1982).

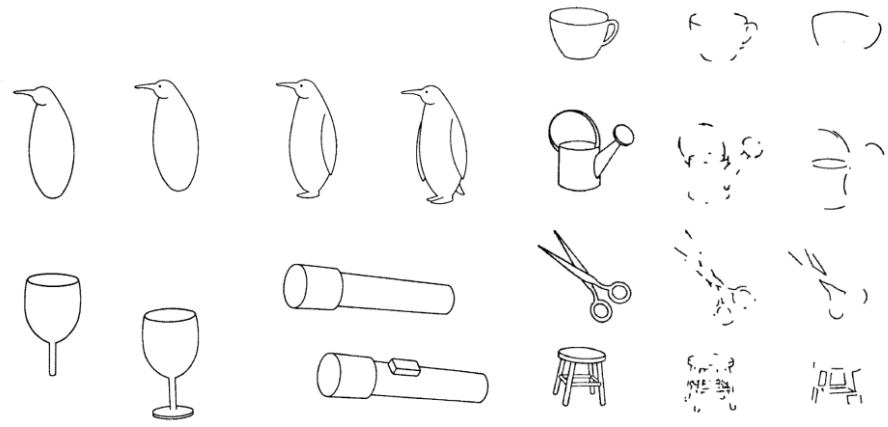

Figure 3.9 On the left, partial and complete version of multiple-component objects. On the right, some example of 5 different stimuli used in the experiment of degraded objects (Biederman, 1987).

Some of the most organic theories regarding the assessment of this process can be traced back to the work of Biederman (Biederman, 1987). This pioneer of visual cognition is the father of the so called recognition-by-components theory. The fundamental assumption of this theory is that even a modest set of components can be sufficient to determine an object using some readily detectable components of the edges in the 2-dimensional image. Such edge components are: curvature, collinearity, symmetry, parallelism and co-termination (or connection between segments' vertexes). These elements alone are sufficient to infer from the 2D image the corresponding object. Surface characteristic, such as colour or texture, have only secondary roles in primal access. This mechanism becomes particularly sophisticated when the task involves the perception of incomplete or degraded objects (**Figure 3.9**). The rate of successful identification with a limited amount of components (3 to 4 components for objects of 6 to 9 components) is above 90%. This denotes the robustness and the massive influence of previous knowledge (and perhaps other hidden layers of processing) in object recognition (**Figure 3.10**).

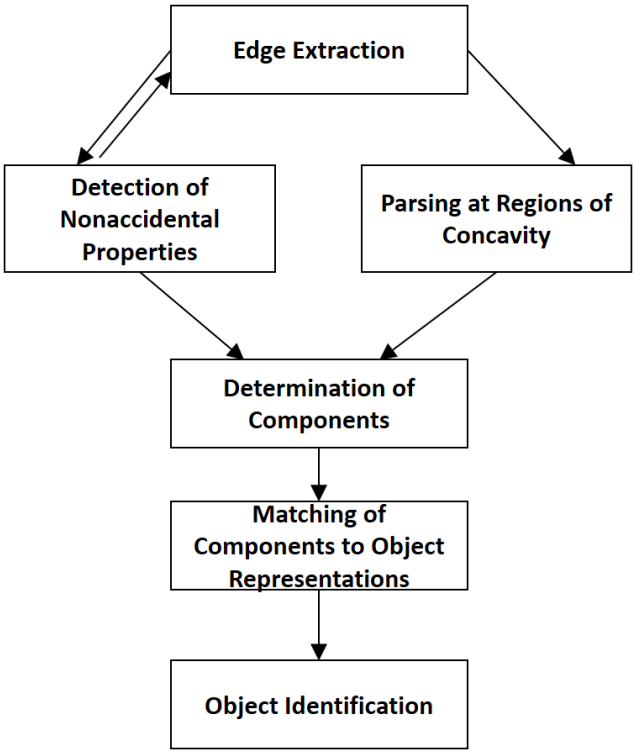

Figure 3.10 Presumed processing diagram for object recognition as designed by Biederman (Biederman, 1987).

More recently, a number of works have explored the role of T-junction, L-junction and end-line in image understanding. In particular, the work of Rubin (Rubin, 2001) demonstrated that junctions play a crucial role in illusory contour perception and model completion, gaining a privilege role in scene segmentation. Yankelovich and Spitzer (Yankelovich and Spitzer, 2018) developed a model able to extract illusory contours from a grey tone image, by introducing simple desired object properties and minimizing a cost function that assign a value for each of the object boundary configurations. Worth mentioning is also the work around the description of filling-in colour illusions triggered by edges (Cohen-Duwek and Spitzer, 2019).

After this overview on how visual perception works, it appears quite clear that we are dealing with a very complex topic, far from been fully extricated. Nonetheless, this process suggests a strategy similar to a Bayes classification (Fukunaga, 2013), which, is similar to the one exploited by some computer vision algorithms for tasks such as object detection.

The other fundamental outcome of these theories is that not all the elements of a 2-D image are strictly essential for its classification/identification. An image that is partially degraded might still contain the information we are looking for. In the context of this research work, a retinal image that is affected by quality distortions can still have the elements the clinicians need to identify the presence of a pathological condition. This is because vision is an inferential process. Understanding where the boundary between measurement and inference is located, could automatically define what is useful clinical information and what is not. As previously indicated, this is still far from being achieved. What can be done, though, is to establish, subjectively, when an image is clinically assessable (or has appropriate clinical quality) or not.

3.2.2 PIXELS AS SPATIAL AND CHROMATIC INFORMATION CARRIERS

A planar digital image (in the following referred to simply as a "digital image") can be defined as a function of a two-dimensional space $f(x, y)$, where x and y are the spatial coordinates and the amplitude of f, at any pair of coordinates, is a vector function that encodes the visual content (intensity function), such as luminance, or colour (Gonzalez and Wintz, 1977). In computer vision, every single element of this 2D matrix is called pixel. According to this description, each pixel is able to provide two pieces of fundamental information: the spatial position within the image and the related intensity value.

Connected regions of the image with the same intensity denote pixels belonging to the same object, or in general to a cluster with similar properties. The intensity, in medical imaging, depends on the physical properties of the region being imaged in respect to the specific source of energy used to acquire the image (electromagnetic, acoustic, ultrasonic, electronic, etc.). A classic example is x-ray imaging, where the radiation emitted by an electromagnetic source hits the body, passes through it, and the remaining energy is collected by a detector. The intensity level depends on the degree of absorption of the tissues, the more the absorption the lower the intensity captured by the X-ray

detectors. Here, absorption is mostly related with density of the tissue. That is why this technique is widely used to inspect the status of bones and soft tissues with different cellular typology (**Figure 3.11**).

Figure 3.11 CT-scan of a thorax. The different tissue densities correspond to different grey levels.

To enrich the level of information, images produced by different energy sources can be overlapped. This strategy is particularly successful mostly because human vision has evolved to deal with edge detection. The retina is sensitive to three different wavelengths, corresponding to the red, green and blue regions of the visible light spectrum, which give rise to three separate streams of information at retinal level (Kalloniatis and Luu, 2007). For the purpose of standardization, the CIE (Commission Internationale de l'Eclairage – the International Commission on Illumination) designated in 1931 the following wavelength values to the three primary colours: blue=435.8nm, green=456.1nm and red=700nm. In **Figure 3.12**, the different absorption of the light by the blue, green and red cones of the human retina and the absorption efficiency of a typical colour image sensor of a camera device are compared.

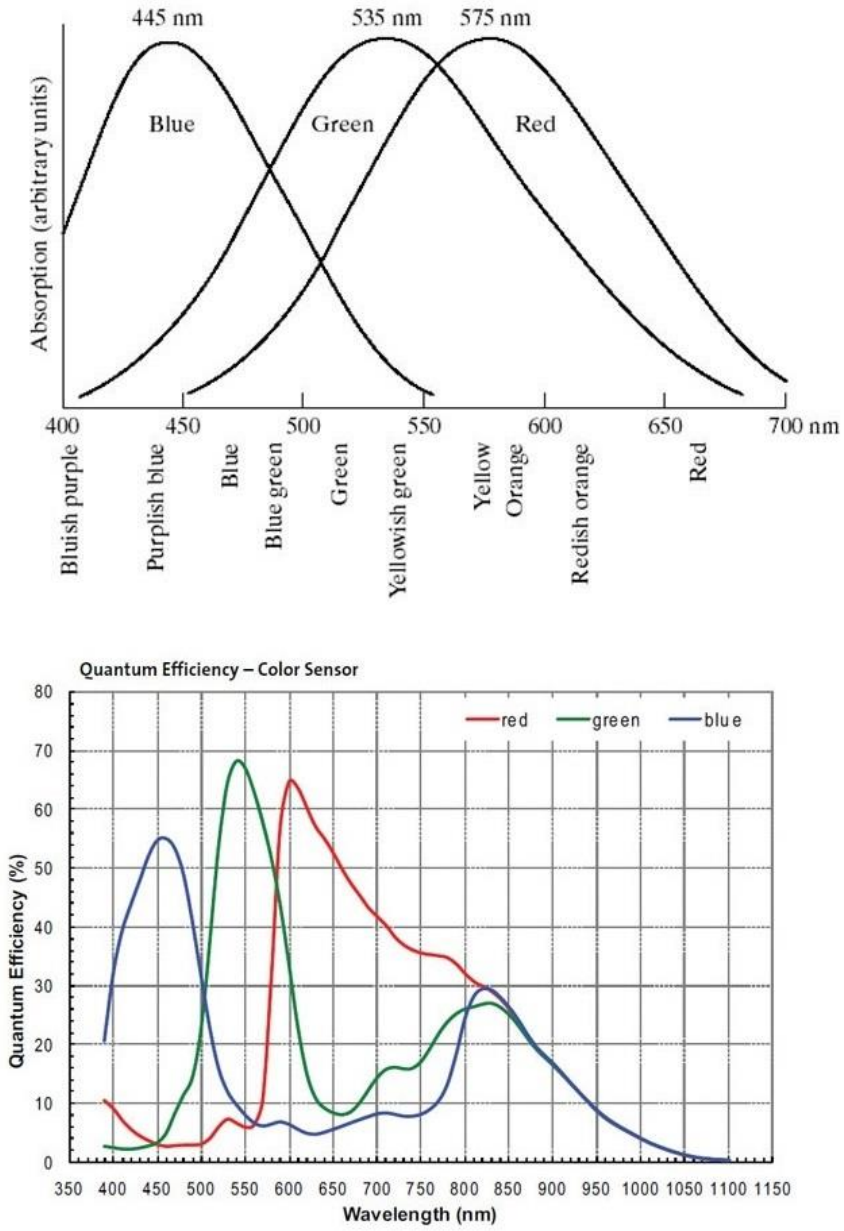

Figure 3.12 On the top, the absorption of light by the blue, green and red cones of a human retina as a function of wavelength (Gonzalez and Wintz, 1977). On the bottom, the absorption efficiency of a CMOS colour image sensor (MT9M034 1/3-Inch CMOS Digital Image Sensor).

As shown in **Figure 3.12**, in the visible range, the retina and the image sensors have a similar behaviour which results in the production of similar images.

In computer vision the tristimulus (amount of red, green and blue) can be decoupled and manipulated to maximize the amount of information provided

by the specific feature under examination. This can be achieved by modelling mathematically the three colour values, as produced by the image sensor, to obtain a colour model where the clinical features have the maximum contrast, for instance. In other words, the intensity level of a pixel can be decomposed into colour spaces where the correlation between neighbour pixels (e.g. pixels that belong to the same anatomical feature) can unlock valuable information.

There are many different colour models, or colour spaces, used to describe the chromatic appearance of a digital image. The majority of the monitors and imaging hardware use an RGB or CMY (cyan, magenta, yellow) system, which are not well suited to describe colours from a human perspective. In fact, we cannot describe the colour of an object by giving the percentage of the red, green and blue components. Instead, we prefer to describe its chromatic components by identifying a dominant wavelength and the intensity, or purity, of such colour. The HSI (*hue*, *saturation, intensity*) colour space does exactly that. It decouples the intensity components from the chromatic information. Hue and saturation taken together are called chromaticity, where the first describes to the dominant wavelength of a mixture of light waves, and the second the purity or the amount of white light mixed with the hue. Intensity is the achromatic (grey level) value of that particular combination of hue and saturation. This colour space is ideal for developing image processing algorithms based on colour description that are natural and intuitive to humans. Another very practical colour space used in image processing involving human perception applications is the CIE L*a*b* colour space (Robertson, 1977, CIE, 1978). This colorimetric, perceptually uniform and device independent (Gonzalez and Woods, 2007) colour space can also decouple the intensity from the colour representation. Its gamut can replicate any colour of the visible spectrum, making it valuable for image manipulation and compression.

The mathematical formulation to obtain these two colour spaces from the RGB digital image needs some mathematical considerations to be introduced. To specify the *tristimulus* as perceived by humans, the CIE chromaticity diagram was formally introduced, **Figure 3.13**. The graph shows colour

composition as a function of *x* (red) and *y* (green). For any combination of *x* and *y*, the corresponding *z* (blue) value can be obtained, considering:

$$x = \frac{R}{R+G+B} \qquad y = \frac{G}{R+G+B} \qquad z = \frac{B}{R+G+B} \tag{3}$$

where R, G and B are the three components of the *tristimulus*, and

$$x + y + z = 1 \Longrightarrow z = 1 - (x + y). \tag{4}$$

Pure colours are positioned around the boundary of the tongue-shaped diagram, covering the visible range from 380 nm to 700 nm.

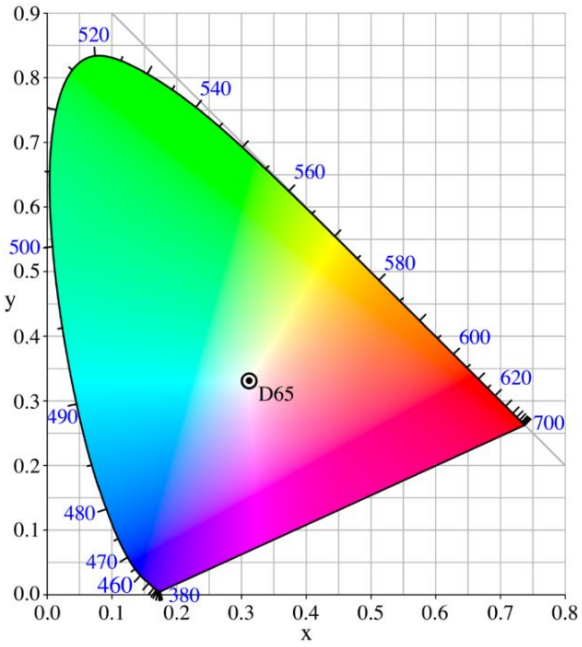

Figure 3.13 CIE chromaticity diagram. D65 corresponds to the white of the perfectly reflective diffuser.

As we approach the centre of the diagram, where the fraction of the three primary colours are equal, lies the point that represents the CIE standard for the white light (point "D65", defined by $x = 0.3127$ and $y = 0.3290$ in the CIE chromatic diagram). Now that we have identify a standard system to univocally identify each colour, we can use these Cartesian coordinates approach to convert the colour space from RGB to CIE L*a*b*. The L* a* b* colour components can be derived as:

$$L^* = 116 \cdot h\left(\frac{G}{y_w}\right) \tag{5.1}$$

$$a^* = 500\left[h\left(\frac{R}{x_w}\right) - h\left(\frac{G}{y_w}\right)\right] \tag{5.2}$$

$$b^* = 200\left[h\left(\frac{G}{y_w}\right) - h\left(\frac{B}{z_w}\right)\right] \tag{5.3}$$

where

$$h(q) = \begin{cases} \sqrt[3]{q}, & q > 0.008856 \\ 7.787q + 16/116, & q \leq 0.008856 \end{cases} \tag{5.4}$$

and x_w, y_w and z_w are reference white tristimulus values (typically the white of a perfectly reflective diffuser under CIE standard D65 illumination, defined by $x = 0.3127$ and $y = 0.3290$ in the CIE chromaticity diagram). For the HSI colour space the transformation from the RGB one can be visualized as in **Figure 3.14**.

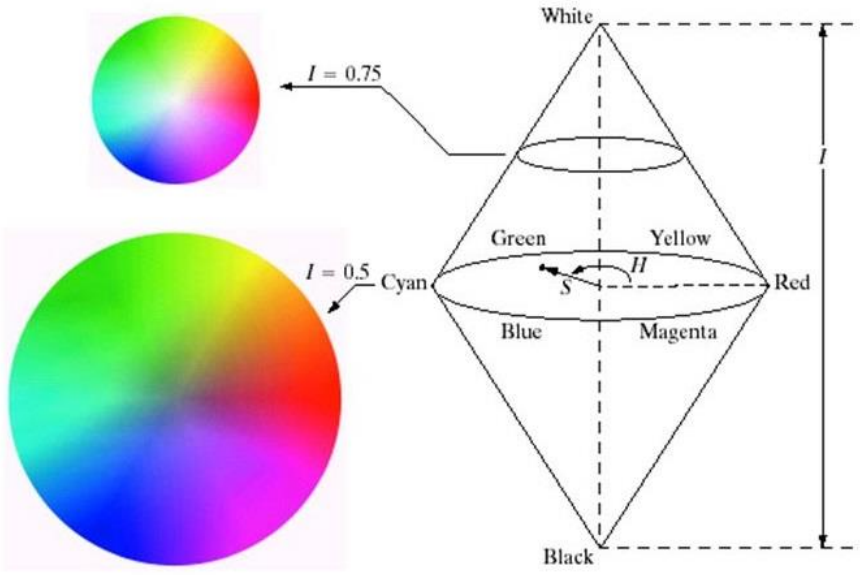

Figure 3.14 The HIS colour model based on circular colour planes. The circles are perpendicular to the vertical intensity axis.

Mathematically, the transformation can be obtained from the following equations:

$$H = \begin{cases} \theta, & \text{if } B \leq G \\ 360 - \theta, & \text{if } B > G \end{cases} \tag{6.1}$$

with

$$\theta = \cos^{-1}\left\{\frac{\frac{1}{2}[(R-G)+(R-B)]}{[(R-G)^2+(R-B)(G-B)]^{1/2}}\right\} \quad (6.2)$$

and

$$S = 1 - \frac{3}{(R+G+B)}[min(R,G,B)] \quad (6.3)$$

$$I = \frac{1}{3}(R+G+B). \quad (6.4)$$

Imaging sensors used in retinal imaging are sensitive to the visible and infrared band of the electromagnetic spectrum. The images they produce are therefore the result of the absorption (scattering and reflection) of the retinal structures to that specific band. As we will point out later, retinas reflect efficiently some specific wavelengths, therefore sensors with high sensitivity in those portions of the spectrum can extract more information. Nonetheless, also with classic photos we can extract information by manipulating the colour content as previously described. As an example, in **Figure 3.15** a retinal image has been processed to obtain the HIS and CIE L*a*b* colour spaces from RGB one.

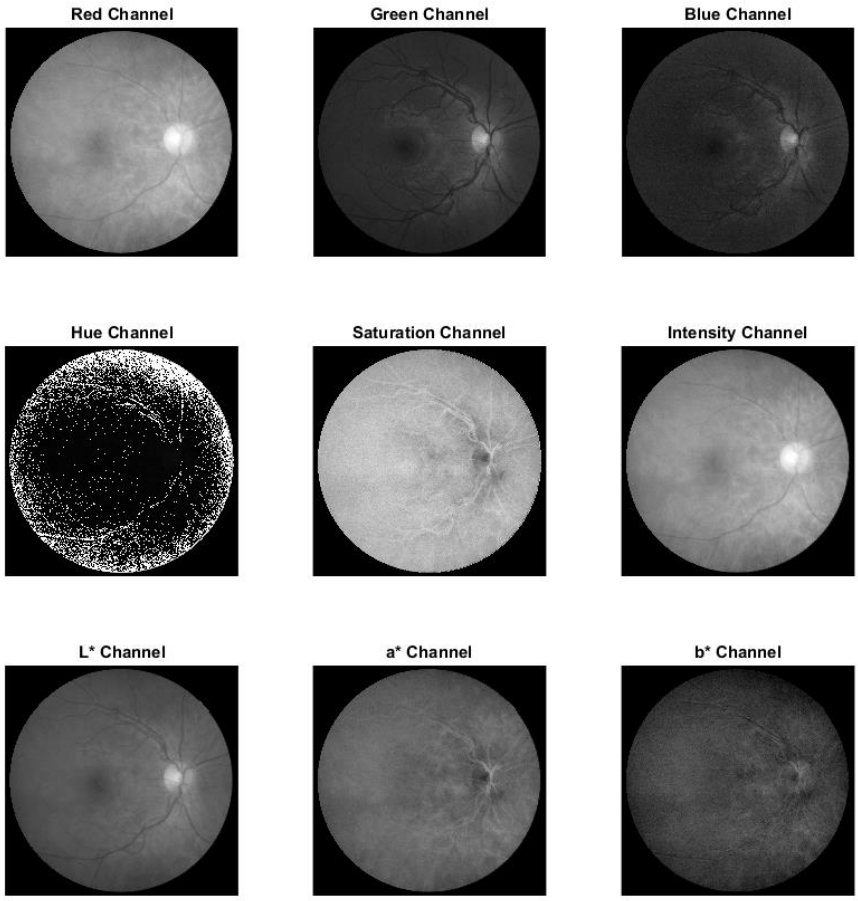

Figure 3.15 Healthy retinal image obtained by a fundus camera, from CORD database (*CORD Comprehensive Ophthalmic Research Database*, CORD 2019). First row, the red, green and blue channels of the RGB colour channel as obtained from the image sensor of the fundus camera. Second and third row, the HIS and CIE L*a*b* colour spaces and their respective channels. Given that the Hue of the retina is centred around the Red=0. The fluctuation around this number (between 0.9 and 0.1) produces the appearance of a binary image.

In the next section of this chapter, some of the classic digital image processing techniques used to extract and enhance the clinical content of retinal images are presented. In particular, we will see how the combination of pixels' colour and spatial position can enable very powerful clinical assessment techniques.

3.2.3 PUBLICLY AVAILABLE DATASETS

The availability of a large quantity of medical images is a fundamental requirement for the development of new digital imaging techniques. This can

be achieved by establishing a formal collaboration between the healthcare services and the research group, usually via a time consuming process, involving many legal and bureaucratic steps. However, this burden is often too arduous for small research groups or where there is no direct access to the clinical world. This is why the publication of open access medical image databases is greatly welcomed by the research community.

When new data are made available in a particular field, not only the quantity of publications will increases, but also the quality of research is expected to rise (Kramer, 2017). This because the direct access to the original data source allows peer researchers to review and replicate the results, overseeing the research validity and integrity. Furthermore, testing and evaluating the performances of different image techniques over the same dataset of images makes comparison and validation work more consistent and effective. This virtuous circle has contributed to create, over time, *de facto* standards, e.g. testing new algorithms over the same databases, that are now used to define new ground truths and frameworks for what is required in future databases (Jordan *et al.*, 2017). Transparency in the data used in research, equal access to data, stimulation of innovation and knowledge development, affordability of research, and de-risking of research requiring medical data are other benefits that publicly available datasets can provide (Saleh,Alameddine and El-Jardali, 2009, Janssen,Charalabidis and Zuiderwijk, 2012).

Compared to the past, there are also some structural facilitations that are making researchers more open to the publication of their own databases. The sizable investments that scientific and policy-making communities have put in developing data access and sharing infrastructures are in fact driving a positive change in the cultural and operational research attitude towards open access data (Arzberger *et al.*, 2004). In **Table 3.1**, the list of the publicly available datasets of ophthalmic images available at the time of this thesis is presented. The bulk of them consist of retinal images, with a wide collection of pathological signs and interpretative data (e.g. ground truth and feature segmentation results) (Jordan *et al.*, 2017). Some databases, such as DRIVE, REVIEW, MESSIDOR and STARE, are still widely used for the development and

validation of image processing algorithms (Staal *et al.*, 2004, Al-Diri *et al.*, 2008, Etienne Decencière *et al.*, 2014, *STructured Analysis of the Retina*).

An almost absent typology of ophthalmic database is the multi-source one, that is a dataset that includes, for each eye, different imaging modalities and techniques. Multi-source paradigm is seeing great interest in the field, due to the possibility to enrich imaging techniques, such as segmentation, registration and fusion, with multiple contextual information, improving diagnostic capabilities, pre-surgery planning and follow-up assessment (James and Dasarathy, 2014, Casey and Damper, 2010). This is the same approach used by the clinician during an eye examination, where data coming from measurement procedures (e.g. slit-lamp examination, measurement of the objective refractive error of the eye, or optical biometry) and different imaging techniques, are used to get the clinical picture of the patient's eye. As a result, some research groups are starting to create their own multi-source datasets, making them publicly available.

The ROD-REP repository, created by Rotterdam Ophthalmology Institute, grants access to three different datasets collected from the same patients: the first includes intraocular pressure (IOP) measurements and 24-2 full threshold visual fields obtained with a Humphrey field analyser, the second collects fundus images from a DR screening program and the last has in-vivo confocal corneal microscopy endothelium images (Adal *et al.*, 2015, Erler *et al.*, 2014, Selig *et al.*, 2015). Of particular interest is the inclusion of some important metadata directly on the landing page, such as exclusion and inclusion criteria and the data content. The Retina Image Bank, a project of the American Society of Retina Specialists, is another example of image dataset created to provide images coming from different imaging techniques (ASRS). To the author knowledge it is, at the time of writing, the largest repository of retinal images publicly available, but also includes images of the anterior chamber, and showcases a variety of medical conditions. The repository is open to the research community with the possibility to download and upload new images (with some restrictions). Here, not just fundoscopy but also OCT, ultrasonography, slit-lamp examination, endoscopy and many other

techniques can be found. Another innovative database is the High-Resolution Fundus (HRF) Image Database (Budai *et al.*, 2013). This contains two datasets, one focuses on feature segmentation, the other on image quality classification. The image quality assessment dataset is unique in that it provides retinal image pairs of the same eye, one classified as “good quality” and the other as “poor quality”. The poor category are ophthalmic images affected by artifacts and general distortions (uneven illumination and chromatic dominants) that have been purposely introduced.

If from one side this is an encouraging first step towards multi-source databases, the low level of homogeneity of the kind of data between databases and the lack of a unified data structure could prevent the establishment of such paradigm. The accessibility of the information within a database, in fact, is as crucial as the data content itself (Janssen,Charalabidis and Zuiderwijk, 2012, Arzberger *et al.*, 2004). Whilst the drive to make data openly available is very important step towards quality research, such data should be fit for purpose and meaningful to an outsider accessing the database.

For example, if the original data collected is a 3D volume, making available only a single slice of such volume (Gholami *et al.*, 2018) reduces the information content provided by that technique and restricts the possible research usage. The lack of hierarchical structures or of appropriate metadata can also create barriers for the user, such as difficulties in searching, interpretation and usability, ultimately limiting the potential for impact of the datasets. Taking the Retinal Image Bank as an example, its website based database employs a searching box that allows the user to highlight a specific element of the archive, displaying all the possible associated results. Although this is a robust mechanism to retrieve single images, it is not ideal if the aim is to isolate a specific category of images. All images, in fact, are linked to at least three different keywords. Therefore, searching for “slit-lamp images”, for instance, produces as result not only images coming from slit-lamp examinations, but also images with other degrees of correlation (e.g. acquired in the same examination/patient) such as fundoscopy and OCT. This can significantly increase the workload and search time of a researcher and

exposes to oversights and errors.

Poor or inappropriate data structure reduces not only accessibility, but also makes inter-database comparison (comparison of the same type of data between different databases) more difficult. This issue can be tackled by implementing, for instance, appropriate guidelines for database creation framework. In fact, many ready available information, at the time of the data acquisition, (e.g. device setting, age and sex of the subject etc.) could be part of the data content of the image itself if the researcher is guided through the proper completion of the image contextual data. In this way, a more effective comparison, and sometime some forms of normalization process, might be enabled.

Table 3.1 Brief description of publicly available ophthalmic datasets.

Database	Tot No of images	Description
BioImLab	536	Sets of ophthalmic databases, including 60 fundus images, 30 images from the sub-basal corneal nerve plexus, 356 images from corneal epithelium layer to corneal endothelium and 90 images of corneal sub-basal epithelium (Scarpa,Fiorin and Ruggeri, 2007, Scarpa,Grisan and Ruggeri, 2008, Scarpa *et al.*, 2011, Grisan,Foracchia and Ruggeri, 2008).
CHASEDB1	28	Retinal image database of multi-ethnic school children, subset of the CHASE dataset. Contains 28 retinal images and blood vessel segmentations obtained from two experts (Owen *et al.*, 2009).
DIARETDB	130	Currently at its V2.1 version, this database, related with the ImageRet project, contains 130 colour fundus images, 20 normal and 110 contain signs of the DR lesions (hard exudates, soft exudates, microaneurysms and haemorrhages) (*IMAGERET Optimal Detection and Decision-Support Diagnosis of Diabetic Retinopathy*)(*IMAGERET Optimal Detection and Decision-Support Diagnosis of Diabetic Retinopathy*)(*IMAGERET Optimal Detection and Decision-Support Diagnosis of Diabetic Retinopathy*)(*IMAGERET Optimal Detection and Decision-Support Diagnosis of Diabetic Retinopathy*)(*IMAGERET Optimal Detection and Decision-Support Diagnosis of Diabetic Retinopathy*)[245].
DRIONS-DB	110	This database contains 110 retinal images for benchmarking optic nerve head segmentation (Carmona *et al.*, 2008).
DRISHTI-GS1	101	101 images split into a test and training set collected and annotated by Aravind Eye Hospital, India. The ground truths for Optic Disc and Cup segmentation are provided for the training set (Sivaswamy *et al.*, 2015).
DRIVE	40	Dataset comprised of 40 randomly selected fundus images obtained from a DR screening program in the Netherlands (Staal *et al.*, 2004).
E-OPHTHA	463	Database of colour fundus images especially designed for scientific research in DR. Two sub databases named e-ophtha-MA

		(MicroAneurysms) 381 images, and e-ophtha-EX (EXudates) 82 images (E. Decencière *et al.*, 2013).
FIRE	134	The dataset consists of 134 retinal image pairs captured from 39 patients (Hernandez-Matas *et al.*, 2017).
HEI-MED	169	(formerly DMED) Collection of 169 fundus images to train and test image processing algorithms for the detection of exudates and diabetic macular oedema (Giancardo *et al.*, 2012).
HRF	81	Two subsets. the first contains 3 groups of 15 images that represent healthy patients, patients with DR and glaucomatous patients. The second contains 18 image pairs of the same eye from 18 subjects (Budai *et al.*, 2013).
INSPIRE [a]	70	Two datasets. The first, 30 stereo colour images of the optic disc including a depth reference standard based on spectral domain OCT (Tang *et al.*, 2011). The second, 40 colour images of the vessels and optic disc and arterial-venous ratio reference standard (M. Niemeijer *et al.*, 2011).
MESSIDOR	1200	Created to facilitate studies on computer-assisted diagnoses of DR, it contains 1200 retinal images with DR Grading and Macula Edema Risk Level (Etienne Decencière *et al.*, 2014).
ONHSD	99	This dataset contains 99 fundus images, with discernible ONH, taken from 50 patients randomly sampled from a DR screening program (Lowell *et al.*, 2004).
REVIEW	16	Consisting in four subsets, for a total of 16 images, selected to assess the accuracy and precision of the vessel width measurement algorithms in the presence of pathology and a central light reflex (Al-Diri *et al.*, 2008).
RIM ONE	169	169 ONH images obtained from 169 full fundus images of different subjects (Fumero *et al.*, 2011).
ROC	100	Set of 50 training and 50 testing retinal images created to improve computer aided detection and diagnosis of DR (M. Niemeijer *et al.*, 2010).
ROD-REP	1120	Contains three datasets made available by the Rotterdam Ophthalmic Institute, including longitudinal glaucomatous visual fields, longitudinal DR screening fundus photos and confocal corneal endothelial microscopy images (Adal *et al.*, 2015, Erler *et al.*, 2014, Selig *et al.*, 2015).
STARE	400	400 fundus images collated by the University of California alongside expert annotated images of features and a list of diagnoses for each image (*STructured Analysis of the Retina*)(*STructured Analysis of the Retina*)(*STructured Analysis of the Retina*)(*STructured Analysis of the Retina*)(*STructured Analysis of the Retina*)[232].
VICAVR & OCTAGON	202	The first, 58 optic disc centred retinal images, the second, 144 healthy OCT-A images and 24 diabetic OCT-A images (*VARPA*)(*VARPA*)(*VARPA*)(*VARPA*)(*VARPA*) [254].
CORD (this work)	548	548 fundus images, 231 photos and 160 videos from slit lamp examination, and 80 scans (composed by ~260 2D slices each) from OCT.

[a] in INSPIRE – stereo, only one image per eye is available in the stereo dataset.

3.3 ENHANCEMENT OF HIDDEN CLINICAL INFORMATION CARRIER

The concept of image enhancement refers to the heuristic procedure of manipulating an image to the information content of the image more accessible for the examiner. This differs from the concept of restoration, which aims instead to recover an image that has been degraded by using *a priori* knowledge of the degradation phenomenon or the content of the image. Enhancement and restoration usually involve the formulation of criteria of "goodness" against which the result of the image manipulation can be assessed. Although these two approaches have some common ground, image enhancement is largely subjective, while image restoration is for the most part objective (Gonzalez and Woods, 2007). In the following paragraph, the state of the art of digital image processing techniques in retinal imaging are presented. These act on the main features of the retinal image aiming at improving those elements that are useful during a clinical assessment procedure. For these reason we will refer to them as image enhancement techniques, as the manipulation is human visual assessment oriented. The majority of these techniques are related to image segmentation, morphological image processing and chromatic manipulation. These are commonly used as fundamental processing steps for feature extraction and classification methods.

3.3.1 TEXTURAL CONTRAST AND CHROMATIC TUNING

In image processing each enhancement method is developed to perform a specific task (e.g. object detection, segmentation etc.). As it will be better highlighted in the following, this task-oriented characteristic means that each technique has some drawbacks if used outside its primary objective. The backbone of the image enhancement theory, upon which almost the entire panorama of retinal image processing (and medical imaging in general) has been built is represented by:

- Intensity transformation
- spatial and frequency filtering,
- wavelet and multiresolution processing
- morphological processing

Following the description order of the anatomical features of section 3.1, the state of the art of feature-based techniques that exploit the textural and chromatic characteristics of the object under examination are presented for each anatomical feature. A summary of such techniques and a review of their outcome results can be found in **Table 3.2**, while **Table 3.3** shows the definition and the mathematical description for each of the performance evaluator used. It should be noticed that the statistical values presented by the reviewed works are obtained by comparing the results of their image processing technique with a dataset of images manually segmented by experts. Therefore, the closer the value are to 100% the more the performance of the algorithm are close to the clinician assessment performance.

Optic Nerve Head – As mentioned, the relation between the OD and the OC morphology is particularly important in the context of glaucoma disk grading. For this reason, most of the image processing techniques have as goal the localization and segmentation of the OD and OC. Such techniques exploit the image contrast and brightness (Sinthanayothin *et al.*, 1999, Walter and Klein, 2001), deformable model (Lowell *et al.*, 2004), principal component analysis (Huiqi Li and Chutatape, 2004) and pyramidal decomposition and template matching (Mookiah *et al.*, 2013a).

Adaptive filters have been implemented by Issac et al. (Issac,Sarathi and Dutta, 2015) and Dashtbozorg et al. (Dashtbozorg,Mendonça and Campilho, 2015), improving robustness in OD and OC boundary identification. In the work of Issac, statistical measures on pixel intensities, such as the mean and standard deviation, are used to determine an adaptive threshold to separate OC from the rim. The main advantage of this technique was its robustness with respect to the quality of the image and the noise content. With this technique the cup-to-disc ratios assessment for glaucoma detection obtained an accuracy (Acc) of 94.4%, with 100% sensitivity (Se) and 90% specificity (Sp), performed on a local database of 67 images. Dashtbozorg et al. demonstrated an adaptive automated OD segmentation, focusing on providing meaningful results in images that contain severe pathological features. Classified as a template matching method (finding elements of an image that match a

template), a sliding band filter (SBF), which enhanced bright regions of the image, was implemented in locating the OD centre and boundary in two steps. First, the blood vessels were removed from the images and a low-resolution SBF was applied to the fundus image to initially locate the OD centre. A second adaptive high-resolution SBF was applied to the image once the OD centre has been found, to isolate the OD boundary, which was segmented and smoothed. This method was proven to demonstrate better detection results in comparison to recently published techniques, with an Acc of 99.9% and 99.6% on the MESSIDOR and INSPIRE-AVR databases, respectively (Etienne Decencière *et al.*, 2014, M. Niemeijer *et al.*, 2011). These two publicly available dataset of retinal images are part of a big family of databases used by researchers to test their algorithms. In **Chapter 4** of this thesis, a more descriptive section about publicly available datasets is presented.

The success of the SBF method is highly connected to its ability to find the centre of the OD, which was found to be poor when image quality is low or in the presence of image artifacts. Mookiah et al. (Mookiah *et al.*, 2013b) were more specifically focused on identifying boundaries in such scenario. Mookiah et al. used a histon-based segmentation based on Attanassov intuitionistic fuzzy image representation to identify a fuzzy or unclear boundary. The histon is similar to the histogram with the difference that it preserves the spatial correlation of same or similar colour value elements, preserving the structural information rather than just the intensity value one (Mohabey and Ray, 2000). The Attanassov intuition fuzzy representation of an image involves the definition of membership functions, which help to emphasise some particular characteristic of the image, in this case intensity value and Euclidean distance. This method was found to identify the OD boundary with 93.4% Acc and an F-score of 0.92 on 100 images, without any shape constraints being applied on healthy, diabetic retinopathy and Glaucoma cases. This study compared results with other conventional histogram based segmentation techniques (Otsu (Nithya and Venkateswaran, 2015) and Gradient Vector Flow (Thongnuch and Uyyanonvara, 2007)) and was found to be superior at detecting unclear OD boundaries. Another technique adapted to improve the

accuracy of OD boundary segmentation is the implementation of prior knowledge into the computer processing. Prior knowledge based on anatomical features of the retina was implemented by Cheng et al. (Cheng *et al.*, 2013) and Basit and Fraz (Basit and Fraz, 2015). Cheng et al. used superpixels, group of connected pixels clustered together as they contain similar intensity values, to differentiate the OD region from the background in the presence of peripapillary atrophy, thinning of retinal pigment epithelium around the OD, by comparing the textures of the two anatomical structures. They classified pixels as either disk or non-disk and then applied a deformable body to identify the contour boundary. To identify the OC boundary, prior knowledge of the position of the cup (usually at the centre of the OD) has been incorporated to the segmented OD, reducing the area in which superpixels are classified as cup or non-cup. One limitation of this method was the trained classifier used for cup segmentation was dominated by medium-sized cups, and therefore underestimation of very large cups, and overestimation of small cups was observed. This method for OD and OC segmentation achieved an area under the curve (AUC) of 0.800, 0.039 lower than the manual disk and cup boundary determination.

Basit and Fraz focused on accurate detection and extraction of the OD region by increasing segmentation specificity. The OD region was detected and properly classified using prior knowledge elements: it contains high intensity pixels (bright spot), it has specific size range (different from bright lesions) and it can be found in the neighbourhood of the main blood vessels. Once the region was correctly isolated, a region-based segmentation (watershed transform) was applied to segment the OD boundary. This method reported results of an average OD detection Acc of 98.9% with an average Sp and Se of 99.2% and 76.2%, respectively, for SHIFA (local database), DRIVE and CHASE_DB1 and DIARETDB1. However, this method had limitations that if the vessels were not extracted accurately or the OD did not contain a region of maximum intensity, the location constraints could not be applied and the initial detection phase failed. Reza et al. (Reza and Ahmad, 2015) looked to significantly reduce the computer processing time of each image by

automatically detecting the OD region using a curve operator, inspired by the work performed by Lu and Lim (Lu and Lim, 2010). The idea is to use the knowledge that pixels inside the OD are not just bright but they also are surrounded by curve gradients of grey tone, which are the boundaries of the OD with the background. Here, no previous vessel segmentation or background mask need to be applied, reducing the processing time per image, and possibly enabling a higher throughput of data when used in computer-aided diagnosis. Efficiency and fast processing are only affecting OD detection, at the expense of boundary segmentation accuracy. This compromise may have been minimised by Welfer et al. (Welfer *et al.*, 2010) who achieved a detection accuracy of 97.7% taking 7.89 s per image on DIARETDB1 in comparison to the reported 94.4% in 6.13 s per image using Reza's technique.

Deep learning techniques have been successfully demonstrated to achieve state-of-the-art performance for image classification (Krizhevsky,Sutskever and Hinton, 2012) and segmentation (Long,Shelhamer and Darrell, 2015). In particular, Huazhu at al. (Fu *et al.*, 2018) explored the use of Convolutional Neural Networks (CNNs) to develop a fully automatic method for joint OD and OC segmentation. After the disc centre is detected, the ROI with the OD is transferred into polar coordinate system and fed into a costumed CNN, where the multi-label probability maps for OD and OC are generated. Finally, the segmentation maps are converted back into Cartesian coordinate. The use of polar transformation in conjunction with CNN has shown an AUC of 0.851 and 0.900 on two local datasets of retinal images with glaucoma cases.

Blood vessels – Retinal blood vessels, along with the ONH, are the retinal feature with the highest contrast visible in a healthy retina. For this reason, blood vessels segmentation is used not only to assess the pathological condition related to the vascular structures, but also as landmarks for several object detection and registration techniques (Lloret *et al.*, 2000, M Niemeijer,Abramoff and Van Ginneken, 2008, Perez-Rovira *et al.*, 2011). A common vessel-related pathology is DR, where high blood sugar level and

ischemia can alter the natural elasticity of the inner walls of the vessels, especially in small capillaries, creating bulges and new vessels in the late proliferative stage. As mentioned before, measuring the width, tortuosity, branching morphology (angle and coefficient), and fractal dimension of the vasculature gives a numerical assessment of possible blood filled dilatations, called microaneurysms, and of new vascularization (Perez-Rovira *et al.*, 2011, Archana *et al.*, 2015, Devaraj and Kumar, 2014, Pourreza,Pourreza and Banaee, 2013). Variations in these biomarkers can also be related to hypertension, obesity, cardiovascular disease, cerebrovascular diseases, and stroke, increasingly common conditions globally (Heneghan *et al.*, 2002a, Leung *et al.*, 2004a, Jie J Wang *et al.*, 2006b, Witt *et al.*, 2006, Patton *et al.*, 2005a).

Classic threshold techniques for vessel segmentation usually result in a runaway number of false positive (FP) or false negative (FN). To overcome this problem, the morphological features of the vessels can be exploited. Retinal vessels can be distinguished among other features that lie on the ocular fundus by their piecewise linear shape, the tree-shape branching and the decrease in diameter as they move radially outward from the OD. Matched filters exploit the abovementioned morphological characteristics, along with the assumption that the cross-section profile of a vessels has a Gaussian-like intensity profile (Katz *et al.*, 1989, Hoover,Kouznetsova and Goldbaum, 1998).

An example has been proposed by Odstrcilik et al. (Odstrcilik *et al.*, 2013). Here, a contrast enhancement algorithm was applied to the green channel, increasing the intensity level of the elements different from the uniform background (vessels, exudates and haemorrhages). After this pre-processing step, five different filters with a Gaussian-like profile were applied to extract the vasculature. The profile of pixel intensity of the cross-section of a vessel, in fact, resembles the shape of a Gaussian distribution, as the intensity values of the pixels move from the background intensity to a higher (or lower) level at the centre of the vessel, and back to the background level again. The final binary representation of the vascular tree was then obtained by thresholding the histogram and removing the unconnected objects. This method was tested

on the DRIVE, STARE, and the HRF databases (Staal *et al.*, 2004, Hoover,Kouznetsova and Goldbaum, 1998, Budai *et al.*, 2013). The Se and Sp were 78.5% and 95.1%, respectively, for the first two databases with an Acc of 93.4%, and 79.0% and 97.5%, respectively, for the HRF database with an Acc of 97.4%. A line detector not based on the Gaussian profile of the vessel was designed by Nguyen et al. (Nguyen *et al.*, 2013). Here, the limit of this technique, which is a high level of FPs at the contour of the vessels, have been partially overcome by combining two different approaches. Firstly, by reducing the length of the lines detector, the inclusion of adjacent vessel pixels is avoided. Secondly, by increasing the dynamic range of the intensity levels of the pixels (using a local contrast enhancement) the background noise is reduced. The resulting effect was tested on the DRIVE and STARE databases, with an Acc of 94.1% and 93.2%, respectively. Akram and Khan used a 2-D Gabor wavelet to enhance vascular structures and thin vessels (Akram and Khan, 2013). This directional selective algorithm has the double advantage of filtering out background noise and adjusting its detectability level by tuning the spatial frequency of the wavelet. The output of such enhancement process was used as input for multi-layered thresholding. In this last stage, several levels of threshold values and validation masks were applied with different rules, eliminating false edges and generating a binary map of the blood vessels. This technique obtained good results in DRIVE and STARE, with an Acc of 94.7% and 95.0%, respectively.

To avoid the issues related to the learning process of image classifiers (learning rate, learning epoch, and local minima), Bala and Vijayachitra implemented an Extreme Learning Machine (ELM) classifier (Bala and Vijayachitra, 2015). An ELM is a feed-forward neural network used to handle problems difficult to solve with classical parametric techniques (Huang,Zhu and Siew, 2006). In particular, the authors chose to employ a three-step single hidden layer feed-forward neural network. This artificial network has three layers (input, hidden, and output) of interconnected nodes that mimics the connection of neurons. The features used to train this neural network were extracted from the pre-processed retinal image (histogram equalization and

segmented by a matched filter). Among the features extracted and used to classify retinal images, there are some first- and second-order statistical texture values, such as entropy, energy, correlation, and homogeneity. The method was tested on DIARETDB0 (Kauppi *et al.*, 2006) and DRIVE databases obtaining a Se of 96.7% and 100%, Sp of 100% and 94.1%, and an Acc of 97.5% and 95.0%, respectively.

Neural networks have also been used by Liskowski and Krawiec (Liskowski and Krawiec, 2016), who designed a pre-trained convolutional neural network for vascular segmentation. This multilayer approach, based on the succession of convolutional, pooling and fully connected layers, has been applied on STARE and DRIVE datasets achieving an Acc up to 97.0% and 95.1%, respectively.

Azzopardi et al. adopted a strategy that aimed to automatically segment vessel trees in low-quality retinal images (Azzopardi *et al.*, 2015). In the pre-processing stage, the strong contrast around the circular border of the FOV area was smoothed to enhance the features of the fundus. The smoothing technique, developed by Soares at al. (Soares *et al.*, 2006), performs dilation of the border, replacing every black pixel with the mean value of its neighbours inside the ROI. This process was repeated several times, augmenting the radius of the ROI by one pixel per iteration. The enhancement was achieved using a histogram equalization algorithm developed by Pizer at al. (Pizer *et al.*, 1987). The actual segmentation, based on a computational model called bar-selective combination of shifted filter responses (B-COSFIRE), employed some difference-of-Gaussian filters to detect the change of intensity typical of a vessel object. This trainable filter has shown to be computationally efficient. By tuning the values of the blurring and shifting operators, used to increase its detectability property, B-COSFIRE filter was able to detect vessels in different orientation and the end of the vessel. Tests on DRIVE, STARE, and CHASE_DB1 obtained values of Se and Sp up to 77.2% and 97.0%, respectively.

A segmentation technique that does not require any pre-processing or training was devised by Wang et al. (Yangfan Wang *et al.*, 2013). To create

the binary map of the vessel tree, the authors combined matched filters with multi-wavelet kernels, and a multiscale hierarchical decomposition as a vessel locator. The wavelet, similarly to the Fourier transform, is used to represent the image in the frequency domain, which in this work is used to highlight the spatial frequency associated with the step edge of the vessels, while the hierarchical decomposition operates an iterative segmentation at varying image resolution, locating smaller and smaller vessels. This segmentation technique exploits the central specular reflection of the vessels. The filter was applied to the image at several orientations to match different profiles of the vessel. The decomposition reduced also of the noise content of the image as it decomposes the image into two components, namely; the part that contains the features of interest and a part related to the noise. The ability of this algorithm to identify small features without confusing them with noise is the main goal of this strategy. An adaptive thresholder is then applied to obtain the binary map. The quantitative analysis of this technique conduced on DRIVE and STARE datasets revealed an Acc of 94.6% and 95.2%, respectively.

Macula and fovea - Locating the position of the macula and fovea is crucial in the automatic detection of pathology related to diabetes, such as diabetic maculopathy. If disease in this area becomes chronic, damage to the composite photoreceptors becomes irreversible (Medhi and Dandapat, 2016). There is increasing evidence that as the surviving diabetic population ages, blindness secondary to maculopathy exceeds that of proliferative retinopathy (Flanagan, 1993). As observed from the literature, most of the techniques used to locate the ROI containing the macula rely on some anatomical assumptions related to the distance between the fovea and OD (Huiqi Li and Chutatape, 2004, M Niemeijer,Abramoff and Van Ginneken, 2008, Sagar,Balasubramanian and Chandrasekaran, 2007, Welfer,Scharcanski and Marinho, 2011). The exact location of the fovea is achieved by various algorithms, such as thresholding or template matching, usually preceded by a filtering stage where blood vessel abnormalities are removed. An example of this procedure was presented by Chin et al. (Chin *et al.*, 2013). To locate the

fovea centre, the authors combined the information provided by the vessels and OD segmentations with some a-priori knowledge about the anatomical structure of the retina. To establish the search area, the vessel arch was used as template to draw a hypothetical parabola with a vertex on the nasal side of the OD. The search interval was selected along the principal meridian of this parabola at a specific distance from the disk, in terms of disk diameter (DD). Such distance was estimated calculating the disk-macula distance from a sample of 126 images. Inside this area, the window with the minimum number of vessel pixels was considered as fovea. To measure the performance of this method, the number of correct detections (NCD) within 25%DD and 50%DD was performed. MESSIDOR and some images from the Tayside diabetic screening program at Ninewells Hospital (Dundee) were used to validate the technique. The performance was better on the latter, with a NCD-25% of 51/66 and a NCD-50% of 61/66 in high resolution images. To overcome the time-consuming process of blood vessel segmentation and vascular arch parabola fitting, Zheng et al. developed a technique based on anatomical structure constraints and their relative location, and on intensity-level information related to the OD (Zheng *et al.*, 2014). In the preprocessing stage, a course localization of the OD was performed analysing the intensity levels of red channel of the retinal image. After the elimination of the blood vessels, the OD boundary was detected using a region-based model (Joshi *et al.*, 2010). From this boundary, a circle was fitted to obtain the position and radius of the OD. This information was used to provide constraints in order to narrow the search area for the fovea. To locate the temporal side of the OD the brighter area was detected, the side less covered by blood vessels. To this side, the distance of 2.5 OD diameter off the centre of the OD and 5-degree below, referred to the x axis of the image, was selected as research area. The final position of the fovea was then detected by applying a morphological geodesic reconstruction (Mukhopadhyay and Chanda, 2003). In the reconstruction based on geodesic dilation the image is repeatedly dilated by an elementary isotropic element until it reaches an image “mask”, which acts as a limit for the dilation (Arefi *et al.*, 2009). In this way the peaks in the image spread out. This allows the removal

of all the undesirable features, such as bright spots, vessels and so on. The outcome is a connected area with constant intensity level. The geometrical centre of this area is the fovea centre. This method was performed on DRIVE, obtaining a detection success rate of 100%, on HEI-MED obtaining 98.8% and DIARETDB1 with 93.3%. An extraction method independent from geometrical relationship estimation and blood vessel removal was described by Medhi and Dandapat (Medhi and Dandapat, 2016). In this work, the colour intensity normalization and the contrast enhancement of the retinal image in the preprocessing stage involved the use of different colour spaces. The first colour normalization took place in the luminance plane of YIQ colour space, where the Y plane was modified according to a specific parametric rule proposed by Sánchez et al. (Sánchez *et al.*, 2008). A second transformation was applied on the HIS colour space. To detect the circular region containing the macula, the authors used two sets of information: the absence of blood vessels and the location of the OD. Because the superior and the inferior arteries of the retina are arranged horizontally with respect to the macula in a fundus image, a horizontal canny edge detector was used to find them. Within the central region between these arteries, the macula and fovea were located. The intensity value was then inverted and the binary image of the macula region obtained through an Otsu's thresholding. The Otsu's method searches for the threshold that minimizes the intra-class variance of the intensity levels of the intensity histogram, returning as result a binary image. A further Hough transformation, which is designed to detect edges, was applied to the edges of the macula in order to define the circular geometry of the macula and its centre, the fovea. A well-established way to evaluate the performances of macula detection methods is to measure the Euclidean Distance between the manual segmented image and the one processed by the feature extractor algorithm (Flanagan, 1993). The analysis was performed on DRIVE and DIARETDB1 datasets obtaining an average distance of m = 6.88 pixel and a standard deviation of s = 5.85 pixel in the first and m = 8.90 pixel and s = 12.89 pixel in the second.

Table 3.2 List of the reviewed methods regarding retinal image anatomical features and their outcome results.

	Authors	Methods	Databases	Performances
Optic Nerve	Issac et al. (Issac,Sarathi and Dutta, 2015)	Adaptive image thresholding to identify OD and OC boundaries	Local Dataset	Se 100%, Sp 90.0%, Acc 94.4%.
	Dashtbozorg et al. (Dashtbozorg,Mendonça and Campilho, 2015)	Sliding Band Filter.	MESSIDOR; INSPIRE-AVR	Acc 99.9%; Acc 99.6%.
	Mookiah et al. (Mookiah *et al.*, 2013b)	Attanassov intuitionistic fuzzy histon segmentation.	Local Dataset	Acc 93.4%, F-score 0.92.
	Cheng et al. (Cheng *et al.*, 2013)	Superpixel Classification.	MESSIDOR.	AUC 0.800
	Basit and Fraz (Basit and Fraz, 2015)	Morphological Operations, Smoothing filters and Watershed Transform	SHIFA (local database); DRIVE; CHASE_DB1; DIARETDB1	AVG Se 99.2%; AVG Sp 76.2%; AVG Acc 98.9%.
	Reza et al. (Reza and Ahmad, 2015)	Curve Operator for automatic OD detection.	STARE; DIARETDB1	Acc 87.7%; Acc 94.4%.
	Huazhu et al. (Fu *et al.*, 2018)	Multi-label deep network with polar transformation	ORIGA; SCES (local datasets)	AUC 0.851; AUC 0.900.
Blood Vessels	Odstrcilik et al. (Odstrcilik *et al.*, 2013)	Illumination correction, contrast equalization, 2D Matched filtering, thresholding.	HRF; DRIVE; STARE	Se 78.6%, Sp 97.5%, Acc 95.4%, AUC 0.974; Se 70.6%, Sp 96.9%, Acc 93.4%, AUC 0.952; Se 78.5%, Sp 95.1%, Acc 93.4%, AUC 0.957.
	Akram and Khan (Akram and Khan, 2013)	2D Gabor wavelet, multilayer and adaptive thresholding.	DRIVE; STARE	Acc 94.7%; Acc 95.0%.

	Bala and Vijayachitra (Bala and Vijayachitra, 2015)	Matched filtering, local entropy thresholding, Grey level co-occurrence matrix for features extraction and Extreme learning machine for classification.	DIARETDB0; DRIVE	Se 96.7%, Sp 100%, Acc 97.5%; Se 100%, Sp 94.1%, Acc 95.0%.
	Liskowski and Krawiec (Liskowski and Krawiec, 2016)	Convolutional Neural Network.	DRIVE; STARE	Acc 95.0%, AUC 0.97; Acc 95.7%, AUC 0.979.
	Azzopardi et al. (Azzopardi *et al.*, 2015)	Difference-of-Gaussians filtering (B-COSFIRE).	DRIVE; STARE; CHASE_DB1	Se 76.6%, Sp 97.0%, Acc 94.3%, AUC 0.961; Se 77.2%, Sp 97.0%, Acc 95.0%, AUC 0.956; Se 75.9%, Sp 95.9%, Acc 93.9%, AUC 0.949.
	Wang et al. (Yangfan Wang *et al.*, 2013)	Multiwavelet kernels vessel enhancement, hierarchical optimal decomposition, adaptive thresholding	DRIVE; STARE	Acc 94.6%; Acc 95.2%.
Macula & Fovea	Chin et al. (Chin *et al.*, 2013)	OD location and vasculature map via geometrical approximation and VAMPIRE, location of the ROI via anatomical priors and fovea location with highest likelihood after 2D Gaussian mask filtering.	Local Dataset; MESSIDOR	Fovea detection rate (FDR) within 25%DD 77.3%, FDR 50%DD 92.4% (with good quality images); FDR 25% DD 56.2%, FDR 50% DD 79.8% (with no risk of macula edema images).

Zheng et al. (Zheng *et al.*, 2014)	OD location via thresholding, morphological bottom-hat transform for blood vessel elimination, OD boundary detection and circle fitting, fovea location via anatomical constraints and morphological geodesic transform.	DRIVE; HEI-MED; DIARETDB1	FDR 100%; FDR 98.8%; FDR 93.3%.
Medhi and Dandapat (Medhi and Dandapat, 2016)	OD detection via thresholding, fovea detection via Canny edge detector, Otsu thresholding, Hough transform and anatomical constraints	DRIVE; DIARETDB1	FDR 100% D 6.88; FDR 95.51%, D 8.90.

Table 3.3 Performance Evaluators – Statistical measures mostly used for the evaluation process of feature extraction methods.

Measure	Description	Formula
Sensitivity (Se) or True Positive Fraction (TPF) or Recall (Rec)	The proportion of pixels that are correctly identified as object	$\frac{TP}{TP+FN}$
Specificity (Sp) or True Negative Fraction (TNF)	The proportion of pixels that are correctly identified as non-object	$\frac{TN}{FP+TN}$
Precision or Positive Predicted Value (PPV)	The proportion of positive results that are true positive	$\frac{TP}{TP+FP}$
Negative Predicted Value (NPV)	The proportion of negative results that are true negative	$\frac{TN}{TN+FN}$
Accuracy (Ac or Acc)	It describes the closeness of a measurement to the true value	$\frac{TP+TN}{TP+FP+FN+TN}$

False Positive Fraction (FPF)	The proportion of pixels that are not correctly identified as object	$\frac{FP}{TP+FN}$
False Negative Fraction (FNF)	The proportion of pixels that are not correctly identified as non-object	$\frac{FN}{TP+TN}$
Receiver Operating Characteristic (ROC)	It plots the TPF versus the FPF	-
Area under the curve (AUC)	The area under the ROC (AUC = 1 in an optimal system)	$AUC = \int_0^1 TPF(FPF)dFPF \approx \frac{Se+Sp}{2}$
Mathew's correlation coefficient (MCC)	Used in machine learning as a measure of the quality of binary (two-class) classifications	$\frac{TP \times TN - FP \times FN}{\sqrt{(TP+FP)(TP+FN)(TN+FP)(TN+FN)}}$
F-score	Measure of a test's accuracy	$2 \times \frac{PPV \times Se}{PPV+Se}$
Euclidean distance (D)	Measure the distance between two points in a 2D space. If P(p1,p2) and Q(q1,q2)	$d(P,Q) = \sqrt{(q1-p1)^2(q2-p2)^2}$

3.4 PRINCIPAL ARTIFACT SOURCES

The terms artifact and noise refer to two different phenomena. In this thesis, artifact is assumed as a chromatic or textural element of the image that doesn't belong to the object being imaged. Noise is an additional contribution to the image caused by a stochastic process. A more detailed definition can be found in **Chapter 4**.

Typically, the optical system configuration during fundoscopy or similar fundus observation, is the one formed by the eye's fundus, the device optics used to get access into the eyeball, the image sensor and a source of light. Every ophthalmic device, capable to access the posterior segment of the eye and acquire an image of the fundus, is based on this configuration, with different levels of complexity in the optics layout. Some classic examples are displayed in **Figure 3.16**, where we can have an overview of the main optical components that allow the light to be projected into the fundus and then been collected from the fundus, so to obtain the image of the retina.

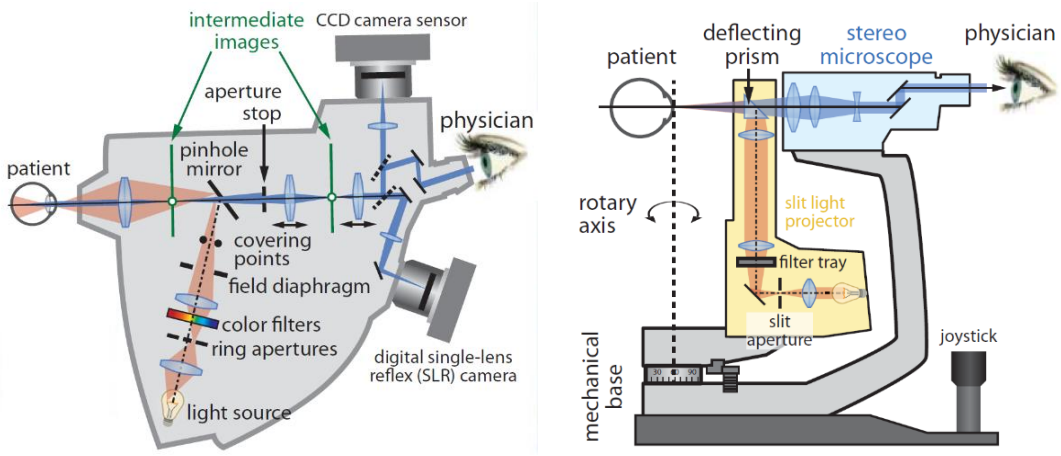

Figure 3.16 Simplified schematic of the optical setup of a ZEISS FF 450^{PLUS} fundus camera, on the left, and a ZEISS SL 120 slit lamp, on the right (Kaschke,Donnerhacke and Rill, 2013).

In the following, an overview of the main causes of artifacts and poor quality in retinal imaging is presented.

3.4.1 OPTICAL PATH DISTORTIONS AND COLOUR DISTORTIONS

Two optical systems stand between the retina and the images sensor: the eyeball and the optical stage of the ophthalmic device. If one of this two elements presents an optical (or geometrical) anomaly or a misalignment, this can cause a distortion in the final retinal image, hence a loss of information of the retina's clinical features. It is important to note that taking a photo does not rely entirely on the proper functioning of the optical, mechanical and electrical subsystems of the device. The way the operator and the subject interact with the device impacts as well on the quality of the retinal photography (Saine, 1984). This is determined by the varying level of experience of the personnel, the different types of cameras and device settings or the individual characteristics of the acquired eye, to name a few (Paulus *et al.*, 2010). For these reasons, the specialists tend to assess the quality of images after each shooting before labelling them as usable for the clinical evaluation, based on their own experience and knowledge about image quality. As introduced in **Chapter 2**, when this assessment take place in a clinical environment under

the supervision of professional personnel, the chances to result in poor quality images is low (Yu *et al.*, 2012a). However, in many mHealth applications, images are acquired directly in the field by trained locals, who cannot rely on the same level of experience in image quality assessment.

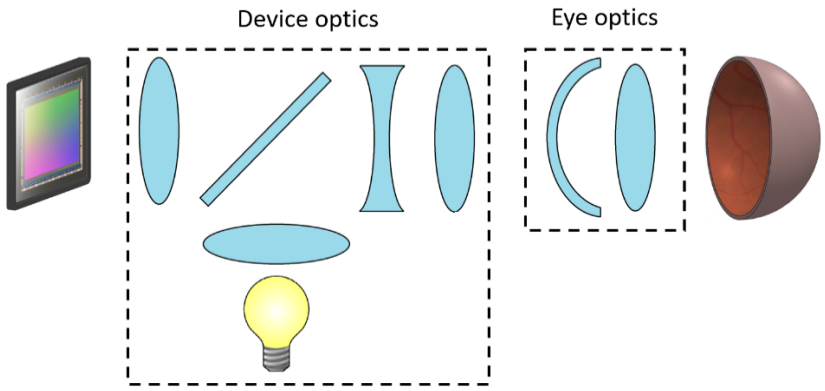

Figure 3.17 Optical path in retinal photography. Between the image sensor, on the left, and the retina, on the right, there are two optical systems formed by the optics of the imaging device and the eye.

Five common sources of artifacts during an eye examination have been identified (S. Wang *et al.*, 2016, Yu *et al.*, 2012a):

- eye movement and blinking
- object obstruction
- incorrect focus
- media opacity
- inadequate illumination.

Eyelashes and dust are the most frequently sources of obstruction observed. Another important source of obstruction has been found in small pupil size (Sangave *et al.*, 2014). Incorrect focus and aberrations in retinal photography can be caused by wrong device settings, optics misalignment or by the severe refractive error of the eye. The loss of contrast is usually associated with media opacity and by illumination problem. The illumination also plays a key role in the chromatic dominance of the photo. The light interacts with the objects along the optical path and with the surrounding media, determining the dominant wavelength therefore the colour of the retinal

features on the final image. Light reflections are also another important source of artifact, that usually is minimized by tilting the optics that projects the light into the eye with respect to the optics that collects the image from the fundus. Interfaces between media with different reflective index, such as between the air and the cornea, are the most subjected to this phenomenon.

3.4.2 PATHOLOGICAL CONDITIONS

Poor quality retinal imaging can be caused by some pathological or congenital conditions or as consequence of natural aging. In general, these are related with the opacification of the clear structures of the eye (cornea and lens) or with some traumas, which can complicate the visual access to the fundus from the front of the eye. A brief description of the main pathological conditions that have an impact on the quality of retinal imaging is presented below, divided according to the anatomical structure involved.

Cornea: as described in **Chapter 2**, the inner and biggest structure of the cornea is the corneal stroma, which packed with more than 200 layers (lamellae) of long cylindrical collagen fibrils, with each lamella being about 2.0 μm thick (Atchison and Smith, 2000). The fibrils that compose each lamella are parallel to each other, and uniform in size and spacing. The lamellae are arranged so that successive lamella runs across the cornea at an angle respect to the previous one. This arrangement guarantees the transparency of the cornea while enhancing mechanical strength. More precisely, the high level of transparency has been associated with the regularity of the fibril size and separation (Hart and Farrell, 1969). When this regularity is compromised, due to aging, pathologies or traumas, the cornea can become cloudy, which induces light scattering phenomena.

Corneal haze can be caused by congenital or neonatal corneal opacification, which includes endothelial dystrophies, corneal dermoids, cornea plana, CYP1B1 cytopathy and kerato-irido-lenticular dysgenesis, also called Peter's anomaly (Nischal, 2015). Corneal degenerations, such as the Salzmann's nodular degeneration (Maharana *et al.*, 2016), can lead to haze. This pathology alters the regularity between the fibrils creating bluish grey

nodules that, if located in the central region of the cornea, induces scattering. Herpetic corneal diseases, keratitis, trachoma and other corneal infections (Teweldemedhin *et al.*, 2017, Kalezic *et al.*, 2018, Shah *et al.*, 2011, Taylor *et al.*, 2014) if not treated are responsible for a range of corneal haze such as scarring, thinning and neovascularization. Limbal stem cell deficiency (LSCD) is another cause of corneal opacity (Fernandez-Buenaga *et al.*, 2018, Shortt,Tuft and Daniels, 2011). The limbal stem cells are situated in the junction between the sclera and the cornea and are responsible for the renovation of the corneal epithelium. LSCD causes loss of transparency, with ulcerations and ingrowth of blood vessels onto the cornea. The most commonly reported causes of LSCD are chemical and thermal burns (75%), followed by ocular surface inflammatory diseases such as Stevens Johnson syndrome and ocular cicatricial pemphigoid (Bobba *et al.*, 2017). Corneal trauma can create discontinuities in the epithelium-stromal interface, and the corneal oedema/fibroblastic activated during the wound healing generates corneal haze (Meek *et al.*, 2003, Moller-Pedersen, 2004). Almost 80% of emergency visits due to eye trauma are account for corneal abrasions or foreign bodies (Willmann and Melanson, 2017). Other sources of trauma responsible for corneal haze arise from complications of refractive surgery, in particular with surface ablations (Chang,Maurice and Ramirez-Florez, 1996). In **Table 3.4**, the summary of the abovementioned epidemiology is presented.

Table 3.4 The most common causes of corneal opacity.

Genetic	Corneal degeneration	Infectious	Physical/ traumatic
Endothelial dystrophies	Salzmann's nodular degeneration	Herpes simplex	LSCD
Corneal dermoids		Keratitis	Corneal injury
Cornea plana		Trachoma	Surgery
Peters anomaly		Allergic eye disease	

Along with optical media opacity, some morphological alteration of the curvature of the cornea can cause distortions and aberrations in retinal imaging. In some cases, such as with keratoconus, the degradation of the

image quality is such that can be used as measurement of the severity of such pathology (Leonard *et al.*, 2016).

Lens: similar to the cornea, the lens fibres form the bulk of the lens. These long and thin structures are wound up together under the surrounding capsule and epithelium, maintaining a circular symmetry with respect the central axis of the lens. Because of its thickness and the presence of cellular body, within the lens the scattering phenomena are more intense than in the other clear components of the eye. Moreover, the constant growth of the lens throughout life, determines an age-related change of the lenticular parameters, observing an increment of the forward-scatter compared to the backward-scatter (Atchison and Smith, 2000).

The symptomatic clouding of some of the lens's layers is usually referred to as cataract, which is one of the leading causes of visual impairment and the first cause of blindness worldwide, according to the WHO (Pascolini and Mariotti, 2012b). There are a wide variety of conditions that can cause cataract, the majority of which are age-related. A recent survey in UK (**Table 3.5**) has shown that the most common lens opacities assessed, which resulted in cataract surgery prescription, are: anterior subcapsular cataract, vacuoles, water clefts, coronary flakes, and focal dots (Frost and Sparrow, 2001). Other more rear causes of cataract are: polychromatic lustre, lenticonus and central nuclear morphology.

Table 3.5 Common lens opacities as observed in the UK survey (Frost and Sparrow, 2001).

Group of opacities	Class of opacities
Subcapsular opacities	Anterior subcapsular opacity
	Posterior subcapsular opacity
Nuclear sclerosis	Nuclear colour, brunescence
	Nuclear light scatter, opalescence
Cortical opacities	Cortical spokes
	Water clefts
	Fibre folds

Eyeball geometry: Severe myopia and hyperopia cause distortions and blurred vision. Similarly, these refractive errors can corrupt the quality of retinal imaging, generating distortion, chromatic aberration and defocusing. Although the impact of such pathologies on the images of the fundus has not been the object of a systemic investigation yet, some researchers are starting to use the information contained in the deformations and in the level of contrast of retinal images to train deep learning algorithms for the automatic assessment of the refractive error (Varadarajan *et al.*, 2018).

3.5 ARTIFACT AND NOISE SUPPRESSION

Unlike image enhancement methods, the purpose of artifact and noise suppression algorithms is to selectively remove the degradation and restore the original clinical content of the image. Here, a wide overview of techniques used for artifact and noise mitigation are presented, providing application examples, when possible, in retinal imaging.

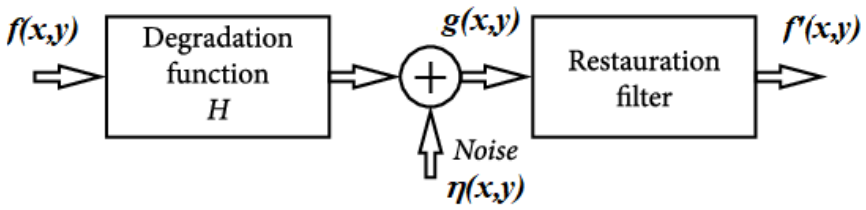

Figure 3.18 Model of image degradation/restoration process.

The theoretical basis of image degradation and restoration is schematised in **Figure 3.18**. Given an input image $f(x,y)$, the degraded image $g(x,y)$ is the result of the degradation process and the noise, considered as an additive process. Knowing (or modelling) the degradation function H, and the noise $\eta(x,y)$, the process of restoration aims to obtain an estimate $f'(x,y)$ of the original image. If H is a linear, position-invariant process, the degraded image in the *spatial domain* is given by

$$g(x,y) = h(x,y) \star f(x,y) + \eta(x,y) \tag{6}$$

where $h(x,y)$ is the spatial representation of the degradation function and the symbol $\star$ indicates convolution. Convolution in the spatial domain is analog to

multiplication in the *frequency domain*, so by using Fourier transform Eq. 6 becomes

$$G(u,v) = H(u,v)F(u,v) + N(u,v) \tag{7}$$

In the restoration process a filter $R(u,v)$ is applied so to obtain $F'(u,v)$ as

$$F'(u,v) = R(u,v)G(u,v) \tag{8.1}$$

$$F'(u,v) = R(u,v)H(u,v)F(u,v) + R(u,v)N(u,v) \tag{8.2}$$

$$F'(u,v) \approx F(u,v) \tag{8.3}$$

as the restoration filter $R(u,v)$ is the inverse of the degradation function, neglecting the noise function.

Spatial filtering –The mechanism of spatial filtering consists in defining a small region (mask) and a predefined operation. Each pixel of the image is then processed by computing the predefined operation on the surrounding region of the pixel (neighbourhood) and the pixel itself **Figure 3.19** and Eq. 9.

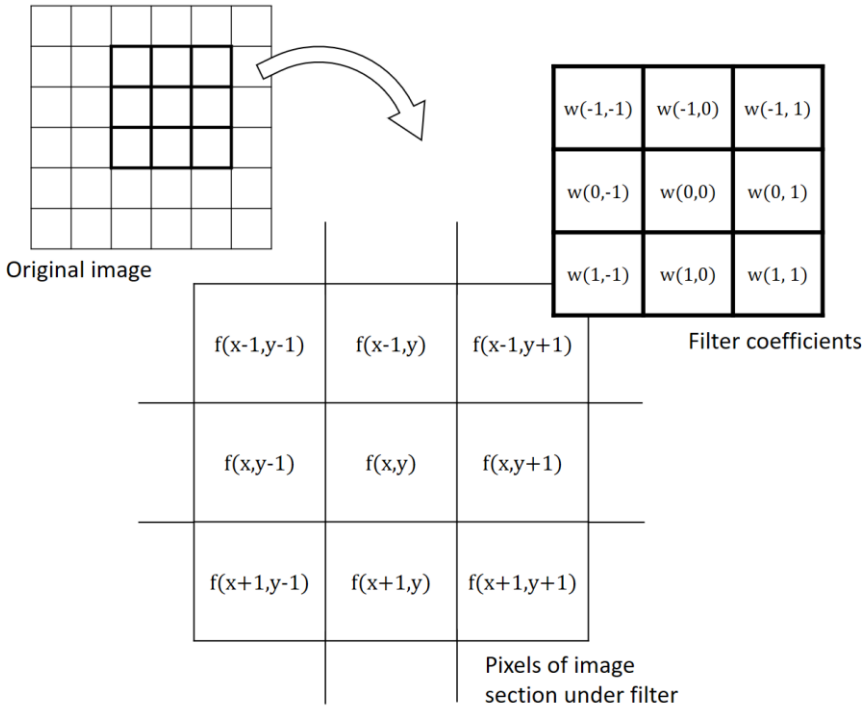

Figure 3.19 The mechanism of lineal spatial filtering using a 3 x 3 filter mask.

$$f'(x,y) = \sum_{s=-a}^{a} \sum_{t=-b}^{b} w(s,t) f(x+s, y+t) \tag{9}$$

where $w(s,t)$ are the coefficients of the filter at the s and t pixel location. Spatial filters can offer larger versatility, because they can be used for linear and nonlinear filtering, something not always possible in the frequency domain for instance. There is a wide variety of filters with the mathematical structure of Eq. 9. They can be clustered as:

1. **Mean filters** – (arithmetic, geometric, harmonic, etc.) where the filtering produces a smooth image, and the noise is reduced as a result of blurring.
2. **Order-static filters** – (median, max&min, midpoint, etc.) which response is based in ordering (ranking) the value of the pixel contained in the image region, defined by the $a \times b$ rectangular window, under processing.
3. **Adaptive filters** – they take advantage of the characteristic of the abovementioned filters but the behaviour changes based on the statistical characteristic of the image region under processing.

Frequency domain filtering – The great intuition of Jean Baptist Fourier was that any periodic function can be expressed as the sum of sines (or/and cosines) of different frequencies, each multiplied by a different coefficient, now called *Fourier series*. Even non-periodic function can be expressed as integral of sines (or/and cosines) multiplied by a weighting function. A classic example is offered by digital music. Any sound waves (musical, vocal, noise, etc.) can be obtained as the sum of multiple sinusoidal components, **Figure 3.20**.

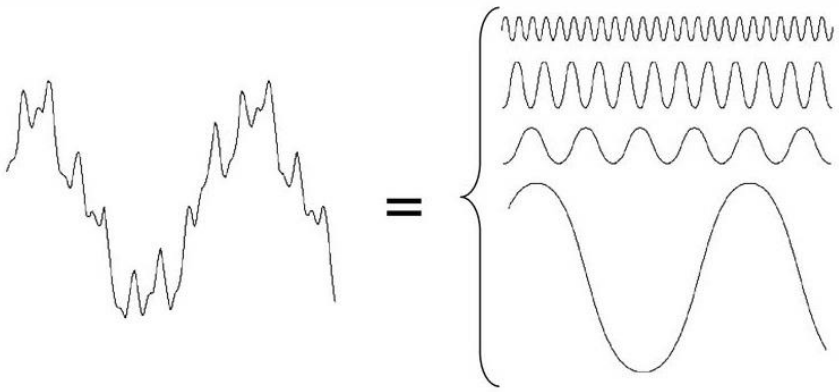

Figure 3.20 The shape of the wave on the left can be obtained as the sum of the sinusoidal components on the right.

As a consequence, every sound can be decomposed in simple sinusoidal waves characterized by the triples: frequency, amplitude and phase. Knowing the triplets of each subcomponent of the wave can fully describe it. Similarly, a digital image can be seen as the combination of all the different pixel intensity distribution in two dimensions. The 2D Discrete Fourier Transform is the mathematical formalism that translate the image into the sum of each frequency component

$$F(u,v) = \sum_{x=0}^{M-1} \sum_{y=0}^{N-1} f(x,y) e^{-j2\pi(ux/M + vy/N)} \quad (10)$$

where $f(x,y)$ is the digital image of size $M \times N$, and F is evaluated for values of the discrete variables u and v in the range $u = 0, 1, 2, \dots, M-1$ and $v = 0, 1, 2, \dots N-1$.

Like in noise filtering for audio recording, if the frequency components of the noise are identified they can be removed by employing the following filers or their combination.

1. **Bandreject filters** – as anticipated in the introduction to filtering in the frequency domain, when the location of the noise components is known, those can be removed selectively.
2. **Bandpass filters** – opposite to bandreject application, this type of filters excludes the entire frequency components above or below an established threshold (low-, high- and band-pass filter).
3. **Notch filters** – a notch filter rejects frequencies in predefined neighbourhoods about a central frequency.

Once the degradation function H (estimated by observation, experimentation or modelling) has been obtained, we can generate the restored image $F'(u,v)$ by using the following methods:

1. **Inverse filtering** – the simplest approach to restoration from degradation is directly inverse filtering, where we obtain the Fourier transform of the estimate image $F'(u,v)$ simply by dividing the transform of the degraded image $G(u,v)$ by the degradation function.

$$F'(u,v) = \frac{G(u,v)}{H(u,v)} \quad (10)$$

Substituting the right side of Eq.7 for $G(u,v)$ in Eq. 10 yields

$$F'(u,v) = F(u,v) + \frac{N(u,v)}{H(u,v)} \tag{11}$$

This first rough approach can be very convenient from a computational prospective, but highlights two important problems. The first regards the noise components $N(u,v)$ which, if not known, prevent us from estimating effectively $F(u,v)$. The second is that if the degradation function has zero or very small values, then the ratio $N(u,v)/H(u,v)$ can easily dominate the estimate $F'(u,v)$. A possible approach to partially prevent this side effect is to limit the filter frequencies to values near the origin. In fact $H(0,0)$ is usually the highest value of $H(u,v)$ in the frequency domain. Thus, by limiting the analysis of frequencies near the origin, we can reduce the probability of encountering zero values.

2. **Least square error filters** – To handle both the degradation function and the statistical characteristics of noise, Norbert Wiener in 1942 proposed an innovative restoration approach. The idea is considering images and noise as random uncorrelated variables, and the goal is to find an estimate f' of the uncorrupted image f such that the mean square error between them is minimised. The error measure is given by

$$e^2 = E\{(f - f')^2\} \tag{12}$$

where $E\{\cdot\}$ is the expected value of the argument. Assumed that one or the other function has zero mean and the intensity levels of the f' are a linear function of the intensity level of f, Eq.12 is given in the frequency domain by

$$F'(u,v) = \left[\frac{H^*(u,v)S_f(u,v)}{S_f(u,v)|H(u,v)|^2 + S_\eta(u,v)}\right] G(u,v) \tag{13.1}$$

$$= \left[\frac{H^*(u,v)}{|H(u,v)|^2 + S_\eta(u,v)/S_f(u,v)}\right] G(u,v) \tag{13,2}$$

$$= \left[\frac{1}{H(u,v)} \frac{|H(u,v)|^2}{|H(u,v)|^2 + S_\eta(u,v)/S_f(u,v)}\right] G(u,v), \tag{13.3}$$

where $H(u,v)$ is the degraded function, $H^*(u,v)$ is the complex conjugate of $H(u,v)$, $|H(u,v)|^2 = H^*(u,v)H(u,v)$. $S_\eta(u,v) = |N(u,v)|^2$ and $S_f(u,v) = |F(u,v)|^2$ are the power spectrum of the noise and the non-degraded image respectively. While this method doesn't suffer from the problem of the inverse filter, since the denominator is usually non-zero, it requires the knowledge of the power spectra of the noise and the degraded image.

3. **Constrained least square filters** – an important improvement to the previous solutions is the constrained least square filter, since here only the mean and variance of the noise are required. To explain this method, it is convenient to express the elements of Eq. 6 as matrixes and vectors:

$$\boldsymbol{g} = \boldsymbol{H}\boldsymbol{f} + \boldsymbol{\eta} \tag{14}$$

The constraint here is given by

$$\|\boldsymbol{g} - \boldsymbol{H}\boldsymbol{f}'\|^2 = \|\boldsymbol{\eta}\|^2 \tag{15}$$

where $\|\boldsymbol{a}\| \triangleq \boldsymbol{a}^T\boldsymbol{a}$ is the Euclidean vector norm. This equation aims to establish a criterion to measure the smoothness, such as the second derivative of the image (Laplacian), of the restoration. The frequency domain solution to this optimization problem is given by the expression

$$F'(u,v) = \left[\frac{H^*(u,v)}{|H(u,v)|^2 + \gamma|P(u,v)|}\right] G(u,v) \tag{16}$$

Where γ is a parameter that must be adjusted to satisfy the constraint, and $P(u,v)$ is the Fourier transform of the Laplacian operator. In order to adjust γ we can define a residual vector $\boldsymbol{r}$ as

$$\boldsymbol{r} = \boldsymbol{g} - \boldsymbol{H}\boldsymbol{f}' \tag{17}$$

Since $F'(u,v)$ is a function of γ, then also $\boldsymbol{r}$ is a function of this parameter. What we need to do is to define the optimum γ so that

$$\|\boldsymbol{r}\|^2 = \|\boldsymbol{\eta}\|^2 \pm a \tag{18}$$

Where a is an accuracy factor. $\|\boldsymbol{r}\|^2$ can be easily obtained by noting that

$$R(u,v) = G(u,v) - H(u,v)F'(u,v) \tag{19}$$

From which $r(x,y)$ can be obtained by computing the inverse transform of $R(u,v)$. Then

$$\|\boldsymbol{r}\|^2 = \sum_{x=0}^{M-1}\sum_{y=0}^{N-1} r^2(x,y) \tag{20}$$

And $\|\boldsymbol{\eta}\|^2$ can be obtained as the summation of the variance σ_η^2 and the mean m_η of the noise as

$$\|\boldsymbol{\eta}\|^2 = MN\left[\sigma_\eta^2 + m_\eta^2\right] \tag{21}$$

where

$$\sigma_\eta^2 = \frac{1}{MN}\sum_{x=0}^{M-1}\sum_{y=0}^{N-1}\left[\eta(x,y) - m_\eta\right]^2 \tag{22}$$

and

$$m_\eta = \frac{1}{MN}\sum_{x=0}^{M-1}\sum_{y=0}^{N-1}\eta(x,y) \tag{23}$$

are the sample mean. These quantities are not difficult to estimate, assuming the noise and the image intensity values are not correlated.

It is important to highlight that while, from a theoretical point of view, the presented solutions show an increasing optimization, this is formally not correlated to an automatic improvement from a clinical quality perspective. As a result, the choice of one method over the other will mostly be determined by the perceived visual quality of the resulting images. It is therefore subjective and, once again, highly task-dependant.

In retinal imaging, two different restoration approaches have been established over the years: classical Gaussian-filtering based techniques and edge-preserving based methods (He *et al.*, 2017, Shin *et al.*, 2005, Buades,Coll and Morel, 2005, Hani *et al.*, 2014). The first is widely used in medical imaging for its robustness and computational advantages, however since the weights of a Gaussian filter depend on the spatial distance, these techniques may lose sharp edges and add blurring effect. In retinal image this

is a major drawback since the majority of blood vessel and ONH segmentation methods rely on edge-detection principles. Edge-preserving methods were introduced to overcome this problem.

The latter methods are more widely used in denoising retinal images, with bilateral filter (BLF) becoming one of the most popular type of algorithm. BLF uses a local weighted average (on the spatial distance and intensity difference between pixels, hence bilateral) without the need for iterations, allowing for a low computational effort. The drawback is that it doesn't perform well with thin tube-like structures, such as the retinal vasculature, therefore some implementations are usually required. He et al. (He *et al.*, 2017) modified a BLF by substituting the spatial kernel with an adaptive spatial kernel, sensitive to different orientations and size of blood vessels. This is computed by measuring the normal distance between each pixel and the straight line passing through the centre of the blood vessel, rather than the Euclidean distance. Such method has proven to improve blood vessel segmentation accuracy (Frangi's filter technique was selected (Frangi *et al.*, 1998)). Another image restoration technique that uses BLF is described by Xian et al. (Xian *et al.*, 2017). Here, a combination of spatial and frequency domain techniques is used to reduce the mixed Gaussian-Poisson noise from retinal images. The corrupted image is initially processed with a BLF, which preserves large amplitudes and results in a denoised image characterised by high contrast. Secondly, the denoised image is subtracted to the original one obtaining a low-contrast output which is processed by a Wavelet shrinkage in the short-time Fourier transform domain. In this way the small amplitudes are filtered, completing the denoising mechanism. The sum of this two component forms the estimated image:

$$f' = s' + S'$$

Where s' and S' are the denoised high-contrast and low-contrast images. This approach is then iteratively processed as shown in **Figure 3.21**.

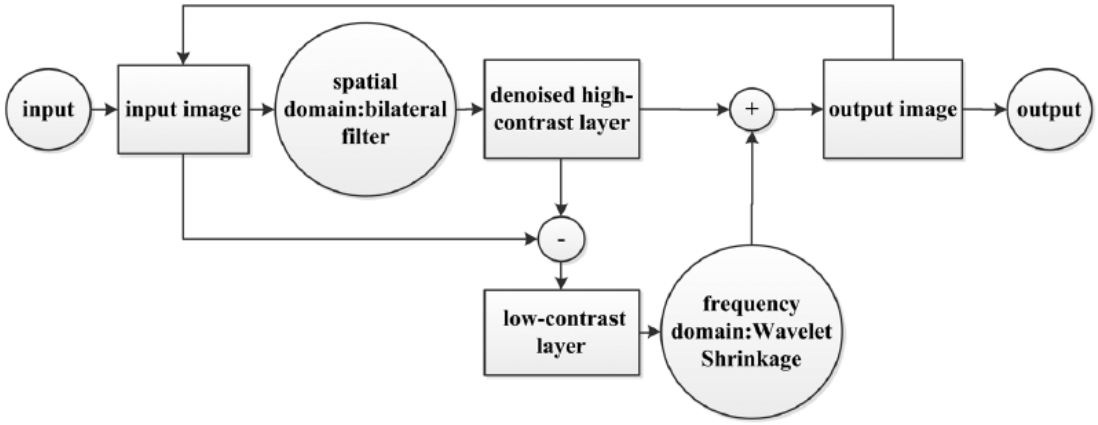

Figure 3.21 the block diagram of the Dual-Domain Image Denoising.

This multi-domain approach was more effective in reducing the error between the original image and the denoised one with improvement of segmentation and detection techniques.

3.5.1 AUTOMATIC AND SEMIAUTOMATIC ASSESSMENT SYSTEMS

Manual grading by an ophthalmologist has been the state of the art of DR and maculopathy screening in the past decades. However, the increase of the population with diabetes and the progressive aging of the population had pushed the health care provision capability, with prediction of an increasing need in the next decades (Tufail *et al.*, 2016, Yung-Hui Li *et al.*, 2019). In particular, the large number of images produced within screening programmes (boost by mHealth services) has to be assessed by the same constant number of ophthalmologists, creating a bottleneck in the screening workload. For this reason, as soon as the technology for automated detection of pathologies became available, many software solutions were developed and tested, some of which have already been employed by NHS.

The principal goal of these software packages is the evaluation of the gradability of the image (the image needs to pass some quality tests) and the

classification of the retinal images as diseases/no disease. The terms automatic and semiautomatic refer to the capability of these algorithms to process the image without the intervention of an operator or with the intervention/supervision of the operator, respectively.

The process of validation of automated retinal image analysis systems (ARIAs) usually involves the measurement of sensitivity and specificity in detecting the targeted retinopathy (Larsen *et al.*, 2003, Usher *et al.*, 2004). However, these absolute values need to be compared with the performance of alternative grading system, including human graders, in order to determine the actual improvement of screening programme efficiency. This is what has been done by the University of Aberdeen, in collaboration with NHS Scotland, in a large-scale study, involving 6722 patients from Grampian, where the software has proven to have a better detection rate, 90.5%, than manual grading, 86.5%, for any retinopathy (Scotland *et al.*, 2007, Sam Philip *et al.*, 2007b). This class I CE marked ARIA software, called iGradingM, is currently being used in Scottish national diabetic retinopathy screening programmes.

As for supervised software packages, of particular interest are the solutions developed for the quantitative evaluation of the morphometry of the retinal vasculature, e.g. IVAN (Tien Yin Wong *et al.*, 2006), SIVA (G. Liew *et al.*, 2008), QUARTZ (Muhammad Moazam Fraz *et al.*, 2015) and VAMPIRE (Perez-Rovira *et al.*, 2011). In particular, VAMPIRE (Vasculature Assessment and Measurement Platform for Images of the REtina), created in collaboration with 10 clinical and image processing centres, has been designed to quantify morphological parameters of blood vessels (cross-section width, tortuosity, fractal dimension etc.) for large sets of fundus images, generating measurements suitable for biomarker discovery. Here biomarkers are considered as elements of the vasculature that are statistically associated with conditions that impact treatment decisions, prognosis, or diagnosis (Trucco *et al.*, 2013).

Other commercial systems currently available in the market are the IDx-DR (Goatman, 2006), the Retmarker (Pires Dias,Oliveira and da Silva Cruz,

2014) and the EyeArt (Solanki *et al.*, 2014). The IDx-DR is a class IIa CE approved medical device, which includes features such as quality assessment, detection of microaneurism detection, haemorrhage, cotton wool spots and fusion algorithms that combined together to generate a diabetic retinopathy index used as classifier. This software has been validated in several large screening populations, reaching a sensitivity and specificity of 96.8% and 59.5 %, respectively. Retmarker, developed in Portugal by the Coimbra University, combines a quality assessment algorithm and a co-registration algorithm, which allows comparisons during follow-up visits of the same retinal area. CE approved as a class IIa medical device in 2010, this system has obtained a sensitivity of 95.8% and a specificity of 63.2%. Finally, EyeArt, developed by Eyenuk and USC Keck School of Medicine, is engineered to perform DR screening on the cloud cluster (Amazon Elastic Cloud; Amazon EC2, Amazon, Seattle, WA, USA). Sensitivity and Specificity are 93.8% and 72.2 respectively. A detailed list of other ARIA systems can be found in (Trucco *et al.*, 2013).

3.6 STATISTICAL DESCRIPTORS OF QUALITY

In objective terms, the definition of “quality” in retinal photography is still a matter of debate (Lalonde,Gagnon and Boucher, 2001). Translating a subjective evaluation into a quantitative value is *per se* an ill-posed problem. As we discussed in the previous paragraph, the assessment of an image is a cognitive task that depends on the experience of the clinician, the viewing conditions, the diagnostic procedure and so on. Nonetheless, the considerable advantage coming from obtaining a measurable quantity of the clinical information content of an image has stimulated the researchers to identify some evaluation criteria.

A retinal image contains many anatomical structures and other features that can be associated to some pathological conditions. When we explore the world around us we usually are able to identify an object only in relation to its immediate background (**Figure 3.22**). This is the same strategy adopted by many image processing procedures, rather than using the overall characteristics of the image.

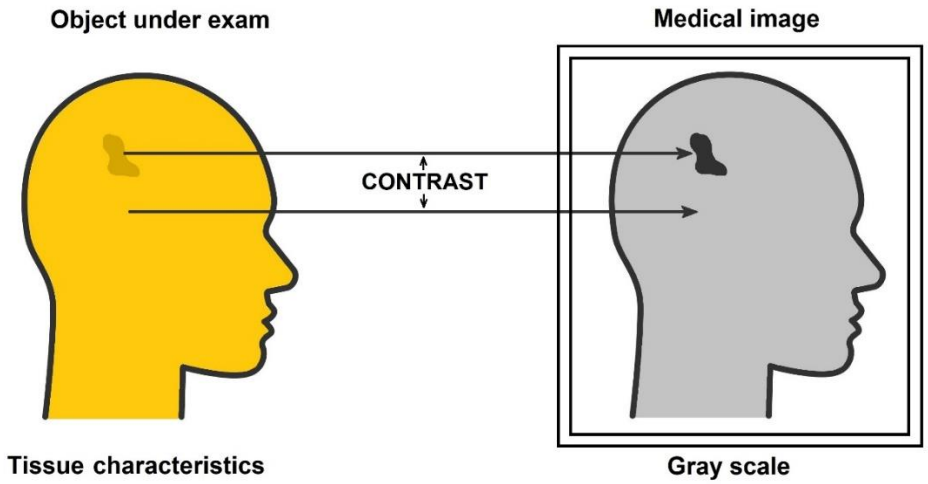

Figure 3.22 Example of the process that convert tissue characteristics in a visual image.

Under these considerations, five different factors have been identified to have direct impact on the visual assessment process in medical imaging: contrast, blur, noise, artifacts, and distortion (Sprawls, 1987). The advantage in using these factors is that they are measurable, since they can be described or modelled mathematically. In the following, the impact that each factor has in retinal imaging will be proposed, as it will clarify the selection of the statistical descriptors used to evaluate them.

Contrast – probably the most fundamental characteristic of an image, it is the difference between the image intensity of an object and the surrounding or background (**Figure 3.22**). In retinal imaging, the identification of a specific object is only possible if the difference between its intensity value and the surrounding area is not zero. Particularly for detection of pathological signs, a device that produces high contrast fundus images is preferable. If we suppose that in a specific colour channel an object has a nominal intensity value I_O and the background a nominal intensity value I_B, we can define local contrast as

$$C = \frac{I_O - I_B}{I_B}. \quad (1)$$

Blur – The variation of the physical characteristics of an object within an image concern not only the intensity level of a specific colour channel but also to its size. Sometimes addressed to in terms of resolution, in fundoscopy it's

the ability to distinguish two retinal structures in space as separate (Prince and Links, 2006) (example in **Figure 3.23**). Since it has an impact on small objects, the higher the resolution, or the lower the blur, the better in terms of diagnostic capability.

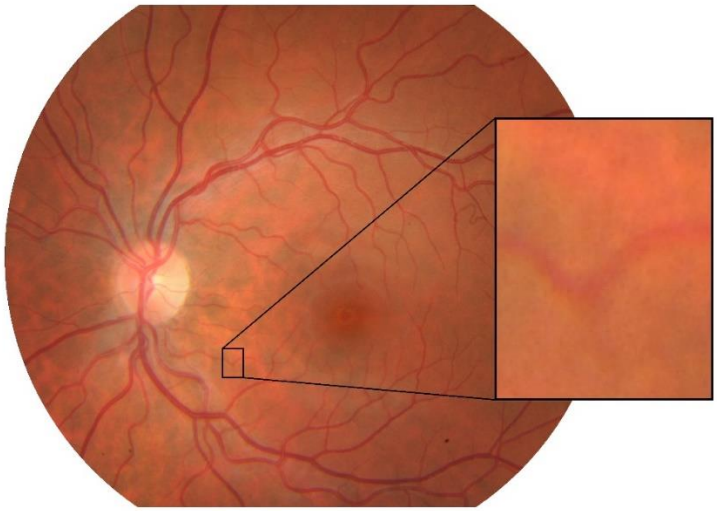

Figure 3.23 Example of blur in fundus imaging. In the magnified portion of the retinal image, the separation between the blood vessels and the fundus appears more as a gradual transition rather than a clear line.

Noise – the effect of noise on retinal images is to add a random fluctuation in the intensity levels of the pixels. If properly modelled, this contribution can be predicted and sometime filtered or mitigated. The type and amount of noise depend on many variables: the imaging system, the imaging method and so on. A more detailed description will be presented in the next chapter on this regard.

Artifacts – this aspect will be described in more details in the next chapter.

Distortion – Closely related with noise and artifact, this term is sometime used to explicitly refer to the resulting effects of noise and artifact on the retinal image (change in the morphology or the chromaticity of an anatomical feature of the retina).

As explained above, dealing with the restoration of images from artifact and noise is commonly related with the problem of obtaining a model of these two elements (or together as a unified model). To help the evaluation of the effect

of degradation phenomena on the image, after obtaining a model of such degradation, the signal-to-noise (SNR) ratio can be used. This measures the level of information carried by the signal power (here the non-degraded image) and the noise power, expressed in the frequency domain as:

$$SNR = \frac{\sum_{u=o}^{M-1}\sum_{v=0}^{N-1}|F(u,v)|^2}{\sum_{u=o}^{M-1}\sum_{v=0}^{N-1}|N(u,v)|^2}$$

Another important parameter used in the evaluation of a degradation filtering process is the mean square error, given by

$$MSE = \frac{1}{MN}\sum_{x=0}^{M-1}\sum_{y=0}^{N-1}[f(x,y) - f'(x,y)]^2$$

In literature, as for retinal image quality evaluation (Yu *et al.*, 2012b, Remeseiro,Mendonca and Campilho, 2017, Yin *et al.*, 2014, S. Wang *et al.*, 2016, Haralick,Shanmugam and Dinstein, 1973), three different groups of statistical descriptors are commonly employed: histogram features, Haralick features and specific textural feature.

3.6.1 HISTOGRAM AND CONTRAST FEATURES

Histogram features

These are mean, standard deviation, skewness, kurtosis, interquartile range (IQR) and contrast sensitivity function (CSF). Where the CSF of a channel X is obtained as:

$$CSF(X) = IQR(X)/\ max(X) - min(X), \quad (1)$$

and is an expression of the statistical dispersion of the between the upper and lower quartile respect to the range of intensities of that channel.

Contrast and blur features

To detect uneven illumination and poor focus, 7 different contrast and blur measures have been selected: contrast ratio, local contrast ratio, blur metric, full intensity range, relative intensity range, interquartile intensity range and saturation metrics *(Yin et al., 2014, Crete et al., 2007)*.

Contrast ratio (CR) is calculated as:

$$CR_j = \bar{p_j}/s_j, \tag{2}$$

where $\bar{p_j}$ is the mean intensity of all of the pixels in a ROI in the channel j while s_j is the standard deviation of the pixels in the same ROI in the channel j. The ROI, in this case, is the whole retinal image excluding the black borders. The higher the CR the higher the blurriness. A similar contrast indicator is the local contrast ratio (LCR) which is the CR calculated on non-overlapping sub-windows of the retinal image as follows:

$$LCR = \left(\sum_{i=1}^{n} \frac{\bar{p}_{w,i}}{s_{w,i}}\right)/n, \tag{3}$$

where w is a $N \times N$ window inside the ROI and n is the total number of sub-windows.

Blur metrics (BM) measures the focal blur and the motion blur by comparing the original image with its low-pass filtered version. Intensity ranges measure the grayscale spread of an image. A larger range usually indicates higher contrast in an image. For the saturation metrics, the proportion of pixels at the highest (P_{max}) and lowest (P_{min}) intensity level are computed, which can reveal over- or underexposure respectively.

3.6.2 HARALICK FEATURES

Texture, along with spectrum and context are the three fundamental pattern elements used in human interpretation of colour images. Haralick at al. developed a classification system for texture based on the statistical evaluation not of the image itself but on grey-tone spatial-dependence matrices obtained from it (Haralick,Shanmugam and Dinstein, 1973). This method is based on the assumption that grey tone and texture have a mutual interconnection to one another. So, if a small region of an image is characterized by small variation of grey tone, the dominant property of that area is the tone. When in a small portion of the image the variation of tone is wide, then the texture is more prominent. From this intuitive assumption it appears clear that the size

of the image's region been processed is crucial. At the extreme point, in fact, if the area is the size of a single pixel, the tone prevails. Vice versa, as the number of pixels increases, the texture raises over the tone. The procedure to obtain this grey-tone spatial-dependence matrix $P(l,d,\theta)$, or co-occurrence matrix, is based on the computation of the number of occurrences of the pair of l grey levels which are distant d and oriented θ degrees from each other in the original image (orientation is described in **Figure 3.24**).

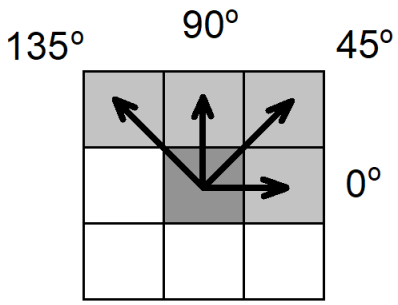

Figure 3.24 Different orientations used to evaluate the co-occurrence matrix.

As an example, considering an image 4x4 with 4 level of grey, from 0 to 3, the evaluation process for $P(4,1,0)$, $P(4,1,45)$, $P(4,1,90)$ and $P(4,1,135)$, which are the co-occurrence matrixes of the 4 grey levels distant 1 at 0°, 45°, 90° and 135° is:

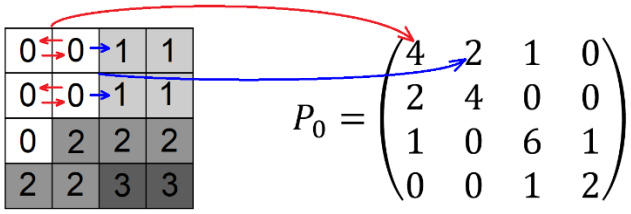

Figure 3.25 The first element of the P_0 matrix is obtained by evaluating the number of 0s that have a 0 as neighbour in the horizontal orientation. The second is obtained by counting the number of 1s that have a 0 as neighbour and so on.

$$P_{45} = \begin{pmatrix} 4 & 1 & 0 & 0 \\ 1 & 2 & 2 & 0 \\ 0 & 2 & 4 & 1 \\ 0 & 0 & 1 & 0 \end{pmatrix} \quad P_{90} = \begin{pmatrix} 6 & 0 & 2 & 0 \\ 0 & 4 & 2 & 0 \\ 2 & 2 & 2 & 2 \\ 0 & 0 & 2 & 0 \end{pmatrix} \quad P_{135} = \begin{pmatrix} 2 & 1 & 3 & 0 \\ 1 & 2 & 1 & 0 \\ 3 & 1 & 0 & 2 \\ 0 & 0 & 2 & 0 \end{pmatrix}$$

This transformation highlights the complexity of the grey tone transitions within the image, revealing the presence of organized structures or homogeneity according to which between texture or tone prevails. Haralick *et al.* identify 14 different textural features that can be measured on this matrix. In this work we will evaluate 5 of these Haralick textural features: energy, contrast, correlation, homogeneity and the (second order) entropy (Haralick,Shanmugam and Dinstein, 1973). Entropy is related to the randomness of the grey level co-occurrence matrix. Contrast and correlation measure the intensity level difference and correlation between a pixel and its neighbourhood respectively. When correlation is high, the complexity of the image is high. Energy and homogeneity are directly related, when energy is high the image is more homogeneous, giving information on the texture roughness of an image. The following equations define these features.

1. Energy: $H_1 = \sum_i \sum_j \{p(i,j)\}^2$
2. Contrast: $H_2 = \sum_{n=0}^{N-1} n^2 \left\{ \sum_{i=1}^{N} \sum_{j=1}^{N} p(i,j) \,\middle|\, |i-j| = n \right\}$
3. Correlation: $H_3 = \frac{\sum_i \sum_j (ij) p(i,j) - \mu_x \mu_y}{\sigma_x \sigma_y}$
4. Homogeneity: $H_4 = \sum_i \sum_j \frac{1}{1+(i-j)^2} p(i,j)$
5. Entropy: $H_5 = -\sum_i \sum_j p(i,j) \log\big(p(i,j)\big)$

Where $p(i,j)$ is the (i,j)th entry in a normalised co-occurrence matrix P. μ_x, μ_y, σ_x and σ_y are the means and standard deviations of p_x and p_y, which represent the marginal-probability matrix obtained as $\sum_{j=1}^{N} P(i,j)$, where the number of distinctive grey level is $n = 1, \dots, N$.

3.6.3 SPECIFIC TEXTURAL FEATURES

In this work, two parameters specifically designed to assess the quality/quantity of clinical information in retinal images were included. The two metrics are the blood vessel density (BVD) and the blood vessel contrast (BVC). To compute these two values for each retinal image, we firstly isolated the blood vessels, allowing the obtainment of the binary map M of them. This

has been achieved using a matching filter algorithm and fixing an arbitrary threshold T, as follows:

$$M(i,j) = \begin{cases} 1, & \tilde{g}(i,j) > T \\ 0, & otherwise \end{cases} \quad (3)$$

where $\tilde{g}$ is the result of the filtering on the histogram equalized green channel g of the retinal image. BVD is a measure of the quantity of pixels that belongs to the blood vessels in relationship to the total amount of pixels in the ROI, expressed as:

$$BVD = \frac{\sum_{i=1,j=1}^{m,n} M(i,j)}{m \times n}, \quad (4)$$

where m and n are the width and height of the image in pixels respectively. Blood vessel contrast is defined as the contrast of the pixels of the blood vessels with respect to the background, and is obtained using the following:

$$BVC = |\bar{p} \in M(i,j) - \bar{p} \notin M(i,j)|. \quad (5)$$

3.7 PROBLEM STATEMENT: IMAGE QUALITY IN THE FIELD

All the statistical features described so far, along with the description of the textural and contextual elements of a retinal image, highlights the intense effort the research community has put in establishing an objective method to “measure” the quality of a digital image. This problem, however, is still far from being fully unwrapped. Some of the reasons are related to the different approaches used to tackle the problem. In particular, there are two different school of thoughts that can be identified in the field: *details-oriented* and *task-oriented*. For the first, quality is based on the capability of the image to provide the larger number of details, while the second builds the definition of quality on the ability of the image to provide the information related to the specific diagnostic purpose for which is used.

To better explain these two different angles, we can make some simple examples. When we look at some old family photos, in general, the quality of the image is low compared to a picture acquired with a current smartphone. We have this perception because our ability to distinguish face tracts or

background objects is poor in old images compared to the modern digital photos, thus relating the quality with level of details perceived. Between the line of this initial statement one can spot a first attempt of defining quality in digital imaging as the ability of distinguishing the largest number of details. This shares some elements with the concept of resolution, which indicates that quality and resolution are somehow connected. This may be a small but promising step towards the establishment of quality as measurable characteristic of a digital image. Let's take few other steps forward. To be able to distinguish two separate objects we also need contrast, or an appreciable transition between two different levels of tone. So also contrast, or better, the ability to provide a large dynamic for the representation of different hues, saturations and intensity, is another key factor that builds up quality in a digital image. Following this path, it seems logical to employ the statistical descriptors presented above as criterion to measure objectively the quality of a retinal image. Unfortunately, this is only one side of the story.

The attribution of a "degree of quality" to a digital image can also be established by its ability to fulfil the purpose for which has been created, in our case perform a diagnostic assessment. Based on this concept, a medical image that appears "unpleasant" is not necessary unfit to perform a reliable clinical assessment, therefore being of diagnostic-oriented good quality. Let's think of an X-ray scan or an ultrasound image for instance. Even if resolution and contrast can be low, for the diagnostic purposes for which these techniques are employed, these are not limitations. Ultimately, the accessibility of the clinical information is the first requirement of a good medical image and all the other characteristics play only a secondary role. The big problem in this approach is that measuring this accessibility is a complex issue. The medical diagnosis is (still) the result of a subjective evaluation, thus based on some of the rules that we are just starting to understand (e.g. considering all the inference elements related to human vision we described initially) (Muhammad Moazam Fraz *et al.*, 2012b, Hoover,Kouznetsova and Goldbaum, 1998). In other words, what appeared to be a promising way to objectively define quality in clinical imaging, has to clash with the subjectivity side of these medical

tasks, therefore losing the conditions of generality and independency typical of a definition. Not all is lost though.

From a practical point of view, the latter path is the one that seems to offer the more effective outcomes. This because, even in conditions of poor quality photography from an “aesthetic level”, if the image still contains the information that the assessment process requires, e.g. cup-to-disc ratio requires OC and OD edges, then the image is usable. This means that even images with noise or artifacts can be effectively used in the assessment process boosting the overall throughput of screening programmes. Studies have reported a rate of inadequate retinal images up to 10% for mydriatic images and up to 20.8% for single field non-mydriatic ones (Teng,Lefley and Claremont, 2002, Liesenfeld *et al.*, 2000, M. Niemeijer,Abramoff and van Ginneken, 2006, Scanlon *et al.*, 2003). Even in the clinical setting this problem can reach similar proportion with Niemeijer at al. (M. Niemeijer,Abramoff and van Ginneken, 2006) reporting a 12% of ungradable images in a web-based screening programme, and Fleming et al. (Fleming *et al.*, 2010) indicating between 5.6% and 20.5% of the number of patients with at least one non assessable image in at least one eye. This has a severe impact especially in screening programmes, where a considerable amount of time, resources and health care personnel is involved (England, 2018, Peto and Tadros, 2012). The adoption of mobile technology is showing promising results in addressing these three aspects. Moreover, now that mobile technology is bridging the gap between health care coverage and hard-to-reach-communities (Bastawrous *et al.*, 2016). Quality however remain a problem. In fact, images acquired with different environmental conditions, by different devices, operated by personnel with different level of experience generate large variability in the image quality.

In this work, focusing on gradability requirements of automatic assessment algorithms, a new artifact removal solution is proposed to boost image throughput of population screening. This new solution has been applied to images affected by artifact and validated by measuring the statistical descriptors of retinal image quality describe in the previous section.

CHAPTER 4. A COMPREHENSIVE DATABASE OF RETINAL IMAGES (CORD)

4.1 PREMISES

The following chapters describe the original work produced during this doctoral research activity. In particular, given our need to study image artifacts and their removal, and the lack in the literature of a suitable dataset, this chapter describes the creation of a database that, amongst other information, contains reference image artifacts and ground truth images, and sets a method for an internal consistency check of image quality. Such work was led primarily by the author, in particular the creation and management of the ethics documentation and submission process, the development of the data collection protocol, as well as the data collection process itself, and the dataset assembly, in concert with ophthalmologists, clinical personnel and colleagues from the research group of the author. Following this, the thesis produces a phenomenological artifact model to be used as a premise to artifact removal (**Chapter 5**), an actual artifact removal strategy and shows its results on a set of retinal images (**Chapter 6**), and draws a set of conclusions (**Chapter 7**).

4.2 CORD DATABASE: RATIONALE AND ORGANIZATION

To address the lack of images reporting artifacts in the field, a new comprehensive database called CORD, (Comprehensive Ophthalmic Research Database) (*CORD Comprehensive Ophthalmic Research Database*, CORD 2019) has been created. To achieve this, a simplified framework for the data collection process and a new hierarchical database structure were designed. The aim of such choice is to facilitate the creation of similar databases, and to optimise information extraction and usage from CORD.

The NHS premise selected for this project was the eye clinic of the Falkirk

Community Hospital, NHS Forth Valley, Falkirk, UK. To minimise impact on the NHS workflows, the database collection was performed during clinical hours. We decided to adopt three basic principles for the selection of the data and imaging modalities to include in this dataset:

- Selecting techniques routinely performed within ophthalmology;
- Maximizing the variety of information;
- Keeping the acquisition time and participant discomfort and inconvenience to broadly acceptable levels.

As part of the database information, we included basic and easy to report parameters such as the ophthalmic device settings (Ravikumar,Thibos and Bradley, 2008) used, the ambient illumination (Ravikumar,Thibos and Bradley, 2008) and patient information that are known to have an impact on image specifics, such as skin type (Wilk *et al.*, 2017), age (Artal *et al.*, 1993) and sex (Wagner,Fink and Zadnik, 2008, Zetterberg, 2016). This information is not just essential to be able to replicate the acquisition conditions, but also contribute to the better understanding of how each single aspect of fundoscopy impact on image quality. We acknowledge the absence of these basic information as one of the most diffuse lack within existing ophthalmic databases, though very useful for image quality evaluation and inter-database data normalisation. Secondly, we included ophthalmic measurements and functional tests, namely optical biometry of the eye (Aguila-Carrasco *et al.*, 2017, Lopez-Gil,Iglesias and Artal, 1998), refractive errors (Aguila-Carrasco *et al.*, 2017), corneal tomography and visual field. In fact, the optical and geometrical parameters of the eye play an important role in the generation of phenomena such as chromatic dominants and blurring. Finally, we included retinal images acquired via fundoscopy and OCT, including the majority of the modality output.

Within these last imaging modalities, we also collected retinal images affected by classic artifacts and quality distortions (uneven illumination, loss of contrast, object obstruction, corneal reflection and chromatic dominants (Yu *et al.*, 2012b)). Often discarded as poor quality images. Such images, which indeed are usually not included in the final corpus of a database, depriving the

research field of noise modelling of valuable resources, are indeed essential to this thesis, and constitute one of the core novelties of this dataset with respect to the literature. Particularly for this doctoral work, artifact images are of crucial importance, as they will be used in the development of the artifact removal strategy.

4.2.1 DATABASE CONTENT

As per the previous paragraph, the CORD database contains:

Participant information - only participant information that are relevant to current knowledge on the interpretation of the content of retinal images was retained: age, sex (M/F) and skin type. No information that can directly identify the participant have been included in the data collection, in accordance with the General Data Protection Regulation 2018 (GDPR) of the European Union.

Numerical measurements - the numerical measurements included for each eye are: autorefraction (spherical error, cylindrical error and slope of the principal meridian), optical biometry (axial length, corneal power, anterior chamber depth, white to white distance and pupil size), corneal topography (anterior axial curvature, pachymetry, anterior elevation and posterior elevation maps), Humphrey visual field 24-2 perimetry and Goldmann tonometry IOP (intra-ocular pressure).

Images and videos - slit-lamp images and videos of the iridocorneal angle pre-dilation and images and videos of the anterior and posterior segments before and after dilation were included. Other post-dilation imaging technique included are: OCT scans of the macula (including the transverse scan of retinal and choroidal layers at a specified depth, called en-face scan), optic disc and dye-free OCT angiography, disc and macula-centred stereo retinal pair images, and images with and without examples of artifacts of the fundus. Moreover, fundus camera images of the retina (macula centred) with and without artifacts.

Metadata - information on how to access and retrieve data from the database, the content of each folder, the data format and the licensing terms

are available in the database in the form of ‘readme’ files, were included as navigational tool and guideline.

All data included are stored in the *native formats* at the time of data collection. Where the data format was not recommended for long term preservation (*eCommons: Cornell's Digital Repository*)(*eCommons: Cornell's Digital Repository*)(*eCommons: Cornell's Digital Repository*)(*eCommons: Cornell's Digital Repository*)(*eCommons: Cornell's Digital Repository*)(*eCommons: Cornell's Digital Repository*)(*eCommons: Cornell's Digital Repository*)(*eCommons: Cornell's Digital Repository*)(*eCommons: Cornell's Digital Repository*)(*eCommons: Cornell's Digital Repository*)[262], a more stable format was additionally produced, to ensure long-term curation and preservation, as sanctioned in the data preservation policy of the University of Strathclyde.

All the fundus camera and slit-lamp biomicroscope images are in JPG format, as this was the native format at data capture. OCT native data are in Tag Image File Format (TIFF) (Commission). TIFF files have been included also for slit-lamp and fundus camera to ensure long term preservation of the data. A DICOM format (DCM) (*DICOM*)(*DICOM*)(*DICOM*)(*DICOM*) for all the images is available to allow the user to access the metadata embedded by the respective imaging devices, and to allow easy visualization on viewers commonly available in medical settings.

Videos obtained from the slit-lamp are stored in MPEG-4 (MP4) format, as this was the native format at data capture. Given this format is likely to enable a long-term preservation, no alternative formats have been produced for videos.

Numerical data, not in digital format, have been retrieved and included in their native printout version from the respective device, alongside thematic tables and Comma-Separated Value (CSV) (Datahub) files for data preservation. Some of the reports and exam results have been directly produced in PDF format by some of the ophthalmic devices employed, therefore they are included in the dataset. “Readme” or similar data content description files have been included for each folder of data and stored in

Markdown format (MD) (*CommonMark Spec*), which is human-readable both with a simple text viewer, and with Markdown-aware viewers.

4.2.2 DATA COLLECTION FRAMEWORK

Given the large number of data collected, a specific labelling system and data structure have been designed to facilitate navigation. Data are labelled with a unique alphanumeric code to ensure the identification of the participant, the anatomic side examined (left/right eye), the ophthalmic test used and the clinical quality (clinical standard/artifact). This labelling code is optimized for data retrieval through simple wildcard searches. Finally, the folder tree allows the user to manually navigate through the ophthalmic techniques to select a specific ophthalmic data within each single participant.

Data Labelling System

A coded file labelling system has been implemented, allowing for unique identification of each datum, for data isolation, and for potential expansion of the database. When creating the labelling system, capital Latin characters and digits have been used, avoiding the 4 letters (B, I, L and O) as these letters inherently contain ambiguity and may be confused/misread for numerical digits (8, 1, 1, 0 respectively). The elements that compose each label are: a 6-digit numeric participant identifier (ID) which allows for potential growth of the database to include up to 1,000,000 participants with a unique identifier, anatomical side (D or S), a unique letter triplet code which identifies each device and acquisition modality (with each triplet for each device beginning with the same letter to enable macro searching), image quality classification (determined as either data captured as per the instrument intended performance, and hence assumed of clinical quality (C) or with artifacts and therefore falling outside the clinical standard quality (A)). Due to the need to maintain timing within reasonable acceptability, the clinical standard images have been defined as such by qualitative inspection by the operator. A final 3-digit serial number starting at 000 accounts for multiple images within the category. For instance, in the label 168522STUJC000: 168522 identifies the participant number, S stands for left eye, TUJ refers to OCT 3D angiography,

C means that the data has been acquired as per the instrument intended performance and 000 means that this is the first of its data type. The complete list of abbreviations used for the labelling is shown in **Table 4.1**.

Table 4.1 List of abbreviation used to build the label of the data.

Description	Label code	Description	Label code
Oculus Dexter	D	CT Anterior Elevation BFA	GEX
Oculus Sinister	S	CT Anterior Elevation BFS	GEY
Clinical Standard	C	CT Anterior Elevation BFTA	GEZ
With Artifacts	A	CT Axial Curve Anterior	GJJ
Fundus Camera	FJQ	CT Axial Curve Posterior	GJU
Humphrey Visual Field	HXE	CT Height Anterior	GJV
SL Anterior Segment (NM)	MJU	CT Height Posterior	GJX
SL Anterior Segment (Blue Illumination)	MJY	CT Indices	GKE
SL Posterior Segment (NM)	MKK	CT Inst Curve Anterior	GKU
SL Gonioscopy	MKU	CT Inst Curve Posterior	GXY
SL IOP	MQV	CT Pachy	GQE
SL Anterior Segment (M)	MXU	CT Posterior Elevation BFA	GQJ
SL Posterior Segment (M)	MYK	CT Posterior Elevation BFS	GQU
Fitzpatrick Skin Type Table	PXY	CT Posterior Elevation BFTA	GQZ
Handheld Autorefractor Table	RZK	CT Refractive Power	GUJ
OCT 3D Disc	TJQ	CT Total Power	GVK
OCT 3D Macula	TKE	CT Asymmetric Report	GVV
OCT 3D Macula En-face	TQJ	CT CLMIX	GVY
OCT 3D Angiography	TUJ	CT Densitometry Report	GXK
OCT Stereo Fundus Image Left	TZV	CT Eye Metrics Report	GXJ
OCT Stereo Fundus Image Right	TXY	CT IOL Power Report	GXQ
OCT Fundus Image	TYE	CT Mapx4 Report	GXU
OCT Report	TEX	CT Mapx1 Report	GXZ
Optical Biometry	WXU	CT Mapx4_3	GYE
Participant Information Table	NEJ	CT Refractive Report	GYJ
CT Galilei Native Files	GEQ	CT Wavefront Report	GZK

SL=Slit-lamp, CT=Corneal Topography, M=Mydriatic, NM=Non-Mydriatic.

4.3 DATA COLLECTION PROTOCOLS

The CORD database has been created in collaboration with the NHS Forth Valley, using the ophthalmic devices and the premises of a running eye clinic. Therefore, all the instrumentation and the data acquisition setup were calibrated and certified for clinical usage at the time of data collection. Below, the full description of the employed ophthalmic devices and setup is detailed.

4.3.1 CLINICAL PREMISES SETUP

The whole project took place at Falkirk Community Hospital, NHS Forth Valley, Falkirk, UK. The time slot scheduled for the data acquisition from volunteers was chosen to be late afternoon, as it was identified to have the minimal impact on the daily clinical activity. All the ophthalmic devices employed in this work were located in different rooms, one close to the other, on the same floor, as per clinical logistics. The ophthalmic instrumentations, the consumables and the room setup were not altered from the ordinal setting, as all the techniques and modalities included in the database are ophthalmic assessment procedures routinely used, therefore already configured for data acquisition.

4.3.2 OPHTHALMIC DEVICES

The ophthalmic devices selected for this database are all part of routine eye exams:

1. Slit-lamp biomicroscope
2. OCT (Optical Coherence Tomography)
3. Fundus camera
4. Optical biometry analyser
5. Handheld autorefractor
6. Corneal topography scanner
7. Humphrey visual field analyser

Slit-Lamp biomicroscope - A slit-lamp biomicroscope is probably the most versatile and widely-used instrument for ophthalmic diagnosis. It is mostly used for the visual inspection of the anterior and posterior eye segments. It also serves as a mechanical and optical support for many accessories, such as those used to measure the IOP or view the iridocorneal angle as well as digital cameras for photo and video documentation. In the CORD database, the images of the anterior segment of the eye, iridocorneal angle (gonioscopy), the IOP and some of the posterior segment images (or fundus images) were acquired using a Topcon SL-D701 slit-lamp (**Figure 4.1** left) integrated with a

Topcon DC-4 5-megapixel CMOS sensor based digital camera (Topcon Corp., Japan). The gonioscopy was performed using an additional Goldmann one-mirror lens (**Figure 4.1** centre) (Ocular Instruments Inc., Washington, USA). The IOP was measured with a Keeler Goldmann Applanation Tonometer (**Figure 4.1** right) (Keeler Ophthalmic Instruments, UK) and an auxiliary handheld 90D lens (Volk Optical Inc., Ohio, USA) enabled visual access to the fundus.

Figure 4.1 Topcon SL-D701 slit-lamp integrated with a Topcon DC-4 (left), Applanation tonometer (centre) and an handheld 90D lens (right).

OCT - OCT is a widely used imaging modality for generating high-resolution three-dimensional images of ocular tissues. In this work, a Topcon DRI OCT Triton Plus (**Figure 4.2**) was used to capture the multi-modal true fundus images, and cross-sections of tissue layers with micrometre resolution. OCT angiography was also implemented, enabling the visualization of retinal microvasculature without the need for injectable dye. The OCT system used returns images in the form of a stack of 2-dimensional slices.

Figure 4.2 DRI OCT Triton Plus.

Fundoscopy - Colour fundus images were obtained using a Topcon TRC-50DX Type IA fundus camera (**Figure 4.3**) fitted with the body of a Nikon D300s (Nikon Corp. Japan) 12.3 megapixel digital camera. This imaging technique is frequently used to analyse the structures of the fundus, such as blood vessels and the ONH, enabling the visualization of potential morphological changes.

Figure 4.3 Topcon TRC-50DX Type IA fundus camera.

Optical biometry, refractive error, corneal topography and visual field information - The biometric measurements of the anterior chamber and the axial length were determined using a Zeiss IOL Master 500 (Carl Zeiss AG, Germany). Refractive error was assessed objectively by using a handheld autorefractor Nidek HandyRef-K (Nidek Co. Ltd, Japan), obtaining the spherical error and astigmatism (cylindrical error and slope of the principal meridian). Corneal topography was performed using a Ziemer Galilei G4 (Ziemer Ophthalmic Systems AG, Germany), which combines Placido Topography, Scheimpflug Tomography and optical biometry. The size and functionality of the visual field, or perimetry, was measured using a Zeiss HFA II 740i (4 participants) and a Zeiss HFA III 840 (6 participants) Humphrey visual field analysers.

Figure 4.4 From left to left: optical biometry analyser, handheld autorefractor, corneal topography scanner and Humphrey visual field analyser.

4.4 WORKFLOW DESIGN AND METHODS

For this study, 10 healthy volunteers aged between 18 and 40 years old were recruited. Due to the large number of imaging modalities and measurements which were performed on each participant, the acquisition workflow (**Figure 4.5**) has been specifically designed to have as low an impact on the clinical routine of the hospital as possible, optimizing timing and resources.

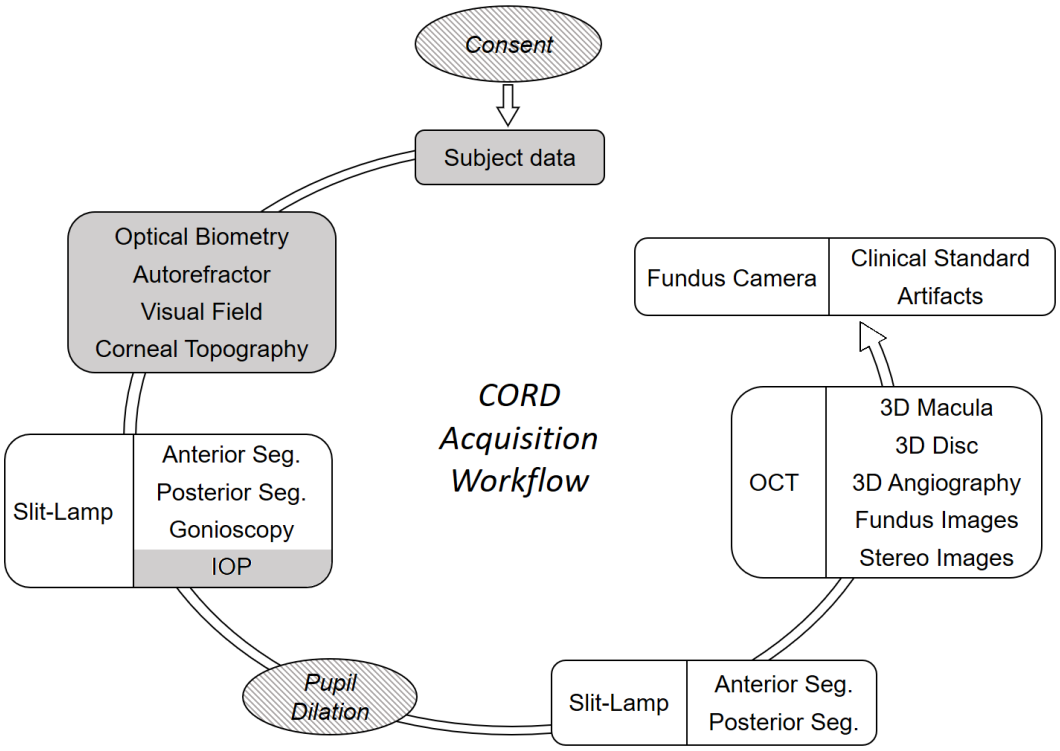

Figure 4.5 Diagram of the workflow used for the CORD database acquisition process. Grey blocks represent ophthalmic tests that produce numerical data, the white blocks represent imaging modalities and a striped background represents administrative steps.

The total acquisition time per participant, including the 15-minute break after dilation drops administration, was approximately 2 hours. The whole data acquisition process was carried out by two trained ophthalmologists.

4.4.1 DATA ACQUISITION

Ethics authorization was secured from the University of Strathclyde Ethics Committee, as per the law in force (University of Strathclyde UEC18-36). Prior to each data acquisition session, informed consent was received from the participant in the presence of a practicing ophthalmologist (Participant Consent Form example provided in **Appendix I**). Appropriate care was taken for personal data protection, as per the guidelines of the GDPR of the European Union and the University of Strathclyde's code of practice on investigations involving human beings. The study also received approval from NHS Forth

Valley, UK, which provided permission to use the premises and equipment for the acquisition of the data.

Once consent was secured, each participant was asked to complete a Fitzpatrick skin phototype questionnaire (Sachdeva, 2009). This test is commonly used to determine the skin type in terms of response to ultraviolet radiation exposure. This information, together with sex and age, are the only subject data included in the database.

The data collection framework is divided into two phases: pre-dilation and post-dilation of the subject's pupils. Between the two phases, dilating drops (Bausch and Lomb, Minims tropicamide 1%) were applied to dilate the pupils of the participant. As for the ambient lighting of the clinic's room, from now on, we will refer to a dimmed light room as a setting with an illuminance, measured at the subject's eyes level, of about 35 lx. We will refer to a dark room as a setting with illuminance of maximum 5 lx. Unless otherwise specified, the illuminance of the room, measured at the subject's eyes level, will be considered at least 240 lx.

Pre-dilation

During the first phase, all the optical and geometrical measurements of the eye were performed, together with IOP and slit-lamp imaging.

The objective refractive error was measured with both the operator and the participant in a seated position, with the operator holding the autorefractor by hand, yielding the spherical error, cylindrical error and slope of the principal meridian for each eye. The optical biometry and corneal topography were determined (in a dark room) following the classic procedure for these tests. For the visual field test (performed under dimmed light), a full-threshold 24-2 Swedish Interactive Thresholding Algorithm (SITA) (Bengtsson *et al.*, 1997) was used.

The non-mydriatic slit-lamp images of the anterior segment were acquired using a diffuse illumination and x10 magnification. Fluorescein dye (Bausch and Lomb, Minims fluorescein sodium 2%) eye drops were also administrated

to obtain fluorescein images of the front of the eye under blue illumination. Videos of the fundus were then taken at x10 magnification while using a direct focal illumination technique with a slit beam width varying between 2-4 mm, as well as diffusely illuminated anterior segment photographs. Images and videos of the fundus were also obtained with a 90D handheld lens. Gonioscopy was performed at x16 magnification with a narrow slit-beam. Before putting the Goldmann one-mirror lens in contact with the eye, topical ocular anaesthetics (Bausch and Lomb, Minims proxymetacaine hydrochloride 0.5%) were administrated to limit discomfort. All of the steps mentioned above were performed in a room with dimmed light. The measurement of the IOP using the Applanation tonometer and cobalt blue illumination filter completed the slit-lamp usage of the first phase.

Post-dilation

The post-dilation phase began at least 15 minutes after the administration of the dilating drops. A second round of anterior and posterior segment images and videos were captured with the slit-lamp biomicroscope. This was followed by OCT and fundus camera. Slit-lamp imaging was performed using the same settings as the pre-dilation phase. Images were acquired with the OCT device using five different modes: macula focused 3D scan, disc focused 3D scan, 3D OCT angiography, stereo-imaging and fundus imaging. The settings of the fundus camera during imaging was: 50 degrees angle of coverage, flash illumination at 50% of the max intensity from the 300W xenon bulb, observation light at 30% of the max intensity from the halogen bulb (used for the alignment procedure) and no filters (true-colour). All these imaging techniques were performed under dimmed light apart from OCT scans which were carried out in a dark room.

4.4.2 ARTIFACT GENERATION

The artifacts that classically determine the reduction of the quality in retinal imaging are: specular reflections, loss of contrast due to defocusing, movement of the eye, media opacity, uneven illumination and object

obstruction (eyelash due to blinking) (Yu *et al.*, 2012b). In this work, only for retinal images (fundus camera and OCT), we collected, together with adequate quality retinal counterpart, images including a selected artifact, purposefully introduced. These artifacts cover the uneven illumination, the defocusing and the object obstruction phenomena, and were manually produced during the image acquisition. In particular, the uneven illumination and the defocusing was achieved by shifting the focusing plane of the optics further or closer to the retina's one, the object obstruction was introduced by asking the participant to blink.

4.5 RETINAL IMAGE QUALITY CLASSIFICATION

The decision of undertaking the substantial amount of work that has led to the creation of CORD, rather than just collecting fundus images, is justified by the unique opportunity to set a course towards the definition of a data collection paradigm that enables the research community to fully exploit the information enclosed in such data. Moreover, the quantity and the variety of data contained in CORD is expected to offer grounding for further, more comprehensive developments.

However, for consistency with the topic of this thesis, from this point in the discourse only the retinal images and related information will be considered.

The retinal image set in CORD consists of 548 fundus images, 231 photos and 160 videos from slit lamp examination, and 80 scans (composed by ~260 2D slices each) from OCT. Excluding the fundus images acquired with the OCT in stereo imaging modality, the total amount of retinal images per each ophthalmic technique, and divided in "clinical standard" quality (CSQ) and artifact, is summarised in **Table 4.2**. Example of retinal images are shown in **Figure 4.6** and **Figure 4.7**.

Table 4.2 Fundus images (macula centred) in CORD. Images subjected to complete object obstruction were excluded from the total dataset.

Imaging Technique	Artifacts	CSQ	Tot.
Fundus Camera	251	37	288
OCT	40	20	60

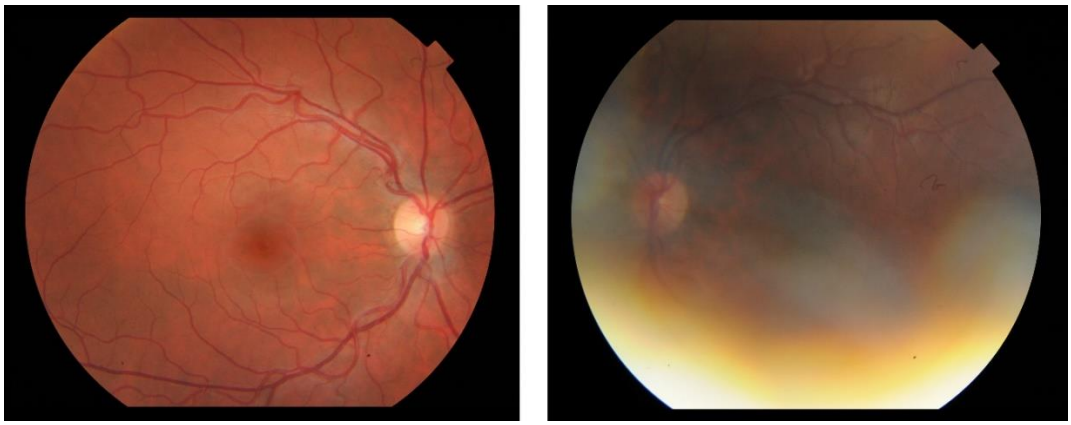

Figure 4.6 Retinal images acquired using a fundus camera Topcon TRC-50DX Type IA fitted with the body of a Nikon D300s. Left: clinical standard quality. Right: artifact caused by patient blinking.

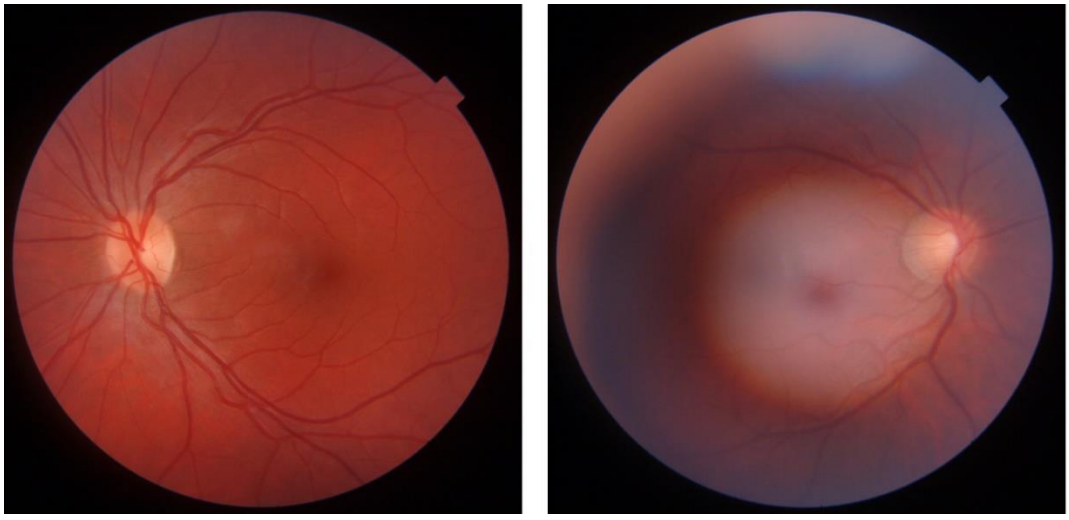

Figure 4.7 Retinal images macula-centred acquired using a Topcon DRI OCT Triton Plus OCT machine. Left: clinical standard quality. Right: artifact caused by shifting the focal plane of the instrument optics away from the retinal plane.

The classification of the images as clinical quality or artifact-affected was done during the image acquisition by an expert operator. The majority of the images affected by artifact were created on purpose with the modalities explained previously. Amongst the artifact group, a successive subdivision in 4 different categories was performed by expert, according to the most prominent typology of artifact, as follow:

- Defocusing (OCT and Fundus Camera)
- Object obstruction (OCT and Fundus Camera)
- Eyelid occlusion (OCT and Fundus Camera)
- Uneven illumination (only Fundus Camera)

Examples of such artifact typology within the CORD dataset is presented in **Figure 4.8**.

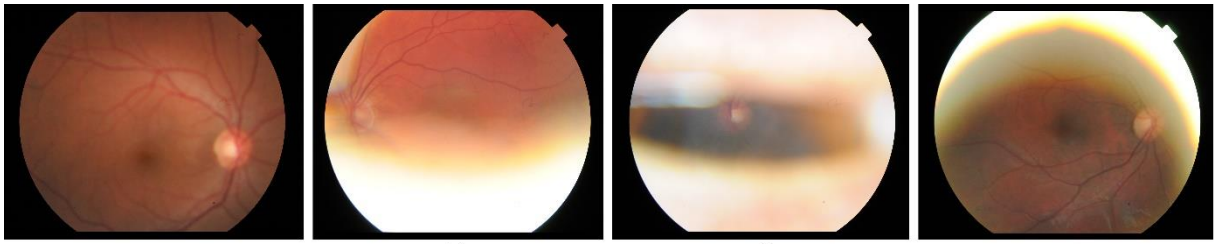

Figure 4.8 a) defocusing, b) object obstruction, c) eyelid occlusion and d) uneven illumination.

4.5.1 INTERNAL CONSISTENCY OF IMAGE QUALITY: METHODS

The unique feature of CORD of having images of the same retina (and the same device setting) acquired with and without distortions, allowed us to answer to the first critical research question of this work: can subjectively "good" or "inadequate" images be clustered on the basis of objective statistical features? And which statistical feature is more significant in such task?

The statistical features used to establish the feasibility of the clustering process are the ones described in **Chapter 3**:

- Histogram features: mean, standard deviation, kurtosis, inter quartile range, contrast sensitivity function.
- Haralick features: entropy, contrast, correlation, energy, homogeneity.
- Contrast and blur features: contrast ratio, local contrast ratio, blur metrics, intensity range and saturation metrics.
- Specific textural features: blood vessel density and the blood vessel contrast.

Given the large number of features the first step has involved the implementation of a “feature selection” algorithm. This operation results in the identification of a subset of features that optimally distinguish between CSQ retinal images and not. In fact, using too many features can degrade prediction performance even if they all contain relevant information about the response variable (Guyon and Elisseeff, 2003). From this a model used to cluster image quality was derived and used to evaluate the performances of the artifact removal algorithm developed in this work.

To reduce the dimensionality of the data and identify the subset of features whose weight in the quality classification method are most significant, a filter type feature selection algorithm was used. The algorithm selected for this purpose is a diagonal adaptation of Neighbourhood Component Analysis (NCA) (Goldberger *et al.*, 2005, Yang,Wang and Zuo, 2012), a distance metric learning methods already implemented in Matlab 2016b and well established in the literature for object classification, image retrieval, image ranking, face identification, kinship verification, clustering, or person re-identification (Dong Wang and Tan, 2017). Given the multi-class problem with a training set containing n observations:

$$S = \{(x_i, y_i), i = 1, 2, \dots, n\}, \quad (1)$$

where $x_i \in \mathbb{R}^p$ are the feature vectors, $y_i \in \{1, 2\}$ are the class labels, in this case only 2 classes, the NCA aims to learn a classifier $f: \mathbb{R}^p \longrightarrow \{1, 2\}$ that can accept a feature vector and makes a prediction $f(x)$ for the true label y of x.

The benefits of using this technique comes from its simple yet effective non-linear decision surface, with only a single parameter λ to tune via simple cross-validation, and it improves automatically as the amount of training data increases.

For each retinal features, both from fundus camera and from OCT, the statistical performances have been evaluated over each channel of the RGB, HSI and CIELab colour spaces, as described in **Chapter 3**.

The features were then processed with the NCA algorithm and the λ parameter was tuned per each channel by splitting the dataset into 5 partition and using 4/5th as training set and 1/5th as test set. The local optimization solver used for the NCA was a quasi-Newton method called Limited memory Broyden-Fletcher-Goldfarb-Shanno algorithm. To establish the best channel for quality classification the data sets of fundus camera and OCT images were split into two parts: the classification training part and the test part. The training section of the database started from 1/8th of the total retinal images and was increased by 1/8th of the total until the classification process was able to correctly classify the remaining test section (**Figure 4.9**).

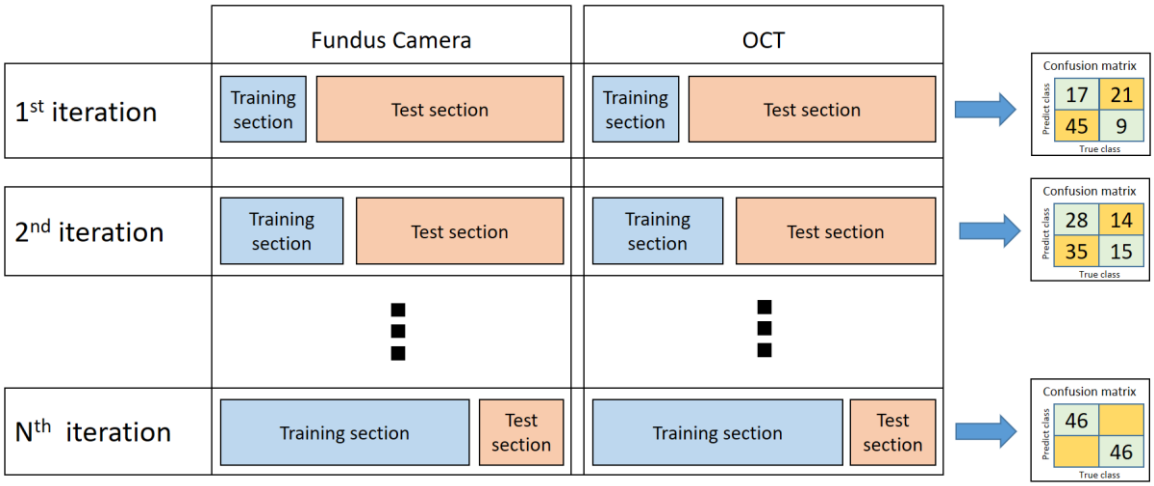

Figure 4.9 Visual description of the iteration process used to find the minimum training dataset able to classify the test dataset correctly.

After identifying the most sensitive channel for quality classification, the features with a weight ≥ 0.4 were considered for the clustering.

4.5.2 RESULTS

The colour channels which model shown the best prediction rate were the second channel of the CIELab colour space as for the fundus camera images, and the green channel of the RGB colour space for the images acquired via OCT, as summarised by **Table 4.3**. The confusion matrices displayed on **Figure 4.10** and **Figure 4.11** show the sensitivity and specificity of the predictive model built on the different channel at the iteration that achieved the best results. The tuned lambda per each channel is shown in **Figure 4.12**.

Table 4.3 Results of the best predictive model for the Fundus Camera and the OCT Images.

Dataset	Best Colour Space	Best Channel	Most Relevant Features	λ	Iteration
Fundus Camera	CIELab	a	Mean, IQR, BVC	$7.94 \cdot 10^{-3}$	7
OCT	RGB	Green	Kurtosis, Mean, R	$3.76 \cdot 10^{-3}$	3

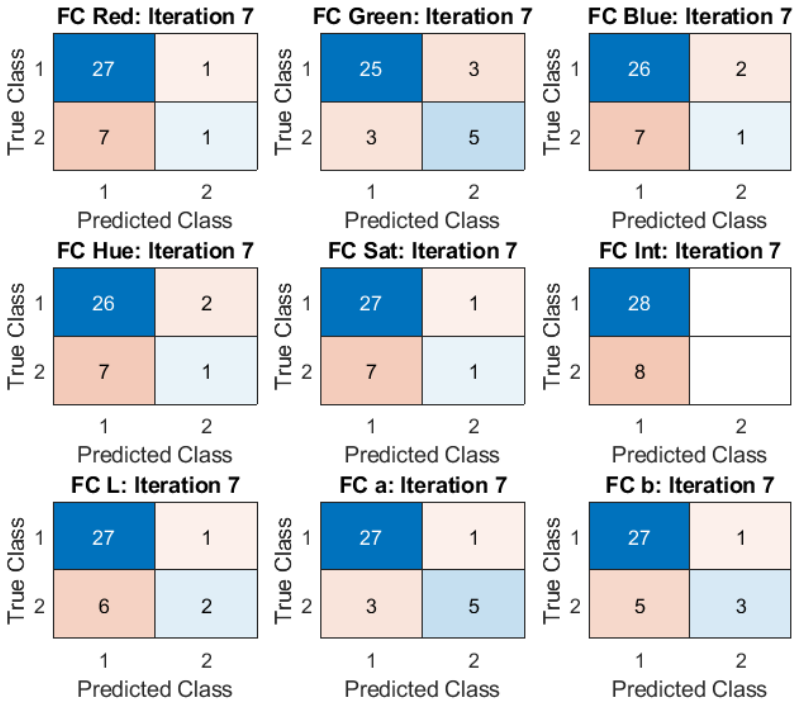

Figure 4.10 Confusion matrixes for the Fundus Camera (FC) images on the three channels of the RGB, HIS and CIELab colour spaces.

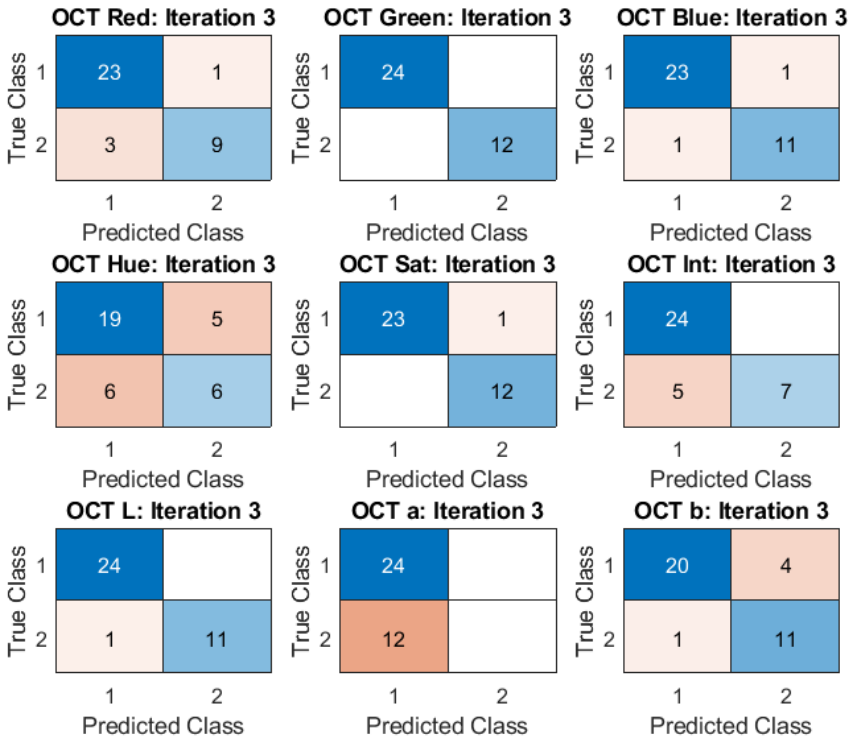

Figure 4.11 Confusion matrixes for the OCT images on the three channels of the RGB, HIS and CIELab colour spaces.

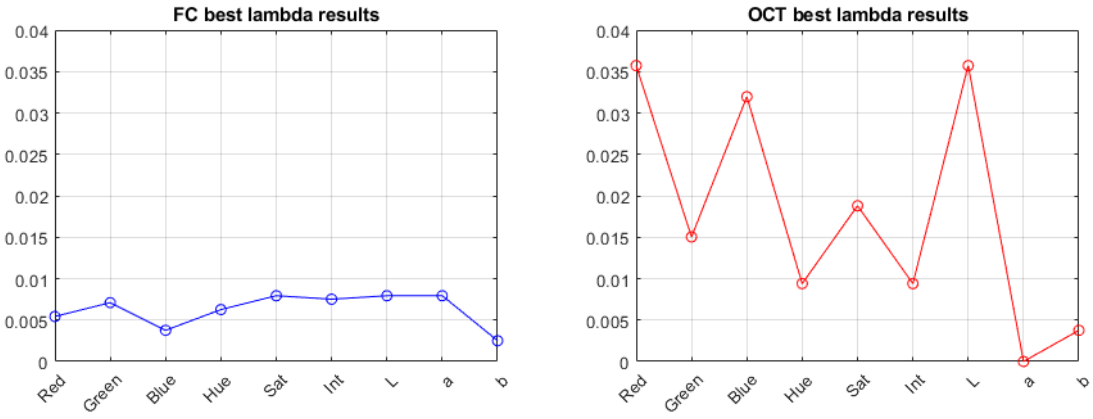

Figure 4.12 Tuning of the lambda parameter for the fundus camera and the OCT images.

The **Figure 4.13** and **Figure 4.14** shows, per each channel, the results coming from the feature selection process operated by the NCA, on the fundus camera and the OCT images. The more the weight of the feature, the stronger the

influence in the classification process. It is noteworthy that the BVC feature results relevant for classification purpose of fundus camera retinal images in the majority of the channels. As for the OCT images, range (R) and kurtosis were the most significant. Trends regarding feature significance for clustering is shown in **Figure 4.15**.

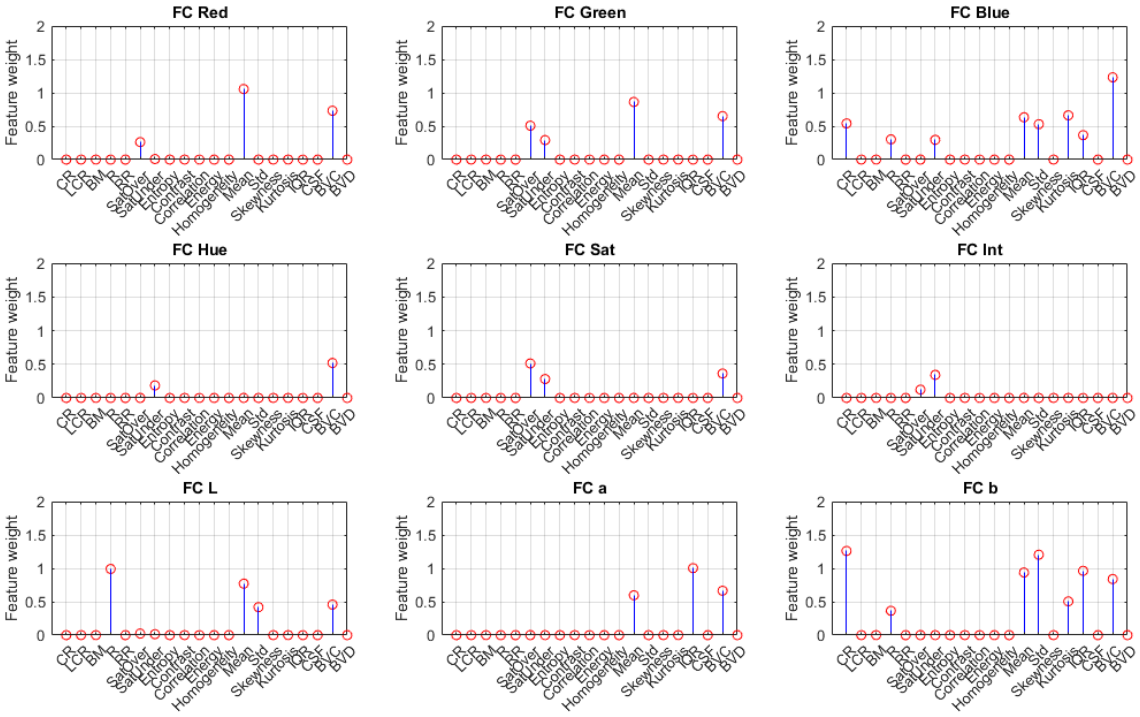

Figure 4.13 Results coming from the feature selection process operated by the NCA algorithm on the FC images.

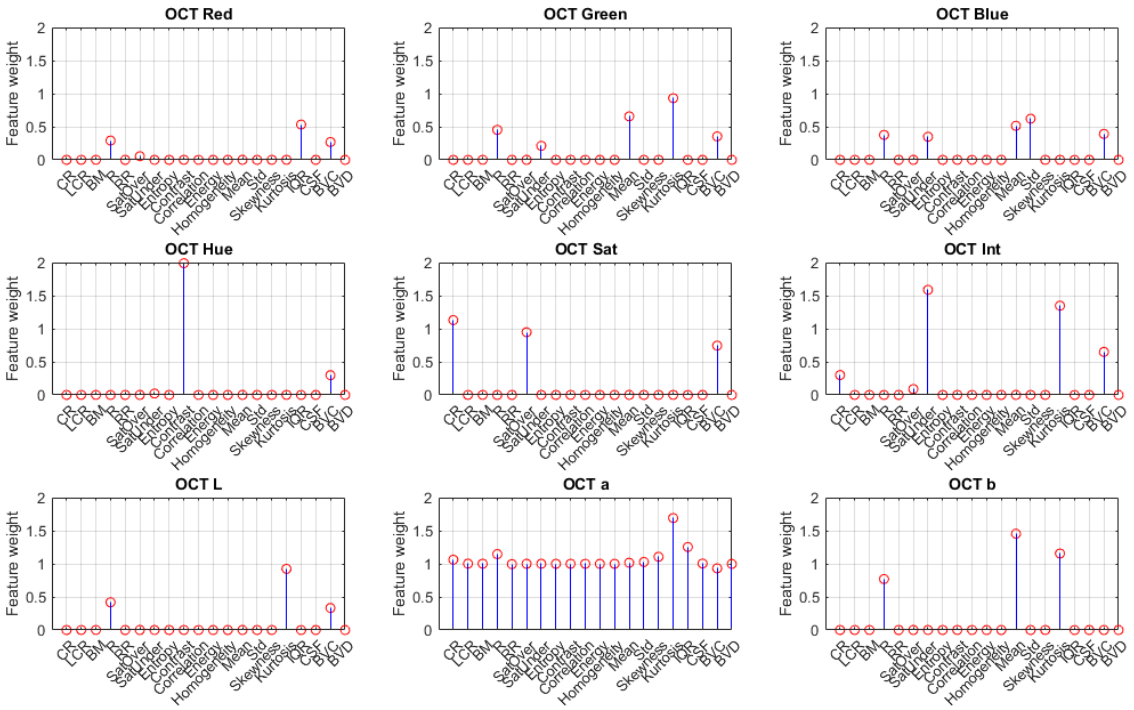

Figure 4.14 Results coming from the feature selection process operated by the NCA algorithm on the OCT images.

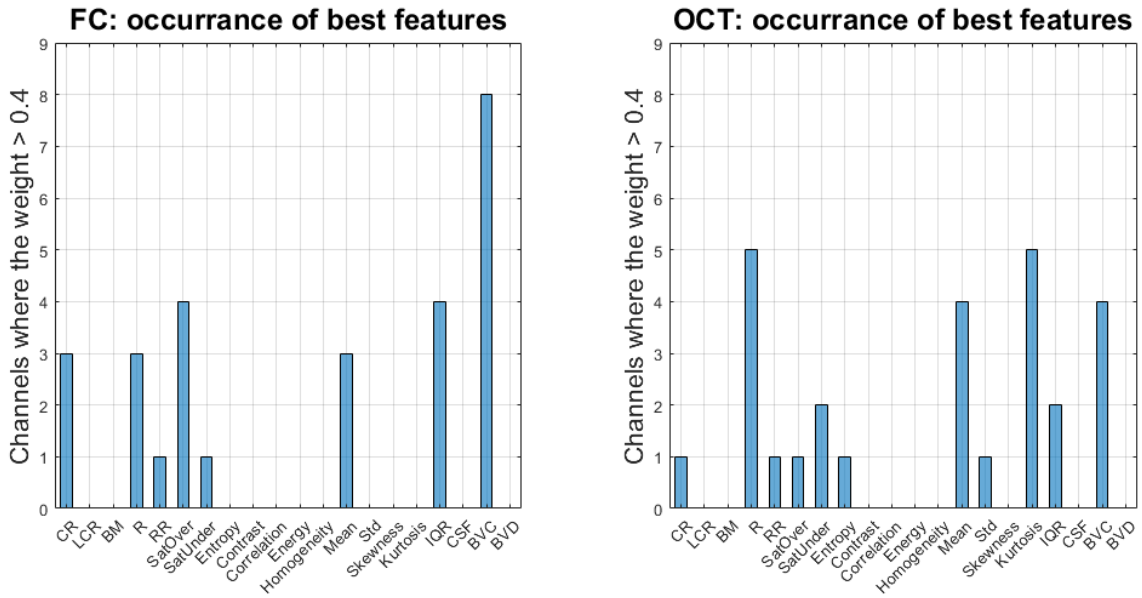

Figure 4.15 Number of times a statistical features reached a with a weight>0.4 for the clustering process over the 9 different channels. BVC reached the best performance for FC images, while R and kurtosis were equally the best features for OCT images.

To better visualise the clustering of the data, according to the most significant features, **Figure 4.16** to **Figure 4.19** present a 3D scatter plot of the images distributed along the 3 more significant features per each channel. **Figure 4.17** and **Figure 4.19** have been proposed to better visualise the clustering capability of the two most significant channels for image quality classification, the a channel for the FC images and the $Green$ channel for the OCT images.

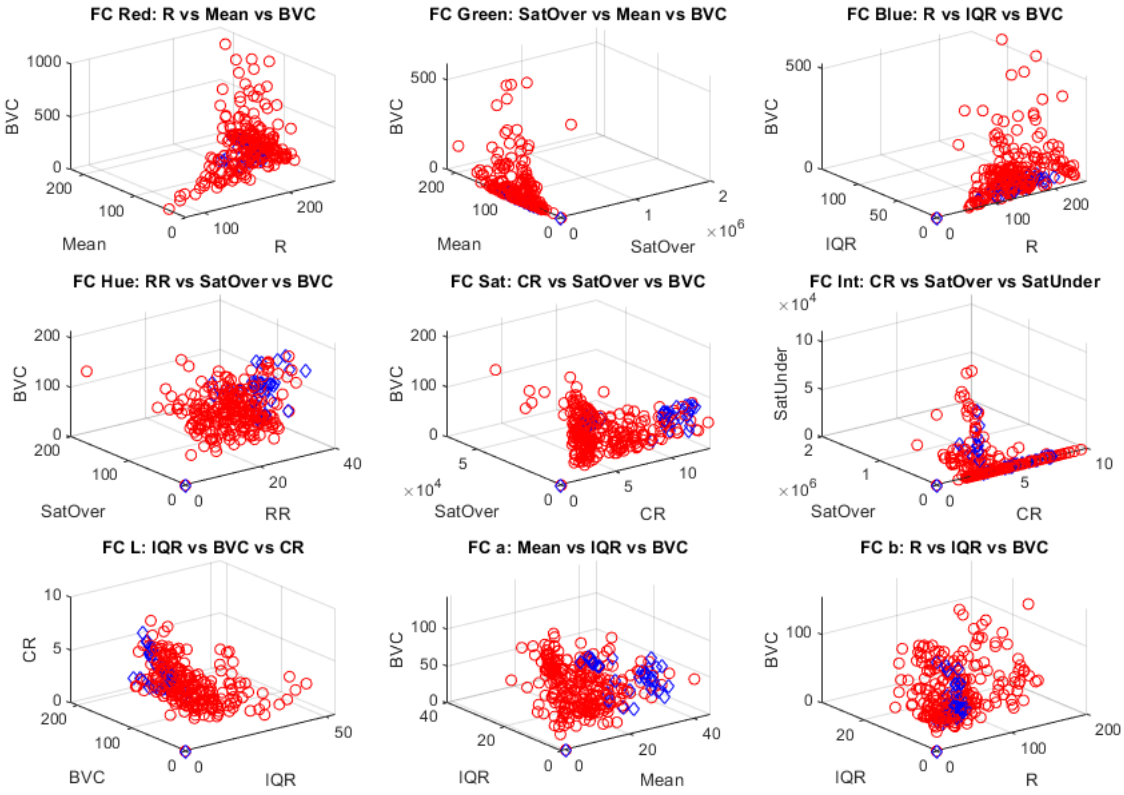

Figure 4.16 3D scatter plot of FC images, distributed along the 3 more significant features per each channel considered.

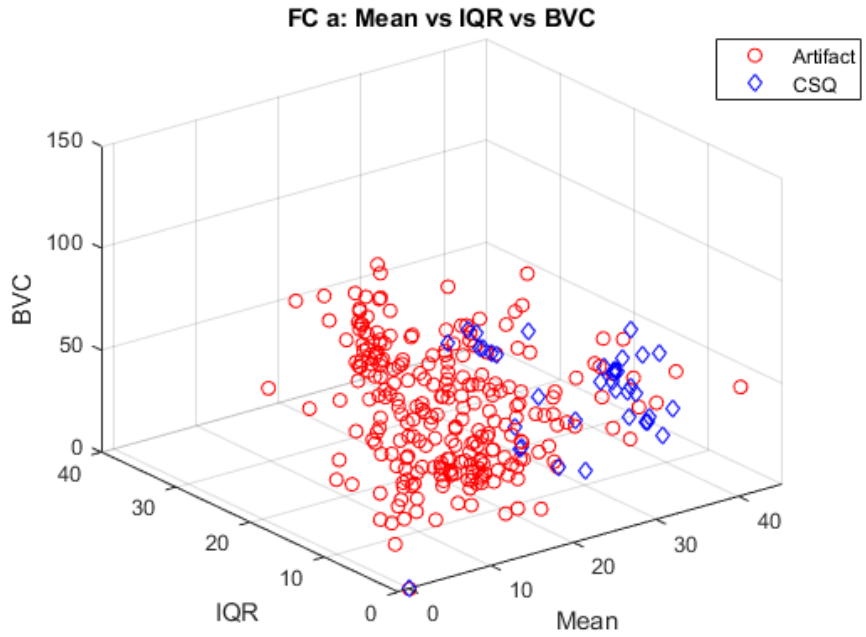

Figure 4.17 3D scatter plot of the best three features used to cluster FC images.

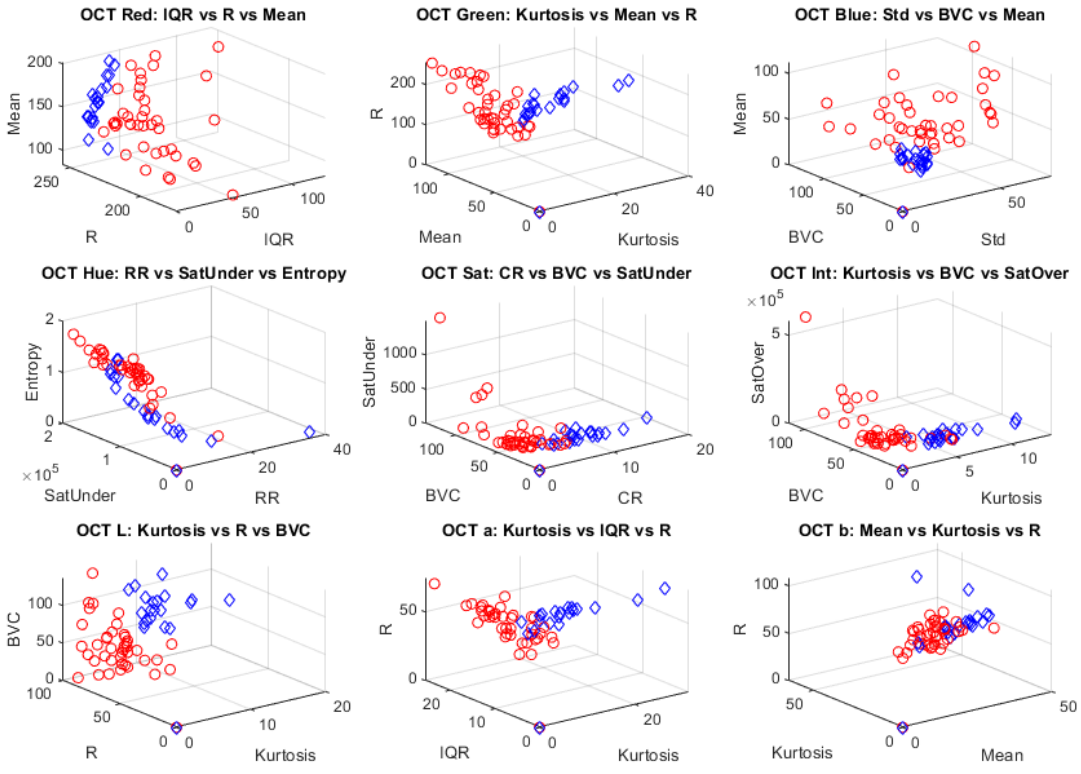

Figure 4.18 3D scatter plot of OCT images, distributed along the 3 more significant features per each channel considered.

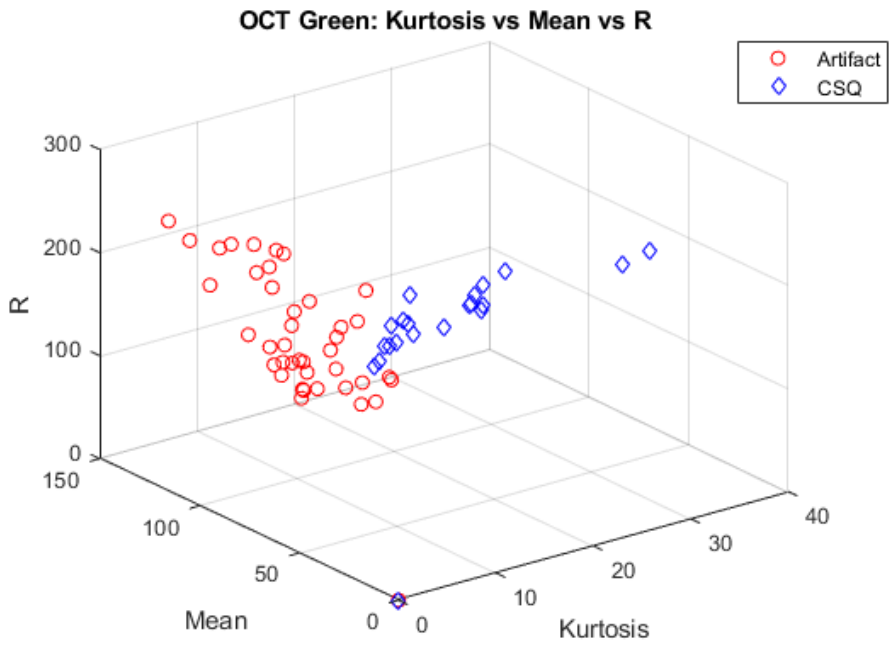

Figure 4.19 3D scatter plot of the best three features used to cluster OCT images.

4.5.3 INTERNAL CONSISTENCY OF IMAGE QUALITY: DISCUSSION

The classification models developed for the FC and the OCT images show better using the triplet [IQR, mean, BVC] calculated for the a channel and [mean, range, kurtosis] calculated for the $green$ channel, respectively. The good performance shown by specific textural features was somehow predictable, given the anatomical features (blood vessels, OD and Macula) are what mostly characterises the information of a retinal image (many semi-automatic and automatic quality classification algorithms rely on textural information). Less predictable was the good performance of common histogram features in quality classification. In general histograms give information about the general aspect of the whole image without providing local information content. This characteristic is very limiting when apply to images where local information is key (anatomical features and pathological signs usually very much localised in retinal images), but it shows advantages in images with artifacts or global distortion.

The decision of analysing separately fundus camera and OCT images was made to account for the different imaging device used (hence different optics, sensors and settings) and the more systematic generation of artifact obtained in the OCT images collection. In fact, OCT image acquisition was made more repeatable due to the device software and modalities, which improved also repeatability of image distortions. As for the fundus camera, this process was far less controllable, generating more random artifacts and distortions in general.

A high level of repeatability boosts the identification of specific patterns in the images, hence improve the classification process. For this reason, the quality clustering of the OCT images is more clear than the fundus camera ones (**Figure 4.17** VS **Figure 4.19**). The big advantage of NCA algorithms is the improvement of the clustering performance as the amount of training data increases. As will be described in the next chapter, this characteristic was exploited by producing many artefact-like images using an ad-hoc mathematical model.

4.5.4 CONCLUSIONS

The collection of a new ophthalmic database, a data collection workflow suitable acquisition during visiting hours and a quality classification approach based on NCA were developed.

Unlike other publicly available databases, in this work, no ground truths or expert manual segmentations have been produced. Interpretive data have been voluntarily left out from this first iteration of the database, although these may be added with future iterations. However, by providing the core set of imaging technologies normally accessible and used in clinical practice, this database aims to provide a consistent and coherent set of data along which to develop extraction strategies for clinical information from multimodal instrumental observations. We predict potential usefulness in having data coming from different technique (7 different imaging techniques and 45 different modalities), contextual data about the acquisition setup and

participant information, especially in the imaging processing research field, in training and education and in data mining applications.

The inclusion of retinal images affected by artifacts is a direct extension of this concept. In particular, the extraction of valuable clinical data from instrumental images is, in principle, possible regardless of the cosmetic quality of the images themselves, as long as some information content is maintained. By providing counterparts of acknowledged clinical quality alongside the images affected by artifacts, a reference dataset that can facilitate the development of noise models and clinical information retrieval strategies for retinal images is provided.

The choice of including only 10 participants in this first iteration of the database has been driven by some practical considerations. Firstly, the recruitment modality of the volunteers, which was not opportunistic (approaching patients attending other clinical investigations) but systematic (inviting participants by letter). This requires proactive initiative by researchers and participants, and we have opted to make the database available as soon as recruitment numbers have reached levels that envisage usefulness of the dataset. Indeed, the recruitment numbers are consistent with e.g. the dataset explored by the DRIVE database. Future extension of the database might increase the number of participants. Secondly, to keep the protocol tolerable for the participant and the hospital workload, the workflow was restricted to a maximum of 2-hours of acquisition time, and to non-invasive measurements. Indeed, fluorescein angiography was not performed, albeit used in clinical practice.

The second important outcome of CORD is the development of an *ad hoc* workflow for the data collection process of a comprehensive dataset in a clinical operating setting, which can be difficult to evaluate without inside knowledge of classic eye clinic equipment and routine, and time consuming to developed. In this regard, the project was supported by two practicing ophthalmologists who played a key role in the selection of the imaging

techniques to include, and in evaluating the logistics of the data collection protocol.

Finally, the unique opportunity of having the same retinal images with and without artifact has allowed the implementation of a classification model based on statistical features. An NCA feature selection algorithms was used to identify those features play a key role in the image quality classification and to build a binary classification model able to distinguish CSQ images from images affected by artifacts. Such model will be used to assess the performance of the artifact removal algorithm presented in the next chapter.

Overall, CORD presents several novelties compared to the databases publicly released so far, making a step towards the definition of a comprehensive tool for the ophthalmic image processing development, and possibly a usable database framework for future reference.

To the author knowledge, at the time of data acquisition, this database does not include pathologies beyond refraction error. Since the majority of the population presents refractive error, emmetropia was not stipulated to be a requirement for this database.

The CORD dataset is available open-access under a CC-BY-4.0 license at https://cord.bioe.strath.ac.uk/, and from the data repository of the University of Strathclyde, with Digital Object Identifier (DOI) 10.15129/39bcd12d-0677-4cf3-a099-b763fbb7d3c4.

CHAPTER 5. DEVELOPMENT OF THE PHENOMENOLOGICAL MODEL OF RETINAL ARTIFACTS

5.1 ARTIFACT MODEL RATIONALE

The creation of a new mathematical model able to simulate the effects of artifacts on retinal images is key to this work, principally for two reasons:

1. Understanding how artifacts impact on the formation of a retinal image, is an essential step for the development of the image clean-up strategy, as this will determine the mathematical operation to put in place to mitigate the distortion once this has been identified and isolated (e.g. subtraction, chromatic shifting, etc.)
2. Data augmentation: the development of machine learning strategy able to recognise the pixels that are affected by distortions caused by artifacts required a massive quantity of data to reach an acceptable accuracy. This model will be used to produce images affected by artifacts starting from clinical quality images, increasing the dataset, initiated by CORD, of retinal images affected by artifacts that have the good quality counterpart.

Other significant applications of this model, not directly related with this work, are described and contextualised in the discussion chapter.

5.2 ARTIFACT MATHEMETICAL DESCRIPTION AND EYE MODELLING

For the purposes of this work, it will be assumed throughout that the term ‘image artifacts’ refer to those non-stochastic image features that are part of the context of the image but that don’t belong to the anatomical object being

imaged. Noise, instead, will be defined as a contribution to the image due to a random process.

Addressing noise modelling in medical imaging involves estimating the variance distribution of such noise, in general considering the noise additive with zero-mean. A common approach is to find the relationship between the intensity of the image I and its noise variance σ^2, in the form

$$\sigma^2 = f(I, \alpha_{1,}\alpha_{2,}\alpha_{3,} \dots) \quad (1)$$

where the parameters $\alpha_{1,}\alpha_{2,}\alpha_{3,}$ ... are determined by the image acquisition conditions, device setting, imaging modality and so on (Gravel,Beaudoin and De Guise, 2004). This method can be applied also to uncorrelated noise. In general, it is more convenient to approximate the resulting variance to a well-known stochastic model. For example, magnetic resonance noise is usually considered having a Rician probability density function, computer tomography produces Gaussian noise, positron-emission tomography noise is commonly associated with a Poisson distribution and so on (Gudbjartsson and Patz, 1995, Rodrigues,Sanches and Bioucas-Dias, 2008). These two strong assumptions, the additive nature of the noise and the approximation of the statistical distribution of its variance, simplify image filtering and deblurring, but it often results in poor quality images. To mitigate this drawback, two approaches can be pursuit: the identification of optimal trade-off between image resolution and contrast-to-noise ratio, or the definition of new noise models with parameters that better fit the real stochastic behaviour (Fuderer, 1988).

As for artifacts modelling, the approach is substantially different. Unlike noise, artifacts have a combination of deterministic and stochastic elements. The phenomena that produce artifacts can be physics-based, patient-based or device-based (Hsieh, 2009). Some of them, such as subject motion, light reflexes or foreign objects can be described mathematically, knowing the boundary conditions. Other physical phenomena, such as scattering or absorption, can be modelled using a combination of stochastic and

deterministic paradigm. In the following, the geometrical and physical assumptions used in developing this parametric model are presented.

5.2.1 GEOMETRICAL EYE MODEL AND LIGHT PATH ANALYSIS

The interaction with the ocular media underpins the same physical considerations used to model the chromatic aberration and optical reflection of the human eye in the hypothesis of a Lambertian fundus (Atchison and Smith, 2000). In the following model, the geometrical and optical characteristics of the tissue are expressed as function of the reflectance R, absorption A and scattering S phenomena. The intensity of the light, for each wavelength λ and for each photosite (x, y) of an hypothetical CCD sensor of $M \times N$ matrix of photosites, have therefore been expressed as:

$$I(x, y, \lambda) = I_O \alpha(R, A, S), \tag{2}$$

where I_O is the intensity of the ophthalmic device's illumination source and α is a proportional term which is function of reflectance, absorption and scattering. Only three main anatomical structures have been considered in the simplify eye model adopted: the cornea, the lens and the retina (**Figure 5.1**). These are the tissues that mainly have an impact on the light in its passage through the eyeball towards the retina, and back to the image sensor. In fact, the total transmittance (direct light plus scattered light) of the cornea and the lens can be seen in **Figure 5.12**, and was found by Boettner and Wolter (Boettner and Wolter, 1962) to be mostly age dependent, with a decrease of transmittance with age. To roughly quantify the loss of light at the passage of these transparent tissues, approximately 10% and 8% of the total information is either absorbed, scattered or reflected respectively from the cornea and the lens in a healthy eye within the portion of the spectrum corresponding to the visible light (380 nm to 700 nm).

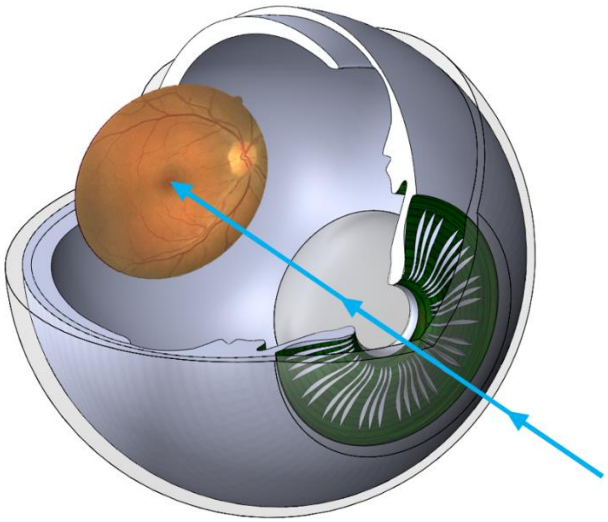

Figure 5.1 Geometrical model of the eye. The light passes through the cornea and the lens reaching the retina. It goes then back to the light sensor passing through lens and cornea again.

5.2.2 DETERMINISTIC COMPONENTS OF THE ARTIFACTS

The ophthalmic instrumentation used to take digital pictures of the retina relies on imaging devices that employ high resolution CCD (charge-coupled device) or CMOS (complementary metal-oxide semiconductor) sensors. These sensors produce as output the discrete numerical value of the light intensity of the wavelengths they are more sensitive to, generally the RGB (red-green-blue). This is, in other terms, the definition of digital image. It follows that a single pixel carries only two information: the intensity level of a specific wavelength (or three) and the position where this intensity was measured (coordinates in the photo-sensor). So there is a direct link between the light intensity and spectrum and the digital value of that corresponding point in the image. Therefore, the phenomena that generate interference usually act at the level of the light being measured or at the level of the digital conversion of the light intensity. The first is mostly associated with artifacts, the second with noise. The contribution of the stochastic noise to the digital value of a single collection site (pixel) has been extensively described (Healey and Kondepudy, 1994, Withagen,Groen and Schutte, 2007). A comprehensive model, developed by Healey and Kondepudy for CCD camera calibration (Healey and Kondepudy, 1994), summarize the main CCD noise sources:

$$D = (KI + N_{DC} + N_S + N_R)G + N_Q, \quad (3)$$

where D is the digital value for a pixel, K is a factor that takes into consideration the spatial variation over the sensor array, I is the number of electrons produced by incident photons at the collection site, N_{DC} is the signal due to dark noise, N_S is shot noise, N_R represent the read noise, G represents the amplification gain and N_Q the quantization noise.

It follows from Eq. 3 that the information content of a retinal image lies within I, which depends on the light source I_O used to illuminate the retina and on its interaction with the optics of the ophthalmic device and the eye's tissues. In the presented model, the final digital image D of the retina is the result of the light scattered from the retina plus an additional diffusive background component B. Such contribution is the only non-first order phenomenon that has been considered since it is the most significant for the overall chromatic reconstruction of the retinal image. During the implementation of the model into the simulating software, this term will be calculated as:

$$B = \frac{\sum_N \sum_M I}{M \times N}. \quad (4)$$

5.3 MATHEMATICAL ASSUMPTIONS

Light-loss phenomena assumptions

Specular Reflection – Part of the illumination light is reflected by each of the 4 smooth surfaces of the eye, the anterior and posterior surfaces of cornea and lens, creating the so called Purkinje images. The fraction of the light reflected R depend on the refractive indices on each side of the surface and is described by the Fresnel equation. For normal incidence the intensity reflectance is:

$$R = [(n' - n)/(n + n')]^2. \quad (5)$$

In this work, specular reflection is considered only at the air-cornea interface since the smoothness of the surface and the difference between the

refractive index between the two media is big enough to be image forming. Below, we refer to R_{Co} as the Fresnel reflectance between the two media.

Absorption – The progressive loss of light while passing through the eye's structures shows a spectral absorption pattern strongly influenced by the absorption properties of water. Below 600 nm however, where the ocular media are more absorbing, the pattern changes, indicating a leading role of proteins and other cellular components (Atchison and Smith, 2000). In this work, absorption is the physical conversion of photons in other forms of energy. No inelastic scattering or fluorescence phenomena are considered. Proportional absorption coefficient A_i is used to account for the fraction of light loss caused by absorption at the i biological medium.

Scattering - Scattering is by far the most complex and perhaps the most relevant phenomenon involving the light interaction with biological media. It is the result of diffraction, refraction and reflection caused by spatial variations in the refractive index within a medium. Some of the light can be scattered either forward or backward. The spatial distribution of the scattered light depends upon a number of factors: size, shape and distribution of inhomogeneities, size of the scattering particles compare to the wavelength and so on. In this work, we consider the scattering occurring only in the lens and at the retina. Corneal haze has been neglected due to its modest contribution compared with the lens. Moreover, at the best of the author's knowledge, no sufficient experimental data on living human cornea has been produced to quantify its amount of back- and forward-scattering. To account for the portion of the overall light-loss caused by scattering at the lens, we introduce the coefficient S_{Le}:

$$S_{Le} = S_{Le}^{b} + S_{Le}^{f}, \tag{6}$$

where S_{Le}^{b} and S_{Le}^{f} are the backward- and forward-scattering components respectively. This distinction must be taken into account since the difference between the weights of these two components, which changes according to the abovementioned factors. At the retina what is not absorbed is scattered

back. S_{Re} will be used to take into account the portion of light scattered from the retina.

Light source: the light source is here represented by discrete rays associated with a single wavelength hitting the (x, y) position of the region of interest (surface of the sonsor). Although geometrical optics is considered in the simulation of the light-surface interaction, geometrical approximations are employed where appropriate. We also assume that the optics of the eye is correctly focused onto the retina (emmetropic eye).

Artifacts

As described in **Chapter 3**, in developing the present model, the most common sources of retinal image distortion have been considered (S. Wang *et al.*, 2016, Yu *et al.*, 2012a):

- eye movement: blurring caused by involuntary eye movement during the shooting.
- object obstruction: in this model the obstruction of eyelashes caused by partial blinking during the shooting have been considered.
- incorrect focus: blurring caused by inappropriate focus adjustment.
- inadequate illumination: uneven illumination of the ROI and camera target (orange ring projected by many fundus cameras to help the ROI alignment with the device optics) misalignment.

5.4 PARAMETRIC MODEL

In the following, the symbols used as subscripts will identify the anatomical part involved and the symbols used as superscript will indicate the biophysical phenomenon that generated that specific intensity contribution. In particular, the subscript Le, Co and Re indicates quantities related to the lens, the cornea and the retina respectively. As for the superscripts, R, A and S will refer to quantities resulting from specular reflection, absorption and scattering phenomena respectively. As for the scattered contributions, S^f for forward-scattering and S^b for backward-scattering will be used. **Table 5.1** summarises

the physical phenomena considered per each anatomical component of the eye.

Another important contribution caused by scattering is the following: while scattering in absolute terms is a loss for the single photosite located in (x, y) position, the illuminance contribution, coming from the light scattered by the surrounding area around (x, y) position, within a radial area included in $(\sqrt{(x-n)^2+(y-m)^2} \leq R)$, needs to be added to the overall luminance intensity hitting the single photosite, with a contribution that is inversely proportional to the distance from point of the object images by that photosite. This spatially localized distribution of light was approximated to Gaussian bell model, in agreement with the Stiles-Crawford effect (Atchison and Smith, 2000). This phenomenon will therefore be considered in the final equation by introducing the terms PSF_{Le} and PSF_{Re} (Point Spread Function of the lens and the retina respectively), which examples of 2D intensity distributions are shown in **Figure 5.2**.

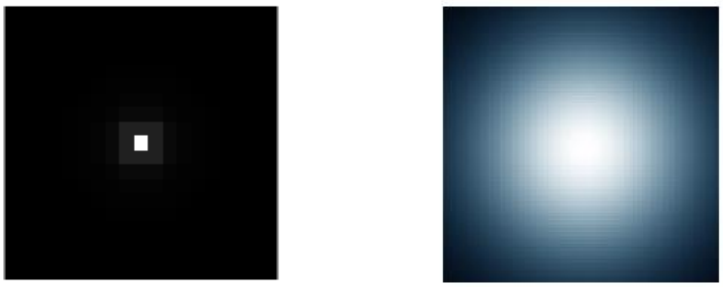

Figure 5.2 two dimensional distribution of the PSF of a healthy lens (left) and PSF of healthy retina (right). The whiter the more intense the PSF is.

As stated above, considering I_0 as the initial luminance $[cd/m^2]$ of a point source of light, projected from the infinite by an hypothetical ophthalmic device at the (x, y) position of the corresponding image sensor of the device, into an emmetropic eye (**Figure 5.3**), for the conservation of energy the following equation is applied:

$$I_{Co}^{T}(x, y, \lambda) = I_0 - I_{Co}^{R} - I_{Co}^{A}, \tag{7}$$

where I_{Co}^{R}, I_{Co}^{A} and I_{Co}^{T} are, respectively, the fraction of the initial luminance that is reflected, absorbed and transmitted at the interaction with the cornea, as in **Figure 5.3**. From now on the dependency from the position and the wavelength (x, y, λ) will be omitted to lighten the notation.

Table 5.1 Physical phenomena considered per each eye's anatomical structure.

Tissue	Phenomena		
	Reflection	Absorption	Scattering
Cornea	x	x	
Lens		x	x
Retina		x	x

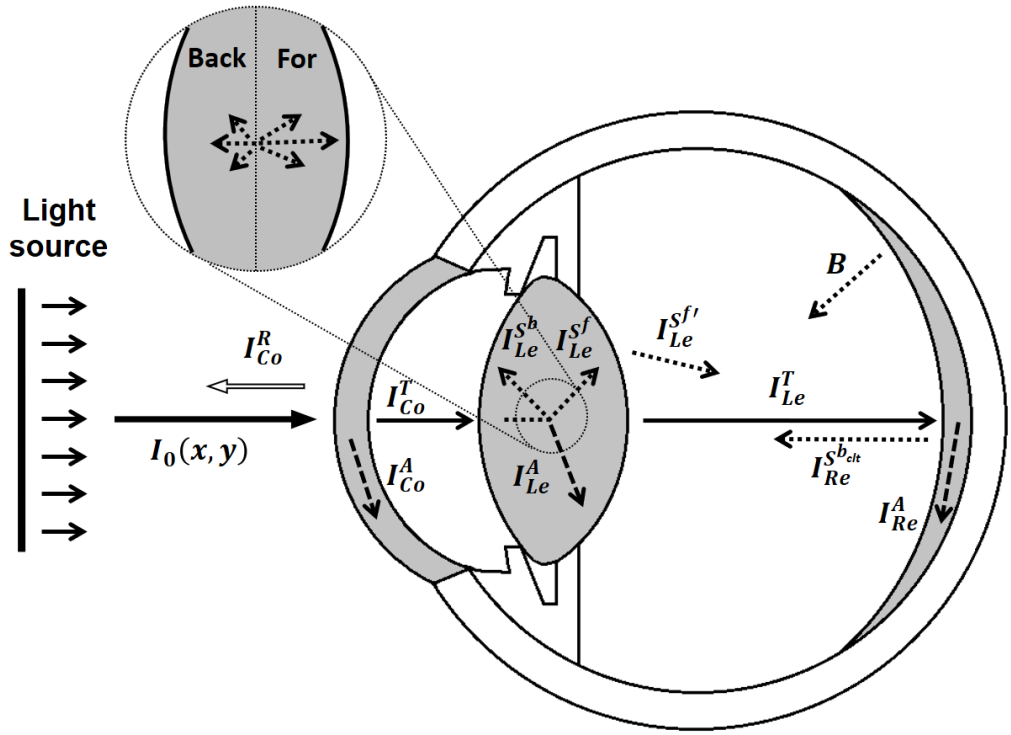

Figure 5.3 Light path through the three main anatomical components of the eye (cornea, lens and retina). On the right, an exploded view of the angular distribution of the scattered light at the retina.

The fraction of light that is reflected back from the cornea is defined as:

$$I_{Co}^{R} = I_0 R_{Co}. \tag{8}$$

In this model at the cornea only absorption and reflection have been considered as scattering is negligible. Therefore, the fraction of light absorbed by the cornea will be:

$$I_{Co}^{A} = (I_0 - I_{Co}^{R})A_{Co} = I_0(1 - R_{Co})A_{Co}. \quad (9)$$

Hence, the light transmitted through the cornea that reaches the lens can be obtained, as function of I_0, by substituting Eq. 8 and 9 to Eq. 7 as follow:

$$I_{Co}^{T} = I_0(1 - R_{Co})(1 - A_{Co}). \quad (10)$$

At the lens, only absorption I_{Le}^{A} and scattering I_{Le}^{S} will reduce the amount of light passing through. Overall, the equation will have the following formulation:

$$I_{Le}^{T} = I_{Co}^{T} - I_{Le}^{A} - I_{Le}^{S}. \quad (11)$$

As before, the absorbed and scattered light by the lens can be obtained as:

$$I_{Le}^{A} = I_{Co}^{T}A_{Le}, \quad (12)$$

and

$$I_{Le}^{S} = (I_{Co}^{T} - I_{Le}^{A})S_{Le} = I_{Co}^{T}(1 - A_{Le})S_{Le}, \quad (13)$$

The resulting transmitted light through the lens is:

$$I_{Le}^{T} = I_{Co}^{T}(1 - A_{Le})(1 - S_{Le})$$

$$I_{Le}^{T} = I_0(1 - R_{Co})(1 - A_{Co})(1 - A_{Le})(1 - S_{Le}) \quad (14)$$

As displayed by **Figure 5.3**, from the lens there are two main components that reach the retina: I_{Le}^{T} and the forward scattered light which impact on the overall contribution will be spatial dependent. The point (x, y) in fact will be affected be the scattered ray passing through position, therefore coming from the scatter generated by near light beams. coming from the surrounding region of the lens $I_{Le}^{Sf'}$ resulting from the scattering phenomena of the surrounding area, which can be expressed as:

$$I_{Le}^{Sf'} = \sum_{i=0}^{L1}\sum_{j=0}^{L2} I_{Le}^{Sf}\left(x - \left(\frac{L1}{2} - i\right), y - \left(\frac{L2}{2} - j\right)\right) PSF_{Le}\left(x - \left(\frac{L1}{2} - i\right), y - \left(\frac{L2}{2} - j\right)\right). \quad (15)$$

$L1$ and $L2$ are the sides of the square area, centered in (x, y), where the scattering phenomena have a relevant impact on the single site and I_{Le}^{Sf} is the intensity of the luminance of the forward scatter, as:

$$I_{Le}^{Sf} = (I_{Co}^{T} - I_{Le}^{A})S_{Le}^{f} = I_{Co}^{T}(1 - A_{Le})S_{Le}^{f} \quad (16)$$

and PSF_{Le} is the profile of the intensity distribution caused by the scattering at each (x, y) point, which will be define in the computer simulation section.

To reduce the complexity of the notation, we refer to the summation as:

$$\sum_{i=0}^{L1}\sum_{j=0}^{L2} I_0\left(x - \left(\frac{L1}{2} - i\right), y - \left(\frac{L2}{2} - j\right)\right) PSF\left(x - \left(\frac{L1}{2} - i\right), y - \left(\frac{L2}{2} - j\right)\right) = \sum\sum I_0 PSF \quad (17)$$

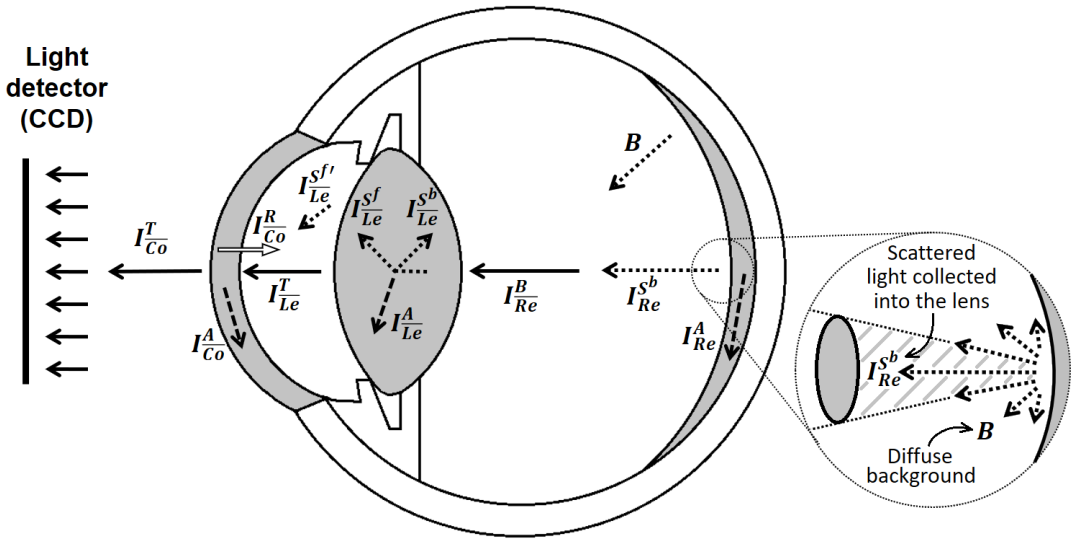

Figure 5.4 Light path from the retina back to the image detector (CCD sensor). On the right, an exploded view of the scattering occurring at the retina. Backward scattering collected directly by the lens I_{Re}^{Sb} and the portion diffusely scattered by the other structure of the posterior segment and collected as a diffuse background contribution B.

The forward scattered light from the lens, in function of I_0, can therefore be written as:

$$I_{Le}^{Sf'} = (1 - R_{Co})(1 - A_{Co})(1 - A_{Le})S_{Le}^{f}\sum\sum I_0 PSF_{Le} \quad (18)$$

Reaching the retina, the light is partially absorbed I_{Re}^{A} by the retinal structures and partially scattered I_{Re}^{S}. The portion of back scattered light $I_{Re}^{S^b}$ from the retina is either collected directly into the lens $I_{Re}^{S^{b_{clt}}}$ or scattered in other direction within the eye forming a spatially uniform background B.

Absorption is by far the most relevant phenomenon that occurs at the retina. It is caused mainly by the visual pigment in the photoreceptors, by the melanin in the pigment epithelium and by the haemoglobin in the choroid. What is not absorbed returns back to the lens contributing, in various proportion, to the formation of the retinal image on the CCD (**Figure 5.4**).

The fraction of light that is scattered from the retina and reaches directly the portion of the clear aperture of the lens is:

$$I_{Re}^{S^{b_{clt}}} = \sum\sum\left(I_{Le}^{T} + I_{Le}^{S^{f\prime}} - I_{Re}^{A}\right) S_{Re}^{b} \varphi_{clt}\, PSF_{Re}. \tag{19}$$

Where φ_{clt} is the fraction of backscatter that is collected directly by the lens as a first order phenomenon, which can be geometrically approximated as the ratio between the surface of the lens and the total surface of the eye ball $\varphi_{clt} = \pi r_{Le}^2 / 4\pi r_{eye}^2$ (≈ 6.2%). As for the light absorbed by retina I_{Re}^{A}, it can be defined as:

$$I_{Re}^{A} = \left(I_{Le}^{T} + I_{Le}^{S^{f\prime}}\right) A_{Re}. \tag{20}$$

The fraction of scattered light collected inside the clear aperture of the lens $I_{Re}^{S^{b_{clt}}}$ can finally be expressed as:

$$I_{Re}^{S^{b_{clt}}} = \sum\sum\left(I_{Le}^{T} + I_{Le}^{S^{f\prime}}\right)(1 - A_{Re}) S_{Re}^{b} \varphi_{clt} PSF_{Re} \tag{21}$$

To obtain such intensity in function of I_0, we substitute I_{Le}^{T} from Eq. 13 and $I_{Le}^{S^{f\prime}}$ from Eq. 17 to obtain:

$$I_{Re}^{S^{b_{clt}}} = (1 - R_{Co})(1 - A_{Co})(1 - A_{Le})(1 - A_{Re}) S_{Re}^{b} \varphi_{clt} \big[(1 - S_{Le}) \sum\sum I_0 PSF_{Re} + S_{Le}^{f} \sum\sum(\sum\sum I_0 PSF_{Le}) PSF_{Re}\big]. \tag{22}$$

In the implementation of the model into the simulating software, this diffusive term will be calculated as:

$$B = \frac{\sum_N \sum_M I_{Le}^{T}(1 - A_{Re})(1 - \varphi_{clt}) S_{Re}^{b}}{M \times N}. \tag{23}$$

This results in a chromatic shift to the red hue of the overall retinal image. This tallies with intuition, as both the retina and the sclera appear red, and therefore impart a red hue to any light reflected or scattered by them. In the following notation the term B will remain a constant value.

Passing through the lens, as in the first passage, the conservation of the total energy gives:

$$I_{Le}^{T} = I_{Re}^{S^{b_{clt}}} + B - I_{Le}^{A} - I_{Le}^{S}. \tag{24}$$

Where the fraction of absorbed light intensity at the eye's lens I_{Le}^{A} can be expressed as:

$$I_{Le}^{A} = A_{Le}\left(I_{Re}^{S^{b_{clt}}} + B\right), \tag{25}$$

the fraction of scattered light at the lens I_{Le}^{S} can be expressed as:

$$I_{Le}^{S} = \left(I_{Re}^{S^{b_{clt}}} + B - I_{Le}^{A}\right)S_{Le} = \left(I_{Re}^{S^{b_{clt}}} + B\right)(1 - A_{Le})S_{Le}. \tag{26}$$

At this point, the fraction of light transmitted through the lens I_{Le}^{T} can be obtained using Eq. 23 and substituting the variables with the expressions so far obtained, as follow:

$$I_{Le}^{T} = \left(I_{Re}^{S^{b_{clt}}} + B\right)(1 - A_{Le})(1 - S_{Le}). \tag{27}$$

The other relevant component that contribute to the amount of light reaching the cornea in a specific point is the forward scattering from the lens. This can be expressed similarly to the previous passage through the lens as:

$$I_{Le}^{S^{f\prime}} = S_{Le}^{f} \sum\sum \left(I_{Re}^{S^{b_{clt}}} + B\right) PSF_{Le} \tag{28}$$

In its last interaction with the cornea, the light is specular reflected back and absorbed once again. According to the conservation of the total energy, the light that comes out from the eye and hits the photodetector can be calculated as:

$$I_{Co}^{T} = I_{Le}^{T} + I_{Le}^{S^{f\prime}} - I_{Co}^{R} - I_{Co}^{A}. \tag{29}$$

Where the specular reflection I_{Co}^{R} and the absorbed light I_{Co}^{A} at the cornea are defined as:

$$I_{Co}^{R} = \left(I_{Le}^{T} + I_{Le}^{S^{f\prime}}\right)R_{Co}, \tag{30}$$

$$I_{\overline{Co}}^{A} = \left(I_{\overline{Le}}^{T} + I_{\overline{Le}}^{Sf'} - I_{\overline{Co}}^{R}\right) A_{Co}. \quad (31)$$

By substituting Eq.26, 27, 29 and 30 to Eq.28, we can finally obtain the fraction of transmitted light that comes out of the cornea and hits the sensor in function of the I_0:

$$I_{\overline{Co}}^{T} = \left(I_{\overline{Le}}^{T} + I_{\overline{Le}}^{Sf'}\right)(1 - R_{Co})(1 - A_{Co})$$

$$I_{\overline{Co}}^{T} = \left[\left(I_{\overline{Re}}^{S^{b}clt} + B\right)(1 - A_{Le})(1 - S_{Le}) + S_{Le}^{f} \sum\sum \left(I_{\overline{Re}}^{S^{b}clt} + B\right) PSF_{Le}\right](1 - R_{Co})(1 - A_{Co}) \quad (32)$$

When no pathological conditions affect the eye, only the specular reflection at the cornea R_{Co}, the absorption and scattering phenomena at the retina, A_{Re} and S_{Re}, and the second order scattering from the sclera, B and PSF_{Re}, are not negligible. All the other coefficient can be considered close to 0, therefore the Eq. 31 can be rewritten as:

$$I_{\overline{Co}}^{T} = S_{Re}^{b} \varphi_{clt} (1 - R_{Co})^2 (1 - A_{Re}) \sum\sum I_0 PSF_{Re} + (1 - R_{Co}) B. \quad (33)$$

5.5 MODEL CONSISTENCY ANALYSIS: METHODS

5.5.1 COMPUTER SIMULATION

Starting from CORD, a new dataset of 200 retinal images affected by artifacts has been created, 5 for each good quality retinal images produced using the fundus camera technique. The mathematical model has been implemented in Matlab 2019a (The MathWorks, Inc., Natick, MA, USA) using a i7-7700HQ CPU laptop with 16GB of RAM and Windows 10 as operating system. Below, the description of the numerical values of the parameters used in the simulation.

Illumination I_0

Two different source of illumination have been implemented: RGB LED and Xenon bulb. In the following simulation, only the xenon bulb model will be considered as closer to the spectrum of the majority of ophthalmic devices' illumination. The three RGB wavelengths selected are 460nm 550nm and

620nm and their relative intensity value was determined based on the spectrum profile shown in **Figure 5.5**.

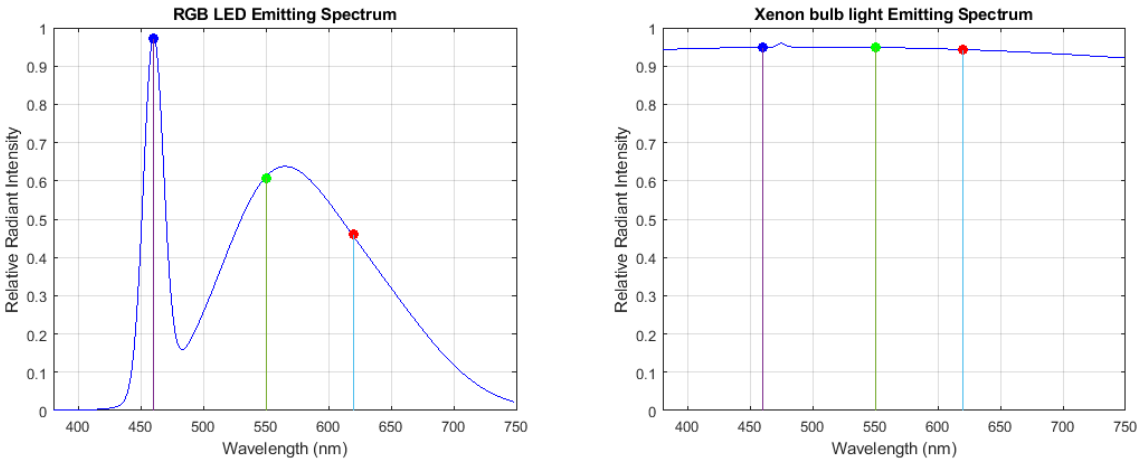

Figure 5.5 Emitting spectrum of two common light sources for ophthalmic devices. The one selected for the test id the Xenon bulb as commonly used in fundus imaging devices.

To simulate the uneven distribution of light intensity along the radial coordinate of the observational area (the image acquisition area), a multivariate normal distribution profile (Z axis) with radial symmetry and with $\text{variance} = 8 \times 10^4$ and $\text{covariance} = 20 \times 10^6$, was used (**Figure 5.6**).

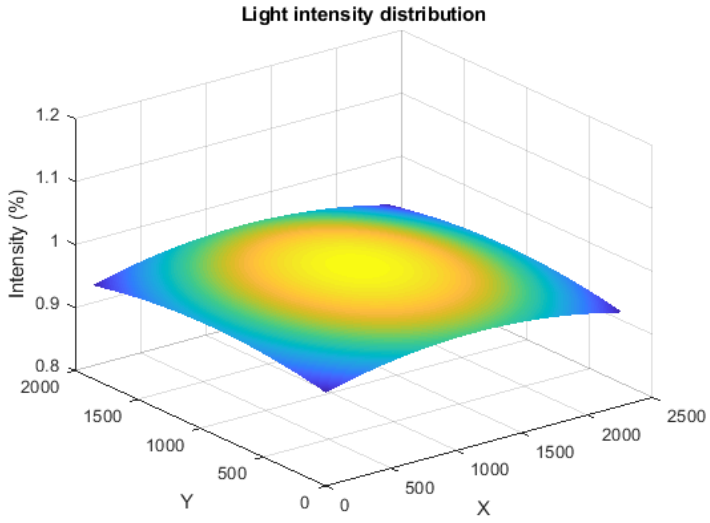

Figure 5.6 3D representation of the radial distribution of the intensity of the illumination light.

Specular reflection R_{Co}

Specular reflection, which in this simplified model occurs only at the cornea surface, can be estimated by considering the reflectance for normal incident light at the interface between two media of refractive index n_o and n_1. Following from Eq. 5, where $n_o = 1.0003$ is the refractive index of the air and $n_1 = 1.3371$ (Atchison and Smith, 2000) the refractive index of the cornea, $R_{Co} = 0.021$. This means that approximately 2% of I_0 is reflected by the cornea back to the photodetector.

Retinal absorption A_{Re}

The information about the absorption of the retina is given by the image complement of the good quality retinal image used (in this work comes from the CORD database). Under the assumptions adopted in this work, reaching the retina, the light can either be absorbed or scattered back to the lens. It follows that the information regarding the absorption of the retina's features is stored in the retinal image itself.

Lens and retina scattering S

As shown in the mathematical model, the scattering produces not only a local loss of information for each single photosite, but also an additional contribution of information coming from the surroundings. Two different models have been adopted to take into account this phenomenon: the CIE general disability glare equation for the lens, derived from the Stiles-Holladay model (Vos, 2003), and an adaptation of the psychophysical Stiles-Crawford model (Marcos,Burns and He, 1998) adopted by reflectometric techniques.

The first one is express by the equation:

$$I = \frac{10}{\theta^3} + \left[1 + \left(\frac{A}{62.5}\right)^4\right] \cdot \left[\frac{5}{\theta^2} + 0.1\frac{p}{\theta}\right] + 0.025p, \qquad (34)$$

where θ is the glare angle domain (in this model valid from $0.1° < \theta < 100°$), A accounts for the age, p is the pigmentation factor ($p = 0$ for very dark eyes, $p = 0.5$ for brown eyes, and $p = 1$ for blue-green Caucasian eyes). **Figure 5.7** and **Figure 5.8** show the profile of intensity caused by scattering in relation

with the distance from the point where such phenomenon originates. It can be seen that age have a bigger impact than pigmentation.

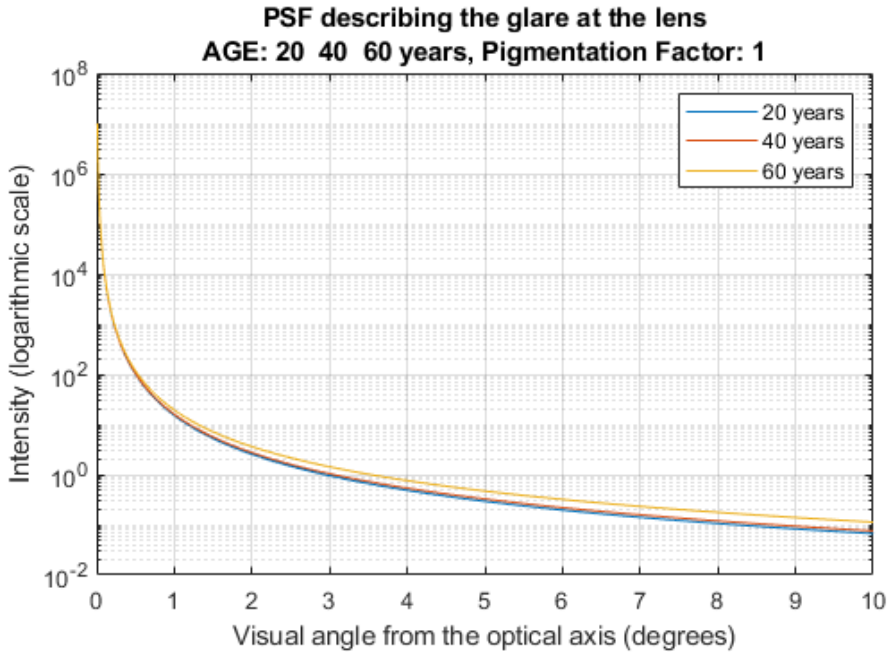

Figure 5.7 Profile of intensity along the optical axis of the eye at different age, keeping the pigmentation factor constant.

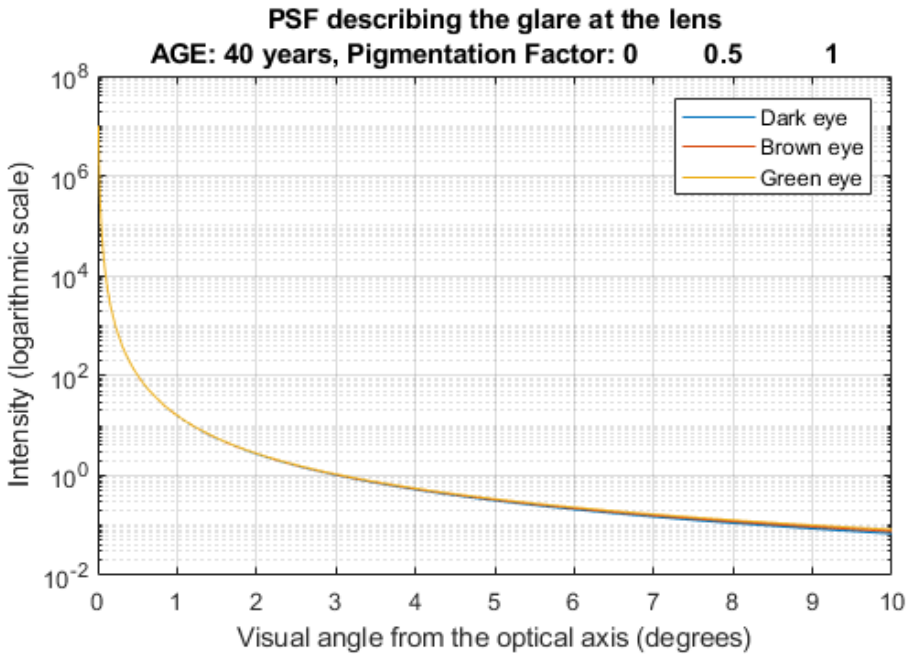

Figure 5.8 Profile of intensity along the optical axis of the eye at different pigmentation, keeping the age factor constant.

The second one is simplified by the Gaussian function:

$$I = B + I_{max} 10^{-\rho r^2} \tag{35}$$

where r is the distance from the centre of the intensity distribution and ρ is the shape factor and it's defined as

$$\rho = \frac{\pi^2 (0.4s)^2}{f^2 \lambda^2 \ln 10} \tag{36}$$

and s is the cone spacing ranging from 2.6 to 6.5 μm in the foveal area, $f = 16.7mm$ and λ is the wavelengths, which in this models are [460 550 620] nm. B is the constant background, which is the only second order contribution included, here calculated as the mean value of the light scattered back from the retina.

CLASSIC SOURCES OF ARTIFACTS

Object obstruction

The simulation of objects between the image sensor and the cornea (e.g. eyelashes and dust on the optics) has been obtained by introducing an image, representing the obstructing object, between the light source plane and the corneal plane. Different levels of severity have been implemented to account for none to severe phenomena (different density of obstructing object, as in **Figure 5.9**, and different blurring level).

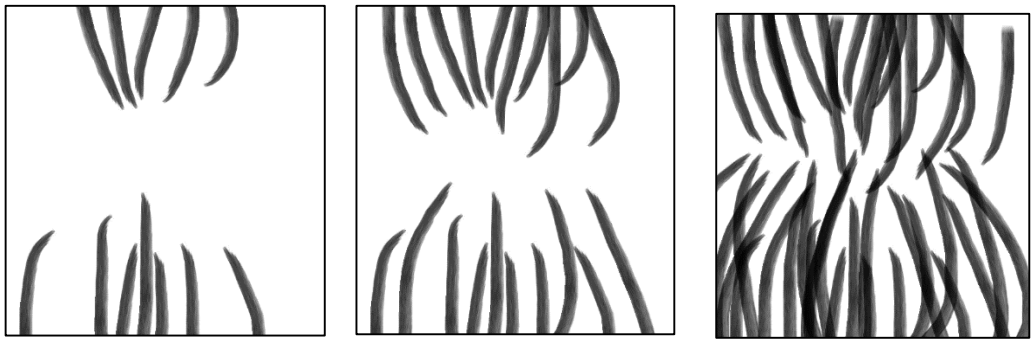

Figure 5.9 Image of eyelashes used to simulate object obstruction.

Optics misalignment – The misalignment between the target ring (intended as the orange/yellowish circular target used to help the operator to align the optics of the ophthalmic device with the centre of the retina) has been

simulated by adding an additional source of light non-coaxial with the main one. This generates the commonly observed saturated yellowish contour on the edges of the retinal image. Five different level of misalignment have been implemented (**Figure 5.10**).

Figure 5.10 Increasing level of misalignment of the target ring. The shape the rig was designed to be as similar as possible with the target ring of a Topcon TRC-50DX Type IA fundus camera.

Light detection efficiency – The detection efficiency of the photodetector conventionally depends on its optical efficiency $\varepsilon_{optical}$, which includes many factors (e.g. geometric and transmission efficiencies). It has been observed that the overall efficiency of a CCD photodetector can be obtained simply as the product of the geometric and transmission efficiencies (Catrysse and Wandell, 2002).

$$\varepsilon_{optical}(E) = \varepsilon_{geom}\varepsilon_{transm}(E) \tag{34}$$

The geometric efficiency ε_{geom} depends on the numerical aperture (NA) of the lens, and the bending of the light due to the different dielectric media along the optical path. Such geometric efficiency can be express as:

$$\varepsilon_{geom} = \frac{G_{detector}}{G_{aperture}}, \tag{35}$$

where $G_{detector}$ is the extension captured by a general photodetector and $G_{aperture}$ is the extension available at the aperture.

The transmission efficiency $\varepsilon_{transm}(E)$ depends on the energy E of the incident ray and on the transparency of the different dielectric layers that compose the photodetector.

For the proposed model we will implement these phenomena by considering different optical efficiency values for the different light source

contribution. Light ray with higher energy and a narrow angle of incidence with the photodetector will have a higher optical efficiency.

The light collected by the sensor, which is the one forming the final retinal image, can be obtained by adding the contribution transmitted from the retina and the specular reflection coming from the first interaction with the cornea:

$$I_{detect}(i,j) = I_{\overline{Co}}^{T}\varepsilon_1 + I_{Co}^{R}\varepsilon_2, \quad (36)$$

where ε_1 and ε_2 have been here arbitrary chosen constants, for simplicity, 90% and 94% respectively, to account for the different energy content of the reflected and transmitted light.

Radial symmetric artifact

Specular reflections caused by the optics of the ophthalmic device and the over exposition of light caused by a partial placement of the patient's eye on the eyepiece of the device was also simulated. To do so a Bessel function of the first kind with different orders was used. This radial symmetric function can be set to simulate circular or macular halos (**Figure 5.11**)

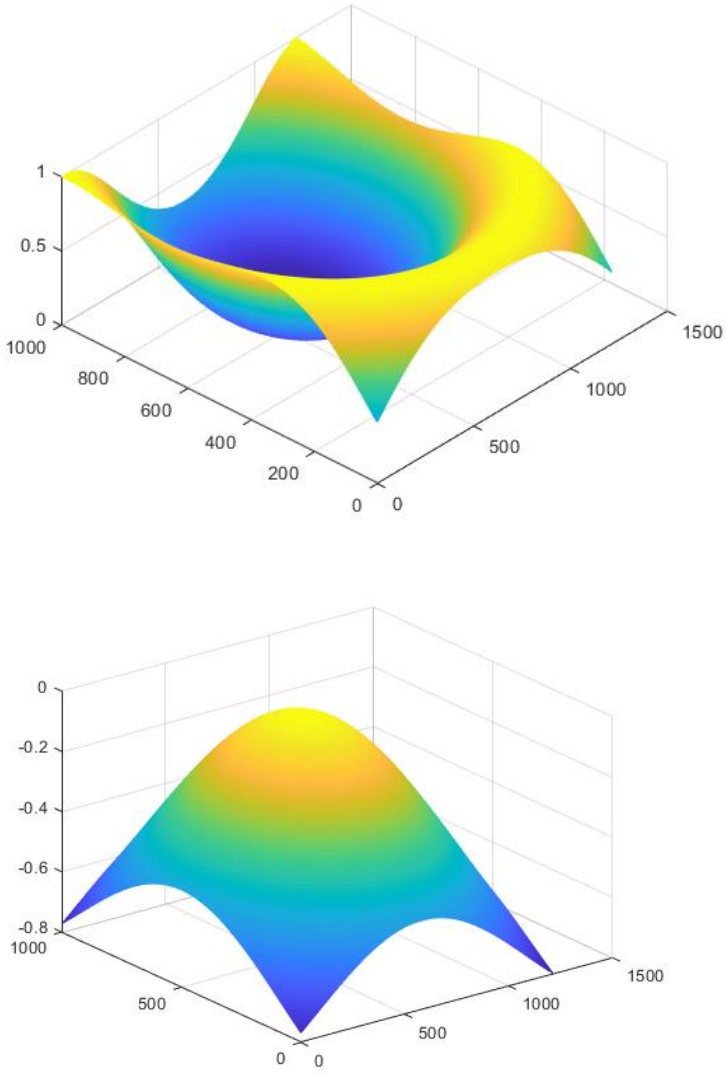

Figure 5.11 Example of Bessel function of the first kind with 3rd (top) and 2nd (bottom) order used to simulate illumination distortions in the retinal image.

Numerical value of the simulation's parameters

The amount of luminance intensity reflected, absorbed and scattered by the cornea and the lens was established based on the literature, and they are here express in percentage of the total luminance intensity hitting the specific tissue. In particular, from the work of Boettner and Wolter (Boettner and Wolter, 1962) (**Figure 5.12**) the amount of light not transmitted was estimated, which was used to determine the combined contribution of absorption, reflection and backward scattering for each tissue.

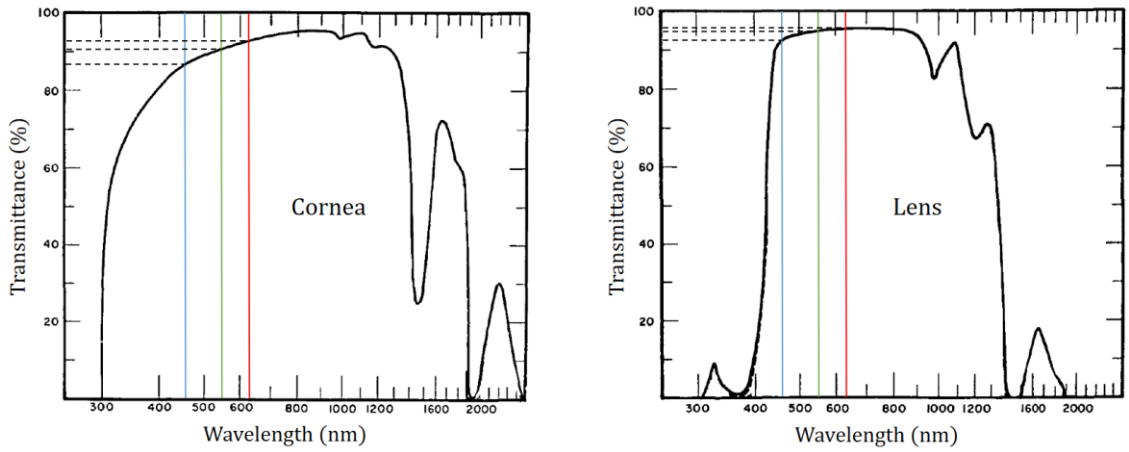

Figure 5.12 Spectral transmittances of the cornea and lens according to Boettner and Wolter (Boettner and Wolter, 1962).

After calculating the amount to light reflected by the cornea according to the Eq.8, the remaining loss was shared between absorption and scattering, 7%, 9% and 13% for the three selected wavelengths respectively. **Figure 5.13** helps to visualise the magnitude of the three losses at the cornea.

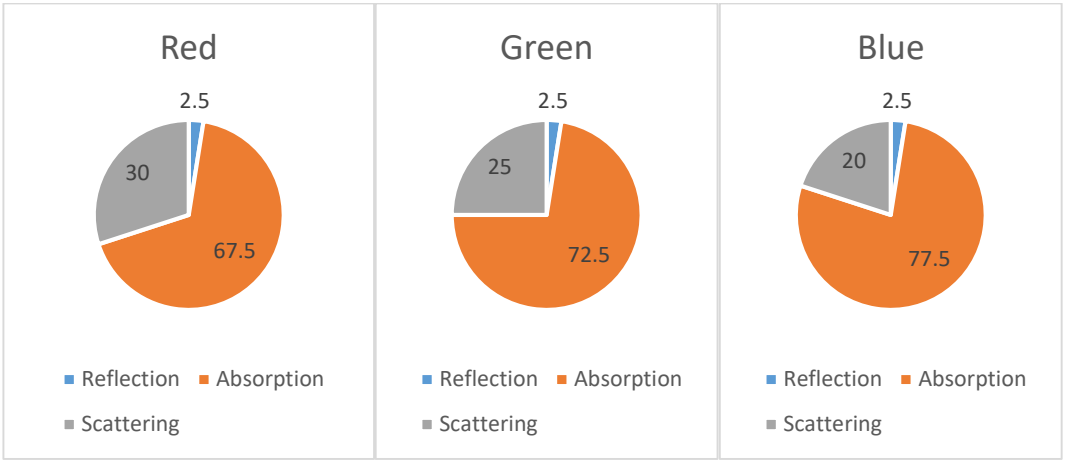

Figure 5.13 Proportion of the different physical phenomena (specular reflection, absorption and scattering) occurring at the cornea.

The proportion of absorbed and backward scattered light was determined based on empirical considerations, in particular in from Rayleigh scattering theory, and are summarised in **Table 5.2**.

As for the lens, only absorption and scattering were considered, in the proportions shown in **Figure 5.14**.

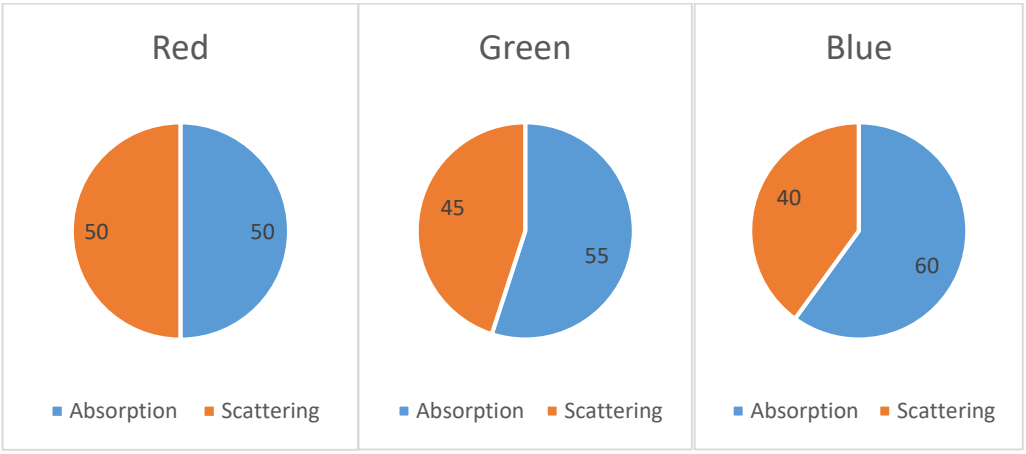

Figure 5.14 Proportion of the different physical phenomena (specular reflection, absorption and scattering) occurring at the lens.

Table 5.2 Proportion of the different phenomena on the cornea and the lens.

	Cornea			Lens			Retina		
	R	G	B	R	G	B	R	G	B
Reflection %	2.5	2.5	2.5	-	-	-	-	-	-
Absorption %	67.5	72.5	77.5	50	55	60	imcomplement(CORD_Image)		
Scattering %	30	25	20	50	45	40	24	22	20

This parametric formulation allows a different redistribution of the loss, if required, to simulate for instance pathological conditions or different light source spectrum. The full script with the implementation of the mathematical model created is included in **Appendix II**.

5.5.2 STATISTICAL ANALYSIS

To validate the mathematical model, the images produced with model have been compared with the images affected by artifact from CORD. The settings of the model are the ones described in the previous section. To be able to compare it with CORD only the quality distortions caused by external sources

of artifacts were produced (no abnormal lens or retinal scattering), since the images from CORD comes from healthy subjects. For the comparison, the statistical descriptors described in **Chapter 3** were computed for the images created with the model and compared with the descriptors of the CORD's dataset. One-way ANOVA test was then used to test statistically significant difference between the two datasets.

5.6 MODEL CONSISTENCY ANALYSIS: RESULTS

The dataset created with the mathematical model includes a wide variety of quality distortions (some examples are shown by **Figure 5.15**), obtained by setting the tuneable parameters in different combinations, from mild effect to severe one.

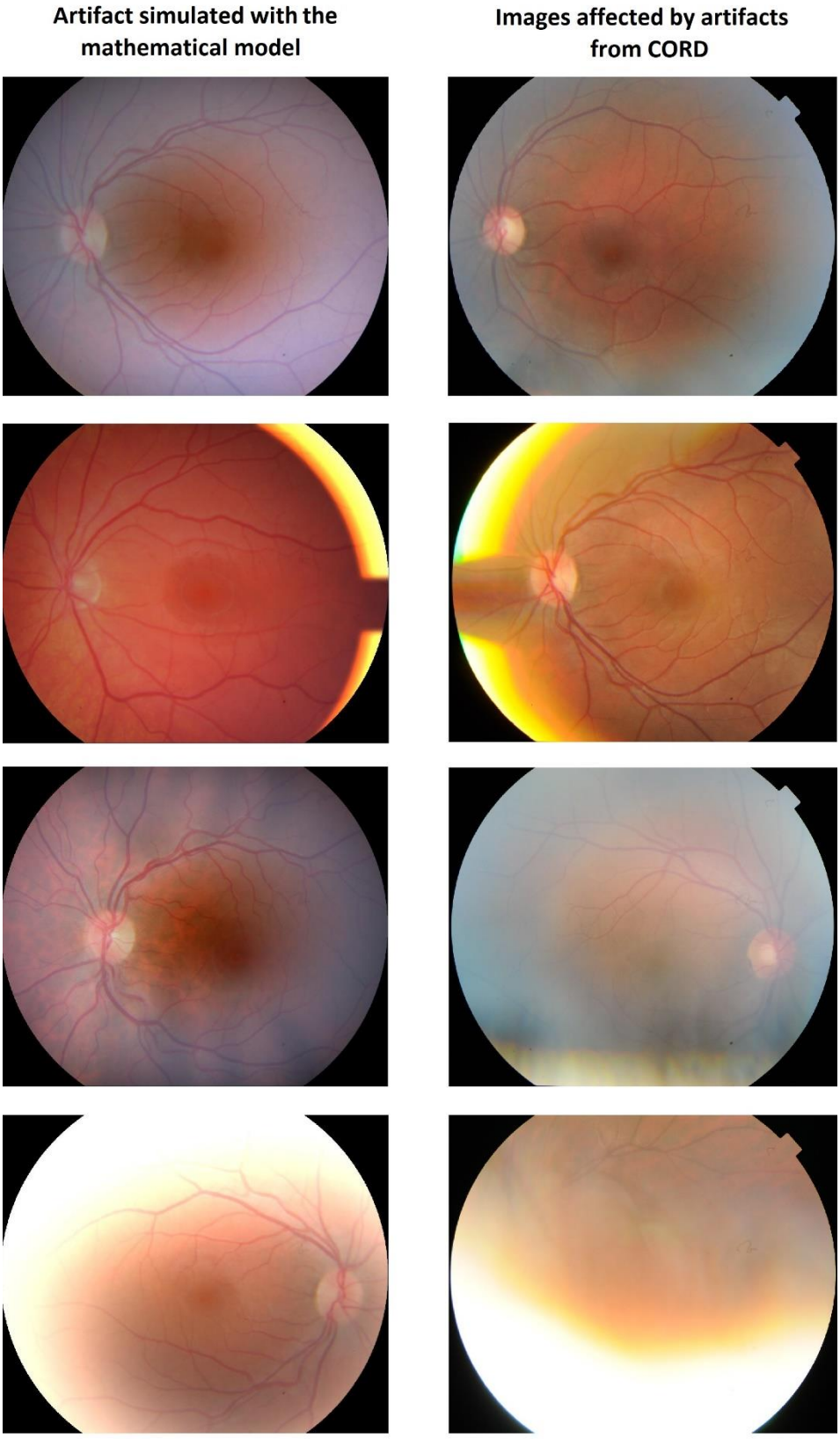

Figure 5.15 Example of images affected by artifacts produced using the mathematical model with different settings (left), in comparison with classic artifacts from CORD (right)

The one-way ANOVA test between the features of the images obtained with the mathematical model and the features evaluated on the images affected by artifacts from CORD, established no statistical difference for the majority of the features. In particular, 7 features over 20 obtained a p-value >0.05 across all the colour channels selected, and only three features were <0.05 for less than 67% of the channels (**Figure 5.16** and **Figure 5.17**).

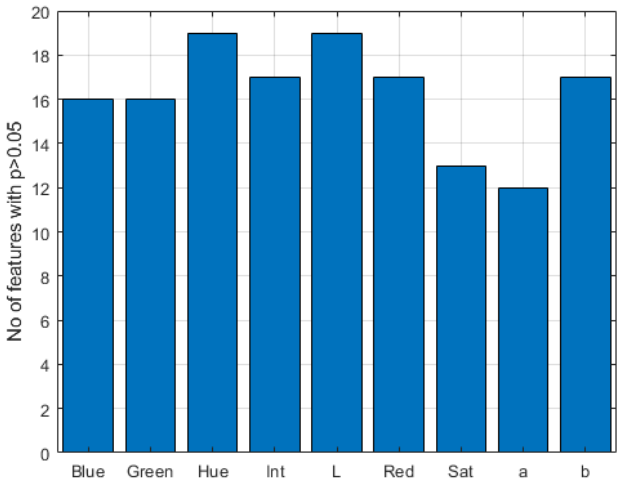

Figure 5.16 Number of features per colour channel with p>0.05

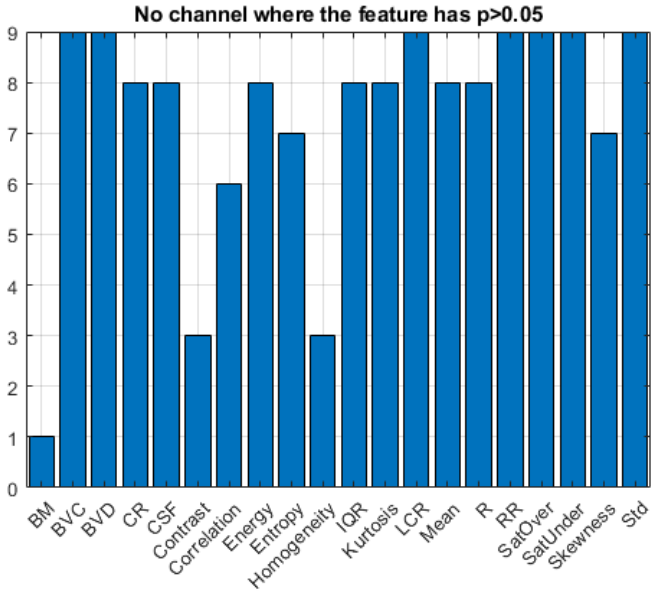

Figure 5.17 Frequency of features with p>0.05 across the 9 different colour channels considered.

In particular, the three features selected for the image classifier of the fundus images (mean, IQR and BVC of the a* channel) are not statistically different from the ones obtained with real artifacts (**Figure 5.18**).

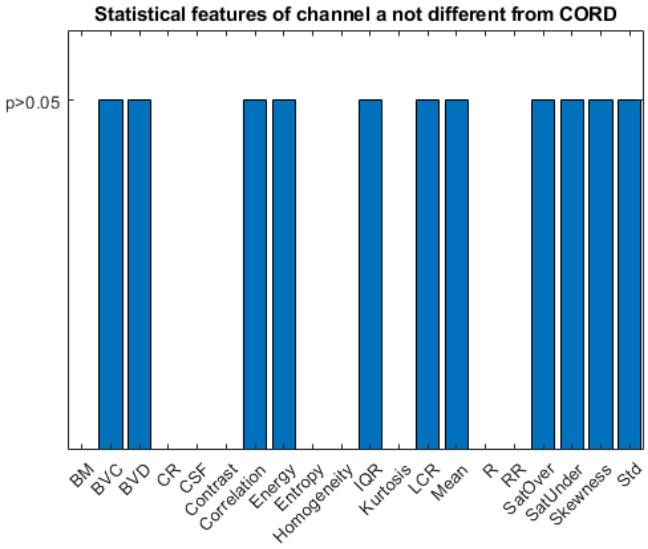

Figure 5.18 Features of the a* channel with p>0.05.

Also the second most significant triplets of features for image classification identified in the previous chapter (mean, SatOver and BVC of the Green channel) has been reported.

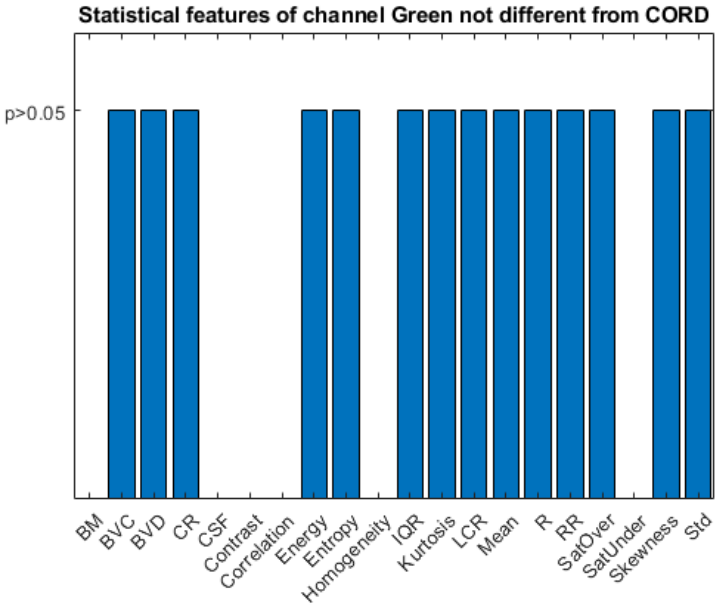

Figure 5.19 Features of the Green channel with p>0.05.

In **Table 5.3** the p-value of such statistical features are reported.

Table 5.3 p-value of the 3 most significant features identified by the classification strategy, for the a* channel and the Green channel.

Colour channel	Statistical feature	p-value
a*	mean	0.7645
	IQR	0.0683
	BVC	0.0891
Green	mean	0.9004
	SatOver	0.0698
	BVC	0.0528

5.7 DISCUSSIONS AND CONCLUSIONS

One of the critical gaps that has been identified in the field of retinal image processing (and in particular in artifact modelling and filtering) is the lack of examples of images affected by artifacts. Such images are fundamental for research groups that do not have direct access to ophthalmic devices or clinical facilities. The creation of CORD represents an important first step towards bridging this gap. However, the time, resources and organizational effort needed to produce a large number of fundus images in a running clinic are considerable. The images so far collected cover a wide variety of quality distortions, but they are still a limited number. While the CORD repository will grow in the future, with more images to be collected by this research group and hopefully with some help of other researchers inspired by this work, within the time of this doctoral work other solutions were considered in order to obtain more artifact examples. Amongst others, the creation of a mathematical model able to reproduce, starting from clinical quality image, the effects of artifacts was eventually selected.

At the best of the authors' knowledge, at time of this work, no image processing tool developed to simulate the quality distortion caused by artifacts in retinal imaging was identified in the field. The choice of using a parametric model to describe the interaction of the light with the eye's tissues and the ophthalmic device was made to keep the whole algorithmic structure as more modular and simple as possible. Such model, in fact, can be easily readapted, upgraded and implemented to fit multiple purposes (e.g. artifact simulation or image restoration) and to account for more phenomena and parameters.

For the purpose of this thesis, such model was used to generate an artificial dataset of images affected by artifact characterised by the same statistical features of images acquired in the field. The ANOVA test proved that the images produced by this mathematical model are similar to the images obtain in real fundoscopy, from a statistical perspective. Together with the images from CORD, this database is going to provide a robust training dataset to develop and optimize the artifact removal algorithm described in the next chapter.

The potential offered by this algorithmic approach, however, goes beyond the aim of this thesis. This image processing tool was designed with the ambition to simulate not only artifact and noise produced by the optics of the image acquisition device or environmental factors, but also to simulate artifact caused by pathological conditions. Having a simplified mathematical description of the interaction between the light and the eye can help the understanding of the phenomena behind the generation of artifact, with potential impact in ophthalmic device design and imaging technique to improve diagnosis in eyes with pathologies that impact on image quality (e.g. keratoconus and cataract).

CHAPTER 6. CLEAN-UP ALGORITHM DEVELOPMENT

6.1 CLEAN-UP STRATEGY

As highlighted throughout this work, "*quality*" in medical imaging is strongly related with the information contained in the image, in relation to the specific diagnostic procedure used. In retinal imaging, the principal carrier of the clinical information is the *textural information*, hence the anatomical features and pathological signs. Such features can be faded, hidden or distorted due to artifacts produced during the image acquisition process. Nevertheless, as long as some textural content is preserved (i.e. no image saturation is masking out the features of interest), the portion of the image affected by the distortion may still give usable insights, provided the artifacts are removed.

The clean-up strategy developed had the primary objective of retrieving two main anatomical features of the retina (blood vessels and ONH) and was developed under the following basic assumptions:

- The contribution of the artifact distortions to the image is additive;
- If the intensity level of the region of the image affected by artifact is saturated (complete loss of textural information), the information cannot be retrieved.

As for the first condition, the artifacts described so far are commonly generated by the combination of scattering, specular reflections, illumination issues (uneven illumination, ring slit target misalignment) and object obstruction. With the proviso that different chromatic components cross-talk with each other due to scattering, the approximation of such distortion as merely additive show good results in the artifact simulator described in **Chapter 5**. Such additive nature has been reported by many research works

involving the collection of retinal image datasets (*STructured Analysis of the Retina,* E. Decencière *et al.*, 2013, *CORD Comprehensive Ophthalmic Research Database*, CORD 2019, *IMAGERET Optimal Detection and Decision-Support Diagnosis of Diabetic Retinopathy*), including CORD (examples in **Figure 6.1**).

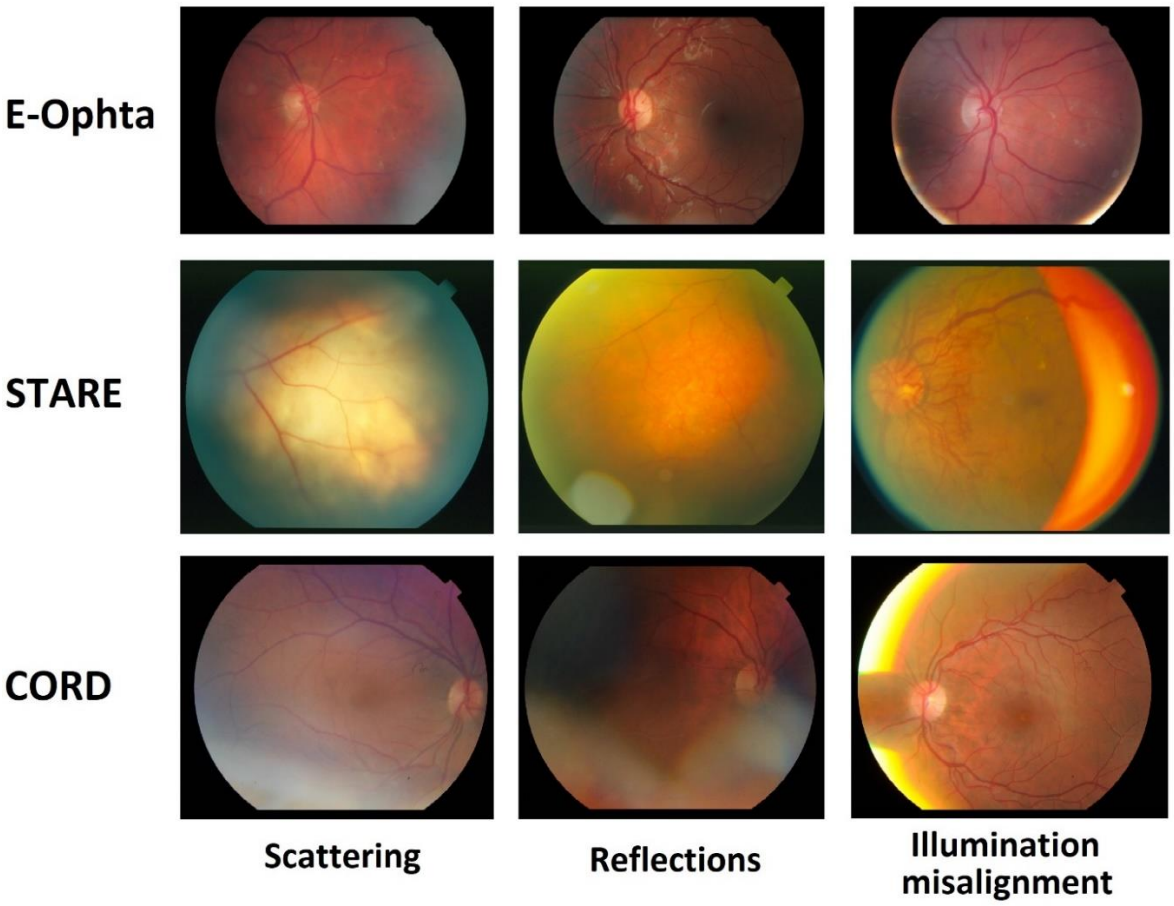

Figure 6.1 Examples of artifacts in fundoscopy. Each row corresponds to a different dataset; each column represents a different typology of artifact.

As for image saturation, this occurs when the intensity level of the pixels reaches its maximum digital level (e.g. 255 for an 8-bit unsigned integer 2D image). This happen because the intensity of the signal captured by the image sensor is greater than the dynamic, or operational range, of the image sensor itself. If saturation affects a portion of the image, the information within it is lost, and no image filtering technique can be used to retrieve the textural content of that area. However, given the sensitivity of image sensors used in fundoscopy is not uniform across the spectrum, the saturation may affect only some colour

channels of the image. In such cases, part of the textural information can be retrieved, although the overall clinical usability may result severely reduced (e.g. detection of dark lesions but not bright ones or vice versa).

The strategy used in this work to isolate, model and mitigate the distortion caused by artifacts, exploits the unique opportunity of having full access to the textural content for each of the retinal image affected by artifacts (CORD + dataset of artificial artifacts). In fact, in both datasets the images affected by artifacts have always the CSQ counterpart (**Chapter 5** and **6**). A classification algorithm is used on half of the images of the two datasets (training set) to identify the pixels affected by artifacts. This classification will take advantage of the statistical feature of the pixel affected by distortions in comparison with pixels free from distortion. This algorithm will be then used on the second half of the datasets (test set) to identify the region of the images affected by artifacts. Those regions will be isolated and fitted by the means of an image interpolation algorithm, obtaining a simplified model of the distortion. Such model will then be subtracted by the artifact image obtaining a cleaned-up image. All the processing steps illustrated in the following were performed using Matlab 2019a (MathWorks, Inc., Natick, MA, USA) as numerical computing software.

6.2 METHODS

The processing steps are reported in **Figure 6.2**. The pixel classifier is developed on half of the database, by comparing the pixel with and without artifact of the same area, thanks to the registration between the image affected by artifact and the CSQ image. The classifier is then applied on the other half of the images and the profile of the distortion extracted via surface fitting. Finally, the distortion is subtracted from the image affected by artifact and the main textural elements of the cleaned-up images are evaluated to assess quality improvement.

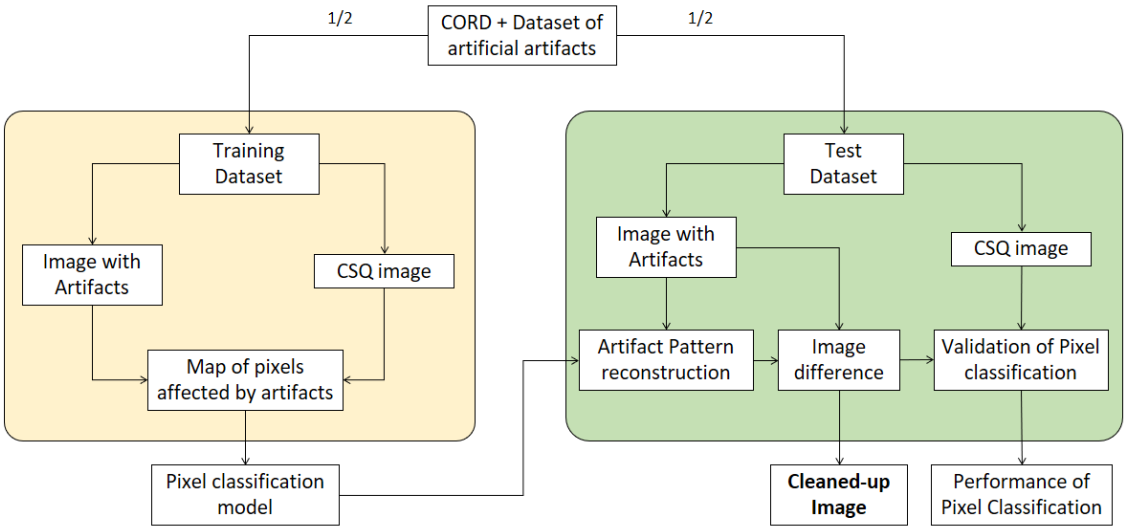

Figure 6.2 Block diagram of the clean-up strategy. The yellow section represent the steps used to train the pixel classification model, starting from the training dataset. The green section shows the steps used to clean-up the artifact from the test dataset using the classification model.

6.2.1 PIXEL CLASSIFICATION MODEL

The first part of the process, where the classification model is trained is better detailed in **Figure 6.3**.

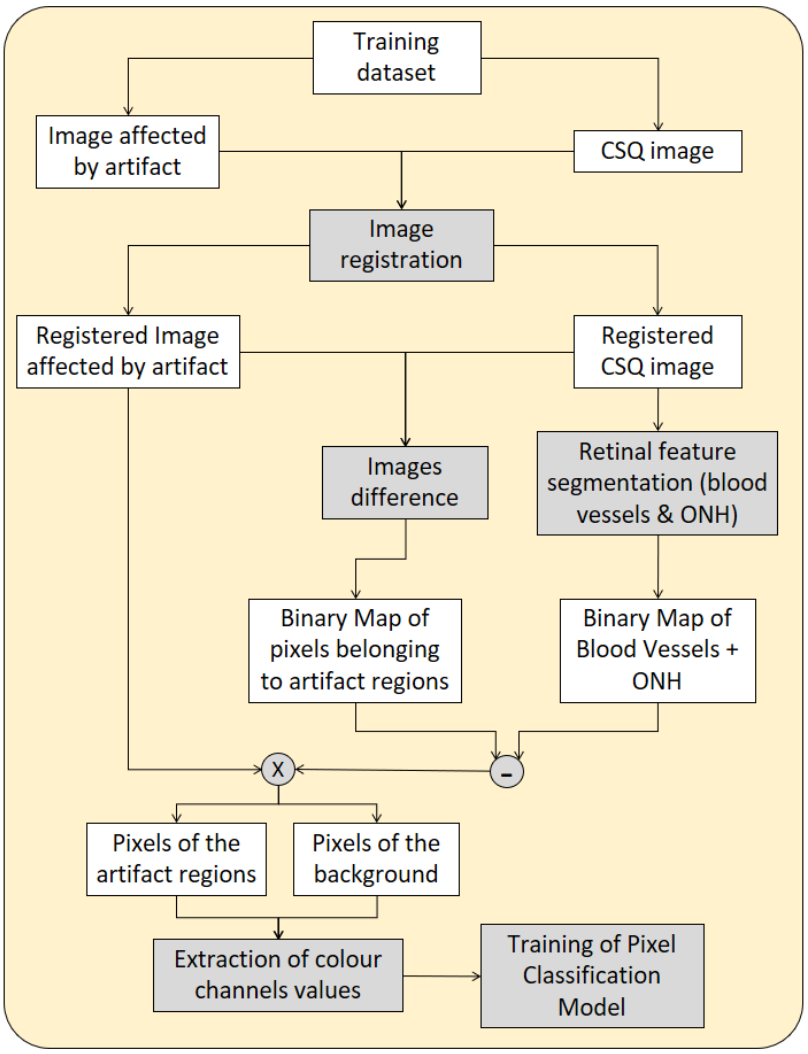

Figure 6.3 Block diagram of algorithmic process used to train the pixel classification model. The white boxes are the input and output images; the grey boxes are the image processing steps.

Image registration

The aim of the image registration is to find the geometric transformation (translation, rotation and scaling) that maps the points in the CSQ image into the points of the same feature in the artifact image. In fact, during the image acquisition process, small ocular movements of the participant cause each image to be slightly translated and/or rotated compared to the previous one.

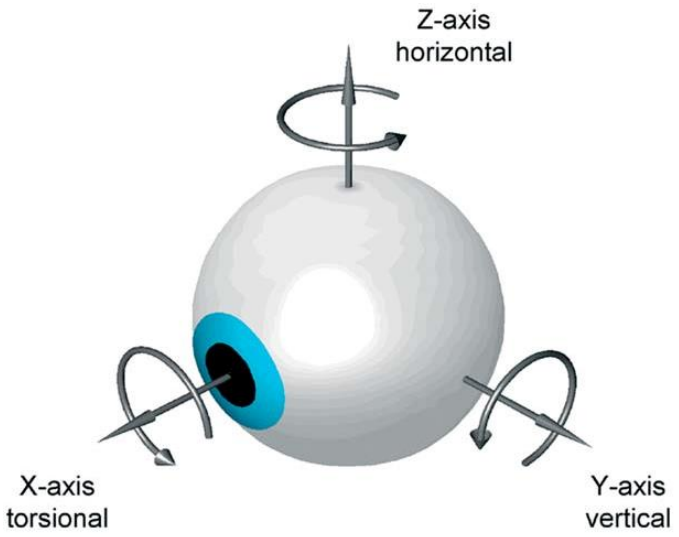

Figure 6.4 Rotation axes of the eye (Büttner and Büttner-Ennever, 1988).

Although the shift is primarily caused by the rotation of the eye along its z axis (**Figure 6.4**), this can be approximated by a translation along the x axis due to the small shift. Similarly, the rotation along the X axis will be approximated by a translation along the Z axis. This transformation, combination of the translation in the XY plane and the rotation around the Y axis, can be formalised as:

$$T: (x, y) \mapsto (x', y') \ . \tag{1}$$

The approach selected for the registration can be classified as landmark-based (Maintz and Viergever, 1998), as the automatic segmentation process of the inadequate quality images can be highly inaccurate, leading to a mismatch. The approach consists in the manual identification of two points per image (distant at least one radius of the ROI from each other) belonging to features easily identifiable in both images. The selection of these two points is performed on the green channel of the image, after an adaptive contrast enhancement (CLAHE) (Pizer *et al.*, 1987) process is applied (**Figure 6.5**).

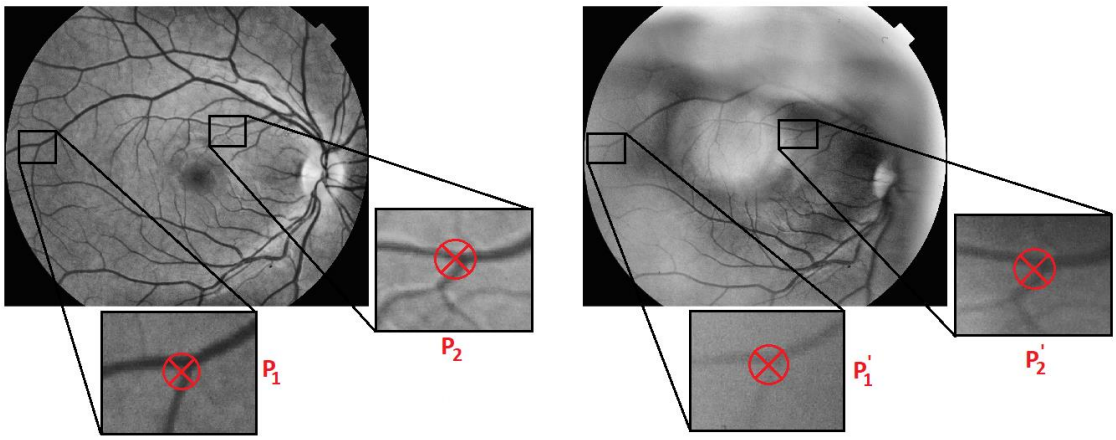

Figure 6.5 CLAHE of the green channel of the CSQ retinal image (left) and the artifact affected counterpart (right). The selection of the two points for the registration process is highlighted in the magnified sections.

To calculate the geometric transformation we can express the points $P(x, y)$ and $P'(x', y')$ related by the matrix relation:

$$\begin{bmatrix} x' \\ y' \\ 1 \end{bmatrix} = RTS \begin{bmatrix} x \\ y \\ 1 \end{bmatrix} \qquad RTS = \begin{bmatrix} x' \\ y' \\ 1 \end{bmatrix} \begin{bmatrix} x \\ y \\ 1 \end{bmatrix}^{-1} \tag{2}$$

where the scaling matrix S, the rotation matrix R and the translation matrix T are:

$$S = \begin{bmatrix} s_x & 0 & 0 \\ 0 & s_y & 0 \\ 0 & 0 & 1 \end{bmatrix} \quad R = \begin{bmatrix} \cos\theta & -\sin\theta & 0 \\ \sin\theta & \cos\theta & 0 \\ 0 & 0 & 1 \end{bmatrix} \quad T = \begin{bmatrix} 1 & 0 & d_x \\ 0 & 1 & d_y \\ 0 & 0 & 1 \end{bmatrix} \tag{3}$$

Once the geometric transformation is obtained, this is applied to the CSQ image, obtaining the overlap of the features in both images.

ROI redefinition

After the registration, some useful measurements and information are collected for both the images:

- Image Mask that defines the margins of the ROI (area inside the circular black frame)
- Extraction of the geometric parameters of the ROI: radius r and centre $C(x, y)$

- Enhancement of the green channel of the CSQ image via adaptive method.

The Mask is a binary image (black and white) used to identify the pixels that belong to the ROI (usually, 1s identify the pixels of the ROI and 0s the pixels outside the ROI). The creation of such mask allows the optimization of some of the processing steps and the evaluation of the geometrical parameters of the ROI.

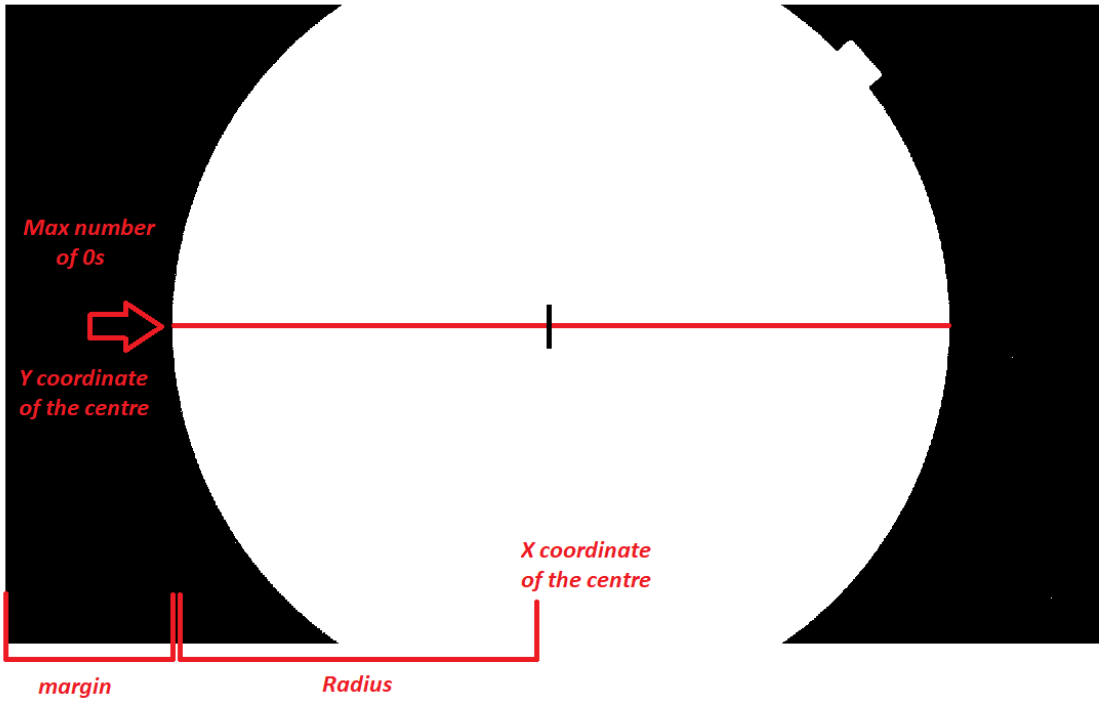

Figure 6.6 Graphical principles used in the evaluation of the geometrical parameters of the ROI.

The radius of the circular ROI, in fact, is evaluated by determining the row of the Mask image with the maximum number of ones, calculating the number of them and dividing the result by half. This row will also be the Y coordinate of the centre of the ROI, and the X coordinate is obtained be summing the margin with the radius, as in **Figure 6.6**. The final value of the radius needs to be reduced so to compensate for the geometrical shift between the registered CSQ image and the artifact-affected one (**Figure 6.7**).

Figure 6.7 Blended overlay image of the artifact image and the registered CSQ image.

The final radius r_f can be evaluated by subtracting the previous radius with the modulus of the total translation, as:

$$r_f = r - \sqrt{x^2 + y^2} - \tau \tag{4}$$

where τ is a safety factor that account for the quantisation errors (here $\tau = 4$). Once the radius is calculated, the registered CSQ image and the artifact one are re-processed so that the ROI of both the images have the same geometrical values (**Figure 6.8**).

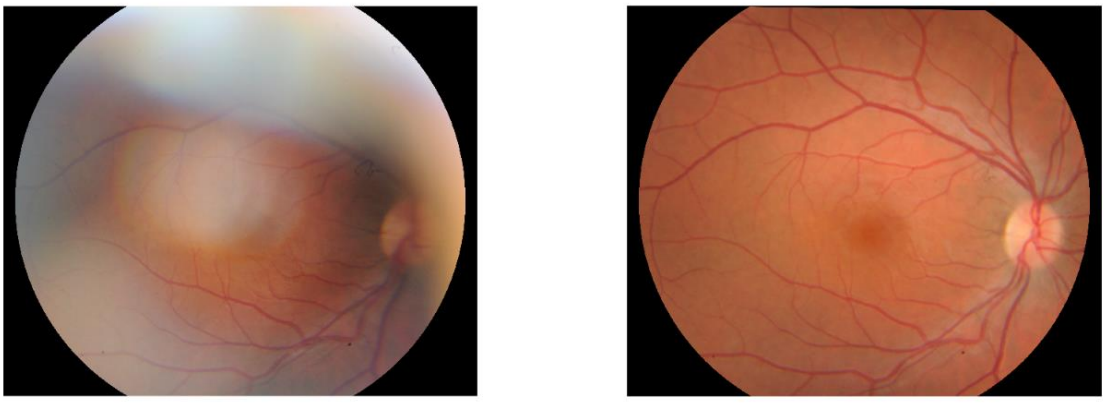

Figure 6.8 Result of the image registration process and the ROI re-definition.

Retinal feature segmentation

The segmentation of the retinal features of the registered CSQ image has the purpose of creating a binary image where 1s are assigned to the background pixels and 0s to the features pixels. This map is then used to exclude the pixels of the features from the evaluation of the statistical features, as their value can vary widely depending on the kind of feature and the position on the retina, while the background has much constant chromatic characteristic across the ROI.

The feature segmentation algorithms selected for this work is a combination of the classic thresholding and an improved matched filter technique (Katz *et al.*, 1989, Al-Rawi,Qutaishat and Arrar, 2007). The selection has been somewhat arbitrary, and the simplest method has been used. The impact of the segmentation method on the clean-up strategy has not been evaluated (time constraints). However, from simple preliminary tests (not reported) the impact of the choice appears to be very minor.

ONH segmentation – the extraction of the ONH was performed via simple thresholding. Once the centre of the ONH was identify, by knowing that the intensity level of the red channel reaches the maximum at the ONH, an image threshold technique was performed within a limited area from the ONH's centre (blue circle of **Figure 6.9**). In this work, the radius of such area was 20% of the radius of the ROI and the threshold value used to isolate the ONH was 210 (of possible digital values that go from 0 to 255).

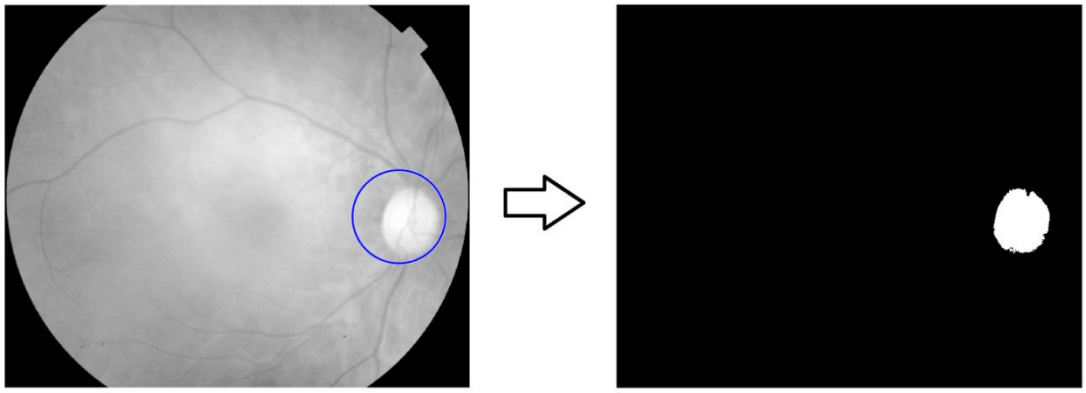

Figure 6.9 Red channel of the CSQ image. The blue circle represents the area where the thresholding was performed. On the right, the binary image resulting from the ONH segmentation.

Blood vessels segmentation – as described in **Chapter 3**, the matched filter is a template matching algorithm that exploit the spatial properties of the object to be recognized. In this case the properties of the blood vessels are:

- Vessels appear darker relative to the background
- Vessel size decreases when moving away from the optic nerve (retinal vessel width range of 2-12 pixels)
- The intensity profile of the cross section of a vessel has a Gaussian shape.

The matched filter kernel can be expressed by:

$$k(x,y) = -e^{\left(-\frac{x^2}{2\sigma^2}\right)} \quad \forall |y| \leq L/2, \tag{5}$$

Where L is the length of the vessel segment that lies on the same orientation, σ is the variance of the Gaussian profile (defines the spread of the bell-shape profile). To be able to detect vessel oriented at different angles, the kernel is rotated and the maximum response from the filter for each angle is registered. The trails of the Gaussian curve are truncated at $u = \pm 3\sigma$. A neighbourhood N is defined such that:

$$N = \{(u,v), |u| \leq T, |v| \leq L/2\} \tag{6}$$

As suggested by the work of Al-Rawi *at al*. (Al-Rawi,Qutaishat and Arrar, 2007), in this work, the value selected are $\sigma = 1.9$, $L = 11$, $T = 8$ and the angle of rotation of the kernel $\theta = 15°$, for a total of 12 rotation. This filtering process produces a grey scale image where the features are brighter than the background.

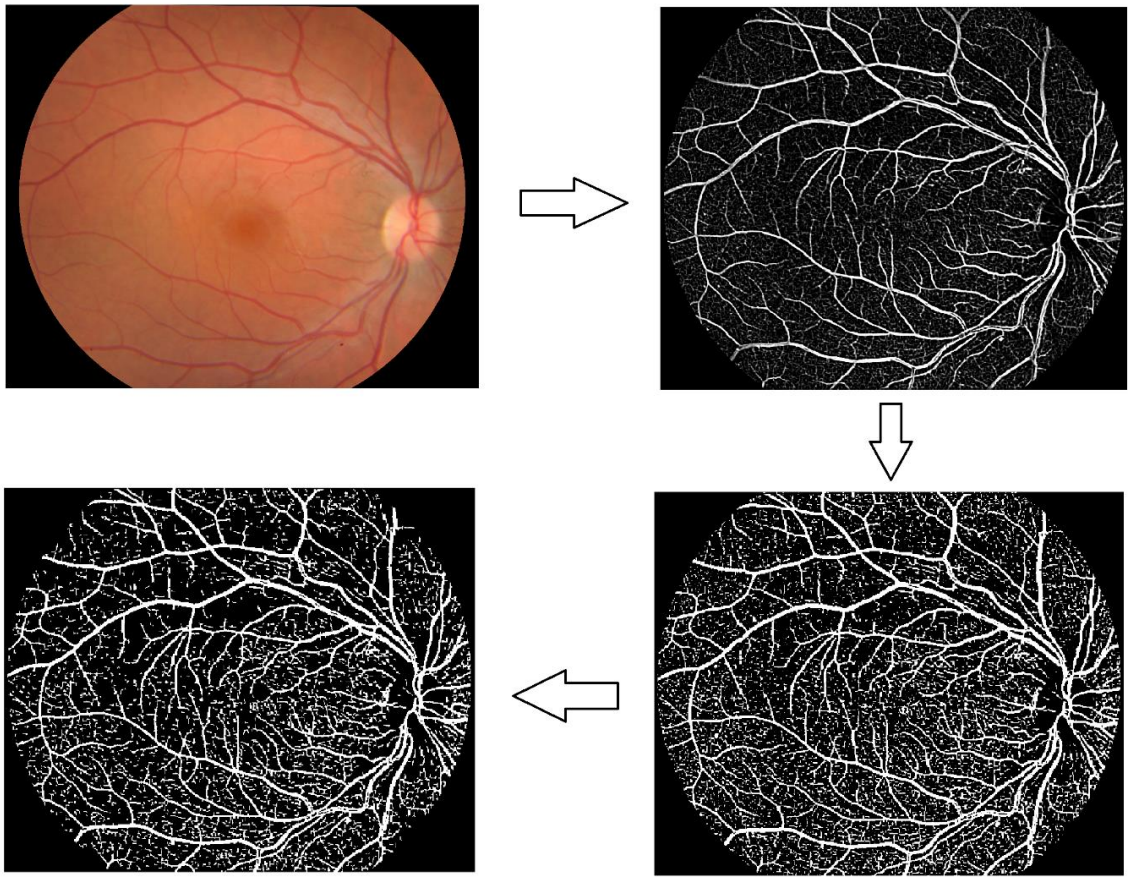

Figure 6.10 Blood vessels segmentation process. Matched filter is applied to the CSQ image resulting in the grey scale map of the vessel. The map is then transformed into a binary image and the small non-connected objects removed.

To obtain the binary image a threshold value is empirically established to include the majority of the retinal features detected previously (here, $Th = 50$). Once the binary image is obtained a further step is implemented to eliminate the non-connected elements formed by a group of pixels < 50. In **Figure 6.10**, the segmentation steps of the blood vessels are shown.

After the two binary maps (ONH and blood vessel) have been created, they were combined together and processed to obtain the complement (example in **Figure 6.11**). In this way only the pixel belonging to the background have value equal to 1, allowing the subsequent stage to be performed.

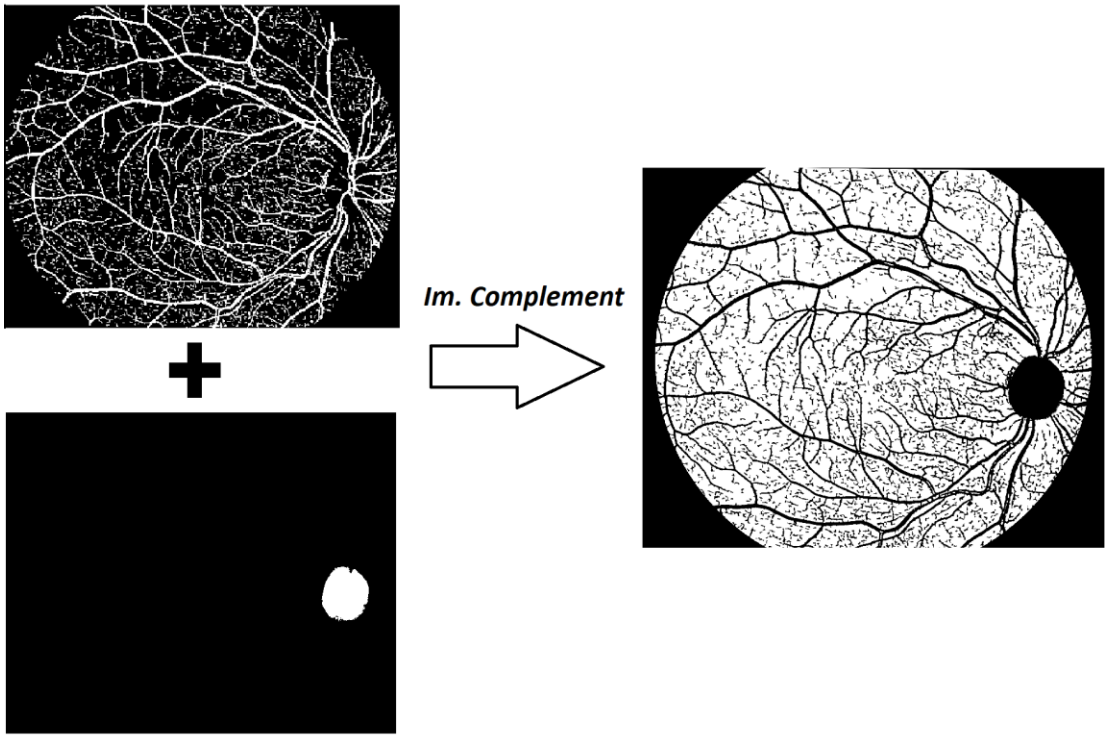

Figure 6.11 Creation of the binary map of the retinal features.

Image difference

The difference between the two registered images isolates the contribution caused by the artifacts, under the hypothesis of additive artifact (**Figure 6.12**). Given the border between the pixels affected by artifact and not affected is fuzzy, to prevent pixels not belonging to the artifact to be considered, a thresholding was applied. In this work, under 5% of the max value of the artifact contribution, of the corresponding channel, was empirically established. The image representing the artifact contribution was then multiplied by the binary image of the background (1 if the pixel belongs to the background, 0 otherwise), obtained in the previous step. The result is the image of the artifact, excluding the pixels that belong to blood vessels and ONH (**Figure 6.12**, right).

Out of this image, the binary maps of the pixels of the background affected by artifacts and the pixels of the background not affected by artifacts were created (**Figure 6.13**).

Figure 6.12 From the left, the registered CSQ and artifact images, in the right corner the image difference between them.

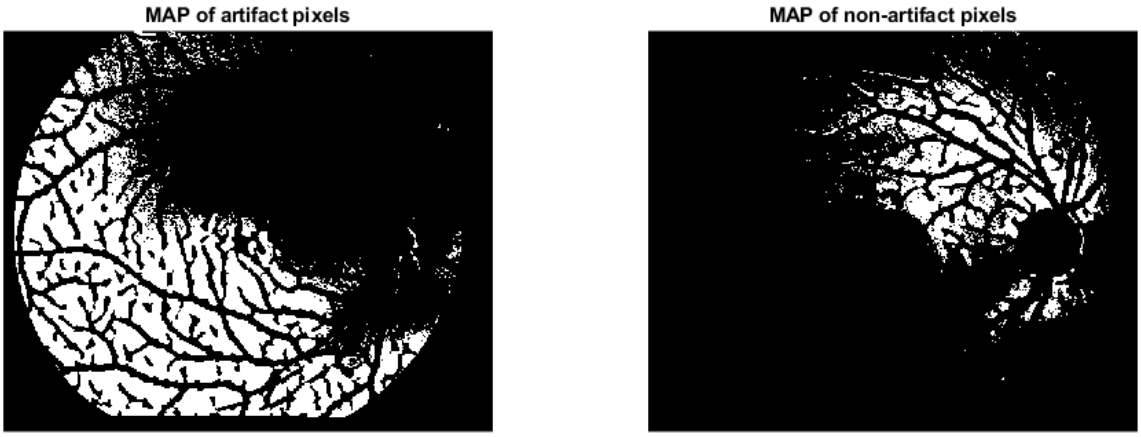

Figure 6.13 Binary maps of pixels of the background affected by artifact distortions (left) and the pixels of the background non-affected by the artifact (right), respectively.

Pixel value extraction

The binary maps are used to distinguish between the pixels of the retinal background affected by artifact and not. The colour channel values of such pixel was stored in separate matrixes and labelled as “Group A” = affected and “Group B” = not affected. Labels and colour channel parameters are the two inputs for the SVM model, which will use such dataset to train its binary classifier. To account for the variability between the retinal images caused by subject characteristics (age, sex, skin colour) the values collected were normalised respect to the mean value of the respective channel of the whole ROI.

Training of the binary classifier

The classifier adopted for the pixel classification is the regularized support vector machine (SVM), a linear classification models for two-class learning with high-dimensional, full or sparse predictor data. This classifier has been used in retinal vessel segmentation with good results, as described in **Chapter 3**, thanks to its robust learning process. Here is used to predict which pixel of the retina's background is affected by quality distortions in the test database.

6.2.2 IMAGE CLEAN-UP PROCESS

The classifier trained in the first part of the process is now applied to the test dataset to evaluate how well the model can identify pixels affected by quality distortions (**Figure 6.14**). Once the distortions have been isolated and extracted, they are subtracted to the original artifact image to counteract the effect of the distortion itself. The mitigation of the quality distortion is then evaluated using the quality classifier developed in **Chapter 4**.

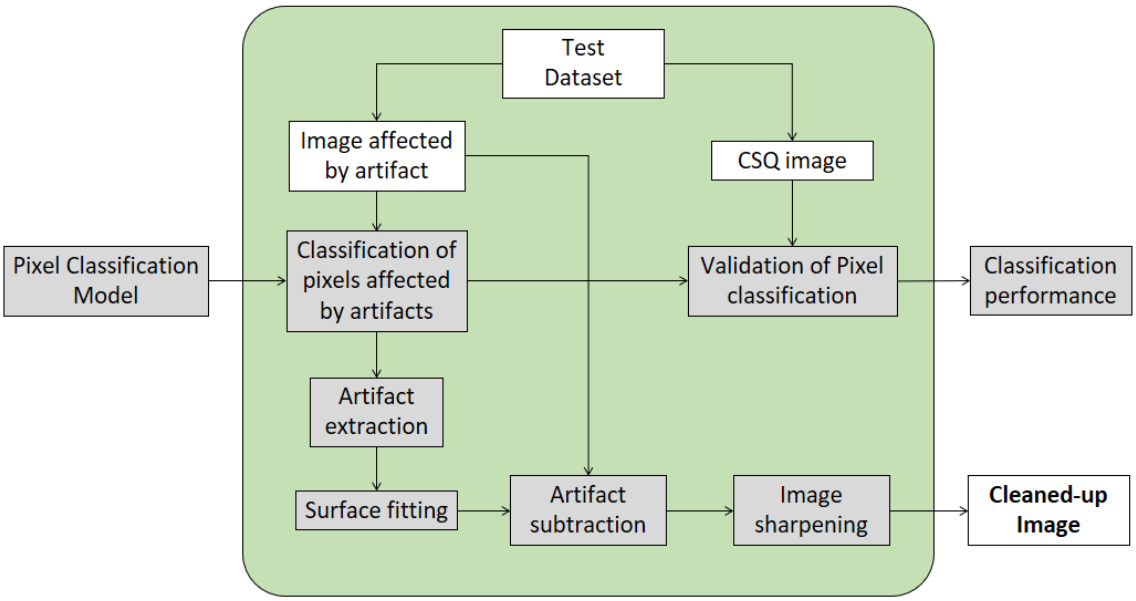

Figure 6.14 Block diagram of algorithmic process used to clean-up the images from the artifact contribution. The white boxes are the input and output images; the grey boxes are the image processing steps.

Pixel classification

For each image affected by artifact (of the half portion of the database used as test dataset) the colour channels values of the pixel of the ROI was collected. These values were processed by the classifier, establishing which one is affected by artifact or not. Pixels recognised by the classifier as affected by artifact were labelled as such, forming the binary image representing the region of the image affected by artifacts.

Pixel classification performance assessment

The pixel classification performance was tested in terms of accuracy, specificity and sensitivity. To do so the number of pixels correctly classified as background affected by artifacts (TP), number of pixels correctly classified as background not affected by artifacts (TN), number of pixels wrongly classified as background affected by artifacts (FP) and number of pixels wrongly classified as background not affected by artifacts (FN) was quantified for each image of the test database (80 images from CORD + 50 images from the artifact model). The total accuracy reached was $Acc = 89.4\%$, $Sp = 98.3\%$ and $Se = 60.3\%$.

Artifact pattern extraction

The extraction of the artifact contribution is achieved by extracting the value of the pixels that belong to the artifact (using the binary map of the previous step). This value is subtracted with the mean value of the intensity value of the entire ROI. This operation is made for each channel.

Surface fitting

The distortion pattern obtained in the previous step is discontinuous, given the outliers and possible interaction of the pixels of the retinal features. To give to the distortion a smoother profile, a surface interpolation process is implemented. The fitting model selected is the biharmonic spline interpolation which allows the interpolation of irregularly spaced two dimensional data points (Sandwell, 1987). This model is based on the physical interpretation of the

spline as an elastic surface that bends under the effect of loads of weight w_i, passing through the points x_i (**Figure 6.15** reports an example in 1 dimension).

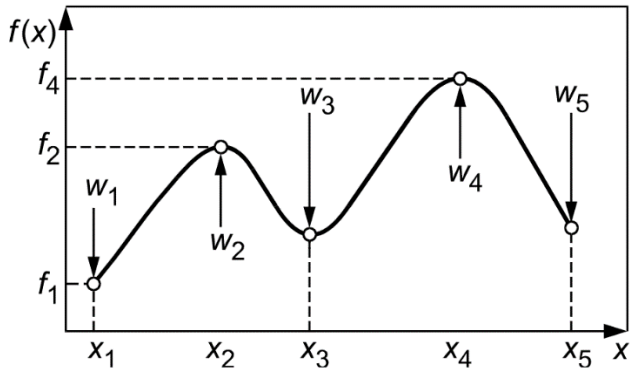

Figure 6.15 Bending of the elastic spline under the effect of loads of weight w_i (Belozubov,Vasil'ev and Chernov, 2014).

The bending of a beam under the action of a point load found at the coordinate origin may be described by the biharmonic differential equation (Belozubov,Vasil'ev and Chernov, 2014)

$$d^4 f(x)/dx^4 = \delta(x), \tag{7}$$

where the function $f(x)$ characterizes the bending of the spline while the point weight is represented by the Dirac delta function $\delta(x)$. The response of the system to an action expressed in the form of a delta function is called Green's function, to which particular solution is:

$$f(x) = |x|^3 \tag{8}$$

By using this function to interpolate N data points w_i located at x_i, the corresponding weight coefficients must be added together:

$$f(x) = \sum_{j=1}^{N} w_j |x - x_j|^3 \tag{9}$$

For known coefficients w_j, the value of a biharmonic spline at any point x_j is found from Eq. 9.

The method used to calculate the weights is the non-linear least square one, using the Levenberg-Marquardt algorithm as fitting method (Levenberg, 1944), where a function $f(x)$ is minimized that is a sum of squares.

$$\min_{x\in\mathbb{R}^n} f(x) = \|\boldsymbol{F}(x)\|_2^2 = \sum_i F_i^2(x), \tag{10}$$

where the vector $\boldsymbol{F}(x)$ is

$$\boldsymbol{F}(x) = \begin{bmatrix} \bar{y}(x,t_1) - \bar{\varphi}(t_1) \\ \bar{y}(x,t_2) - \bar{\varphi}(t_2) \\ \cdots \\ \bar{y}(x,t_m) - \bar{\varphi}(t_m) \end{bmatrix} \tag{11}$$

and $\bar{y}(x,t)$ and $\bar{\varphi}(t)$ are scalar functions representing the output and the continuous model trajectory of the surface. In the Levenberg-Marquardt method the searching direction d_k for the minimum is set by the solution of the linear equation:

$$(J(x_k)^T J(x_k) + \lambda_k I)d_k = -J(x_k)^T F(x_k), \tag{12}$$

where $J(x_k)$ is the Jacobian matrix of $F(x_k)$ and λ_k is a scalar that controls both the direction and the magnitude of d_k.

To reduce the computational complexity needed for the surface interpolation process, a small number of pixels (400) is randomly selected across the ROI of the distortion pattern, following a normal distribution. As an example, the result of the curve interpolation process of the three channels of the RGB colour space, for the retinal image in **Figure 6.8**, is shown in **Figure 6.16** and **Figure 6.17**.

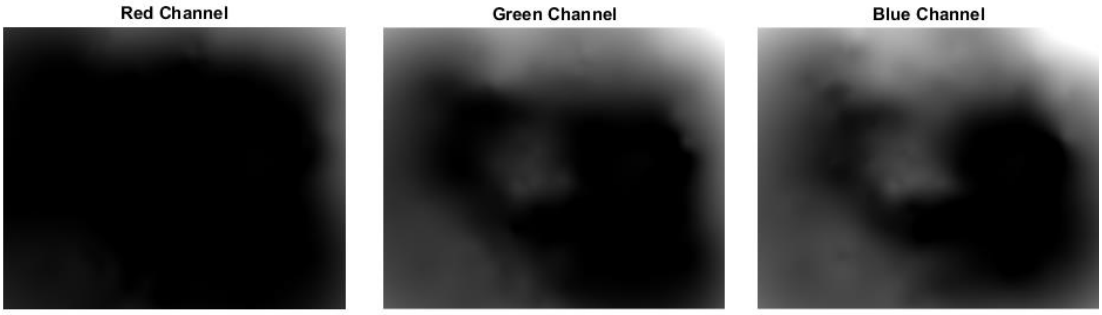

Figure 6.16 Curve interpolation of the biharmonic model into the distortion pattern caused by scattering and artifact phenomena.

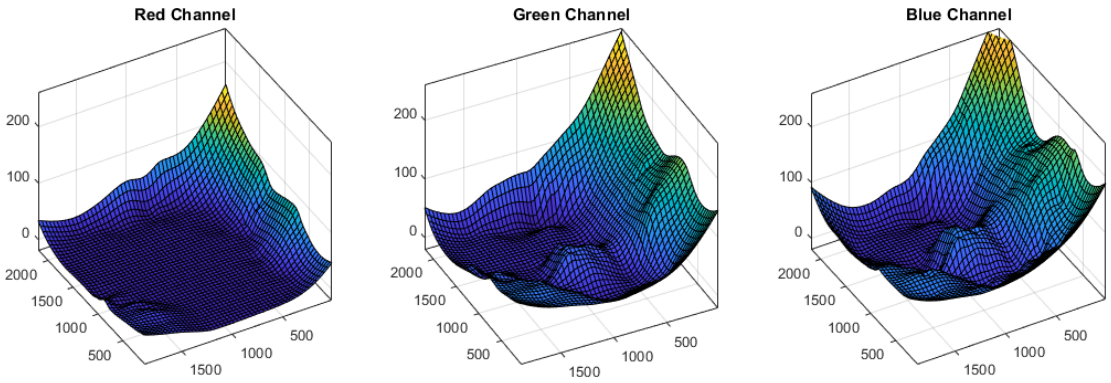

Figure 6.17 3D map of the modelled surface of the distortion.

Artifact pattern subtraction

The model of artifact obtained is then subtracted to the corresponding image. As stated before, this is possible giving the additive nature of such contribution to the image. In the region with no saturation, the chromatic value has mostly been restored by the artifact model subtraction. The contrast of portion of the image affected by the artifact distortion, however, results in lower than in the region non affected by quality distortion. This is due the loss in the overall dynamic of the textural information and the scattering phenomena. To improve contrast of the textural features an image sharpening technique in the spatial frequency domain is employed. Because the edges and other sudden changes in intensity are associated with high-frequency components, the textural sharpening can be performed via high-pass filtering, which attenuate the low-frequency components without altering the high-frequency information in the Fourier transform.

To compensate the reduction of the average value of the image due to the highpass filtering, a high-frequency emphasis filtering approach is employed. Here, an offset is combined to the filter in order to mitigate the amplitude reduction of the low-frequency components. The transfer function of the high-frequency filter is:

$$H(u,v) = a + bH_{HP}(u,v) \tag{13}$$

Where a is the offset, b is the multiplier and $H_{HP}(u,v) = 1/(1 + [D_0/D(u,v)]^{2n})$ is the Butterworth highpass filter, where D_0 denotes the cut-off frequency (radius outside which the frequencies can pass in the Fourier spectrum) and $D(u,v)$ is the distance between the point (u,v) in the domain frequency and the centre of the frequency rectangle (**Figure 6.18**).

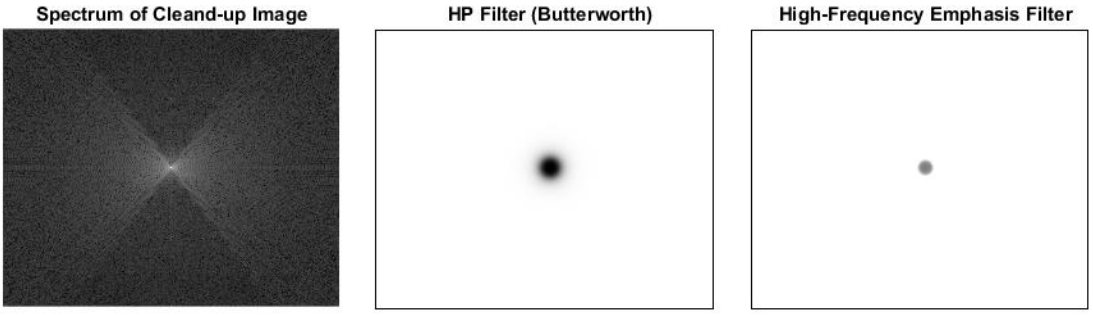

Figure 6.18 From the left: the spectrum of the image affected by artifact after the artifact model subtraction, the spectrum visualization of the Butterworth HP filter (where the black circle is the cut-off area) and the spectrum visualization of the high-frequency emphasis filter.

The filtering process was performed on the L (lightness) channel of the CIE L*a*b* colour space. This colour space was selected because, by design (CIE, 1978), numerical changes in the CIE L*a*b* colour space correspond to roughly the same amount of visually perceived changes. The sharpening process steps are described by the block diagram in **Figure 6.19**.

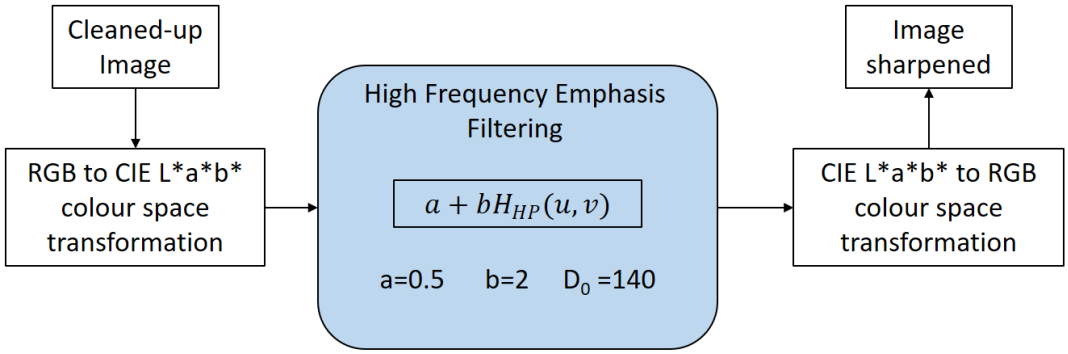

Figure 6.19 Block diagram of the image sharpening.

This is the last step of the retinal filtering strategy which result for the example used so far can be seen in **Figure 6.20**.

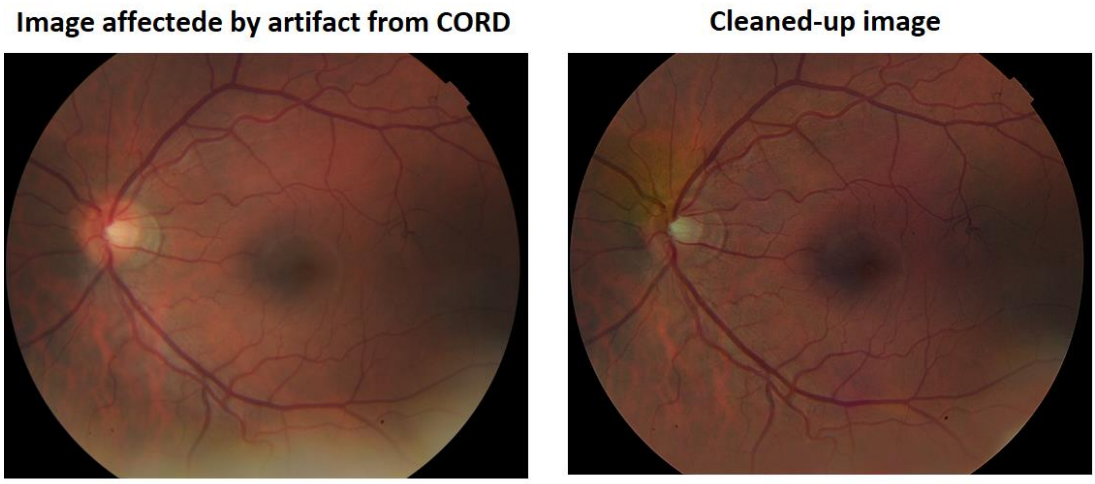

Figure 6.20 Comparison between the image affected by artifacts and the result of the artifact clean-up strategy.

6.3 VALIDATION OF THE CLEAN-UP STRATEGY

To assess the improvement on the quality of the cleaned-up images the specific textural features were evaluated before and after the imaging clean-up to assess the improvement of the textural content of the image, which have been found to be critical in the clinical assessment.

6.4 ARTIFACT CLEAN-UP RESULTS

A total of 80 images affected by artifacts (40 from CORD + 40 from the dataset created with the mathematical model), which is half of the retinal images available, have been processed using the clean-up strategy developed.

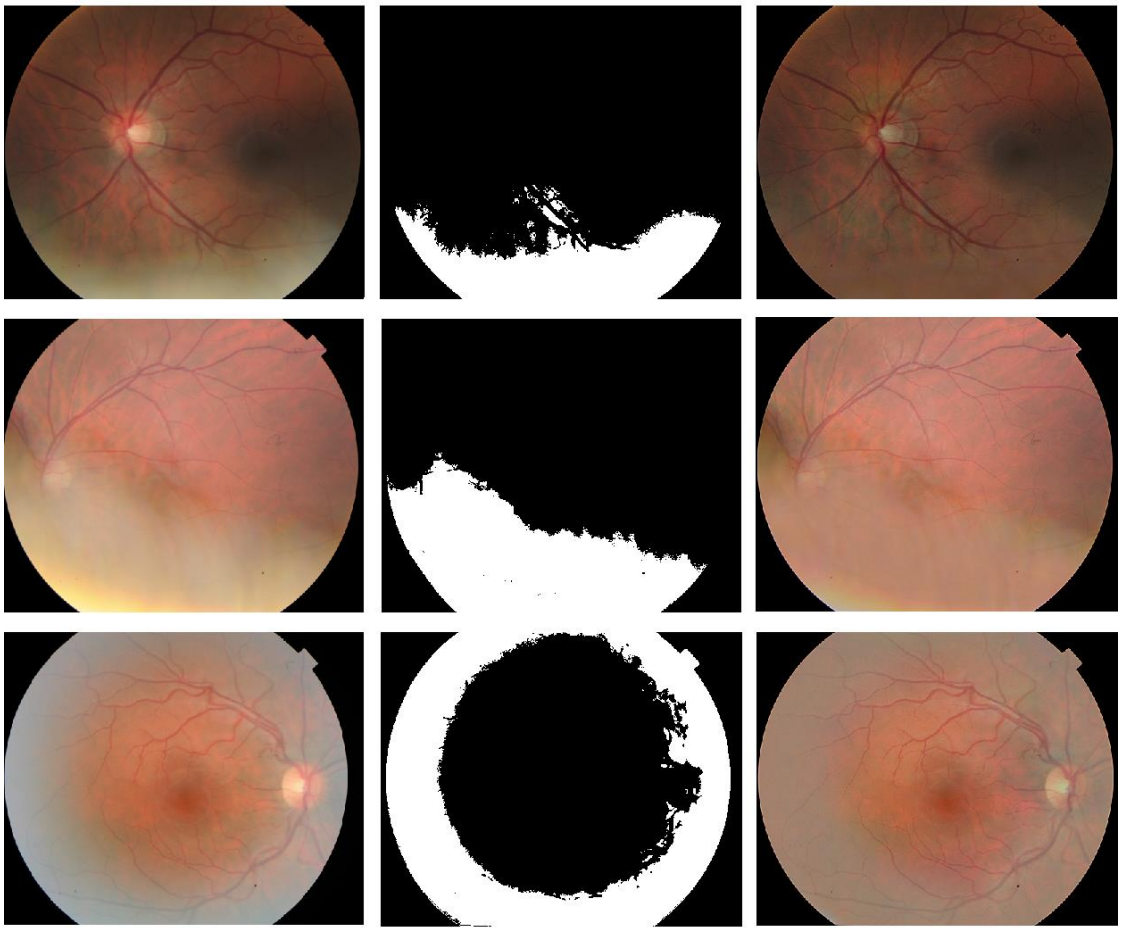

Figure 6.21 Result from the artifact removal strategy on the fundus images acquired via fundus camera. In the left column, the images affected by artifact, in the middle one the binary map of the pixels identified by the classifier as affected by artifacts and the right column the cleaned-up images.

Following the steps described in the previous chapter, for each image the pixels affected by artifacts were identified via the SVM binary classifier trained on the first half the dataset, their value subtracted to the mean value of the corresponding ROI and then used to fit a 3D surface model that recreated the additive contribution of the artifact. The image subtraction between the image affected by artifact and the estimated artifact contribution was then performed, finishing with an image sharpening step. Some example of the result of the artifact clean-up are shown in **Figure 6.21**. In particular, **Figure 6.22** offers a close-up visualisation of the textural components improvement after the implementation of the artifact removal strategy.

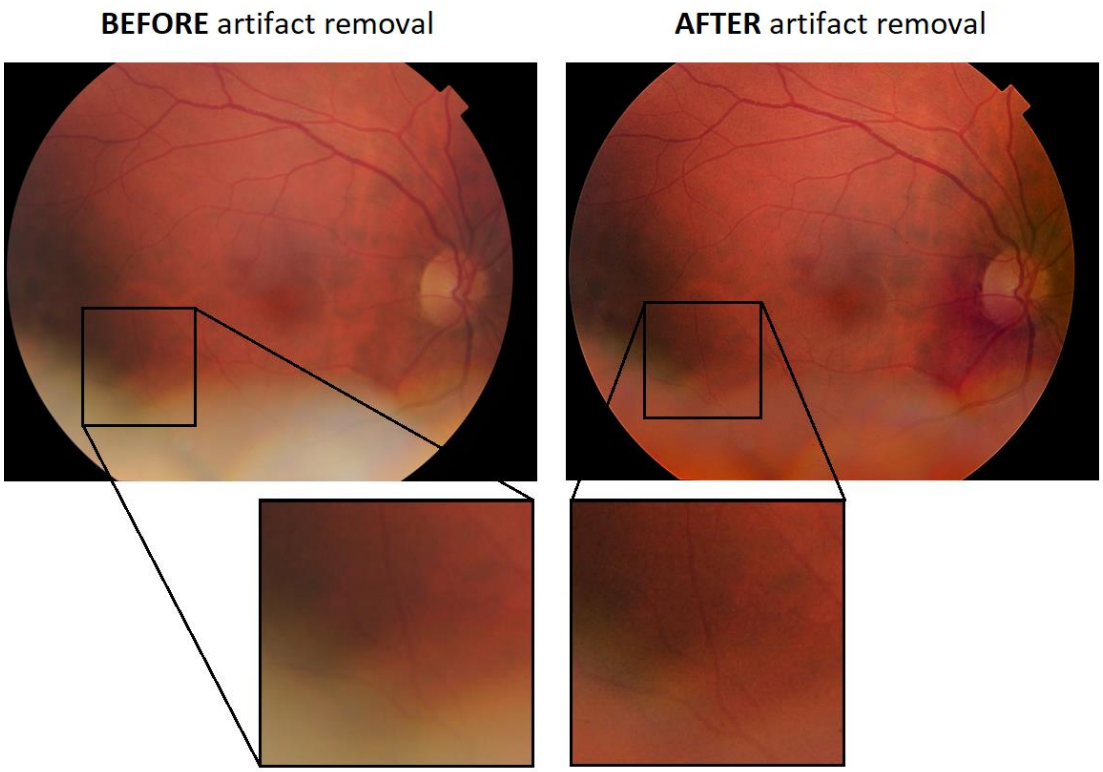

Figure 6.22 Enlargement of some retinal vessel of the peripheral macular area. In the left image, the contrast of the blood vessels is reduced by the artifact, while in the right image the artifact removal procedure has restored some visibility.

6.4.1 IMAGE QUALITY IMPROVEMENT EVALUATION

The improvement of the textural content was measured via Haralick and specific textural features, in particular:

- Energy - gives an indication about the quantity of information within an image. Therefore, the higher the energy of an image the higher is the information content.
- Entropy - measures the randomness of an image. When the value of all the pixels of the image are maximally random, entropy has its highest value. In other words, images with low entropy has more correlated elements (textural features) than images with high entropy.
- Blood vessel density (BVD) – it is a measure of the quantity of pixels that belongs to the blood vessels in relationship to the total amount of pixels in the ROI. This is determined via segmentation of the blood

vessel and the creation of a binary map where a value equal to 1 corresponds to those pixels that belong to the blood vessel and 0 is assigned to the background, as described in **Chapter 3** and **Chapter 4**.

From **Figure 6.23** to **Figure 6.25** the value of energy, entropy and BVD is shown per each image affected by artifact before and after the artifact removal process.

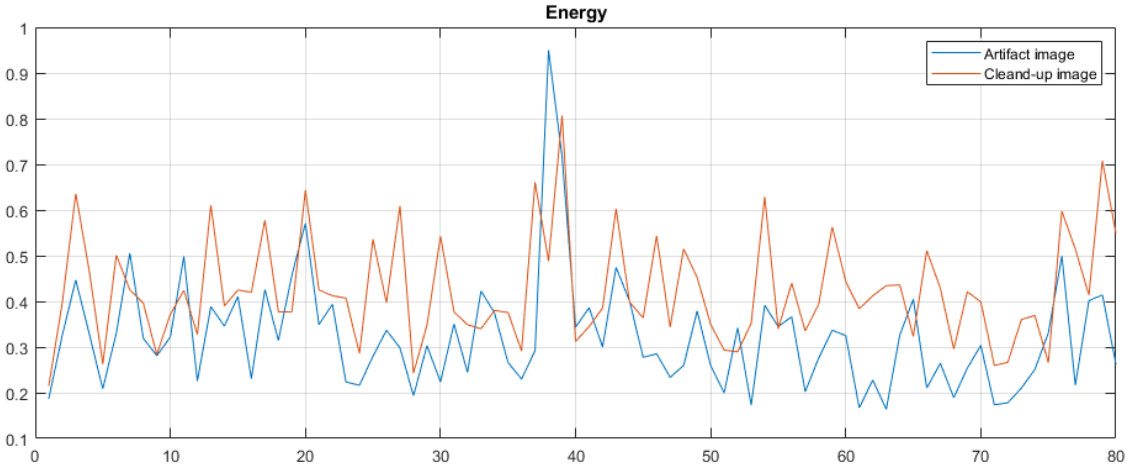

Figure 6.23 Comparison between the energy measured in the images affected by artifacts (blue line) and the same images after the artifact removal process (orange line) for the retinal images acquired using the fundus camera.

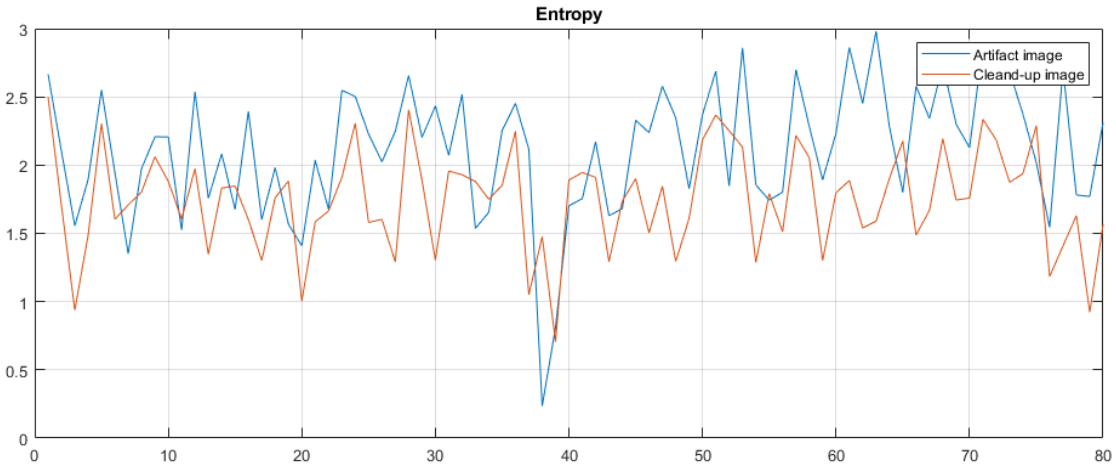

Figure 6.24 Comparison between the entropy measured in the images affected by artifacts (blue line) and the same images after the artifact removal processing (orange line) for the retinal images acquired using the fundus camera.

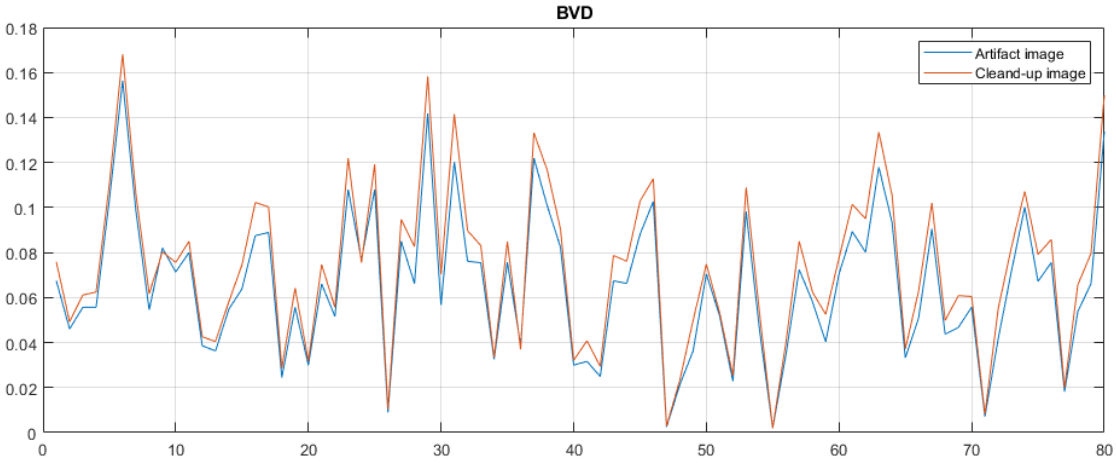

Figure 6.25 Comparison between the BVD measured in the images affected by artifacts (blue line) and the same images after the artifact removal processing (orange line) for the retinal images acquired using the fundus camera.

Table 6.1 Statistical descriptors selected to verify the improve of the textural information of the retinal images after the artifact removal process.

Imaging Device	Stat. Descriptor	Retinal image	Mean Value	Std. Deviation	Improvement
Fundus Camera	Energy	Artifact	0.3224	0.1240	+23.8%
		Cleaned-up	0.4230	0.1178	
	Entropy	Artifact	2.1129	0.3937	-17.4%
		Cleaned-up	1.7455	0.3740	
	BVD	Artifact	0.0653	0.0323	+11.2%
		Cleaned-up	0.0735	0.0357	

In **Table 6.1** the mean value and the standard deviation of energy, entropy and BVD are listed. Overall, energy and BVD improved and Entropy is reduced, as expected in images where the textural content increases. In particular, the BVD values shown that the quantity of detectable textural information, e.g. for blood vessel segmentation, is increased by more than 11%, as also shown in **Figure 6.26**.

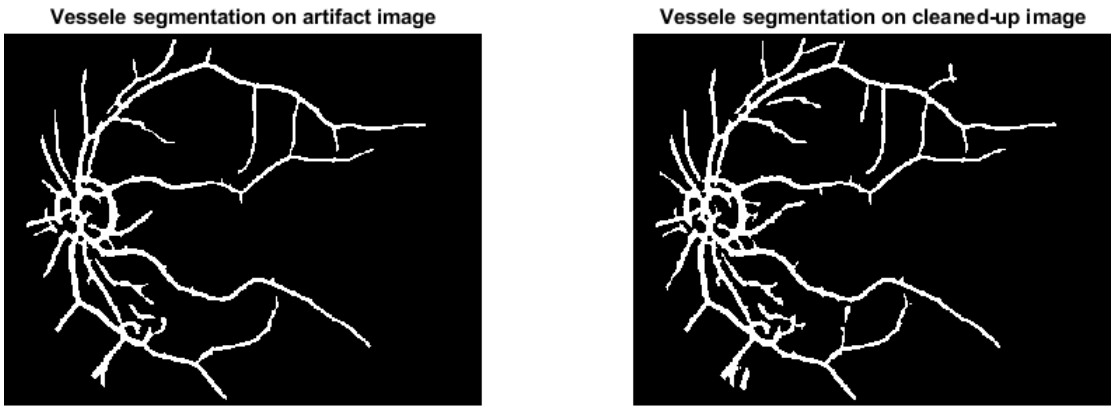

Figure 6.26 Comparison between the results of vessel segmentation obtained via matching filters technique on the image affected by artifact (left) and the same image after clean-up (right). More vessel could be segmented using the same segmentation parameters

6.5 COMPUTATIONAL PERFORMANCE

The most computational demanding step of the artifact removal strategy is the surface fitting process of the distortion pattern. In particular, the number of points chosen for the surface fitting has a direct impact on the computational time. The artifact model, in fact, is shaped around a set of pixel values selected from the image obtained by the pixel-by-pixel subtraction between the poor quality image and the registered good quality counterpart in those areas where there are no retinal features, **Figure 6.27**. As stated in the methods section, these points are sampled uniformly across the whole ROI. The selection of the minimum number of points to fit properly the surface was empirically established to be at least 0.4% of the total number of points. Giving the average number of non-zero pixels on the ROI is around 100000, the average set of points sampled was around 400 for each image.

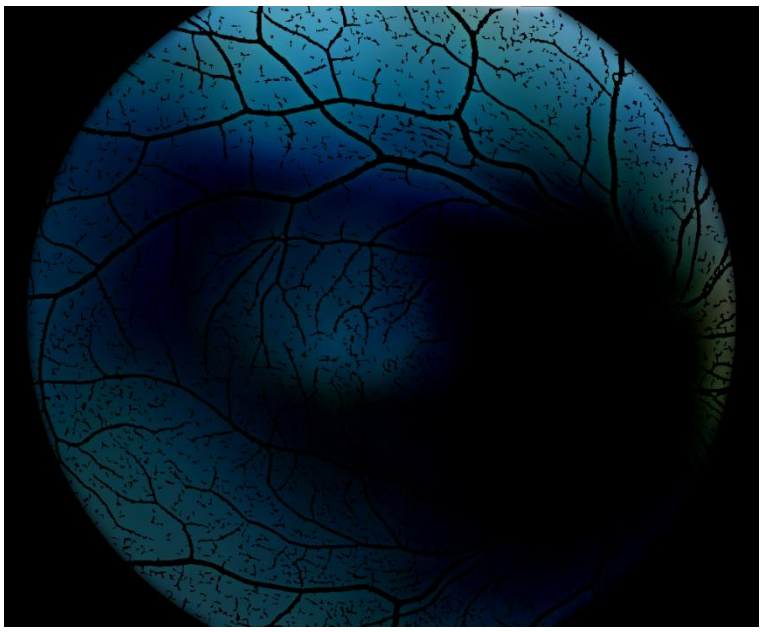

Figure 6.27 Result from the subtraction between the poor quality image and the clinical standard quality counterpart multiplied by the binary map to exclude of the retinal features.

6.5.1 PROCESSING TIME

The Matlab script was built and tested on a Window 10 SO, 8GB of RAM laptop, mounting an Intel 64 processor (core i7-7700HQ @ 2.80GHz), running 4 physical cores and 8 logical cores, 4 of which used in the computation. The digital format and size of the retinal images from CORD database and from the artifact simulator are:

- Fundus camera images – JPEG format, 3216 x 2136 pixels (12 of the 50 images selected for the image clean-up are 4288 x 2848 in size. They were resized to 3216 x 2136) (~2MB each).
- Simulated artifact images - JPEG format, 1832 x 1797 pixels (~1MB each).

The relation between the number of points (in percentage of the ROI) selected from the ROI for the surface fitting and the processing time for the biharmonic model fitting and the surface creation is shown in **Figure 6.28** and **Figure 6.29**.

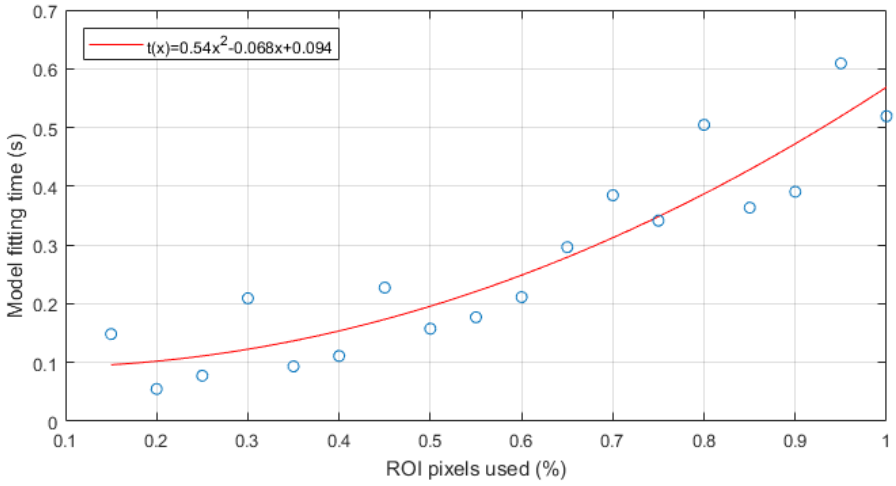

Figure 6.28 Model fitting time vs percentage of number of pixel of the ROI considered.

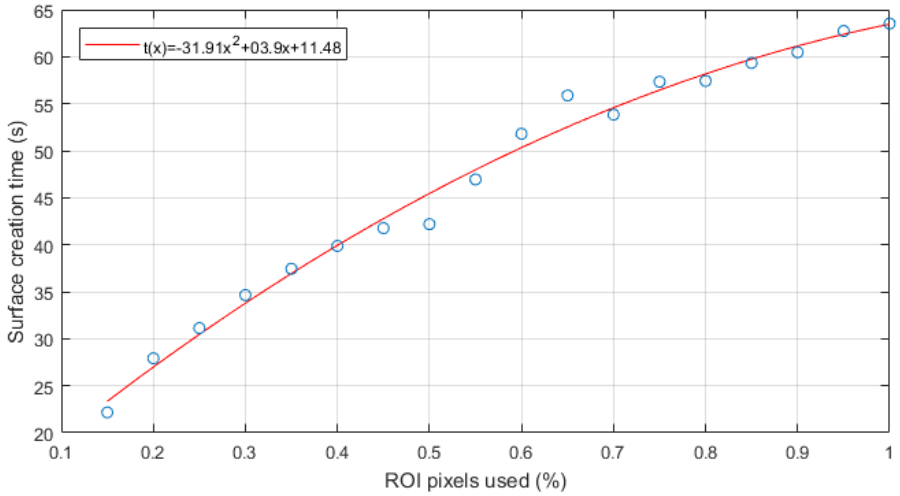

Figure 6.29 Surface creation time vs percentage of number of pixel of the ROI considered.

The average time of the principal computational steps is listed in **Table 6.2**. The artifact surface fitting time is the sum of the surface modelling and the surface creation, and was evaluated considering the 0.4% point of the ROI.

Table 6.2 – Mean processing time per each computational step.

Processing step	Time (s)
Image registration	1.19
Binary map creation	4.13
Artifact surface fitting	32.71
Image sharpening	3.86

CHAPTER 7. DISCUSSION AND CONCLUSION

7.1 QUALITY IN RETINAL IMAGING

As highlighted from the literature review, there is not a unique way to define quality in retinal imaging diagnostic. Many factors contribute to classify an image as useful or not for the clinical assessment: different imaging techniques, different diagnostic methods, different anatomical features under examination, and so on. Moreover, some cognitive mechanisms related to the visual perception play a not fully understood role in this. Experience, memory and contextual information are always used by the clinician to draw connections between what he/she is seeing in the image and the health status of the eye.

On the other hand, what also emerges from the literature is that the texture of the main retinal features (optic disc, vessels, exudates, etc.) act as information carriers. Despite no clinical evaluation having been done at this stage to corroborate such connection, the wide production of image processing techniques designed to identify and extract retinal features suggests that the visibility of the textural content is of primary importance. This is why the artifact removal algorithm, developed in this work, was specifically designed to improve the visibility of some of the main textural anatomical features of the retina (blood vessels and ONH).

Dealing with digital images, the possible approach to objectively quantify the textural content is to calculate statistical parameters out of the digital value of the pixels. Such a technique has been widely documented in the field, with many works converging in the use of features such as entropy, energy or contrast, to quantify the level of detail in an image or how “sharp” such details are. In this regard, one of the major findings of this work has been the identification of those statistical figures that varies the most when measured

on images with artifacts in comparison with the same image without artifacts and the creation of an image quality classifier based on such features which is completely agnostic with respect to the diagnostic process. This was possible also thanks to CORD, the comprehensive ophthalmic database developed within this research work. What resulted from the statistical feature classification, via NCA algorithm, was that features such as entropy and energy differ between adequate and inadequate quality in retinal imaging, as expected. What was less predictable is that even histogram features, like mean value or IQR can also be used as quality classifiers if evaluated on specific colour channels of the image.

In conclusion, a new agnostic image quality classifier based on objective statistical features was developed and tested on CORD. Although more work needs to be done to better understand how these statistical features are correlated with the kind of artifact of the image or with different characteristics of the eye under examination (for instance, when the eye pigmentation is darker some statistical features are more robust than others), this approach offers a starting point that can be implemented for future works.

7.2 COMPREHENSIVE OPHTHALMIC RESEARCH DATABASE

At the present, CORD represents a novelty in the panorama of the publicly available ophthalmic databases. For the first time, within a single online repository, a user can find, for each eye, the comprehensive geometric, optical and functional description, along with images of the front and back of the eye acquired using the majority of the imaging techniques employed in clinical diagnostic.

Such a comprehensive set of information can be used as a didactic and training tool for ophthalmologists and operators in the ophthalmic field in general, but it is in the medical image processing that this database expresses its full potential. CORD, in fact, was specifically structured and designed to aid the development of computer aided diagnostic tools. The multimodal images (and the information about the device setting used to acquire them) and the ophthalmic related measurements, are arranged and labelled to be easily

cross referenced. This simulates the same strategy adopted by clinicians during the diagnostic process. For instance, when assessing glaucoma, the combination of field of view test, slit lamp examination, IOP, OCT images and fundus images is used to formulate the diagnosis (Thomas and Parikh, 2006). Similarly, macular degeneration is assessed by testing the field of view, and imaging the retina via OCT and fundoscopy (Cook,Patel and Tufail, 2008), or again cataracts are diagnosed via field of view test, biometry, corneal topography and OCT (Kenneth CS Fong and Malhotra, 2008). Such process allows the clinician to have different sources of information that can be cross correlated to perform a more robust assessment of the pathological condition. Databases with large multi-modal data like CORD are therefore the elective tools of machine learning techniques, like the one used in this thesis. But even more classic imaging techniques, such as thresholding and segmentation, can take advantage of different imaging modalities. ONH segmentation, for instance to find the ratio between OD and OC, can be improved by using images coming from OCT scans. The problem of 2D fundus images is the limited information with respect to the third dimensionality of the anatomical features' morphology, like at the boundary between OD and OC, which instead can be more easily identified via 3D scan (**Figure 7.1**).

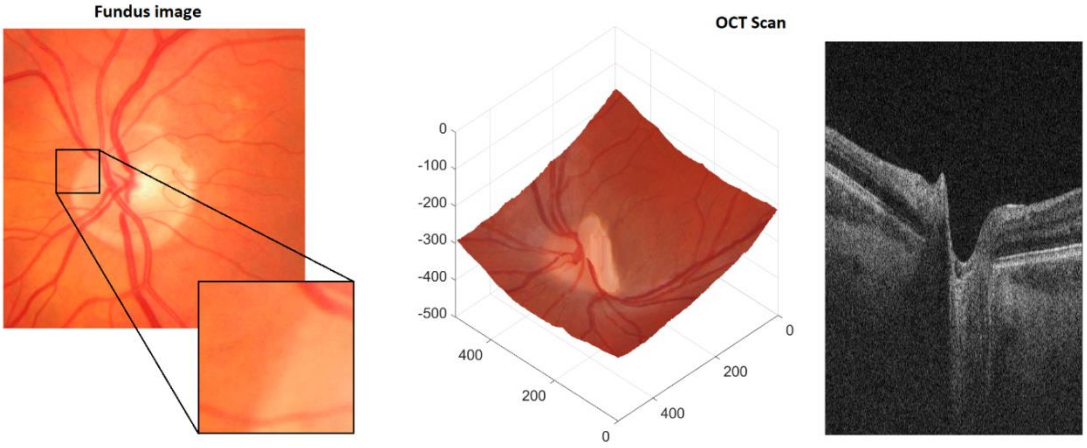

Figure 7.1 Example of a classic problem in retinal imaging (detection of OD and OC boundaries). The boundary between the OD and OC is somehow fuzzy and it's difficult to establish a univocal threshold. With the help of the 3D prospective from the OCT scan this operation can be more objective.

The other novelty is the systematic inclusion of fundus images affected by common artifacts, along with the clinical quality image counterpart. This offers some samples for image filtering and noise reduction strategies and an objective ground truth for algorithmic performance evaluation and improvement. This unique feature of CORD was massively exploited by this research work, yet only just scratching the surface of its real potential though. In fact, much work can be done on understanding how the contextual characteristics (e.g. device setting, subject pigmentation) impact on the formation of quality distortion in fundoscopy. All these research paths are now enabled by this database, opening the way for a better understanding of such phenomena on image quality and developing new methods that can take advantage of this knowledge.

Finally, the database structure is the other enabling factor of CORD. The data collection workflow described and provided in the repository allows other researchers to data with similar characteristics. This will potentially enlarge CORD in the future, and we hope will stimulate the creation of similar platforms that can be used consistently and, possibly, cross-referenced, establishing a *de facto* standard for comprehensive database collection and sharing.

In conclusion, this sizable work has led to the creation of a new open source ophthalmic dataset, aimed to enabling other research groups and clinicians to develop computer vision solutions, training programmes and more. To the best of our knowledge, this is the first database to include, for each eye, the most complete clinical description (images, videos obtained using multiple techniques and modalities) and the information of the parameters under which such data have been produced. It is also the only database to include artifact examples along with clinical image counterparts and with the information regarding the subject that are known to have an impact on image specifics.

7.3 PARAMETRIC MODEL OF ARTIFACTS

The lack of examples of artifacts in retinal databases was also tackled with the development of a quality distortion simulator which, starting from good

quality images, can replicate some of the classic artifacts in fundoscopy. Such parametric model was conceived as an image processing tool, rather than as a new bio-physical model for the description of the interaction between the light and the eye. In fact, the strong physical assumptions under which the model was developed, and the algorithmic strategies adopted, do not add anything more to what is already available in terms of scattering, absorption and reflection modelling in the field. Nonetheless, while several physical models have been developed to describe the effect of pathological conditions (e.g. myopia, cataract) on the visual perception of the patient, no model that simulates the formation of the retinal image from the device prospective capable of generating quality distortions has been identified.

Computer programs that reproduce blurring effects and artifacts are available for graphic and rendering purposes (e.g. in the field of photography and cinema), where specific filers are applied on top of the images to obtain the desired effect. On the contrary, the artifact simulator developed in this thesis creates a physically-compliant distortion applied directly to the layer where such distortion is supposed to be generated. This gives more control on how the distortion is created, relating it to the fundamental mechanisms that generate the distortion in the first place, with the possibility to change specific key parameters of the model (e.g. subject's age or pigmentation, percentage of light absorption or severity of uneven illumination), and see how those parameters, although in a simplified way, impact on image quality.

This model has also led to the identification of the most suitable algorithmic strategy for the artifact mitigation process. In fact, the way the artifacts are generated with this model has suggested an additive nature of the artifact contribution to the retinal image.

The modularity and the parametric nature of the model allow possible users to freely readapt some of the elements of its structure or implement it with more modules. Moreover, simulating the distortion caused by artifact from the imaging device perspective can be useful for ophthalmic device developers and for clinicians, allow them to develop techniques or strategies to

compensate them, be it digitally or through compensation of the core artifact mechanisms.

7.4 IMAGE CLEAN-UP STRATEGY

The mitigation of the distortion caused by artifact was achieved in the dataset of images selected for the test. In particular, the success of the clean-up was proved by the increased capacity of the vessel segmentation algorithm, selected to evaluate the BVD, to identify more vessels. In the field, this is one of the first attempts to build an algorithm to reduce artifacts in fundoscopy. The majority of the efforts in the literature focus of the identification of image quality classifier, to label image as assessable or not, bypassing the problem of retrieving information from degraded images. This because the variety and the different severity of the distortions caused by artifacts make this task particularly difficult. Here, thanks to CORD and to the modelling of artifacts, this problem was tackled not by designing the clean-up algorithm around a specific characteristic of the artifact, but by extracting the knowledge of which elements of the image make it a “good” image.

The image segmentation techniques available in the field mostly rely on the *a priori* knowledge of the retinal feature they are designed to extract (e.g. Gaussian cross-sectional profile of the vessels, circularity of the OD). Similarly, noise filtering techniques exploit the knowledge of the characteristics of the noise itself to be able to extract it from the image. All these approaches introduce some form of bias in the resulting image, as they work more efficiently where the feature has the characteristic predicted, overlooking the feature where such characteristics are more variable. This, per se, can lead to a loss of valuable clinical information. Such loss is acceptable when the clinical assessment focuses on a specific feature or a specific pathology, because the advantage of enhancing those features over the others is higher than the disadvantages. In a more general scenario however, where for instance the clinician wants to check the general health of the retina, or when there is no previous suspicion of pathological conditions, such loss can prevent valuable information from being detected. For this reason, the approach followed by this

work aimed to use as few elements about the features as possible. In fact, the pixel classifier uses only the knowledge of how pixels of retinal images should look like, as opposed to pixels of artifacts.

In conclusion, the image clean-up strategy developed in this work was able to classify pixels as affected / not affected by artifact distortions using a machine learning technique (trained regularised SVM) based on the statistical features previously identified. A surface fitting algorithm was then used on the group of pixels affected by artifacts and then subtracted to the original image. The results show an increase in the textural content, in particular, a drop of the entropy by 17.4% and an increase in the energy and the BVD of the image by 23.8% and 11.2% respectively. This improvement has a direct impact on image processing techniques, such as blood vessels segmentation, with an increase of 11% of the blood vessel detected on cleaned-up images, with respect to the original ones. This is the very first example in the literature of a retinal image quality retriever which is agnostic to the features to be retrieved, i.e. not focused on improving a specific image processing technique (therefore the typology of diagnostic assessment). In other words, rather than eliminating the “non-feature” elements of the images on the basis of an assumption of the feature characteristic properties, it positively identified the artifacts, improving the overall textural characteristics of the image, hence retrieving, as much as possible, the overall clinical information content of the image.

The suppression of the distortion by simple image subtraction can be improved in the future. In fact, this was one of the simplest approaches, which was derived by the artifact simulator. However, while the dataset of training images grows, more information on the specific identity of distortions can be stored in the classifier. This ideally can lead to the definition of a differentiated artifact suppression strategy based on the kind of artifact, for instance, or on its severity.

7.5 REVIEW OF THE AIMS OF THE STUDY

The challenge that, in the first place, triggered this PhD project was the idea of developing a pixel classification model able to identify the pixels

affected by quality distortion without any knowledge of the distortion per se, but only knowing how usually a clinically-assessable retinal image looks like. In this way, artifact removal strategies could be applied only where the distortion acts, leaving the clinical information as intact as possible. This was in the context of helping emerging mHealth retinal imaging solutions to increase the rate of clinical quality images acquired in the field, and more generally to improve the image collection throughput and the overall effectiveness of population screening programmes.

To achieve this objective, an extensive research around the definition of quality and, in particular, around the identification of those elements that make a retinal image assessable was done. Thanks to CORD and to the artifact model produced within this research work, a big step forward was possible with respect to what has so far been identified in the field. In fact, while texture and contrast are still crucial in image processing (image segmentation and filtering mostly rely on these parameters), these not always are a sign of high quality in fundus images. The NCA analysis on the statistical features performed on the images affected by artifact and the CSQ counterparts highlighted a more complex correlation between texture, histogram characteristic of the pixels and Haralick features (energy, entropy, etc.). This was explored throughout many colour spaces, so as to explore how different organisation of the intensity level of the pixels impacted in quality assessment. In this work, such research was primarily focused on identifying a way to assess quality objectively, based on classic characteristics of CSQ images.

The second objective was to establish the algorithmic criteria to be used in the artifact removal strategy. With respect to what is available in the field in terms of noise filtering, which usually exploit the *a priori* knowledge of the noise to work, here no artifact model was available. The development of the artifact simulator and the verification that the images obtained are comparable, in terms of statistical features, to the images affected by artifacts acquired during classic fundoscopy was used to identify the clean-up steps. The improvement of the image segmentation capability on the cleaned-up images are the proof that the overall textural content was improved. However, due to time limits, no

clinical test was performed at this stage. To better validate the clean-up strategy a quality evaluation performance should be tested by clinicians, for instance by manually segmenting the images and/or extracting actual diagnostic information, be it by trained clinicians or validated diagnostic software.

Thanks to these steps the main aim of this research work was tackled and partially achieved. In fact, while the pixel classification model has already an accuracy close to 90%, with the potential of growing as CORD or similar data sources grow, more work needs to be done on the artifact model. So far, fitting the distortion identified in the image to a biharmonic surface model has produced promising results. An example of artifact clean-up applied on an image obtained via smartphone is shown in **Figure 7.2**, where a low computational blood vessel segmentation is performed on both images without modifying the algorithmic parameters. Although premature, given the low field of view and low resolution of such images, this example gives an idea of what this clean-up strategy can do at present, namely improve feature segmentation, and what still need to be done, namely improving a more subjective visual appearance, that does not render justice to the improvement in information retrieval.

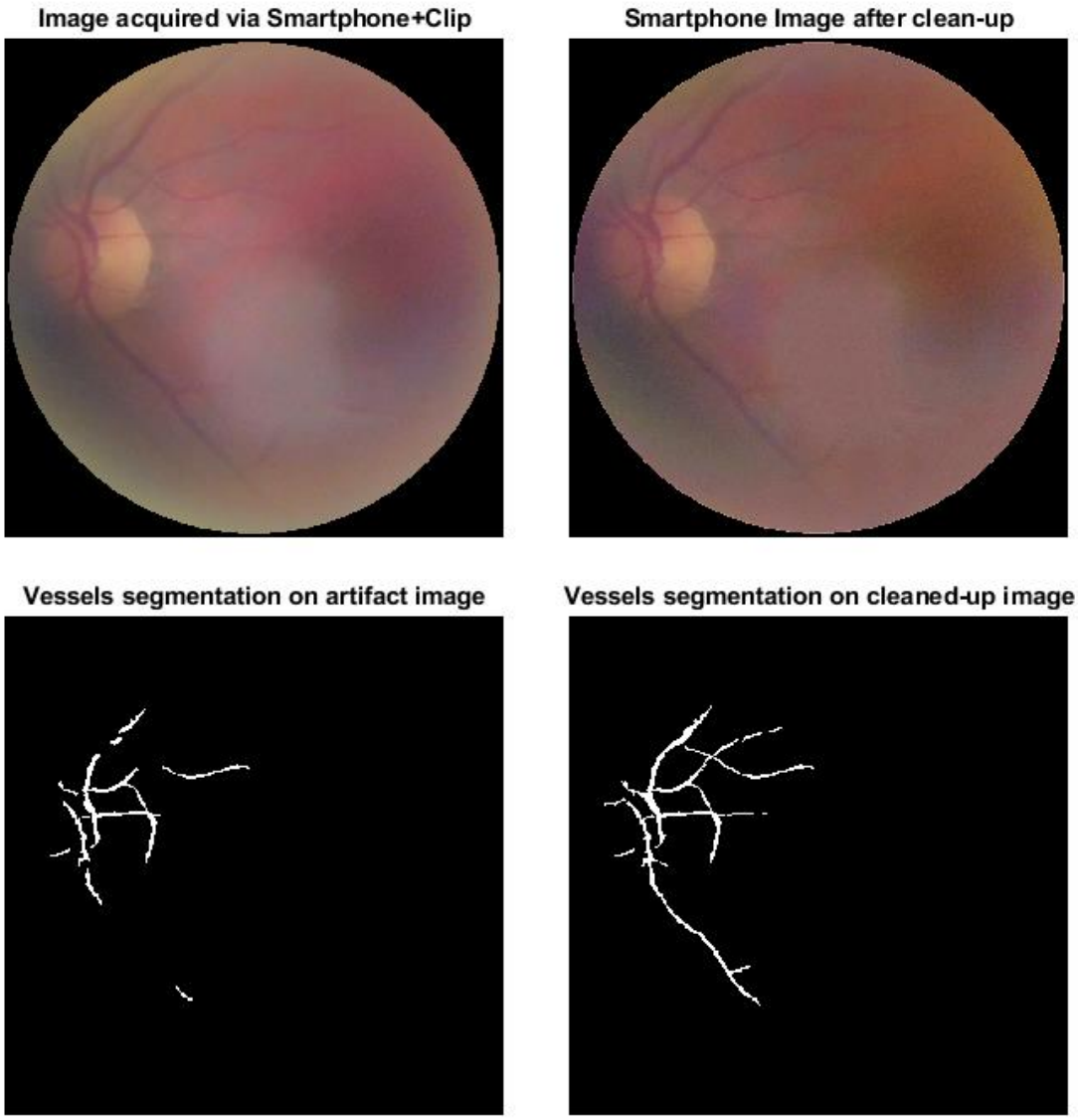

Figure 7.2 Comparison between a retinal image acquired using a smartphone clip on a low-resolution camera of a commercial smartphone (left column) and the same image after artifact mitigation (right column). The same blood vessel segmentation algorithm was used without modifying the segmentation parameters.

7.6 BENEFITS FOR THE CLINICAL WORKLOAD

Current reports on the percentage of images not usable for the final diagnosis in screening programmes is on the order of 20% (Yu *et al.*, 2012b, Teng,Lefley and Claremont, 2002, Liesenfeld *et al.*, 2000, S. Philip,Cowie and Olson, 2005, Scanlon *et al.*, 2003), or higher when the screening is in the field, like what is now happening in low-income countries in image acquisition via mHealth technology by minimally-trained operators.

For this reason, increasing the rate of images with adequate quality for automatic assessment can massively improve any clinical activity involving the collection of a large number of images. The advantage is not only economic (more usable images per hour of acquisition means lower costs for the health system), but also the effectiveness of screenings and their social perception and acceptance improve. Less time of acquisition means less stress for the patient. Less unusable images mean also less chances to be summoned again for more acquisitions. These aspects can all potentially impact on the general perception of the health service activity, and are very important when considering the effectiveness of a screening programme. In many settings, such as in low-income countries, where the welfare system has just started to reach those portions of the population previously isolated, it is extremely important to build trust and show the beneficial aspects of screening.

mHealth, and telemedicine in general, is aiming to bridge some of these gaps, shortening the distance between the patients and the health system not only in the low-income settings. Smartphones and tablets have already been successfully employed for fundus images collection in rural areas (Bastawrous *et al.*, 2016, Bastawrous,Giardini and Jordan, 2014) and in clinical practice (Livingstone *et al.*, 2019). We will assist in the near future to a partial transition of the clinical assessment, from the clinical premises to the patient's home. wide cellular network coverage and high resolution camera mobile devices are already a reality. In this perspective, the quality of the images, especially if not acquired by an expert, will have a big impact on the overall success of such transition. Clean-up strategies and more reliable quality evaluation algorithm will be therefore crucial.

7.7 RECOMMENDATIONS FOR FUTURE WORK

As previously mentioned, many implementations to the main outputs of this work are possible. In this study, the selection of the statistical descriptors of quality was limited to those commonly used to assess segmentation algorithm performance and general quality in digital imaging. However, many other textural descriptors have been developed in the field, in particular features

related to illumination and contrast (Pires Dias,Oliveira and da Silva Cruz, 2014, Remeseiro,Mendonca and Campilho, 2017, Yu *et al.*, 2012b). Therefore, pixel classification models based on other statistical descriptors should be considered for future implementations. Ideally, a catalogue of different textural descriptors should be optimally established for each specific diagnostic use (vessel segmentation, dark lesion detection, etc.).

The publication of CORD as open access database enables its usage as a versatile tool for the research community, particularly for projects involving the development of medical image processing, teaching aid and ophthalmic devices. The number of participants recruited for the study was kept at the minimum, in line with some of the most used publicly available database (DRIVE, REVIEW, HRF). This decision is the result of time and resource management considerations, given the volume of data to acquire per each eye and the use of multiple ophthalmic devices during clinic hours of a running eye clinic. This first version of the database, however, represents only the first stage. The whole structure of the dataset is modular as it is its labelling system, which can guarantee unique identification up to two million eyes. The implementation of CORD can be done by any research groups with access to similar resources, without limiting the collection to a specific research purpose or geographical area. This is possible thanks to detailed metadata included in the database, providing the data acquisition information (devices used, set up, ambient luminance, etc.). The whole structure of the dataset is modular as it is its labelling system, which can guarantee unique identification up to two million eyes. Accordingly, the future steps will involve firstly the publication of the work in a suitable journal. Even if this database is already openly accessible and downloadable online, this will give more visibility to CORD amongst the research community, advocating the usage of its data content for image processing research and more, such as in the recent EMBC conference (Coghill *et al.*, 2019). Secondly, the enlargement of the dataset will be pursued, potentially in collaboration with other research groups, given that the full description of the data collection process, the labelling system and the data structure are openly available.

The parametric model of retinal artifacts was developed to generate controlled distortions on CSQ retinal images. The model can also be used to simulate the effect of scattering, and similar phenomena, caused by pathological conditions (e.g. cataract or corneal opacification) on the final image. The parameters of the model can be modified (absorption, PSF, etc.) or implemented with more complex steps, to be used to study the interaction between the light and the eye, for the production of *ad hoc* distortions for image filtering technique development and for the optimization of image sensors, devices or acquisition technique able to robustly perform in wide range of different conditions. Moreover, the indirect use of this model can be potentially use to extract clinical parameters from pathological images. In fact, starting from an image affected by distortion, for instance caused by cataract, it would be possible to objectively quantify the parameters that have determined the blurring, effectively assessing the progress and/or the typology of cataract. In other words, theoretically this model can be used as a diagnostic tool.

Finally, the strategy developed in this work to mitigate the effect of artifacts and quality distortions on retinal images has shown promising initial results. However, though no formal analysis of the learning curve of the machine learning classifier has been performed, the dataset is small by any reasonable machine learning practice, and we have therefore good reason to believe that by adding more training data, and/or selecting a more performant machine learning algorithm than a simple SVM, is likely to lead to higher accuracy in pixel classification. Moreover, different surface fitting models can be used to reconstruct the distortion contribution, for instance circular symmetrical models. Given the geometrical characteristics of the optics of the imaging device and the transparent structures of the eye (close to spherical or elliptical surface), it is likely that the spline model used in this thesis, effectively a convenience choice, may be better replaced by assuming a spatial distribution described as a combination of modes, such as the more traditional Bessel, Laguerre-Gauss, Hermite-Gauss function sets, or specifically optimised eigenfuctions, such as e.g. traditionally done in face analysis (Sirovich and Kirby, 1987).

References

Abramoff, M.D., Garvin, M.K. and Sonka, M. (2010) 'Retinal imaging and image analysis'. *IEEE Rev Biomed Eng,* 3 169-208.

Adal, K.M. *et al.* (2015) 'Accuracy assessment of intra- and intervisit fundus image registration for diabetic retinopathy screening'. *Invest Ophthalmol Vis Sci,* 56 (3), pp. 1805-1812.

Aguila-Carrasco, A.J. *et al.* (2017) 'The effect of aberrations on objectively assessed image quality and depth of focus'. *J Vis,* 17 (2), pp. 2.

Akram, M.U. and Khan, S.A. (2013) 'Multilayered thresholding-based blood vessel segmentation for screening of diabetic retinopathy'. *Engineering with computers,* 29 (2), pp. 165-173.

Al-Diri, B. *et al.* (2008) Published. 'A reference data set for retinal vessel profiles'. *Engineering in Medicine and Biology Society,* 2008. pp.2262-2265.

Al-Rawi, M., Qutaishat, M. and Arrar, M. (2007) 'An improved matched filter for blood vessel detection of digital retinal images'. *Computers in Biology and Medicine,* 37 (2), pp. 262-267.

Archana, D. *et al.* (2015) Published. 'Detection of abnormal blood vessels in diabetic retinopathy based on brightness variations in SDOCT retinal images'. *2015 IEEE International Conference on Engineering and Technology (ICETECH),* 2015. IEEE, pp.1-4.

Arefi, H. *et al.* (2009) Published. 'Automatic generation of digital terrain models from cartosat-1 stereo images'. 2009. ISPRS.

Armfield, N.R., Gray, L.C. and Smith, A.C. (2012) 'Clinical use of Skype: a review of the evidence base'. *Journal of Telemedicine and Telecare,* 18 (3), pp. 125-127.

Artal, P. *et al.* (1993) 'Effects of aging in retinal image quality'. *JOSA A,* 10 (7), pp. 1656-1662.

Arun, C. *et al.* (2009) 'Long-term impact of retinal screening on significant diabetes-related visual impairment in the working age population'. *Diabetic Medicine,* 26 (5), pp. 489-492.

Arzberger, P. *et al.* (2004) 'Science and government. An international framework to promote access to data'. *Science,* 303 (5665), pp. 1777-1778.

ASRS *Retina Image Bank®.* Available at: https://imagebank.asrs.org/home?path=%2F.

Atchison, D.A. and Smith, G. (2000) *Optics of the human eye.* Butterworth-Heinemann.

Ayatollahi, H. *et al.* (2017) 'Teleophthalmology in practice: lessons learned from a pilot project'. *The open medical informatics journal,* 11 20.

Azzopardi, G. *et al.* (2015) 'Trainable COSFIRE filters for vessel delineation with application to retinal images'. *Medical image analysis,* 19 (1), pp. 46-57.

Bachmann, M.O. and Nelson, S.J. (1998) 'Impact of diabetic retinopathy screening on a British district population: case detection and blindness prevention in an evidence-based model'. *Journal of Epidemiology & Community Health,* 52 (1), pp. 45-52.

Bala, M.P. and Vijayachitra, S. (2015) 'Extraction of retinal blood vessels and diagnosis of proliferative diabetic retinopathy using extreme learning machine'. *Journal of Medical Imaging and Health Informatics,* 5 (2), pp. 248-256.

Bandura, A. (1977) 'Self-efficacy: toward a unifying theory of behavioral change'. *Psychological review,* 84 (2), pp. 191.

Bandura, A. (2001) 'Social cognitive theory: An agentic perspective'. *Annual review of psychology,* 52 (1), pp. 1-26.

Bartling, H., Wanger, P. and Martin, L. (2009) 'Automated quality evaluation of digital fundus photographs'. *Acta ophthalmologica,* 87 (6), pp. 643-647.
Basit, A. and Fraz, M.M. (2015) 'Optic disc detection and boundary extraction in retinal images'. *Applied optics,* 54 (11), pp. 3440-3447.
Bastawrous, A. *et al.* (2016) 'Clinical validation of a smartphone-based adapter for optic disc imaging in Kenya'. *JAMA ophthalmology,* 134 (2), pp. 151-158.
Bastawrous, A., Giardini, M.E. and Jordan, S. (2014) 'Peek: Portable eye examination kit. The smartphone ophthalmoscope'. *Investigative Ophthalmology & Visual Science,* 55 (13), pp. 1612-1612.
Beare, N.A. *et al.* (2006) 'Malarial retinopathy: a newly established diagnostic sign in severe malaria'. *The American journal of tropical medicine and hygiene,* 75 (5), pp. 790-797.
Belozubov, E., Vasil'ev, V. and Chernov, P. (2014) 'Use of Biharmonic Spline Interpolation for Decreasing the Errors of Smart Sensors'. *Measurement Techniques,* 57 (9), pp. 997-1003.
Benbassat, J., Polak, B.C. and Javitt, J.C. (2012) 'Objectives of teaching direct ophthalmoscopy to medical students'. *Acta ophthalmologica,* 90 (6), pp. 503-507.
Bengtsson, B. *et al.* (1997) 'A new generation of algorithms for computerized threshold perimetry, SITA'. *Acta Ophthalmol Scand,* 75 (4), pp. 368-375.
Bernardes, R., Serranho, P. and Lobo, C. (2011) 'Digital ocular fundus imaging: a review'. *Ophthalmologica,* 226 (4), pp. 161-181.
Bhuiyan, A. *et al.* (2014) 'Development and reliability of retinal arteriolar central light reflex quantification system: a new approach for severity grading'. *Investigative ophthalmology & visual science,* 55 (12), pp. 7975-7981.
Bidot, S. *et al.* (2013) 'Nonmydriatic retinal photography in the evaluation of acute neurologic conditions'. *Neurology: Clinical Practice,* 3 (6), pp. 527-531.
Biederman, I. (1987) 'Recognition-by-components: a theory of human image understanding'. *Psychological review,* 94 (2), pp. 115.
Blechinger, F. and Achtner, B. (2008) *Handbook of Optical Systems: Survey of Optical Instruments.* Wiley-VCH GmbH & Company KGaA.
Bobba, S. *et al.* (2017) 'Nature and incidence of severe limbal stem cell deficiency in Australia and New Zealand'. *Clin Exp Ophthalmol,* 45 (2), pp. 174-181.
Boettner, E.A. and Wolter, J.R. (1962) 'Transmission of the ocular media'. *Investigative ophthalmology & visual science,* 1 (6), pp. 776-783.
Bolster, N.M., Bastawrous, A. and Giardini, M.E. (2015) 'Towards a workflow driven design for mHealth devices within temporary eye clinics in low-income settings'. *Conf Proc IEEE Eng Med Biol Soc,* 2015 7312-7315.
Bolster, N.M. *et al.* (2014) 'How the smartphone is driving the eye-health imaging revolution'. *Expert Review of Ophthalmology,* 9 (6), pp. 475-485.
Bonevski, B. *et al.* (2014) 'Reaching the hard-to-reach: a systematic review of strategies for improving health and medical research with socially disadvantaged groups'. *BMC medical research methodology,* 14 (1), pp. 42.
Bourne, R.R. (2006) 'The optic nerve head in glaucoma'. *Community eye health,* 19 (59), pp. 44.
Brown, N. (1974) 'The change in lens curvature with age'. *Experimental eye research,* 19 (2), pp. 175-183.
Bruce, B.B. *et al.* (2013) 'Non-mydriatic ocular fundus photography and telemedicine: past, present, and future'. *Neuro-ophthalmology,* 37 (2), pp. 51-57.

Buades, A., Coll, B. and Morel, J.-M. (2005) Published. 'A non-local algorithm for image denoising'. *2005 IEEE Computer Society Conference on Computer Vision and Pattern Recognition (CVPR'05),* 2005. IEEE, pp.60-65.

Budai, A. *et al.* (2013) 'Robust vessel segmentation in fundus images'. *Int J Biomed Imaging,* 2013 154860.

Büttner, U. and Büttner-Ennever, J. (1988) 'Present concepts of oculomotor organization'. *Reviews of oculomotor research,* 2 3-32.

Care, o.E. Available at: https://odocseyecare.shop/.

Carmona, E.J. *et al.* (2008) 'Identification of the optic nerve head with genetic algorithms'. *Artif Intell Med,* 43 (3), pp. 243-259.

Casey, M.C. and Damper, R.I. (2010) 'Special issue on biologically-inspired information fusion'. *INFORM FUSION,* 11 (1), pp. 2-3.

Catrysse, P.B. and Wandell, B.A. (2002) 'Optical efficiency of image sensor pixels'. *J Opt Soc Am A Opt Image Sci Vis,* 19 (8), pp. 1610-1620.

Cavanagh, P. (2011) 'Visual cognition'. *Vision research,* 51 (13), pp. 1538-1551.

Chang, S.S., Maurice, D.M. and Ramirez-Florez, S. (1996) 'Quantitative measurement of corneal haze after myopic PRK'. *J Refract Surg,* 12 (3), pp. 412-416.

Chatziralli, I.P. *et al.* (2012) 'The value of fundoscopy in general practice'. *Open Ophthalmol J,* 6 4-5.

Cheng, J. *et al.* (2013) 'Superpixel classification based optic disc and optic cup segmentation for glaucoma screening'. *IEEE transactions on Medical Imaging,* 32 (6), pp. 1019-1032.

Chin, K.S. *et al.* (2013) 'Automatic fovea location in retinal images using anatomical priors and vessel density'. *Pattern Recognition Letters,* 34 (10), pp. 1152-1158.

CIE, C. (1978) 'Publication No. 15, Supplement Number 2 (E-1.3. 1, 1971): Official Recommendations on Uniform Color Spaces, Color-Difference Equations, and Metric Color Terms'. *Commission Internationale de L'Eclairage, Paris*.

Coghill, I. *et al.* (2019) Published. 'Synthetic stereo images of the optic disc from the CORD dataset'. *41st Annual International Conference of the IEEE Engineering in Medicine and Biology Society (EMBC),* 2019.

Cohen-Duwek, H. and Spitzer, H. (2019) 'A compound computational model for Filling-in processes triggered by edges: watercolor illusions'. *Frontiers in Neuroscience,* 13.

Commission, E. *Tagged Image File Format (TIFF).* Available at: http://ec.europa.eu/ipg/standards/image/tiff/.

CommonMark Spec. Available at: https://spec.commonmark.org/.

Cook, H.L., Patel, P.J. and Tufail, A. (2008) 'Age-related macular degeneration: diagnosis and management'. *Br Med Bull,* 85 127-149.

CORD Comprehensive Ophthalmic Research Database. (CORD 2019) Available at: https://cord.bioe.strath.ac.uk/ (Accessed: 30 August 2019).

Crete, F. *et al.* (2007) 'The blur effect: Perception and estimation with a new no-reference perceptual blur metric'. *Human Vision and Electronic Imaging Xii,* 6492.

Cummings, E. *et al.* (2002) 'Organisation of Services for Diabetic Retinopathy Screening'. *Health Technology Assessement Report,* 1.

D-Eye Available at: https://www.d-eyecare.com/en_GB/shop.

Dashtbozorg, B., Mendonça, A.M. and Campilho, A. (2015) 'Optic disc segmentation using the sliding band filter'. *Computers in Biology and Medicine,* 56 1-12.

Datahub Available at: https://datahub.io/docs/data-packages/csv.

Decencière, E. *et al.* (2013) 'TeleOphta: Machine learning and image processing methods for teleophthalmology'. *Irbm,* 34 (2), pp. 196-203.

Decencière, E. *et al.* (2014) 'Feedback on a Publicly Distributed Image Database: The Messidor Database'. *Image Analysis & Stereology,* 33 (3), pp. 231-234.
Devaraj, D. and Kumar, S.P. (2014) Published. 'Blood vessels segmentation with GUI in digital fundus images for automated detection of diabetic retinopathy'. *2014 International Conference on Contemporary Computing and Informatics (IC3I),* 2014. IEEE, pp.915-920.
DICOM. Available at: https://www.dicomstandard.org/current/.
The Discovery Eye Foundation. Available at: https://discoveryeye.org/layers-of-the-retina.
Drexler, W. and Fujimoto, J.G. (2008) *Optical coherence tomography: technology and applications.* Springer Science & Business Media.
eCommons: Cornell's Digital Repository. Available at: http://guides.library.cornell.edu/ecommons/formats.
England, N. (2018) *Screening Programme Pathway.* Available at: https://assets.publishing.service.gov.uk/government/uploads/system/uploads/attachment_data/file/493991/DES_-_revision_2.pdf.
Erler, N.S. *et al.* (2014) 'Optimizing structure-function relationship by maximizing correspondence between glaucomatous visual fields and mathematical retinal nerve fiber models'. *Invest Ophthalmol Vis Sci,* 55 (4), pp. 2350-2357.
Excellence, N.I.f.C. (2001) 'Diabetic Retinopathy-Early Management and Screening'. *National Institute for Clinical Excellence (NICE), London, United Kingdom*.
Eye7 Eye Hospitals. Available at: https://www.eye7.in/cornea/.
Fernandez-Buenaga, R. *et al.* (2018) 'Twenty years of limbal epithelial therapy: an update on managing limbal stem cell deficiency'. *BMJ Open Ophthalmol,* 3 (1), pp. e000164.
Flanagan, D. (1993) 'Current management of established diabetic eye disease'. *Eye,* 7 (2), pp. 302.
Fleming, A.D. *et al.* (2010) 'Automated grading for diabetic retinopathy: a large-scale audit using arbitration by clinical experts'. *British Journal of Ophthalmology,* 94 (12), pp. 1606-1610.
Fong, D.S. *et al.* (2004) 'Retinopathy in diabetes'. *Diabetes care,* 27 (suppl 1), pp. s84-s87.
Fong, K.C. and Malhotra, R. (2008) 'Assessment of the patient with cataract'. *Cataract.* Elsevier, pp. 17-32.
Frangi, A.F. *et al.* (1998) Published. 'Multiscale vessel enhancement filtering'. *International conference on medical image computing and computer-assisted intervention,* 1998. Springer, pp.130-137.
Fraz, M.M. *et al.* (2012a) 'Blood vessel segmentation methodologies in retinal images--a survey'. *Comput Methods Programs Biomed,* 108 (1), pp. 407-433.
Fraz, M.M. *et al.* (2012b) 'Blood vessel segmentation methodologies in retinal images–a survey'. *Computer methods and programs in biomedicine,* 108 (1), pp. 407-433.
Fraz, M.M. *et al.* (2015) 'QUARTZ: Quantitative Analysis of Retinal Vessel Topology and size–an automated system for quantification of retinal vessels morphology'. *Expert Systems with Applications,* 42 (20), pp. 7221-7234.
Frost, N.A. and Sparrow, J.M. (2001) 'The assessment of lens opacities in clinical practice: results of a national survey'. *Br J Ophthalmol,* 85 (3), pp. 319-321.
Fu, H. *et al.* (2018) 'Joint optic disc and cup segmentation based on multi-label deep network and polar transformation'. *IEEE transactions on medical imaging,* 37 (7), pp. 1597-1605.
Fuderer, M. (1988) 'The information content of MR images'. *IEEE Trans Med Imaging,* 7 (4), pp. 368-380.
Fukunaga, K. (2013) *Introduction to statistical pattern recognition.* Elsevier.

Fumero, F. *et al.* (2011) Published. 'RIM-ONE: An open retinal image database for optic nerve evaluation'. *2011 24th international symposium on computer-based medical systems (CBMS),* 2011. IEEE, pp.1-6.

Gagnon, M.-P. *et al.* (2015) 'm-Health adoption by healthcare professionals: a systematic review'. *Journal of the American Medical Informatics Association,* 23 (1), pp. 212-220.

Geisler, W. and Banks, M. (1995) *Handbook of Optics: Fundamentals, Techniques and Design.* McGraw-Hill, Inc.

Gholami, P. *et al.* (2018) '*Optical Coherence Tomography Image Retinal Database'*.

Giancardo, L. *et al.* (2012) 'Exudate-based diabetic macular edema detection in fundus images using publicly available datasets'. *Medical Image Analysis,* 16 (1), pp. 216-226.

Giardini, M.E. *et al.* (2014) Published. 'A smartphone based ophthalmoscope'. *2014 36th Annual International Conference of the IEEE Engineering in Medicine and Biology Society,* 2014. IEEE, pp.2177-2180.

Goatman, K.A. (2006) 'A reference standard for the measurement of macular oedema'. *British journal of ophthalmology,* 90 (9), pp. 1197-1202.

Goldbaum, M. *et al.* (1996) Published. 'Automated diagnosis and image understanding with object extraction, object classification, and inferencing in retinal images'. *Proceedings of 3rd IEEE International Conference on Image Processing,* 1996. IEEE, pp.695-698.

Goldberger, J. *et al.* (2005) Published. 'Neighbourhood components analysis'. *Advances in neural information processing systems,* 2005. pp.513-520.

Gonzalez, R.C. and Wintz, P.J.R., Mass., Addison-Wesley Publishing Co., Inc. (1977) *Digital image processing.*

Gonzalez, R.C. and Woods, R.E. (2007) *Image processing.*

Gravel, P., Beaudoin, G. and De Guise, J.A. (2004) 'A method for modeling noise in medical images'. *IEEE Trans Med Imaging,* 23 (10), pp. 1221-1232.

Grisan, E., Foracchia, M. and Ruggeri, A. (2008) 'A novel method for the automatic grading of retinal vessel tortuosity'. *IEEE Trans Med Imaging,* 27 (3), pp. 310-319.

Grossberg, S. (1997) 'Cortical dynamics of three-dimensional figure–ground perception of two-dimensional pictures'. *Psychological review,* 104 (3), pp. 618.

Grunfeld, E. (1997) 'Cervical cancer: screening hard-to-reach groups'. *CMAJ: Canadian Medical Association Journal,* 157 (5), pp. 543.

Gudbjartsson, H. and Patz, S. (1995) 'The Rician distribution of noisy MRI data'. *Magn Reson Med,* 34 (6), pp. 910-914.

Han, H.C. (2012) 'Twisted blood vessels: symptoms, etiology and biomechanical mechanisms'. *J Vasc Res,* 49 (3), pp. 185-197.

Hani, A.F.M. *et al.* (2014) Published. 'Denoising methods for retinal fundus images'. *2014 5th international conference on intelligent and advanced systems (ICIAS),* 2014. IEEE, pp.1-6.

Haralick, R.M., Shanmugam, K. and Dinstein, I.H. (1973) 'Textural Features for Image Classification'. *IEEE Transactions on Systems, Man, and Cybernetics,* SMC-3 (6), pp. 610-621.

Hart, R.W. and Farrell, R.A. (1969) 'Light scattering in the cornea'. *J Opt Soc Am,* 59 (6), pp. 766-774.

He, Y. *et al.* (2017) 'Retinal Image denoising via bilateral filter with a spatial kernel of optimally oriented line spread function'. *Computational and mathematical methods in medicine,* 2017.

Healey, G.E. and Kondepudy, R. (1994) 'Radiometric Ccd Camera Calibration and Noise Estimation'. *Ieee Transactions on Pattern Analysis and Machine Intelligence,* 16 (3), pp. 267-276.

Heneghan, C. *et al.* (2002a) 'Characterization of changes in blood vessel width and tortuosity in retinopathy of prematurity using image analysis'. *Medical image analysis,* 6 (4), pp. 407-429.

Heneghan, C. *et al.* (2002b) 'Characterization of changes in blood vessel width and tortuosity in retinopathy of prematurity using image analysis'. 6 (4), pp. 407-429.

Hernandez-Matas, C. *et al.* (2017) 'FIRE: fundus image registration dataset'. *Journal for Modeling in Ophthalmology,* 1 (4), pp. 16-28.

Hogan, M.J. (1971) 'Histology of the human eye'. *an Atlas and Textbook*.

Hoover, A., Kouznetsova, V. and Goldbaum, M. (1998) Published. 'Locating blood vessels in retinal images by piece-wise threshold probing of a matched filter response'. *Proceedings of the AMIA Symposium,* 1998. American Medical Informatics Association, pp.931.

Hsieh, J. (2009) *Image artifacts: appearances, causes, and corrections.*

Hu, Q., Abràmoff, M.D. and Garvin, M.K. (2013) Published. 'Automated separation of binary overlapping trees in low-contrast color retinal images'. *International conference on medical image computing and computer-assisted intervention,* 2013. Springer, pp.436-443.

Huang, G.-B., Zhu, Q.-Y. and Siew, C.-K. (2006) 'Extreme learning machine: theory and applications'. *Neurocomputing,* 70 (1-3), pp. 489-501.

IMAGERET Optimal Detection and Decision-Support Diagnosis of Diabetic Retinopathy. Available at: http://www.it.lut.fi/project/imageret/.

Issac, A., Sarathi, M.P. and Dutta, M.K. (2015) 'An adaptive threshold based image processing technique for improved glaucoma detection and classification'. *Computer methods and programs in biomedicine,* 122 (2), pp. 229-244.

ITU Available at: https://www.itu.int/en/mediacentre/Pages/2018-PR40.aspx.

James, A.P. and Dasarathy, B.V. (2014) 'Medical image fusion: A survey of the state of the art'. *Information Fusion,* 19 4-19.

Janssen, M., Charalabidis, Y. and Zuiderwijk, A. (2012) 'Benefits, Adoption Barriers and Myths of Open Data and Open Government'. *Information Systems Management,* 29 (4), pp. 258-268.

Jordan, K.C. *et al.* (2017) 'A review of feature-based retinal image analysis'. *Expert Review of Ophthalmology,* 12 (3), pp. 207-220.

Joshi, G.D. *et al.* (2010) Published. 'Optic disk and cup boundary detection using regional information'. *2010 IEEE International Symposium on Biomedical Imaging: From Nano to Macro,* 2010. IEEE, pp.948-951.

Kalezic, T. *et al.* (2018) 'Herpetic eye disease study: lessons learned'. *Curr Opin Ophthalmol,* 29 (4), pp. 340-346.

Kalloniatis, M. and Luu, C. (2007) 'The perception of color*'. Webvision: the organization of the retina and visual system [internet].* University of Utah Health Sciences Center, pp.

Kaschke, M., Donnerhacke, K.-H. and Rill, M.S. (2013) *Optical devices in ophthalmology and optometry: technology, design principles and clinical applications.* John Wiley & Sons.

Kaschke, M., Donnerhacke, K.-H. and Rill, M.S. (2014) *Optical Devices in Ophthalmology and Optometry.*

Katz, N. *et al.* (1989) 'Detection of blood vessels in retinal images using two-dimensional matched filters'. *IEEE Trans. Med. Imaging,* 8 (3), pp. 263-269.

Kauppi, T. *et al.* (2006) 'DIARETDB0: Evaluation database and methodology for diabetic retinopathy algorithms'. *Machine Vision and Pattern Recognition Research Group, Lappeenranta University of Technology, Finland,* 73 1-17.

Keeler, R. (2003) 'A brief history of the ophthalmoscope'. *Optometry in Practice,* 4 137-145.

Kong, H.-J. *et al.* (2009) Published. 'Indirect ophthalmoscopic stereo video system using three-dimensional LCD'. *Stereoscopic Displays and Applications XX,* 2009. International Society for Optics and Photonics, pp.72371L.

Körding, K.P. *et al.* (2007) 'Causal inference in multisensory perception'. *PLoS one,* 2 (9), pp. e943.

Kramer, D. (2017) 'Steady, strong growth is expected for open-access journals'. *Physics Today,* 70 (5), pp. 24-28.

Krizhevsky, A., Sutskever, I. and Hinton, G.E. (2012) Published. 'Imagenet classification with deep convolutional neural networks'. *Advances in neural information processing systems,* 2012. pp.1097-1105.

Lalonde, M., Gagnon, L. and Boucher, M.-C. (2001) Published. 'Automatic visual quality assessment in optical fundus images'. *Proceedings of vision interface,* 2001. Ottawa, pp.259-264.

Larsen, M. *et al.* (2003) 'Automated detection of fundus photographic red lesions in diabetic retinopathy'. *Investigative ophthalmology & visual science,* 44 (2), pp. 761-766.

Leese, G.P. *et al.* (2008) 'Screening uptake in a well-established diabetic retinopathy screening program: the role of geographical access and deprivation'. *Diabetes Care,* 31 (11), pp. 2131-2135.

Leonard, A.P. *et al.* (2016) 'Double-Pass Retina Point Imaging for the Evaluation of Optical Light Scatter, Retinal Image Quality, and Staging of Keratoconus'. *J Refract Surg,* 32 (11), pp. 760-765.

Leung, H. *et al.* (2004a) 'Impact of current and past blood pressure on retinal arteriolar diameter in an older population'. *Journal of hypertension,* 22 (8), pp. 1543-1549.

Leung, H. *et al.* (2004b) 'Impact of current and past blood pressure on retinal arteriolar diameter in an older population'. 22 (8), pp. 1543-1549.

Levenberg, K. (1944) 'A method for the solution of certain non-linear problems in least squares'. *Quarterly of applied mathematics,* 2 (2), pp. 164-168.

Li, H. and Chutatape, O. (2004) 'Automated feature extraction in color retinal images by a model based approach'. *IEEE Transactions on biomedical engineering,* 51 (2), pp. 246-254.

Li, Y.-H. *et al.* (2019) 'Computer-Assisted Diagnosis for Diabetic Retinopathy Based on Fundus Images Using Deep Convolutional Neural Network'. *Mobile Information Systems,* 2019.

Liesenfeld, B. *et al.* (2000) 'A telemedical approach to the screening of diabetic retinopathy: digital fundus photography'. *Diabetes care,* 23 (3), pp. 345-348.

Liew, G. and Wang, J.J. (2011) 'Retinal vascular signs: a window to the heart?'. *Revista Española de Cardiología (English Edition),* 64 (6), pp. 515-521.

Liew, G. *et al.* (2008) 'The retinal vasculature as a fractal: methodology, reliability, and relationship to blood pressure'. *Ophthalmology,* 115 (11), pp. 1951-1956.

Liew, G. *et al.* (2009) 'Retinopathy predicts coronary heart disease mortality'. *Heart,* 95 (5), pp. 391-394.

Lim, L.S. *et al.* (2012) 'Age-related macular degeneration'. *The Lancet,* 379 (9827), pp. 1728-1738.

Liou, H.-L. and Brennan, N.A. (1997) 'Anatomically accurate, finite model eye for optical modeling'. *JOSA A,* 14 (8), pp. 1684-1695.

Liskowski, P. and Krawiec, K. (2016) 'Segmenting retinal blood vessels with deep neural networks'. *IEEE transactions on medical imaging,* 35 (11), pp. 2369-2380.
Livingstone, I. *et al.* (2019) 'Testing Pediatric Acuity With an iPad: Validation of "Peekaboo Vision" in Malawi and the UK'. *Transl Vis Sci Technol,* 8 (1), pp. 8.
Lloret, D. *et al.* (2000) Published. 'Retinal image registration using creases as anatomical landmarks'. *Proceedings 15th International Conference on Pattern Recognition. ICPR-2000,* 2000. IEEE, pp.203-206.
Lo, V. *et al.* (2012) 'The use of smartphones in general and internal medicine units: a boon or a bane to the promotion of interprofessional collaboration?'. *Journal of interprofessional care,* 26 (4), pp. 276-282.
London, A., Benhar, I. and Schwartz, M. (2013) 'The retina as a window to the brain—from eye research to CNS disorders'. *Nature Reviews Neurology,* 9 (1), pp. 44.
Long, J., Shelhamer, E. and Darrell, T. (2015) Published. 'Fully convolutional networks for semantic segmentation'. *Proceedings of the IEEE conference on computer vision and pattern recognition,* 2015. pp.3431-3440.
Looker, H. *et al.* (2013) 'Predicted impact of extending the screening interval for diabetic retinopathy: the Scottish Diabetic Retinopathy Screening programme'. *Diabetologia,* 56 (8), pp. 1716-1725.
Lopez-Gil, N., Iglesias, I. and Artal, P. (1998) 'Retinal image quality in the human eye as a function of the accommodation'. *Vision Research,* 38 (19), pp. 2897-2907.
Lowell, J. *et al.* (2004) 'Optic nerve head segmentation'. *IEEE Trans Med Imaging,* 23 (2), pp. 256-264.
Lu, S. and Lim, J.H. (2010) 'Automatic optic disc detection from retinal images by a line operator'. *IEEE transactions on biomedical engineering,* 58 (1), pp. 88-94.
MacGillivray, T. *et al.* (2014) 'Retinal imaging as a source of biomarkers for diagnosis, characterization and prognosis of chronic illness or long-term conditions'. *The British journal of radiology,* 87 (1040), pp. 20130832.
Maguire, R. *et al.* (2008) 'Nurse's perceptions and experiences of using of a mobile-phone-based Advanced Symptom Management System (ASyMS©) to monitor and manage chemotherapy-related toxicity'. *European Journal of Oncology Nursing,* 12 (4), pp. 380-386.
Maharana, P.K. *et al.* (2016) 'Salzmann's Nodular Degeneration'. *Ocul Surf,* 14 (1), pp. 20-30.
Maintz, J.A. and Viergever, M.A. (1998) 'A survey of medical image registration'. *Medical image analysis,* 2 (1), pp. 1-36.
Marcos, S., Burns, S.A. and He, J.C. (1998) 'Model for cone directionality reflectometric measurements based on scattering'. *J Opt Soc Am A Opt Image Sci Vis,* 15 (8), pp. 2012-2022.
Marewski, J.N. *et al.* (2010) 'From recognition to decisions: Extending and testing recognition-based models for multialternative inference'. *Psychonomic Bulletin & Review,* 17 (3), pp. 287-309.
Medhi, J.P. and Dandapat, S. (2016) 'An effective fovea detection and automatic assessment of diabetic maculopathy in color fundus images'. *Computers in biology and medicine,* 74 30-44.
Meek, K.M. *et al.* (2003) 'Transparency, swelling and scarring in the corneal stroma'. *Eye (Lond),* 17 (8), pp. 927-936.
Millbank, L. (2013) 'Optical Coherence Tomography (OCT): background and applications'. *International Journal of Ophthalmic Practice,* 4 (4), pp. 138-144.
Mohabey, A. and Ray, A.K. (2000) 'Fusion of rough set theoretic approximations and FCM for color image segmentation.'. *Smc 2000 Conference Proceedings: 2000 Ieee International Conference on Systems, Man & Cybernetics, Vol 1-5,* 2 1529-1534.

Moller-Pedersen, T. (2004) 'Keratocyte reflectivity and corneal haze'. *Exp Eye Res,* 78 (3), pp. 553-560.
Mookiah, M.R.K. *et al.* (2013a) 'Computer-aided diagnosis of diabetic retinopathy: A review'. *Computers in biology and medicine,* 43 (12), pp. 2136-2155.
Mookiah, M.R.K. *et al.* (2013b) 'Automated detection of optic disk in retinal fundus images using intuitionistic fuzzy histon segmentation'. *Proceedings of the Institution of Mechanical Engineers, Part H: Journal of Engineering in Medicine,* 227 (1), pp. 37-49.
Mukhopadhyay, S. and Chanda, B. (2003) 'Multiscale morphological segmentation of gray-scale images'. *IEEE transactions on Image Processing,* 12 (5), pp. 533-549.
Nguyen, U.T. *et al.* (2013) 'An effective retinal blood vessel segmentation method using multi-scale line detection'. *Pattern recognition,* 46 (3), pp. 703-715.
Niemeijer, M., Abramoff, M. and Van Ginneken, B. (2008) Published. 'Automated localization of the optic disc and the fovea'. *2008 30th Annual International Conference of the IEEE Engineering in Medicine and Biology Society,* 2008. IEEE, pp.3538-3541.
Niemeijer, M., Abramoff, M.D. and van Ginneken, B. (2006) 'Image structure clustering for image quality verification of color retina images in diabetic retinopathy screening'. *Med Image Anal,* 10 (6), pp. 888-898.
Niemeijer, M. *et al.* (2010) 'Retinopathy online challenge: automatic detection of microaneurysms in digital color fundus photographs'. *IEEE Trans Med Imaging,* 29 (1), pp. 185-195.
Niemeijer, M. *et al.* (2011) 'Automated measurement of the arteriolar-to-venular width ratio in digital color fundus photographs'. *IEEE Trans Med Imaging,* 30 (11), pp. 1941-1950.
Nischal, K.K. (2015) 'Genetics of Congenital Corneal Opacification-Impact on Diagnosis and Treatment'. *Cornea,* 34 S24-S34.
Nithya, R. and Venkateswaran, N. (2015) 'Analysis of segmentation algorithms in colour fundus and OCT images for glaucoma detection'. *Indian Journal of Science and Technology,* 8 (24), pp. 1.
Norris, D. and Kinoshita, S. (2008) 'Perception as evidence accumulation and Bayesian inference: insights from masked priming'. *Journal of Experimental Psychology: General,* 137 (3), pp. 434.
Odstrcilik, J. *et al.* (2013) 'Retinal vessel segmentation by improved matched filtering: evaluation on a new high-resolution fundus image database'. *IET Image Processing,* 7 (4), pp. 373-383.
Ophthalmic Imaging. (2008).
Organization, W.H. (2011) 'mHealth: new horizons for health through mobile technologies'. *mHealth: new horizons for health through mobile technologies.*
Owen, C.G. *et al.* (2009) 'Measuring retinal vessel tortuosity in 10-year-old children: validation of the Computer-Assisted Image Analysis of the Retina (CAIAR) program'. *Invest Ophthalmol Vis Sci,* 50 (5), pp. 2004-2010.
Pascolini, D. and Mariotti, S.P. (2012a) 'Global estimates of visual impairment: 2010'. *British Journal of Ophthalmology,* 96 (5), pp. 614-618.
Pascolini, D. and Mariotti, S.P.J.B.J.o.O. (2012b) 'Global estimates of visual impairment: 2010'. 96 (5), pp. 614-618.
Patel, S., Marshall, J. and Fitzke, F. (1993) 'Shape and radius of posterior corneal surface'. *Journal of Refractive Surgery,* 9 (3), pp. 173-181.

Patton, N. *et al.* (2005a) 'Retinal vascular image analysis as a potential screening tool for cerebrovascular disease: a rationale based on homology between cerebral and retinal microvasculatures'. *Journal of anatomy,* 206 (4), pp. 319-348.
Patton, N. *et al.* (2005b) 'Retinal vascular image analysis as a potential screening tool for cerebrovascular disease: a rationale based on homology between cerebral and retinal microvasculatures'. 206 (4), pp. 319-348.
Patton, N. *et al.* (2006) 'Retinal image analysis: concepts, applications and potential'. *Progress in retinal and eye research,* 25 (1), pp. 99-127.
Paulus, J. *et al.* (2010) 'Automated quality assessment of retinal fundus photos'. *Int J Comput Assist Radiol Surg,* 5 (6), pp. 557-564.
Perera, C. (2012) 'The evolution of E-Health–mobile technology and mHealth'. *Journal of Mobile Technology in Medicine,* 1 (1), pp. 1-2.
Perez-Rovira, A. *et al.* (2011) Published. 'VAMPIRE: vessel assessment and measurement platform for images of the REtina'. *2011 Annual International Conference of the IEEE Engineering in Medicine and Biology Society,* 2011. IEEE, pp.3391-3394.
Peto, T. and Tadros, C. (2012) 'Screening for diabetic retinopathy and diabetic macular edema in the United Kingdom'. *Current diabetes reports,* 12 (4), pp. 338-345.
Philip, S., Cowie, L.M. and Olson, J.A. (2005) 'The impact of the Health Technology Board for Scotland's grading model on referrals to ophthalmology services'. *Br J Ophthalmol,* 89 (7), pp. 891-896.
Philip, S. *et al.* (2007a) 'The efficacy of automated "disease/no disease" grading for diabetic retinopathy in a systematic screening programme'. *Br J Ophthalmol,* 91 (11), pp. 1512-1517.
Philip, S. *et al.* (2007b) 'The efficacy of automated “disease/no disease” grading for diabetic retinopathy in a systematic screening programme'. *British Journal of Ophthalmology,* 91 (11), pp. 1512-1517.
Pires Dias, J.M., Oliveira, C.M. and da Silva Cruz, L.A. (2014) 'Retinal image quality assessment using generic image quality indicators'. *Information Fusion,* 19 73-90.
Piyasena, M.M.P.N. *et al.* (2019) 'Systematic review on barriers and enablers for access to diabetic retinopathy screening services in different income settings'. *PloS one,* 14 (4), pp. e0198979.
Pizer, S.M. *et al.* (1987) 'Adaptive histogram equalization and its variations'. *Computer vision, graphics, and image processing,* 39 (3), pp. 355-368.
Pourreza, H.R., Pourreza, M. and Banaee, T. (2013) Published. 'Simple and efficient method to measure vessel tortuosity'. *ICCKE 2013,* 2013. IEEE, pp.219-222.
Poyser, O. *et al.* (2019) 'Real-Time Tele-ophthalmology in the Emergency Department “Eye Pad” Emergency Triage'.
Prince, J.L. and Links, J.M. (2006) *Medical imaging signals and systems.* Pearson Prentice Hall Upper Saddle River, NJ.
Probert, C. (2016) *Examination of the retina.* Available at: https://www.opticianonline.net/cet-archive/128.
Pylyshyn, Z. (1999) 'Is vision continuous with cognition?: The case for cognitive impenetrability of visual perception'. *Behavioral and brain sciences,* 22 (3), pp. 341-365.
Qureshi, R.J. *et al.* (2012) 'Combining algorithms for automatic detection of optic disc and macula in fundus images'. *Computer Vision and Image Understanding,* 116 (1), pp. 138-145.
Ravikumar, S., Thibos, L.N. and Bradley, A. (2008) 'Calculation of retinal image quality for polychromatic light'. *J Opt Soc Am A Opt Image Sci Vis,* 25 (10), pp. 2395-2407.

Remeseiro, B., Mendonca, A.M. and Campilho, A. (2017) 'Objective Quality Assessment of Retinal Images Based on Texture Features'. *2017 International Joint Conference on Neural Networks (Ijcnn),* 4520-4527.

Reza, M.N. and Ahmad, M. (2015) Published. 'Automatic detection of optic disc in fundus images by curve operator'. *2015 2nd International Conference on Electrical Information and Communication Technologies (EICT),* 2015. IEEE, pp.143-147.

Robertson, A.R. (1977) 'The CIE 1976 color-difference formulae'. *Color Research & Application,* 2 (1), pp. 7-11.

Rodrigues, I., Sanches, J. and Bioucas-Dias, J. (2008) Published. 'Denoising of medical images corrupted by Poisson noise'. *2008 15th IEEE International Conference on Image Processing,* 2008. IEEE, pp.1756-1759.

Rosenfield, M. and Logan, N. (2009) *Optometry: science, techniques and clinical management.* Elsevier Health Sciences.

Rubin, N. (2001) 'The role of junctions in surface completion and contour matching'. *Perception,* 30 (3), pp. 339-366.

Russo, A. *et al.* (2015) 'Comparison of smartphone ophthalmoscopy with slit-lamp biomicroscopy for grading diabetic retinopathy'. *American journal of ophthalmology,* 159 (2), pp. 360-364. e361.

Sachdeva, S. (2009) 'Fitzpatrick skin typing: applications in dermatology'. *Indian J Dermatol Venereol Leprol,* 75 (1), pp. 93-96.

Sagar, A.V., Balasubramanian, S. and Chandrasekaran, V. (2007) Published. 'Automatic Detection of Anatomical Structures in Digital Fundus Retinal Images'. *MVA,* 2007. pp.483-486.

Saine, P.J. (1984) 'Errors in Fundus Photography'. *15th annual meeting of the Ophthalmic Photographer's Society.* Atlanta, Georgia USA.

Sairenchi, T. *et al.* (2011) 'Mild retinopathy is a risk factor for cardiovascular mortality in Japanese with and without hypertension: the Ibaraki Prefectural Health Study'. *Circulation,* 124 (23), pp. 2502-2511.

Sakaguchi, H. *et al.* (2017) Published. 'Analysis of relationship between target visual cognition difficulties and gaze movements in visual search task'. *2017 IEEE International Conference on Systems, Man, and Cybernetics (SMC),* 2017. IEEE, pp.1423-1428.

Saleh, S.S., Alameddine, M.S. and El-Jardali, F. (2009) 'The case for developing publicly-accessible datasets for health services research in the Middle East and North Africa (MENA) region'. *BMC Health Serv Res,* 9 197.

Sánchez, C.I. *et al.* (2008) 'A novel automatic image processing algorithm for detection of hard exudates based on retinal image analysis'. *Medical engineering & physics,* 30 (3), pp. 350-357.

Sandwell, D.T. (1987) 'Biharmonic spline interpolation of GEOS-3 and SEASAT altimeter data'. *Geophysical research letters,* 14 (2), pp. 139-142.

Sangave, A. *et al.* (2014) 'Pupil Size and Quality of Retinal Photos in Tele-I-Care: A Diabetic Retinopathy Surveillance Project'. *Investigative Ophthalmology & Visual Science,* 55 (13), pp. 2288-2288.

Scanlon, P.H. (2008) 'Article Commentary: The English national screening programme for sight-threatening diabetic retinopathy'. *Journal of Medical Screening,* 15 (1), pp. 1-4.

Scanlon, P.H. *et al.* (2003) 'Comparison of two reference standards in validating two field mydriatic digital photography as a method of screening for diabetic retinopathy'. *British journal of ophthalmology,* 87 (10), pp. 1258-1263.

Scarpa, F., Fiorin, D. and Ruggeri, A. (2007) 'In vivo three-dimensional reconstruction of the cornea from confocal microscopy images'. *Conf Proc IEEE Eng Med Biol Soc,* 2007 747-750.
Scarpa, F., Grisan, E. and Ruggeri, A. (2008) 'Automatic recognition of corneal nerve structures in images from confocal microscopy'. *Invest Ophthalmol Vis Sci,* 49 (11), pp. 4801-4807.
Scarpa, F. *et al.* (2011) 'Automatic evaluation of corneal nerve tortuosity in images from in vivo confocal microscopy'. *Invest Ophthalmol Vis Sci,* 52 (9), pp. 6404-6408.
Scotland, G.S. *et al.* (2007) 'Cost-effectiveness of implementing automated grading within the national screening programme for diabetic retinopathy in Scotland'. *British Journal of Ophthalmology,* 91 (11), pp. 1518-1523.
Selig, B. *et al.* (2015) 'Fully automatic evaluation of the corneal endothelium from in vivo confocal microscopy'. *BMC Med Imaging,* 15 13.
Shah, A. *et al.* (2011) 'Geographic variations in microbial keratitis: an analysis of the peer-reviewed literature'. *Br J Ophthalmol,* 95 (6), pp. 762-767.
Shin, D.-H. *et al.* (2005) 'Block-based noise estimation using adaptive Gaussian filtering'. *IEEE Transactions on Consumer Electronics,* 51 (1), pp. 218-226.
Shortt, A.J., Tuft, S.J. and Daniels, J.T. (2011) 'Corneal stem cells in the eye clinic'. *Br Med Bull,* 100 (1), pp. 209-225.
Sinthanayothin, C. *et al.* (1999) 'Automated localisation of the optic disc, fovea, and retinal blood vessels from digital colour fundus images'. *British journal of ophthalmology,* 83 (8), pp. 902-910.
Sirovich, L. and Kirby, M. (1987) 'Low-dimensional procedure for the characterization of human faces'. *J Opt Soc Am A,* 4 (3), pp. 519-524.
Sivaswamy, J. *et al.* (2015) 'A comprehensive retinal image dataset for the assessment of glaucoma from the optic nerve head analysis'. 2 (1), pp. 1004.
Smith, G., GEORGE, S. and Atchison, D.A. (1997) *THE EYE AND VISUAL OPTICAL INSTRUMENTS. Edition en anglais.* Cambridge University Press.
Soares, J.V. *et al.* (2006) 'Retinal vessel segmentation using the 2-D Gabor wavelet and supervised classification'. *IEEE Transactions on medical Imaging,* 25 (9), pp. 1214-1222.
Solanki, K. *et al.* (2014) 'EyeArt: Advanced Image Analysis Tools for Diabetic Retinopathy Screening and Telemedicine Applications'. *Investigative Ophthalmology & Visual Science,* 55 (13), pp. 5883-5883.
Sorsby, A. (1956) 'Emmetropia and its aberrations'. *Transactions. Ophthalmological Society of the United Kingdom,* 76 167-169.
Soto-Pedre, E. *et al.* (2015) 'Evaluation of automated image analysis software for the detection of diabetic retinopathy to reduce the ophthalmologists' workload'. *Acta ophthalmologica,* 93 (1), pp. e52-e56.
Sprawls, P. (1987) *Physical principles of medical imaging.* Aspen Publishers.
Staal, J. *et al.* (2004) 'Ridge-based vessel segmentation in color images of the retina'. *IEEE Trans Med Imaging,* 23 (4), pp. 501-509.
Stenstrom, S. and Woolf, D. (1948) 'INVESTIGATION OF THE VARIATION AND THE CORRELATION OF THE OPTICAL ELEMENTS OF HUMAN EYES† §'. *Optometry and Vision Science,* 25 (5), pp. 218-232.
STructured Analysis of the Retina. Available at: http://cecas.clemson.edu/~ahoover/stare/.
Tang, L. *et al.* (2011) 'Robust multiscale stereo matching from fundus images with radiometric differences'. *IEEE Trans Pattern Anal Mach Intell,* 33 (11), pp. 2245-2258.
Taylor, H.R. *et al.* (2014) 'Trachoma'. *The Lancet,* 384 (9960), pp. 2142-2152.

Teng, T., Lefley, M. and Claremont, D. (2002) 'Progress towards automated diabetic ocular screening: a review of image analysis and intelligent systems for diabetic retinopathy'. *Medical and Biological Engineering and Computing,* 40 (1), pp. 2-13.
Teweldemedhin, M. *et al.* (2017) 'Bacterial profile of ocular infections: a systematic review'. *BMC Ophthalmol,* 17 (1), pp. 212.
Thomas, R. and Parikh, R.S. (2006) 'How to assess a patient for glaucoma'. *Community eye health,* 19 (59), pp. 36.
Thongnuch, V. and Uyyanonvara, B. (2007) 'Automatic optic disk detection from low contrast retinal images of ROP infant using GVF snake'. *Suranaree J Sci Technol,* 14 (3), pp. 223-234.
Tory, M. and Moller, T. (2004) 'Human factors in visualization research'. *IEEE transactions on visualization and computer graphics,* 10 (1), pp. 72-84.
Trucco, E. *et al.* (2013) 'Validating retinal fundus image analysis algorithms: issues and a proposal'. *Investigative ophthalmology & visual science,* 54 (5), pp. 3546-3559.
Tufail, A. *et al.* (2016) 'An observational study to assess if automated diabetic retinopathy image assessment software can replace one or more steps of manual imaging grading and to determine their cost-effectiveness'. *Health Technology Assessment,* 20 (92), pp. xxviii, 1-72.
Ungerleider, L.G. (1982) 'Two cortical visual systems'. *Analysis of visual behavior,* 549-586.
Usher, D. *et al.* (2004) 'Automated detection of diabetic retinopathy in digital retinal images: a tool for diabetic retinopathy screening'. *Diabetic Medicine,* 21 (1), pp. 84-90.
Varadarajan, A.V. *et al.* (2018) 'Deep Learning for Predicting Refractive Error From Retinal Fundus Images'. *Invest Ophthalmol Vis Sci,* 59 (7), pp. 2861-2868.
VARPA. Available at: http://www.varpa.es/research/ophtalmology.html#vicavr.
Vision, P. Available at: https://www.peekvision.org/en_GB/peek-solutions/peek-retina/buy-peek-retina/.
Volk Available at: https://volk.com/index.php/volk-products/ophthalmic-cameras/volk-inview.html.
Vos, J.J. (2003) 'Reflections on glare'. *Lighting Research and Technology,* 35 (2), pp. 163-176.
Wagner, H., Fink, B.A. and Zadnik, K. (2008) 'Sex- and gender-based differences in healthy and diseased eyes'. *Optometry,* 79 (11), pp. 636-652.
Walter, T. and Klein, J.-C. (2001) Published. 'Segmentation of color fundus images of the human retina: Detection of the optic disc and the vascular tree using morphological techniques'. *International Symposium on Medical Data Analysis,* 2001. Springer, pp.282-287.
Wang, D. and Tan, X. (2017) 'Bayesian neighborhood component analysis'. *IEEE transactions on neural networks and learning systems,* 29 (7), pp. 3140-3151.
Wang, J.J. *et al.* (2006a) 'Retinal vessel diameters and obesity: a population-based study in older persons'. *Obesity (Silver Spring),* 14 (2), pp. 206-214.
Wang, J.J. *et al.* (2006b) 'Retinal vessel diameters and obesity: a population-based study in older persons'. *Obesity,* 14 (2), pp. 206-214.
Wang, S. *et al.* (2016) 'Human Visual System-Based Fundus Image Quality Assessment of Portable Fundus Camera Photographs'. *IEEE Trans Med Imaging,* 35 (4), pp. 1046-1055.
Wang, Y. *et al.* (2013) 'Retinal vessel segmentation using multiwavelet kernels and multiscale hierarchical decomposition'. *Pattern Recognition,* 46 (8), pp. 2117-2133.
Webb, R.H., Hughes, G.W. and Delori, F.C. (1987) 'Confocal scanning laser ophthalmoscope'. *Applied optics,* 26 (8), pp. 1492-1499.

Weinreb, R.N. and Khaw, P.T. (2004) 'Primary open-angle glaucoma'. *The Lancet,* 363 (9422), pp. 1711-1720.
Welch, E. (2014) 'No fundoscopy, no defence'. *MPS Casebook,* 22 (2), pp.
Welfer, D. *et al.* (2010) 'Segmentation of the optic disk in color eye fundus images using an adaptive morphological approach'. *Computers in Biology and Medicine,* 40 (2), pp. 124-137.
Welfer, D., Scharcanski, J. and Marinho, D.R. (2011) 'Fovea center detection based on the retina anatomy and mathematical morphology'. *Computer methods and programs in biomedicine,* 104 (3), pp. 397-409.
Widomska, J. and Subczynski, W.K. (2019) 'Why Is Very High Cholesterol Content Beneficial for the Eye Lens but Negative for Other Organs?'. *Nutrients,* 11 (5), pp. 1083.
Wilk, M.A. *et al.* (2017) 'The Effect of Retinal Melanin on Optical Coherence Tomography Images'. *Transl Vis Sci Technol,* 6 (2), pp. 8.
Willmann, D. and Melanson, S.W. (2017) 'Corneal Injury'. *StatPearls [Internet].* StatPearls Publishing, pp.
Withagen, P.J., Groen, F.C.A. and Schutte, K. (2007) 'CCD color camera characterization for image measurements'. *Ieee Transactions on Instrumentation and Measurement,* 56 (1), pp. 199-203.
Witt, N. *et al.* (2006) 'Abnormalities of retinal microvascular structure and risk of mortality from ischemic heart disease and stroke'. *Hypertension,* 47 (5), pp. 975-981.
Wong, T.Y. *et al.* (2016) 'Diabetic retinopathy'. *Nat Rev Dis Primers,* 2 16012.
Wong, T.Y. *et al.* (2006) 'Retinal vascular caliber, cardiovascular risk factors, and inflammation: the multi-ethnic study of atherosclerosis (MESA)'. *Investigative ophthalmology & visual science,* 47 (6), pp. 2341-2350.
Wong, T.Y. *et al.* (2001) 'Retinal microvascular abnormalities and incident stroke: the Atherosclerosis Risk in Communities Study'. *Lancet,* 358 (9288), pp. 1134-1140.
Xian, Y.-L. *et al.* (2017) 'Dual-wavelength retinal images denoising algorithm for improving the accuracy of oxygen saturation calculation'. *Journal of biomedical optics,* 22 (1), pp. 016004.
Xiao, S. and Liu, X. (2013) Published. 'Global visual cognition based on visual imagery and its mental connectivity'. *2013 6th International Conference on Biomedical Engineering and Informatics,* 2013. IEEE, pp.75-79.
Yang, W., Wang, K. and Zuo, W. (2012) 'Neighborhood Component Feature Selection for High-Dimensional Data'. *JCP,* 7 (1), pp. 161-168.
Yankelovich, A. and Spitzer, H. (2018) 'Predicting Illusory Contours Without Extracting Special Image Features'. *Frontiers in computational neuroscience,* 12 106.
Yin, F. *et al.* (2014) 'Automatic retinal interest evaluation system (ARIES)'. *Conf Proc IEEE Eng Med Biol Soc,* 2014 162-165.
Yip, C.H. *et al.* (2008) 'Guideline implementation for breast healthcare in low-and middle-income countries: Early detection resource allocation'. *Cancer,* 113 (S8), pp. 2244-2256.
Yu, H. *et al.* (2012a) Published. 'Automated image quality evaluation of retinal fundus photographs in diabetic retinopathy screening'. *Image analysis and interpretation (SSIAI), 2012 IEEE southwest symposium on,* 2012a. IEEE, pp.125-128.
Yu, H. *et al.* (2012b) 'Automated image quality evaluation of retinal fundus photographs in diabetic retinopathy screening'. *2012 IEEE Southwest Symposium on Image Analysis and Interpretation.*
Zetterberg, M. (2016) 'Age-related eye disease and gender'. *Maturitas,* 83 19-26.

Zheng, S. *et al.* (2014) Published. 'Automatic and efficient detection of the fovea center in retinal images'. *2014 7th International Conference on Biomedical Engineering and Informatics,* 2014. IEEE, pp.145-150.

APPENDIX I – Participant consent form

Consent Form for:

Name of department: Department of Biomedical Engineering
Title of the study: Comprehensive Ophthalmic Research Database (CORD)

- I confirm that I have read and understood the information sheet for the above project and the researcher has answered any queries to my satisfaction.
- I understand that my participation is voluntary and that I am free to withdraw from the project at any time before data collection has begun (not possible beyond this point due to full anonymization of data), without having to give a reason and without any consequences. If I exercise my right to withdraw and I don't want my data to be used, any data which have been collected from me will be destroyed.
- I understand that anonymised data (i.e. data which do not identify me personally) cannot be withdrawn once they have been included in the study.
- I understand that anonymised data will be made publically available to the research community.
- I understand that any information recorded in the investigation will remain confidential and no information that identifies me will be made publicly available.
- I consent to being a participant in the project.
- I consent to video of my eye(s), that will not show my face, being recorded as part of the research project.
- I consent to my name, surname and signature being retained and stored within the Department of Biomedical Engineering as evidence of consent being provided for participation in this study.

(PRINT NAME)	
Signature of Participant:	Date:

APPENDIX II – Mathematical model of retinal artifacts: Matlab scripts

```
% ARTIFACTS SIMULATOR FOR RETINAL IMAGES
%
% This file contains the algorithm to generate retinal images
% affected by common artifacts, starting from clinical quality
% retinal images.
%
% This algorithm uses the model developed in the work Thesis of
% Matteo Menolotto (2020) to simulate the effects caused by the
% interaction between the light produced by the illumination of the
% ophthalmic instrumentation and the tissues of the eye (cornea,
% lens and retina).
%
% This parametric model describes each interaction with the tissue
% of the eye in terms of transmission (T), absorption (A),
% scattering (S) and specular reflection (R). Most of the parameters
% can be tuned to simulate common artifact caused by pathological
% conditions (e.g. cataract).
% On top of this model, a wide variety of common artifact are also
% made following the respective legend.

clc
close all
clear all

%% Eye model parameters
% Absorbance of the 3 tissues: cornea, lens, retina (wavelength dep)
thickness_cornea = 0.580; % mm from Atchinson and Smith pag. 12
thickness_lens = 3.6;     % mm relaxed state from Atchinson and
Smith
% Total loss
Loss_Co = [0.07 0.09 0.13];
Loss_Le = [0.04 0.05 0.07];

% Fraction of reflected light (only at the cornea)
n_air = 1.0003;  % refractive index of air
```

```
n_co = 1.376;     % mean refractive index of the cornea's layers
n_aqh = 1.336;    % refractive index of aqueous humor
n_le = 1.4;       % refractive index of lens
air_co = ((n_air - n_co)/(n_air + n_co))^2; % Specular reflection of
the source of light
co_air = ((n_co - n_air)/(n_co + n_air))^2;
co_aqh = ((n_aqh - n_co)/(n_aqh + n_co))^2; % Specular reflection of
the source of light
R_co = [air_co air_co air_co];      % [R G B]
Rf_aqh = [co_aqh co_aqh co_aqh];    % [R G B]

% Fraction of absorbed light
A_co = Loss_Co-R_co;                % [R G B]
A_le = [0.50 0.55 0.60].*Loss_Le;   % [R G B]
% A_re=imcomp(I) IS WHERE THE INFORMATION IS STORED!!! (which is the
clinical quality image)

% Fraction of scattered light (wavelength dep) respect to the total
loss
S_co = [0.2 0.22 0.24].*Loss_Co;    % [R G B]

S_le = [0.5 0.54 0.58].*Loss_Le;    % [R G B] if cataract = [0.2
0.26 0.32]
S_le_f = 0.7*S_le;
S_le_b = 0.3*S_le;

S_re_b = [0.30 0.32 0.38];

% Insert the directory of the folders that contains the clinical
% quality retinal images to be used.
% In this example we are using the CORD Database:
%   * Spatial Resolution -> 4288 x 2848
%   * FOV -> 50 deg
FundusCameraImages_dir = '…';   % Insert here the path for the
clinical quality retinal images.

Retinal_Images = dir(fullfile(FundusCameraImages_dir, '*.jpg'));

for NoRetIm = 1:numel(Retinal_Images)  % for each retinal images
contained in the selected folder

    I_retina =
imread([FundusCameraImages_dir,Retinal_Images(NoRetIm).name]);

    % resize the images to be more manageble keeping its original
ration.
    small_side = 1000;  % increase or decrese at your own discretion
    side_ratio = min(size(I_retina,1),
size(I_retina,2))/(max(size(I_retina,1), size(I_retina,2)));
    I = imresize(I_retina,[small_side
round(small_side/side_ratio)]);

%% -------------------------Pre-processing-------------------------
    % create Mask for the ROI of the Retinal image
    Mask = ones(size(I,1),size(I,2));
    for k = 1:size(I,2)
        for j = 1:size(I,1)
```

```
            if I(j,k,1) <= 40
                I(j,k,:) = 0;
                Mask(j,k)=0;
            end
        end
    end

    stats = regionprops(Mask,'Extrema','Centroid');
    Radius = round((stats.Extrema(3,1)-stats.Extrema(8,1))/2)-2;
    ctr_X = round(stats.Centroid(1,1));
    ctr_Y = round(stats.Centroid(1,2));

    % if you are using CORD uncomment this line
    I = imcrop(I,[ctr_X-Radius ctr_Y-
round(round(size(I,1)*0.87266)/2) Radius*2
round(size(I,1)*0.87266)]);
    % if you are using another Dataset uncomment this line
    % I = imcrop(I,[ctr_X-Radius ctr_Y-Radius Radius*2 Radius*2]);

    ctr_X = round(size(I,2)/2);
    ctr_Y = round(size(I,1)/2);
    NN = size(I,1);
    MM = size(I,2);
    I = im2double(I);
    lambda = [460 550 620];  % we consider the contrinbution of
these three wavelengths
    A_re = imcomplement(I);  % IS WHERE THE INFORMATION IS STORED!!!


%% -------------------------Source of light-----------------------

    for uuu=1:10 % 5 artifact images per each good clincal images

        %% External artifact parameters:
        % - UNEVEN ILLUMINATION
        Pos_X = randi([-400 400]); % random position
        Pos_Y = randi([-400 400]);
        Var = randi([48000 55000]);
        Covar = randi([550000 580000]);
        % - SPECULAR REFLECTION
        % - MISALIGNED TARGET RING
        misalignment = randi([0 4]); % 5 different misalignments [0
- 4]. 0 means no misalignment
        % - INVOLUNTARY MOVEMENT
        % - EYELASHES AND BLINKING
        Eyelash_severity = randi([0 1]); % 6 level of severity from
[0 - 5]. Severity = 0 means no eyelashes

        Wavelen = 380:1:749;   % visible range [380nm - 750nm]


        clear XenonLight LEDLight
        % Simulation of the emitting spectrum of LED light (from
samsung smartphone camera LED)
        % Estimation of the emitted light intensity for the three
wavelengths
        LED_R = 0.34 * gaussmf(Wavelen,[55 lambda(3)]);
```

```
        LED_G = 0.46 * gaussmf(Wavelen,[42 lambda(2)]);
        LED_B = 0.93 * gaussmf(Wavelen,[8 lambda(1)]);
        LED = LED_R + LED_G + LED_B;

% Simulation of the source of Xenon bulb light
Xenon_base = .95 * gaussmf(Wavelen,[1000 500]);
Xenon_Peack1 = 0.01 * gaussmf(Wavelen,[3 475]);
% Xenon_Peack2 = 0.3 * gaussmf(Wavelen,[4 450]);
Xenon = Xenon_base + Xenon_Peack1;

% Simulation of the characteristic radiation pattern produced by
these light sources
% Matix of 584x565 Xenon bulb
XenonLight(:,:,1) = Xenon(lambda(3)-380) * ones(NN,MM);
XenonLight(:,:,2) = Xenon(lambda(2)-380) * ones(NN,MM);
XenonLight(:,:,3) = Xenon(lambda(1)-380) * ones(NN,MM);
% Matix of 584x565 LED
LEDLight(:,:,1) = LED(lambda(3)-380) * ones(NN,MM);
LEDLight(:,:,2) = LED(lambda(2)-380) * ones(NN,MM);
LEDLight(:,:,3) = LED(lambda(1)-380) * ones(NN,MM);

mu = [round(size(LEDLight,2)/2) round(size(LEDLight,1)/2)];
Var_F = 80000;
Covar_F = 20000000;
Sigma = [Covar_F Var_F; Var_F Covar_F];
x1 = 1:1:size(LEDLight,2);
x2 = 1:1:size(LEDLight,1);
[X1,X2] = meshgrid(x1,x2);
F = mvnpdf([X1(:) X2(:)],mu,Sigma);
F = reshape(F,length(x2),length(x1))*125700000;

MaxF = max(max(F));

for f2=1:size(XenonLight,2)
    for f1=1:size(XenonLight,1)
        XenonLight(f1,f2,1) = XenonLight(f1,f2,1) - MaxF + F(f1,f2);
        XenonLight(f1,f2,2) = XenonLight(f1,f2,2) - MaxF + F(f1,f2);
        XenonLight(f1,f2,3) = XenonLight(f1,f2,3) - MaxF + F(f1,f2);
    end
end

for f2=1:size(LEDLight,2)
    for f1=1:size(LEDLight,1)
        LEDLight(f1,f2,1) = LEDLight(f1,f2,1) - MaxF + F(f1,f2);
        LEDLight(f1,f2,2) = LEDLight(f1,f2,2) - MaxF + F(f1,f2);
        LEDLight(f1,f2,3) = LEDLight(f1,f2,3) - MaxF + F(f1,f2);
    end
end

% %% ---------------------------------ARTIFACTS----------------------
%
% % ------------------------------------------------------------------
% % 1 --------------------Uneven illumination----------------------
% % ------------------------------------------------------------------
Seed = [ctr_X+Pos_X ctr_Y+Pos_Y];
mu = [Seed(1) Seed(2)];
Sigma = [Covar Var; Var Covar];
```

```
x_g = 1:1:size(I,2);
y_g = 1:1:size(I,1);
[X1,Y1] = meshgrid(x_g,y_g);

F = mvnpdf([X1(:) Y1(:)],mu,Sigma);
F = reshape(F,length(y_g),length(x_g));

F = F.*(1/max(max(F)));
MaxF = max(max(F));

F = F - (randi([0 10])*0.1);

% Un-comment this section to introduce an uneven illumination effect
on the
% retinal image
XenonLight_hsi = rgb2hsv(XenonLight);
LEDLight_hsi = rgb2hsv(LEDLight);

% Comment this to don't intoduce UNDER-illumination
for j=1:size(XenonLight,1)
    for i=1:size(XenonLight,2)
        %XenonLight(j,i,1) = XenonLight(j,i,1)-F(j,i)/2;%+(MaxF-
F(j,i));
        %XenonLight(j,i,2) = XenonLight(j,i,2)-(MaxF-F(j,i));
        XenonLight_hsi(j,i,3) = XenonLight_hsi(j,i,3)+(F(j,i)-MaxF);
        %LEDLight(j,i,1) = LEDLight(j,i,1)-F(j,i)/2;%+(MaxF-F(j,i));
        %LEDLight(j,i,2) = LEDLight(j,i,2)-(MaxF-F(j,i));
        LEDLight_hsi(j,i,3) = LEDLight_hsi(j,i,3)+(F(j,i)-MaxF);
    end
end

XenonLight = hsv2rgb(XenonLight_hsi);
LEDLight = hsv2rgb(LEDLight_hsi);

% % ------------------------------------------------------------------
% % 2 ---------------------Camera-Target misalignment---------------
% % ------------------------------------------------------------------

% creation of a circular target (to use only with fundus cameras!)

displacement = round(Radius/5);

% misalignment=0;
% for kjk=1:5
 switch misalignment
     case 0
         misX=0;
         misY=0;
     case 1
         misX=randi([-round(displacement/3) round(displacement/3)]);
         misY=randi([-round(displacement/3) round(displacement/3)]);
     case 2
         misX=randi([-round(displacement/2) round(displacement/2)]);
         misY=randi([-round(displacement/2) round(displacement/2)]);
     case 3
         misX=randi([-round(displacement) round(displacement)]);
         misY=randi([-round(displacement) round(displacement)]);
```

```
     case 4
         misX=randi([-round(displacement*1.5)
round(displacement*1.5)]);
         misY=randi([-round(displacement*1.5)
round(displacement*1.5)]);
 end

Int_r = Radius + round(Radius/15);
Ext_r = Int_r + round(Radius/4);

Tar_X = ctr_Y + misX;
Tar_Y = ctr_X + misY;

Target_Light = zeros(size(I,1),size(I,2),3);
for i=1:size(Target_Light,2)
    for j=1:size(Target_Light,1)
        if sqrt((j-Tar_X)^2 + (i-Tar_Y)^2) <= Ext_r && ...
                sqrt((j-Tar_X)^2 + (i-Tar_Y)^2) >= Int_r && ...
                (j <= Tar_X-round(Radius/7) ||
j>=Tar_X+round(Radius/7)) && ...
                (i <= Tar_Y-round(Radius/7) ||
i>=Tar_Y+round(Radius/7))
            Target_Light(j,i,1) = 240/255;
            Target_Light(j,i,2) = 200/255;
            Target_Light(j,i,3) = 100/255;
        end
    end
end

% dim the intensity t=with a gaussian profile
Target_Light_hsi = rgb2hsv(Target_Light);
Seed = [ctr_Y + misY ctr_X + misX];
mu = [Seed(1) Seed(2)];
Var = 50000;
Covar = 200000;
Sigma = [Covar Var; Var Covar];
x_g = 1:1:size(I,2);
y_g = 1:1:size(I,1);
[X1,Y1] = meshgrid(x_g,y_g);

F_mis = mvnpdf([X1(:) Y1(:)],mu,Sigma);
F_mis = reshape(F_mis,length(y_g),length(x_g)); %125700000;
F_mis = F_mis.*(1/max(max(F_mis)));

Target_Light_hsi(:,:,3) = (1-F_mis);%.*255;

Target_Light = hsv2rgb(Target_Light_hsi);

for i=1:size(Target_Light,2)
    for j=1:size(Target_Light,1)
        if Target_Light_hsi(j,i,1)>0
            LEDLight(j,i,1) = Target_Light(j,i,1);
            LEDLight(j,i,2) = Target_Light(j,i,2);
            LEDLight(j,i,3) = Target_Light(j,i,3);

            XenonLight(j,i,1) = Target_Light(j,i,1);
            XenonLight(j,i,2) = Target_Light(j,i,2);
```

```
            XenonLight(j,i,3) = Target_Light(j,i,3);
        end
    end
end

% blur the edges to simulate scattering
LEDLight=imgaussfilt(LEDLight,4);
XenonLight=imgaussfilt(XenonLight,4);

% ------------------------------------------------------------------
% 3 ----------Eyelash and eye blinking (shadows in the image)-------
% ------------------------------------------------------------------

% 5 degrees of severity

Sigma_eyel = 40;

switch Eyelash_severity
    case 1
        Eyelash = imread('Eyelash\eyelash_1.png');
        Eyelash = imresize(Eyelash,[NN MM]);
        Eyelash = im2double(Eyelash);
        Eyelash = rgb2gray(Eyelash) + 0.3;
        for i=1:size(Eyelash,2)
            for j=1:size(Eyelash,1)
                if Eyelash(j,i) > 1
                    Eyelash(j,i) = 1;
                end
            end
        end
        w = 45;  % window
        Eyelash = integralImage(Eyelash);          % Compute the
integral image.
        avgH = integralKernel([1 1 w w], 1/(w^2)); % Apply a w-by-w
average filter.
        Eyelash = integralFilter(Eyelash, avgH);
        Eyelash = imresize(Eyelash,[size(I,1) size(I,2)]);
        Eyelash = imgaussfilt(Eyelash, Sigma_eyel);

        for i=1:size(XenonLight,2)
            for j=1:size(XenonLight,1)
                XenonLight(j,i,1) = XenonLight(j,i,1)-(1-
Eyelash(j,i));
                XenonLight(j,i,2) = XenonLight(j,i,2)-(1-
Eyelash(j,i));
                XenonLight(j,i,3) = XenonLight(j,i,3)-(1-
Eyelash(j,i));
                LEDLight(j,i,1) = LEDLight(j,i,1)-(1-Eyelash(j,i));
                LEDLight(j,i,2) = LEDLight(j,i,2)-(1-Eyelash(j,i));
                LEDLight(j,i,3) = LEDLight(j,i,3)-(1-Eyelash(j,i));
            end
        end
    case 2
        Eyelash = imread('Eyelash\eyelash_1.png');
        Eyelash = imresize(Eyelash,[NN MM]);
        Eyelash = im2double(Eyelash);
        Eyelash = rgb2gray(Eyelash);
        for i=1:size(Eyelash,2)
```

```
            for j=1:size(Eyelash,1)
                if Eyelash(j,i) > 1
                    Eyelash(j,i) = 1;
                end
            end
        end
        w = 38;  % window
        Eyelash = integralImage(Eyelash);         % Compute the
integral image.
        avgH = integralKernel([1 1 w w], 1/(w^2)); % Apply a w-by-w
average filter.
        Eyelash = integralFilter(Eyelash, avgH);
        Eyelash=imresize(Eyelash,[size(I,1) size(I,2)]);
        Eyelash = imgaussfilt(Eyelash, Sigma_eyel);

        for i=1:size(Eyelash,2)
            for j=1:size(Eyelash,1)
                XenonLight(j,i,1) = XenonLight(j,i,1)-(1-
Eyelash(j,i));
                XenonLight(j,i,2) = XenonLight(j,i,2)-(1-
Eyelash(j,i));
                XenonLight(j,i,3) = XenonLight(j,i,3)-(1-
Eyelash(j,i));
                LEDLight(j,i,1) = LEDLight(j,i,1)-(1-Eyelash(j,i));
                LEDLight(j,i,2) = LEDLight(j,i,2)-(1-Eyelash(j,i));
                LEDLight(j,i,3) = LEDLight(j,i,3)-(1-Eyelash(j,i));
            end
        end
    case 3
        Eyelash = imread('Eyelash\eyelash_2.png');
        Eyelash = imresize(Eyelash,[NN MM]);
        Eyelash = im2double(Eyelash);
        Eyelash = rgb2gray(Eyelash) + 0.3;
        for i=1:size(Eyelash,2)
            for j=1:size(Eyelash,1)
                if Eyelash(j,i) > 1
                    Eyelash(j,i) = 1;
                end
            end
        end
        w = 45;  % window
        Eyelash = integralImage(Eyelash);         % Compute the
integral image.
        avgH = integralKernel([1 1 w w], 1/(w^2)); % Apply a w-by-w
average filter.
        Eyelash = integralFilter(Eyelash, avgH);
        Eyelash=imresize(Eyelash,[size(I,1) size(I,2)]);
        Eyelash = imgaussfilt(Eyelash, Sigma_eyel);

        for i=1:size(Eyelash,2)
            for j=1:size(Eyelash,1)
                XenonLight(j,i,1) = XenonLight(j,i,1)-(1-
Eyelash(j,i));
                XenonLight(j,i,2) = XenonLight(j,i,2)-(1-
Eyelash(j,i));
                XenonLight(j,i,3) = XenonLight(j,i,3)-(1-
Eyelash(j,i));
                LEDLight(j,i,1) = LEDLight(j,i,1)-(1-Eyelash(j,i));
```

```
                LEDLight(j,i,2) = LEDLight(j,i,2)-(1-Eyelash(j,i));
                LEDLight(j,i,3) = LEDLight(j,i,3)-(1-Eyelash(j,i));
            end
        end
    case 4
        Eyelash = imread('Eyelash\eyelash_2.png');
        Eyelash = imresize(Eyelash,[NN MM]);
        Eyelash = im2double(Eyelash);
        Eyelash = rgb2gray(Eyelash);
        for i=1:size(Eyelash,2)
            for j=1:size(Eyelash,1)
                if Eyelash(j,i) > 1
                    Eyelash(j,i) = 1;
                end
            end
        end
        w = 38;  % window
        Eyelash = integralImage(Eyelash);         % Compute the
integral image.
        avgH = integralKernel([1 1 w w], 1/(w^2)); % Apply a w-by-w
average filter.
        Eyelash = integralFilter(Eyelash, avgH);
        Eyelash = imresize(Eyelash,[size(I,1) size(I,2)]);
        Eyelash = imgaussfilt(Eyelash, Sigma_eyel);

        for i=1:size(Eyelash,2)
            for j=1:size(Eyelash,1)
                XenonLight(j,i,1) = XenonLight(j,i,1)-(1-
Eyelash(j,i));
                XenonLight(j,i,2) = XenonLight(j,i,2)-(1-
Eyelash(j,i));
                XenonLight(j,i,3) = XenonLight(j,i,3)-(1-
Eyelash(j,i));
                LEDLight(j,i,1) = LEDLight(j,i,1)-(1-Eyelash(j,i));
                LEDLight(j,i,2) = LEDLight(j,i,2)-(1-Eyelash(j,i));
                LEDLight(j,i,3) = LEDLight(j,i,3)-(1-Eyelash(j,i));
            end
        end
    case 5
        Eyelash = imread('Eyelash\eyelash_3.png');
        Eyelash = imresize(Eyelash,[NN MM]);
        Eyelash = im2double(Eyelash);
        Eyelash = rgb2gray(Eyelash);
        for i=1:size(Eyelash,2)
            for j=1:size(Eyelash,1)
                if Eyelash(j,i) > 1
                    Eyelash(j,i) = 1;
                end
            end
        end
        w = 45;  % window
        Eyelash = integralImage(Eyelash);         % Compute the
integral image.
        avgH = integralKernel([1 1 w w], 1/(w^2)); % Apply a w-by-w
average filter.
        Eyelash = integralFilter(Eyelash, avgH);
        Eyelash=imresize(Eyelash,[size(I,1) size(I,2)]);
        Eyelash = imgaussfilt(Eyelash, Sigma_eyel);
```

```
        for i=1:size(Eyelash,2)
            for j=1:size(Eyelash,1)
                XenonLight(j,i,1) = XenonLight(j,i,1)-(1-
Eyelash(j,i));
                XenonLight(j,i,2) = XenonLight(j,i,2)-(1-
Eyelash(j,i));
                XenonLight(j,i,3) = XenonLight(j,i,3)-(1-
Eyelash(j,i));
                LEDLight(j,i,1) = LEDLight(j,i,1)-(1-Eyelash(j,i));
                LEDLight(j,i,2) = LEDLight(j,i,2)-(1-Eyelash(j,i));
                LEDLight(j,i,3) = LEDLight(j,i,3)-(1-Eyelash(j,i));
            end
        end
end


%% ------------------------------------------------------------------
%  --------------------ARTIFACTS PARAMETRIC MODEL-------------------
%  ------------------------------------------------------------------

% ------------------------------------------------------------------
% ------------------------------ CORNEA ----------------------------
% ------------------------------------------------------------------

% --------Fracion of specular REFLECTION generated at the cornea----
% I0 = LEDLight;
I0 = XenonLight;

I_R_co(:,:,1) = I0(:,:,1) * R_co(1);
I_R_co(:,:,2) = I0(:,:,2) * R_co(2);
I_R_co(:,:,3) = I0(:,:,3) * R_co(3);

% --------------------Light ABSORPTION at the CORNEA----------------
% choose the source of light between Xenon bulb and LED
I_A_co(:,:,1) = (I0(:,:,1)-I_R_co(:,:,1)) * A_co(1);
I_A_co(:,:,2) = (I0(:,:,2)-I_R_co(:,:,2)) * A_co(2);
I_A_co(:,:,3) = (I0(:,:,3)-I_R_co(:,:,3)) * A_co(3);

% -----------------TRANSMITTED light through the CORNEA-------------
% choose the source of light between Xenon bulb and LED

I_T_co = I0 - I_R_co - I_A_co;
% Cleaning of the region outside the ROI
for i=1:size(I,2)
    for j=1:size(I,1)
        if sqrt((j-ctr_Y)^2 + (i-ctr_X)^2) >= Radius
            I_T_co(j,i,1) = 0;
            I_T_co(j,i,2) = 0;
            I_T_co(j,i,3) = 0;
        end
    end
end
% ------------------------------------------------------------------
% ------------------------------ LENS ------------------------------
% ------------------------------------------------------------------
```

```
% --------------------Light absorption at the LENS------------------
I_A_le(:,:,1) = I_T_co(:,:,1) * A_le(1);
I_A_le(:,:,2) = I_T_co(:,:,2) * A_le(2);
I_A_le(:,:,3) = I_T_co(:,:,3) * A_le(3);

% ----------------Fracion of scattered light at the LENS------------
I_S_le(:,:,1) = (I_T_co(:,:,1) - I_A_le(:,:,1)) * S_le(1);
I_S_le(:,:,2) = (I_T_co(:,:,2) - I_A_le(:,:,2)) * S_le(2);
I_S_le(:,:,3) = (I_T_co(:,:,3) - I_A_le(:,:,3)) * S_le(3);

% ------------------Transmitted light through the LENS--------------
I_T_le = I_T_co - I_A_le - I_S_le;

% Cleaning of the region outside the ROI
for i=1:size(I,2)
    for j=1:size(I,1)
        if sqrt((j-ctr_Y)^2 + (i-ctr_X)^2) >= Radius
            I_T_le(j,i,1) = 0;
            I_T_le(j,i,2) = 0;
            I_T_le(j,i,3) = 0;
        end
    end
end

% --------------- PSF function Lens to calculate I_Sf_le -----------
% From the 1999 CIE General Disability Glare Equation, which has a
validity
% that stretches from 0.1deg to almost 100deg. Derived from Stiles-
Holladay
% equation

p=0:0.5:1;   % p is the pigmentation factor (p=0 for very dark eyes,
p=0.5 for brown eyes, and p=1.0 for blue-green-eyed Caucasians)
A= [20 40 60];  % A the age in years
phi=0.01:0.01:30; % phi is the glare angle in degrees
clear PSF
for age=1:numel(A)
    for i=1:numel(phi)
        PSF(age,i) = (10/(phi(i)^3)) + (((5/(phi(i)^2)) +
0.1*(p(2)/phi(i)))*(1+((A(age)/62.5)^4))) + (0.0025*p(2));
    end
end

PSF = PSF + phi;
L_le = 19; % the area affected by the point spread function
age_range = 3;

PSF_le_profile = [10^7 PSF(age_range,2) PSF(age_range,3)
PSF(age_range,4) PSF(age_range,5) ...
    PSF(age_range,6) PSF(age_range,7) PSF(age_range,8)
PSF(age_range,9) PSF(age_range,10)]/(max(PSF(1,:)));
PSF_le = ones(L_le,L_le);
for i=1:19
    for j=1:19
        if sqrt((j-10)^2 + (i-10)^2) > 9
            PSF_le(j,i) = 0;
        else
            if sqrt((j-10)^2 + (i-10)^2) == 0 % peak
```

```
                PSF_le(j,i) = 1;
            else
                PSF_le(j,i) = PSF_le_profile(round(sqrt((j-10)^2 +
(i-10)^2)) + 1);
            end
        end
    end
end

% Fracion of forward scattered light at the LENS produced by
neighbours
I_Sf_le(:,:,1) = I_S_le(:,:,1) * S_le_f(1);
I_Sf_le(:,:,2) = I_S_le(:,:,2) * S_le_f(2);
I_Sf_le(:,:,3) = I_S_le(:,:,3) * S_le_f(3);

I_Sf_leI = imfilter(I_Sf_le,PSF_le);  %%%%%%%%%

% ------------------------------------------------------------------
% ------------------------------- RETINA -------------------------
% ------------------------------------------------------------------

% --------------------Light absorption at the RETINA----------------
% --------------------!!!WHERE THE MAGIC HAPPEN!!!-----------------
I_A_re = zeros(size(I_T_le,1),size(I_T_le,2),3);
for i=1:size(I_T_le,2)
    for j=1:size(I_T_le,1)
        if sqrt((j-ctr_Y)^2 + (i-ctr_X)^2) <= Radius
           I_A_re(j,i,1) = (I_T_le(j,i,1) + I_Sf_leI(j,i,1)) *
A_re(j,i,1);
           I_A_re(j,i,2) = (I_T_le(j,i,2) + I_Sf_leI(j,i,2)) *
A_re(j,i,2);
           I_A_re(j,i,3) = (I_T_le(j,i,3) + I_Sf_leI(j,i,3)) *
A_re(j,i,3);
        end
    end
end

% ----------------Fracion of scattered light from the RETINA -------
I_S_re(:,:,1) = (I_T_le(:,:,1) + I_Sf_leI(:,:,1) - I_A_re(:,:,1));
I_S_re(:,:,2) = (I_T_le(:,:,2) + I_Sf_leI(:,:,2) - I_A_re(:,:,2));
I_S_re(:,:,3) = (I_T_le(:,:,3) + I_Sf_leI(:,:,3) - I_A_re(:,:,3));

% Cleaning of the region outside the ROI
for i=1:size(I,2)
    for j=1:size(I,1)
        if sqrt((j-ctr_Y)^2 + (i-ctr_X)^2) >= Radius
            I_S_re(j,i,1) = 0;
            I_S_re(j,i,2) = 0;
            I_S_re(j,i,3) = 0;
        end
    end
end

% ----------------------- PSF function Retina --------------------
% From Marcos and Burns, scattering model
s = 2.6:0.1:6.5;  % cone spacing [um]
lambdaBis = lambda/1000; % wavelenght [um] 1000
f = 16.7; % axial lenght [mm]
```

```
i=1;j=1;
clear I_psf
for l = 1:3
    for x = -8:0.1:8
        for y = -8:0.1:8
            rho =
(pi^2*(0.4*s(10)))/((f^2)*(lambdaBis(l)^2)*log(10));  % shape factor
[mm^-2]

            I_psf(i,j,l) = 10^(-rho*((x-0)^2+(y-0)^2));
            j=j+1;
        end
        i=i+1;
        j=1;
    end
    i=1;
end

for l = 1:3
    for i=1:numel(s)
        rho(i,l) =
(pi^2*(0.4*s(i)))/((f^2)*(lambdaBis(l)^2)*log(10));
    end
end

PSF_re = imcrop(I_psf, [50 50 60 60]);

I_S_reb(:,:,1) = I_S_re(:,:,1) .* S_re_b(1);
I_S_reb(:,:,2) = I_S_re(:,:,2) .* S_re_b(2);
I_S_reb(:,:,3) = I_S_re(:,:,3) .* S_re_b(3);

I_Sb_clt_re = imfilter(I_S_reb, PSF_re(:,:,1));  %%%%%%%%

% ----- Fracion diffuse backward scattered light from the RETINA (B)
k=1;
B_temp = ones(3673339,3);
for i=1:size(I_S_re,2)
    for j=1:size(I_S_re,1)
        if sqrt((j-ctr_Y)^2 + (i-ctr_X)^2) <= Radius - 5
            B_temp(k,1)= I_S_re(j,i,1);%*(1-S_re_clt);
            B_temp(k,2)= I_S_re(j,i,2);%*(1-S_re_clt);
            B_temp(k,3)= I_S_re(j,i,3);%*(1-S_re_clt);
            k=k+1;
        end
    end
end
B_mean(1) = mean(B_temp(:,1))* 0.6;
B_mean(2) = mean(B_temp(:,2))* 0.6;
B_mean(3) = mean(B_temp(:,3))* 0.6;

B = zeros(size(I_S_re,1),size(I_S_re,2),3);
for i=1:size(B,2)
    for j=1:size(B,1)
        if sqrt((j-ctr_Y)^2 + (i-ctr_X)^2) <= Radius
            B(j,i,1)= B_mean(1);
            B(j,i,2)= B_mean(2);
            B(j,i,3)= B_mean(3);
        end
```

```
    end
end

% ------------------------------------------------------------------
% ------------------------------ LENS I ----------------------------
% ------------------------------------------------------------------

% --------------------Light absorption at the LENS------------------
I_A_leI(:,:,1) = (I_S_re(:,:,1) + B(:,:,1)) * A_le(1);%I_Sb_clt_re
I_A_leI(:,:,2) = (I_S_re(:,:,2) + B(:,:,2)) * A_le(2);
I_A_leI(:,:,3) = (I_S_re(:,:,3) + B(:,:,3)) * A_le(3);

% ----------------Fracion of scattered light at the LENS ----------
I_S_leI(:,:,1) = ((I_S_re(:,:,1) + B(:,:,1)) - I_A_leI(:,:,1)) *
S_le(1);
I_S_leI(:,:,2) = ((I_S_re(:,:,2) + B(:,:,2)) - I_A_leI(:,:,2)) *
S_le(2);
I_S_leI(:,:,3) = ((I_S_re(:,:,3) + B(:,:,3)) - I_A_leI(:,:,3)) *
S_le(3);

% Fracion of bacward scattered light at the LENS produced by
neighbours
I_Sf_leI(:,:,1) = I_S_leI(:,:,1)* S_le_f(1);
I_Sf_leI(:,:,2) = I_S_leI(:,:,2)* S_le_f(2);
I_Sf_leI(:,:,3) = I_S_leI(:,:,3)* S_le_f(3);

I_Sf_leI = imfilter(I_Sf_leI,PSF_le);    %%%%%

% -----------------Transmitted light through the LENS I-------------
I_T_leI = I_Sb_clt_re + B - I_A_leI - I_S_leI;
% Cleaning of the region outside the ROI
for i=1:size(I,2)
    for j=1:size(I,1)
        if sqrt((j-ctr_Y)^2 + (i-ctr_X)^2) >= Radius
            I_T_leI(j,i,1) = 0;
            I_T_leI(j,i,2) = 0;
            I_T_leI(j,i,3) = 0;
        end
    end
end

% ------------------------------------------------------------------
% ------------------------------ CORNEA I --------------------------
% ------------------------------------------------------------------

% --------Fracion of specular REFLECTION generated at the cornea----
I_R_coI(:,:,1) = (I_T_leI(:,:,1) + I_Sf_leI(:,:,1)) * R_co(1);
I_R_coI(:,:,2) = (I_T_leI(:,:,2) + I_Sf_leI(:,:,2)) * R_co(2);
I_R_coI(:,:,3) = (I_T_leI(:,:,3) + I_Sf_leI(:,:,3)) * R_co(3);
% figure(27)
% set(figure(27),'Position',[800 100 1865 2273])
% imshow(I_R_coI), title('I_R_coI')

% -------------------Light absorption at the CORNEA I---------------
------
I_A_coI(:,:,1) = ((I_T_leI(:,:,1) + I_Sf_leI(:,:,1))-I_R_co(:,:,1))
* A_co(1);
```

```
I_A_coI(:,:,2) = ((I_T_leI(:,:,2) + I_Sf_leI(:,:,2))-I_R_co(:,:,2))
* A_co(2);
I_A_coI(:,:,3) = ((I_T_leI(:,:,3) + I_Sf_leI(:,:,3))-I_R_co(:,:,3))
* A_co(3);

% ------- AND FINALLY!...Transmitted light through the CORNEA I ----
I_T_coI = I_T_leI + I_Sf_leI - I_R_coI - I_A_coI;
% Cleaning of the region outside the ROI
for i=1:size(I,2)
    for j=1:size(I,1)
        if sqrt((j-ctr_Y)^2 + (i-ctr_X)^2) >= Radius
            I_T_coI(j,i,1) = 0;
            I_T_coI(j,i,2) = 0;
            I_T_coI(j,i,3) = 0;
        end
    end
end

%% ---------------COLLECTION EFFICIENCY of the image sensor---------
eps1 = 0.94; % COLLECTION EFFICIENCY of the specular reflection at
the CORNEA
eps2 = 0.90; % COLLECTION EFFICIENCY of the direct transmitted light
through the CORNEA

FINAL_RETINAL_IMG = (I_R_co * eps1) + (I_T_coI * eps2);

% Cleaning of the region outside the ROI
for i=1:size(I,2)
    for j=1:size(I,1)
        if sqrt((j-ctr_Y)^2 + (i-ctr_X)^2) >= Radius
            FINAL_RETINAL_IMG(j,i,1) = 0;
            FINAL_RETINAL_IMG(j,i,2) = 0;
            FINAL_RETINAL_IMG(j,i,3) = 0;
        end
    end
end

%% ---------------------ILLUMINATION RING SATURATION----------------

Segm_ran = rand(1);
Target_Light = zeros(size(I,1),size(I,2),3);
for i=1:size(Target_Light,2)
    for j=1:size(Target_Light,1)
        if sqrt((j-Tar_X)^2 + (i-Tar_Y)^2) <= Ext_r && ...
                sqrt((j-Tar_X)^2 + (i-Tar_Y)^2) >= Int_r && ...
                (j <= Tar_X-round(Radius/7) ||
j>=Tar_X+round(Radius/7)) && ...
                (i <= Tar_Y-round(Radius/7) ||
i>=Tar_Y+round(Radius/7))

            Target_Light(j,i,2) = (Ext_r - sqrt((j-Tar_X)^2 + (i-
Tar_Y)^2))/(Ext_r - Int_r);
            Target_Light(j,i,3) = 1;
            if sqrt((j-Tar_X)^2 + (i-Tar_Y)^2) <= Int_r +
round(((Ext_r - Int_r)/4) * Segm_ran)
                Target_Light(j,i,1) = 0.06;
            else
```

```
                if sqrt((j-Tar_X)^2 + (i-Tar_Y)^2) > Int_r +
round(((Ext_r - Int_r)/4) * Segm_ran) ...
                        && sqrt((j-Tar_X)^2 + (i-Tar_Y)^2) <= Ext_r
- round(((Ext_r - Int_r)/4) * Segm_ran)
                    Target_Light(j,i,1) = 0.15;
                else
                    Target_Light(j,i,1) = 0.3;
                end
            end
        end
    end
end

Target_Light = imgaussfilt(hsv2rgb(Target_Light),10);

FINAL_RETINAL_IMG = FINAL_RETINAL_IMG + Target_Light;
% Cleaning of the region outside the ROI
for i=1:size(I,2)
    for j=1:size(I,1)
        if sqrt((j-ctr_Y)^2 + (i-ctr_X)^2) >= Radius
            FINAL_RETINAL_IMG(j,i,1) = 0;
            FINAL_RETINAL_IMG(j,i,2) = 0;
            FINAL_RETINAL_IMG(j,i,3) = 0;
        end
    end
end

%% ----------------------RADIAL SYMMETRIC ARTIFACTS-----------------
clear Shape

[X_b, Y_b] = meshgrid(-1:(1/(size(I,2)-1)):1,-1:(1/(size(I,1)-
1)):1);
R = sqrt(X_b.^2+Y_b.^2);

% Random number of peaks
No_peaks = 1;%randi([1 2]);

% Bessel function
a = (-1 +4*rand)*pi;
index = randi([1 3]);
f1 = (2*besselj(index, a*R(:))./R(:)).^2;
f1 = reshape(f1,size(X_b));

a = (-1 +4*rand)*pi;
index = randi([1 3]);
f2 = (2*besselj(index, a*R(:))./R(:)).^2;
f2 = reshape(f2,size(X_b));

% move the peak randomly
f1 = imcrop(f1,[randi([1 round((size(f1,2)-size(I,2))/2)]) ...
    randi([1 round((size(f1,1)-size(I,1))/2)]) ...
    size(I,2)-1 size(I,1)-1]);

f2 = imcrop(f2,[randi([1 round((size(f2,2)-size(I,2))/2)]) ...
    randi([1 round((size(f2,1)-size(I,1))/2)]) ...
    size(I,2)-1 size(I,1)-1]);
```

```
if No_peaks==1
    Shape = f1;
else
    Shape = f1+f2;
end

FINAL_RETINAL_IMG(:,:,1) = FINAL_RETINAL_IMG(:,:,1) + (Shape*.02);
FINAL_RETINAL_IMG(:,:,2) = FINAL_RETINAL_IMG(:,:,2) + (Shape*.03);
FINAL_RETINAL_IMG(:,:,3) = FINAL_RETINAL_IMG(:,:,3) + (Shape*.05);


%% ---------------------------BLURRING & MOTION---------------------

% % Gaussian noise
% var_x = 4;
% var_y = 4;
% IblurGaus = imgaussfilt(FINAL_RETINAL_IMG,[var_x var_y]); % 2-D
Gaussian filtering
%
% % Median filter blurring
% window = 20;
% IblurMed(:,:,1) = medfilt2(FINAL_RETINAL_IMG(:,:,1),[window
window]);  % 2-D median filtering
% IblurMed(:,:,2) = medfilt2(FINAL_RETINAL_IMG(:,:,2),[window
window]);
% IblurMed(:,:,3) = medfilt2(FINAL_RETINAL_IMG(:,:,3),[window
window]);
%
% % Circular averaging filter blurring
% radius = 4; % averaging filter within the square matrix of size
2*radius+1
% DiscFilt = fspecial('disk',radius);  % Circular averaging filter
% IblurDisc = imfilter(FINAL_RETINAL_IMG,DiscFilt);
%
% % Two-dimensional Laplacian filter blurring
% alpha = 0.9; % controls the shape of the Laplacian and must be in
the range 0.0 to 1.0
% LaplFilt = fspecial('laplacian',alpha);  % Approximates the two-
dimensional Laplacian operator
% IblurLap = imfilter(FINAL_RETINAL_IMG,LaplFilt);
%
% % Linear motion of a camera
% len = 20; % linear motion of a camera by len pixels
% theta = 45; % with an angle of theta degrees
% MotFilt = fspecial('motion', len, theta); % Approximates the
linear motion of a camera
% IblurMot = imfilter(FINAL_RETINAL_IMG,MotFilt);
%
% % % Simulation of the electronic noise introduced during the
conversion from
% % % photons to digital value
% % M = 0;    % mean of Gaussian noise
% % V = 0.0009; % variance of Gaussian noise
% % I_sensor = imnoise(I_T_coI,'gaussian',M,V); % adds Gaussian
white noise of mean m and variance v to the image I
% % sigma = 0.9;
% % I_sensor = imgaussfilt(I_sensor,sigma); % filters image I_sensor
with a 2-D Gaussian smoothing kernel with standard deviation sigma
```

```
%
% FINAL_RETINAL_IMG = IblurGaus;
%
% %
imwrite(I_T_coI,['Artifacts\Lens_Transmission\I_after_lens_',num2str
(num_pic),'.tif']);
% %
imwrite(FINAL_RETINAL_IMG,['Artifacts\Artifact_Model\I_art_sim_',num
2str(num_pic),'.tif']);
% % imwrite(I_T_coI,'Artifacts\Eyelashes\I_eyelash_1.tif');

% ------------------------------------------------------------------
% 4 ------- Specular Reflection of the illumination light spot -----
% ------------------------------------------------------------------

Spec_ref = zeros(size(I,1),size(I,2),3);
tras_ref_x = 0; %-Radius/3;
tras_ref_y = - Radius/3;
Radius_prop = 12;

% first Purkinje image
Refl_radius = round(Radius/Radius_prop);
ref_X = ctr_X - Pos_Y;
ref_Y = ctr_Y + Pos_X;
for i=1:size(Spec_ref,2)
    for j=1:size(Spec_ref,1)
        if sqrt((j-Tar_X)^2 + (i-Tar_Y)^2) <= Refl_radius
            Spec_ref(j,i,1) = XenonLight(j,i,1)*R_co(1);
            Spec_ref(j,i,2) = XenonLight(j,i,2)*R_co(2);
            Spec_ref(j,i,3) = XenonLight(j,i,3)*R_co(3);
        end
    end
end
% second Purkinje image
for i=1:size(Spec_ref,2)
    for j=1:size(Spec_ref,1)
        if sqrt((j-Tar_X)^2 + (i-Tar_Y)^2) >= Refl_radius && ...
                sqrt((j-Tar_X+randi([-20 20]))^2 + (i-Tar_Y+randi([-
20 20]))^2) <= Refl_radius*1.4
            Spec_ref(j,i,1) = XenonLight(j,i,1)*R_co(1)*.7;
            Spec_ref(j,i,2) = XenonLight(j,i,2)*R_co(1)*.7;
            Spec_ref(j,i,3) = XenonLight(j,i,3)*R_co(1)*.7;
        end
    end
end
Spec_ref=imgaussfilt(Spec_ref,3.2);

FINAL_RETINAL_IMG = FINAL_RETINAL_IMG + Spec_ref;

% FINAL Cleaning of the region outside the ROI
for i=1:size(I,2)
    for j=1:size(I,1)
        if sqrt((j-ctr_Y)^2 + (i-ctr_X)^2) >= Radius
            FINAL_RETINAL_IMG(j,i,1) = 0;
            FINAL_RETINAL_IMG(j,i,2) = 0;
            FINAL_RETINAL_IMG(j,i,3) = 0;
        end
    end
```

```
end

Art_name = strcat(Retinal_Images(NoRetIm).name(1:10), 'A00',
num2str(uuu), '.jpg');
imwrite(FINAL_RETINAL_IMG,['…',Art_name]) % Insert here the path of
the directory where you want to save the image

    end
   end
```